Inkjet Printing of Bragg Mirrors and Microlens Arrays for Optical Systems

Zur Erlangung des akademischen Grades einer

DOKTORIN DER INGENIEURWISSENSCHAFTEN
(Dr.-Ing.)

von der KIT-Fakultät für
Elektrotechnik und Informationstechnik
des Karlsruher Instituts für Technologie (KIT)

genehmigte

DISSERTATION

von

M.Sc. Qiaoshuang Zhang
geb. in Chengdu, V.R. China
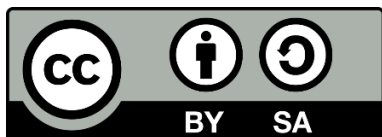
Abstract

Optics and photonics have experienced rapid development, emerging as key enabling technologies for widespread applications in industrial automation and monitoring, consumer electronics, biomedical technologies, automotive, agriculture, and solar technologies. Advanced manufacturing technologies play a crucial role in fostering further innovation and progress in optics and photonics, facilitating complex and customized designs, versatile processes, rapid prototyping, and cost-effective fabrication. In this thesis, the focus is on the development of inkjet printing as the advanced manufacturing method for key optics and photonics components – microlens arrays (MLAs) and Bragg mirrors. This additive manufacturing approach offers significant advantages, including high manufacturing precision, enhanced scalability, improved throughput, excellent flexibility in rapid prototyping, and remarkable adaptability to a diverse range of applications. Hence, inkjet printing demonstrates its potential to be a strong competitor for both laboratory- and industrial-scale optics and photonics component production.

However, employing inkjet printing for fabricating MLAs and Bragg mirrors poses multiple challenges. Firstly, the ink formulations require meticulous engineering of solvent systems to ensure a stable ink ejection process. Secondly, both printing parameters and post-treatment parameters need to be carefully optimized. The fluid dynamics involved throughout the printing and post-treatment processes entail a complex interplay among the inks, printing parameters, and post-treatment parameters. Thirdly, the inkjet-printed layers have to meet the morphological as well as optical requirements of the optics and photonics components, which is a challenging task, especially in the context of multi-layer inkjet printing.

The aim of this thesis is to address these challenges and develop suitable inks, printing, and post-treatment parameters to achieve the fabrication of MLAs and Bragg mirrors through inkjet printing. Firstly, the fabrication of MLAs with an unprecedented fill factor of 88% and exceptional uniformity on unstructured substrates using inkjet printing is presented. Solvent-free UV-curable inks are developed, and a reliable printing process is established with optimized printing parameters. The tunability of the geometrical parameters of the MLAs is demonstrated by applying selected self-assembled monolayers on the substrate, leading to different optical properties. Statistical results show the outstanding uniformity of the printed microlenses as well as the arrays, as evidenced by very low standard deviations of the geometrical parameters. Inkjet printing is proven to be versatile, allowing the fabrication of MLAs in customized patterns, varying dimensions, and on diverse rigid and flexible substrates. The printed MLAs exhibit excellent imaging capabilities. Hence, the application of inkjet-printed MLAs in a multispectral light field camera is subsequently investigated. Color filter arrays are inkjet printed on the opposite

side of the MLA to code the MLA spectrally. The accomplished multispectral light field cameras demonstrate the capability to provide simultaneous information in both 3D spatial and spectral dimensions from a single snapshot. Last but not least, transitioning from micro-optics to nanophotonics, the achievement of the inkjet printing of Bragg mirrors is highlighted. The developed ink formulations and optimized fabrication parameters enable precise control of layer thickness with sub-nanometer resolution and repeatable layer deposition. The photonic bandgaps of the inkjet-printed Bragg mirrors can be tuned from visible light to the near-infrared range by adjusting the number of droplets deposited per unit area. The inkjet-printed Bragg mirrors reach a remarkable reflectance of approximately 99% with only ten printed bilayers. Quantitative spectral and morphological characterization results prove excellent layer uniformity and outstanding optical quality. Furthermore, inkjet printing is employed to produce Bragg mirrors in different sizes, on various substrates, and in designed lateral patterns.

Kurzfassung

Das Forschungsfeld der Optik und Photonik erlebt eine rasante Entwicklung und bildet sich zur Schlüsseltechnologie für weit verbreitete Anwendungen für industriellen Automatisierung und Überwachung, Verbraucherelektronik, Biomedizintechnik, Automobilindustrie, Landwirtschaft und der Solartechnik aus. Fortschrittliche Fertigungstechnologien spielen eine entscheidende Rolle bei der Förderung weiterer Innovationen und Fortschritte in der Optik und Photonik, da sie komplexe und spezialangefertigte Designs, flexible Prozesse, schnelles Prototyping und eine kostengünstige Fertigung ermöglichen. In dieser Dissertation liegt der Schwerpunkt auf der Entwicklung des Tintenstrahldrucks als fortschrittliches Fertigungsverfahren für Schlüsselkomponenten der Optik und Photonik - Mikrolinsenarrays (MLAs) und Bragg-Spiegel. Dieser additive Fertigungsansatz bietet erhebliche Vorteile, darunter eine hohe Fertigungspräzision, eine verbesserte Skalierbarkeit, ein erhöhter Durchsatz, eine hervorragende Flexibilität für schnelles Prototyping und eine bemerkenswerte Anpassungsfähigkeit an eine Vielzahl von Anwendungen. Das Tintenstrahldrucken hat daher das Potenzial, ein starker Konkurrent für die Herstellung von optischen und photonischen Komponenten im Labor- und Industriemaßstab zu sein.

Der Einsatz des Tintenstrahldrucks zur Herstellung von MLAs und Bragg-Spiegeln ist jedoch mit zahlreichen Herausforderungen verbunden. Erstens erfordert die Tintenformulierung ein sorgfältiges Design von Lösemittelsystemen, um eine stabile Tropfenbildung zu gewährleisten. Zweitens müssen sowohl die Druckparameter als auch die Parameter der Nachbehandlung sorgfältig optimiert werden. Die Strömungsdynamik während des Druck- und Nachbehandlungsprozesses erfordert ein komplexes Zusammenspiel zwischen den Tinten, den Druck- und den Nachbehandlungsparametern. Drittens müssen die mit dem Tintenstrahldrucker hergestellten Schichten sowohl die morphologischen als auch die optischen Anforderungen der optischen und photonischen Komponenten erfüllen, was insbesondere im Zusammenhang mit dem mehrschichtigen Tintenstrahldruck eine anspruchsvolle Aufgabe darstellt.

Ziel dieser Arbeit ist es, diese Herausforderungen anzugehen und geeignete Tinten, Druck- und Nachbehandlungsparameter zu entwickeln, um die Herstellung von MLAs und Bragg-Spiegeln durch Tintenstrahldruck zu ermöglichen. Zunächst wird die Herstellung von MLAs mit einem rekordhohen Füllfaktor von 88% und außergewöhnlicher Gleichmäßigkeit auf unstrukturierten Substraten mittels Tintenstrahldruck vorgestellt. Es wurden lösungsmittelfreie UV-härtbare Tinten entwickelt und ein zuverlässiger Druckprozess mit optimierten Druckparametern etabliert. Die Abstimmbarkeit der geometrischen Parameter der MLAs wird durch das Aufbringen ausgewählter selbstorganisierender Monoschichten auf dem Substrat demonstriert, was zu unterschiedlichen optischen

Eigenschaften führt. Statistische Ergebnisse zeigen die herausragende Gleichmäßigkeit der gedruckten MLAs, die sich in sehr geringen Standardabweichungen der geometrischen Parameter äußert. Es wird gezeigt, dass der Tintenstrahldruck vielseitig ist und die Herstellung von MLAs in kundenspezifischen Mustern, unterschiedlichen Abmessungen und auf verschiedenen starren und flexiblen Substraten ermöglicht. Die gedruckten MLAs weisen hervorragende Abbildungseigenschaften auf. Daher wird im Anschluss die Anwendung von tintenstrahlbedruckten MLAs in einer multispektralen Lichtfeldkamera untersucht. Farbfilter-Arrays werden per Tintenstrahldruck auf die gegenüberliegende Seite der MLA gedruckt, um die MLA spektral zu kodieren. Die realisierten multispektralen Lichtfeldkameras zeigen, dass sie in der Lage sind, mit einem einzigen Schnappschuss gleichzeitig Informationen in räumlicher und spektraler 3D-Dimension zu liefern. Zuletzt wird beim Übergang von der Mikrooptik zur Nanophotonik noch die Errungenschaft des Tintenstrahldruckens von Bragg-Spiegeln hervorgehoben. Die entwickelten Tintenformulierungen und optimierten Herstellungsparameter ermöglichen eine präzise Kontrolle der Schichtdicke mit einer Auflösung im Sub-Nanometerbereich und eine reproduzierbare Schichtabscheidung. Die phonischen Bandlücken der Inkjet-gedruckten Bragg-Spiegel können vom sichtbaren Licht bis in den nahen Infrarotbereich eingestellt werden, indem die Anzahl der pro Flächeneinheit abgeschiedenen Tröpfchen angepasst wird. Die im Tintenstrahldruckverfahren hergestellten Bragg-Spiegel erreichen mit nur zehn gedruckten Doppelschichten einen bemerkenswerten Reflexionsgrad von ca. 99 %. Quantitative spektrale und morphologische Charakterisierungsergebnisse belegen eine exzellente Schichtgleichmäßigkeit und hervorragende optische Qualität. Darüber hinaus lassen sich mit dem Inkjet-Druck Bragg-Spiegel in verschiedenen Größen, auf unterschiedlichen Substraten und in entworfenen lateralen Mustern herstellen.

Contents

1   Introduction

1.1   Motivation

景不徒，说在改为…鉴位，景一小而易，一大而正，说在中之外内。

(Engl: An illuminated person shines as if he was shooting forth (rays)… With a concave mirror, the image may be smaller and inverted, or larger and upright.[1])

Book of Mozi (5th-3rd centuries BC)

The straight-line propagation of light and the reflection and focusing of light by concave mirrors – more than two thousand years ago, the phenomena of optics have been observed and documented. The understanding of optics has evolved since then, with a significant spurt in research during the seventeenth century, laying the foundation for modern optics and photonics [2]. A report on the optics and photonics industry published by SPIE in July 2022 highlights the steady growth and high innovation of the industry. Optics and photonics apply as enabling technologies across a wide range of applications, such as consumer electronics, biomedical systems, industrial automation, automotive, sensing, advanced manufacturing and solar technologies [3]. Due to the highly diverse end-use applications, the industry of optics and photonics components, including optical lenses, optical filters, laser chips, image sensors, and others, has proven its robustness and resilience, even during the global pandemic. A rapid growth of core components has been observed, with revenue reaching 302 billion USD in 2020 and a predicted compound annual growth rate of 12% until 2022 [3].

In 2018, the European Commission identified six key enabling technologies (KETs) as research and innovation priorities [4]. Among these, micro/nano-electronics and photonics, advanced manufacturing, and advanced materials were highlighted as three KETs. The innovations of these KETs can mutually enhance each other. With the development of micro/nano-photonics, the scale of the component or system becomes much broader, ranging from nano/micrometer high integration to meter-size large areas with increasingly complex designs. As a result, there is a growing demand for advanced manufacturing technologies to align with these trends and ensure high competitiveness in terms of quality. Furthermore, the symbiotic relationship between manufacturing and materials underscores the crucial role of advanced materials in supporting advanced manufacturing technologies.

Among all advanced manufacturing technologies, inkjet printing stands out and shows high potential for fabricating micro- and nano-photonic components. First of all, inkjet printing enables highly precise deposition of the ink materials in picoliter-scale amounts [5], allowing for direct fabrication of microstructures in the lateral directions and nanostructures in the vertical direction. Since it is a non-contact and solution-processing method, it can produce high-quality surfaces that are essential for optics and photonics. The flexibility of inkjet printing in terms of ink materials and substrates enables the fabrication of photonic components with novel materials, which may encounter challenges with traditional fabrication methods. Besides, the photonic components can be directly fabricated onto various substrates, such as flexible substrates, or directly on the top surfaces of devices. The additive manufacturing nature of inkjet printing reduces fabrication steps, thereby increasing manufacturing efficiency. In addition, this digitalized manufacturing tool allows for unlimited lateral patterning capabilities, rapid prototyping, and precise alignment. The low wastage of valuable functional optical materials and the lower energy consumption during the manufacturing processes align well with the sustainability development goals (SDG) of the United Nations [6]. These advantages are valuable, especially for intricate and expensive photonic components, where fabrication efficiency and rapid prototyping contribute to time, economic, and ecological aspects.

To implement advanced manufacturing technologies for micro-optical and nanophotonic devices, this thesis focuses on developing solvent systems for advanced optical inks, optimizing the associated inkjet printing process, engineering the post-treatment process, and applying comprehensive characterization methods. The micro-optical devices, including microlens arrays (MLAs), are first investigated. The uniform MLAs with direct micro-structuring are successfully fabricated by inkjet printing. Secondly, a potential application for the fabricated MLAs in a light field camera is demonstrated. In order to acquire both spectral and depth information from the objects, the MLAs and color filter arrays (CFAs) are fabricated by inkjet printing. The specifications and precise registrations of the arrays are realized, allowing for high-quality advanced imaging with the fabricated systems. Furthermore, going from the micro- to nanoscale, nanophotonic components—Bragg mirrors—are fabricated layer-by-layer with an exceptional sub-nanometer resolution. The high spectral and optical quality of inkjet-printed Bragg mirrors exhibits the potential of inkjet printing to become a highly competitive fabrication technology, which brings vast advantages compared to conventional technologies. With inkjet printing, the possibility of fabricating micro-optical and nanophotonic devices in a modern, digitalized, and additive way offers numerous advantages for existing applications. Moreover, its larger potential lies in the possibility of enabling unprecedented designs and applications.

1.2   Structure of the Thesis

The scope of this thesis is outlined as follows:

Chapter 2: This chapter delves into the comprehensive fundamentals associated with the following results chapters, including the fundamental working principle of a multispectral light field camera, the geometrical and optical properties of MLAs, the interference theories of Bragg mirrors, and the fundamentals of the inkjet printing technology, including the working principles and the fluid dynamics involved in the printing process.

Chapter 3: This chapter provides an overview of the state-of-the-art fabrication technologies for MLAs and Bragg mirrors. The respective advantages and disadvantages of different manufacturing methods are discussed, and comparative analyses are outlined.

Chapter 4: This chapter presents the materials, experimental, and characterization methods for the inks, substrates, and final devices.

Chapter 5: This chapter introduces the fabrication of MLAs on unstructured substrates by inkjet printing. It starts with the optimized ultraviolet-curable ink formulations, followed by the fabrication and adjustment of the MLAs with different surface treatments. Applying developed automated quantitative evaluations, excellent uniformity of the printed MLAs and an unprecedented fill factor are proven. In the end, the scalability and versatility of the fabrication method are demonstrated on various substrates in different sizes.

Chapter 6: This chapter demonstrates an attractive advanced imaging application for inkjet-printed MLAs and inkjet-printed CFAs. Firstly, a novel concept of a compact multispectral light field camera is introduced. The fabrication of the key miniaturized components for the camera by inkjet printing, including the MLAs and CFAs, is demonstrated, where exceptional precision and seamless integration are realized.

Chapter 7: This chapter presents the nanofabrication of Bragg mirrors by multilayer inkjet printing. The ink formulations and the manufacturing of the Bragg mirrors consisting of up to ten bilayers are introduced. An ultra-high reflectance of 99% is achieved with the printed mirrors. In addition, the tunability of the central wavelength is demonstrated, covering the visible and near-infrared range. In the end, the scalability and versatility of the inkjet-printed Bragg mirrors are showcased. Bragg mirrors are printed with defined lateral patterns on diverse substrates such as glass and foils and in different sizes.

Chapter 8: This chapter summarizes the key results in this thesis and provides an outlook for future research, development, and applications for the presented topics.

2   Theoretical Background

In this chapter, the foundational aspects of imaging systems, optical components, and inkjet printing technology are thoroughly discussed. Section 2.1 outlines the fundamental working principle of a compact multispectral light field camera comprising microlens arrays (MLAs) and spectral filters. This is followed by Section 2.2, where the geometrical, physical, and imaging properties of MLAs are explored. Moving from geometrical optics to wave optics, Section 2.3 discusses the theories of Bragg mirrors, with a particular focus on multilayer interference. The chapter concludes in Section 2.4 with a description of the fabrication technology for the optical components, the inkjet printing technology, encompassing the principles of inkjet printing, fluid dynamics during droplet generation and the formation of the printed pattern.

2.1   Multispectral Light Field Camera

In many of today's rapidly advancing and broadening technology fields, acquiring both three-dimensional (3D) and spectral information of specific scenarios, mainly within the visible light and near-infrared (NIR) spectrum range, is of paramount importance. The information provides the basis for a comprehensive understanding of the recorded scenes in various applications in agriculture [7, 8], food industry [9, 10], biological and medical technology [11, 12], automotive applications [13-16], remote sensing [17, 18], cultural heritage documentation [19, 20], and consumer electronics [21, 22]. Different imaging techniques, ranging from stereo cameras, infrared cameras, and light detection and ranging (LIDAR) systems to multi- and hyperspectral cameras, have been employed to obtain part of the whole desired dataset. Usually, two-dimensional (2D)/3D cameras provide information on the shapes and positions of the objects. In contrast, spectral cameras help with the classification of objects and the analysis of their material composition. The fusion of spatial information with spectral data is crucial for the completeness of the object details and, therefore, leads to a clearer depiction of the overall scenario. Even though it is technically possible to realize the integration of the data from different detection sources using an algorithm, incorporating multiple detection devices is, in general, unfavorable concerning device compactness and ease of calibration. Therefore, the simultaneous capture of the spatial and spectral information in one compact device holds considerable significance.
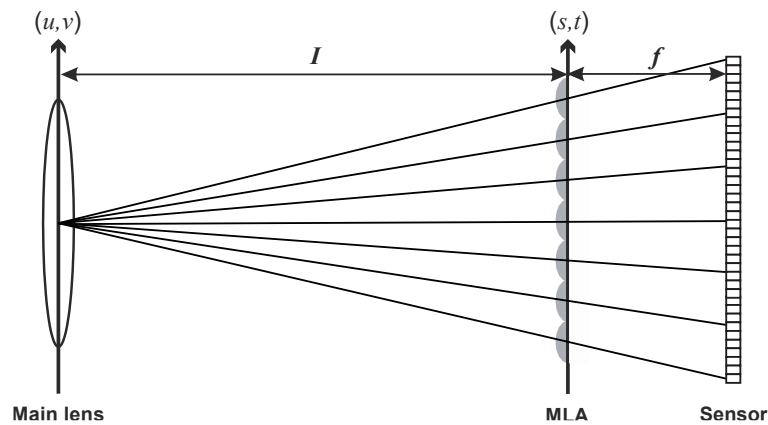
Figure 2.1: Conceptual model of the light field camera in cross-section. The light field camera comprises a main lens, a microlens array (MLA), and a sensor. The main lens has a focal length of *I*, and the MLA has a focal length of *f*. The MLA is placed at the focal plane of the main lens, and the sensor is placed at the focal plane of the MLA. A light ray can be characterized by its intersection at the main lens plane at *(u,v)* and the MLA plane at *(s,t)*.

A light field camera is a computational imaging technique that possesses the capability to capture 3D information of the object field in a single snapshot [23-25]. Generally, an object scene can be defined through the plenoptic function, also known as the five-dimensional light field. This function provides a comprehensive description of how light rays flow in every direction at every spatial point and, therefore, encompasses immense information about the object. In extended geometrical optics, the plenoptic function, or the light field, denoted as $L(x,y,z,\varphi,\theta;\lambda,t)$, can be used to describe the radiance of a scene. Specifically, this function describes the light ray at a specific position *(x,y,z)*, in a particular direction *(φ,θ)*, of a specific wavelength λ, and at a given time *t*. In the case of a light field camera, as it operates in snapshot mode, the temporal component *t* becomes irrelevant and is thereby neglected. Furthermore, the power of light is considered constant along the rays in homogeneous media; therefore, the spatial dimensionality is reduced from five to four. Under these conditions, the spectral 4D light field, denoted as $L(u,v,s,t)$, is derived utilizing a spatio-angular parameterization *(u,v,s,t)*. This parameterization is apt for describing the light rays in the light field camera, as illustrated in **Figure 2.1**. As can be seen, a light field camera typically comprises a primary objective lens, a microlens array (MLA), and a photosensor array of a higher pixel density. In this configuration, a specific light ray can be characterized by its intersections at the plane of the MLA, denoted as *(s,t)*, and at the primary lens plane, denoted as *(u,v)*.
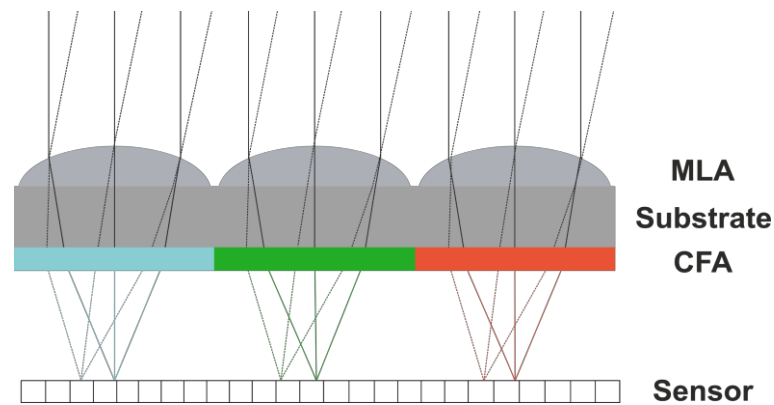
Figure 2.2: Detailed schematic of the microlens array (MLA) and the sensor at the receiving end of the light field camera. The light rays incident on the MLA converge, then pass through the color filter array (CFA), and are collected by the sensor.

The MLA is placed at the focal plane of the main lens, while the image sensor is positioned at the focal plane of the MLA. Each microlens (ML) is associated with several subpixels, each serving as a distinct detector for incident light. After the light rays from one single object point are converged to a point onto the MLA plane by the main lens, these rays diverge again from that point, striking different subpixels on the image sensor. As can be better seen in **Figure 2.2**, when light rays incident parallel to the optical axis on the ML, they converge and are focused onto the central pixel behind the ML. Similarly, rays arriving at oblique angles converge and focus on adjacent pixels. Hence, it is essential to identify the precise centers of the MLs. Subsequently, by determining the distance of a pixel from the central pixel underneath an ML, the *(u,v)* coordinates can be derived. At the same time, the position of the corresponding ML encodes the *(s,t)* coordinates. In the end, the 4D light field *L(u,v,s,t)* can be reconstructed by employing ray tracing methods.
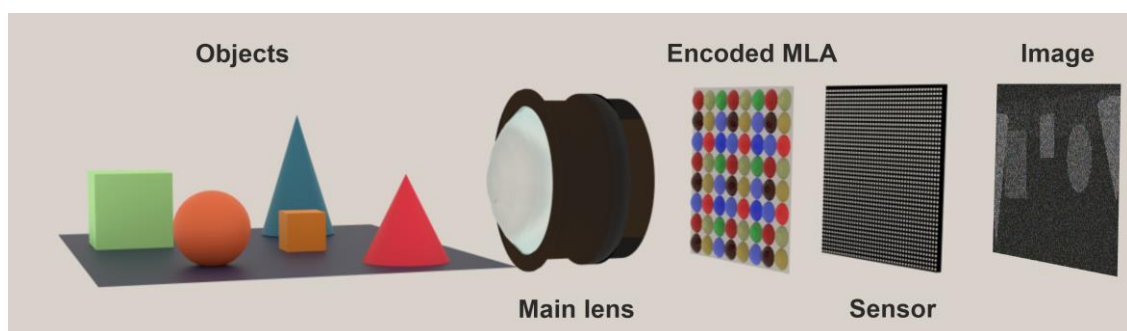
Figure 2.3: Schematic illustration of the multispectral light field camera. The microlens array (MLA) is spectrally coded by incorporating a color filter array, and each microlens is associated with one color filter.

7

Furthermore, in order to obtain the spectral information simultaneously, the light field camera can be spectrally encoded to obtain the information in one more dimension. One approach is to spectrally encode the angular component by adding a color filter array (CFA) at the main lens plane [26-29]. The precise alignment between the CFA, the MLA, and the sensor is necessary in such a configuration. Considering the dimensions of the individual ML and color filter (CF), the distance between the CFA and the MLA is long, and the deviations in the placement of the CFA can lead to a deterioration in the light field reconstruction. Reaching the required accuracy in the position of the CFA, however, is very challenging and hard to maintain in practical scenarios, especially when dealing with unavoidable vibrations. Alternatively, as depicted in **Figure 2.2** and **Figure 2.3**, the CFA can be incorporated at the MLA plane. This configuration allows for higher tolerance in the placement of the components and enhanced resilience when operating in dynamic situations. In this design, each ML is associated with one CF. In practical measurements, the obtained light field can be written as [30]:

$$L^*(u, v, s, t, \lambda) = M(s, t, \lambda) \cdot L(u, v, s, t, \lambda) \tag{2.1}$$

The binary spectral encoding mask $M \in \{0,1\}^{S \times T \times \Lambda}$ should satisfy the following constraint, considering that behind each ML, there is one CF:

$$\sum_{\lambda=1}^{\Lambda} M(s, t, \lambda) = 1 \tag{2.2}$$

In the practical measurements, the spectrally encoded light field represents a projection of the plenoptic function in the spectral dimension as defined below:

$$L_p^*(u, v, s, t) = \sum_{\lambda=1}^{\Lambda} L^*(u, v, s, t, \lambda) \tag{2.3}$$

After the calibration process, the values in the encoding mask matrix M are gathered. M is a binary one-hot matrix, so the encoded light field L^* can be calculated.
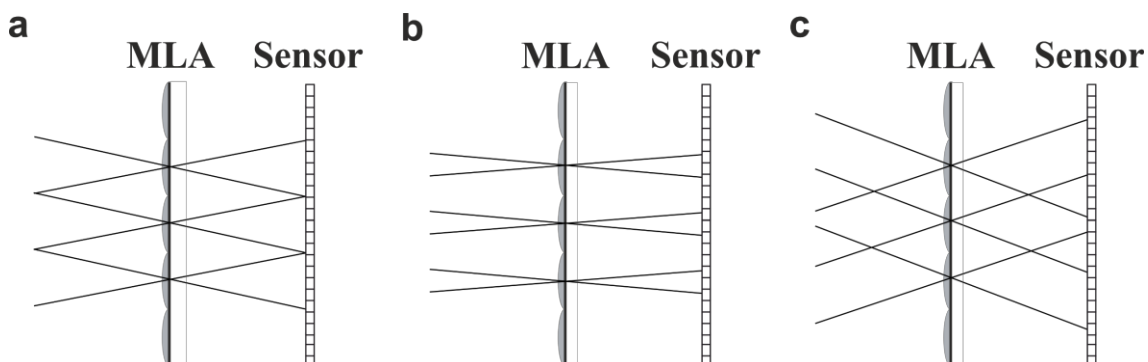
Figure 2.4: Schematic illustration of the *f*-number matching between the main lens and the microlens array (MLA). The light rays come from the edges of the main lens. (a) The *f*-numbers of the main lens and the MLA are identical. The sub-pixels on the sensor are

all used for imaging without any overlapping. (b) The *f*-number of the main lens is larger than that of the MLA. Many sub-pixels on the sensor are not used for imaging, so the angular resolution is not maximized. (c) The *f*-number of the main lens is smaller than that of the MLA. The light rays passing through different microlenses overlap on some sub-pixels. Crosstalk is introduced in this case.

In an optical imaging system, the *f*-number is an important indicator of its ability to gather and direct light onto the image plane. The *f*-number is expressed as [31]:

$$f/\# = \frac{f}{D} \tag{2.4}$$

Here, *f/#* is a single symbol representing the *f*-number. *f* is the focal length of the lens, and *D* is the diameter of the entrance pupil. In order to maximize the usage of the MLs and, consequently, the angular resolution without introducing overlapping and crosstalk between adjacent pixels, it is crucial to ensure the *f*-number matching between the MLA and the main lens. As illustrated in Figure 2.4, when the *f*-number matching condition is met, the largest number of sensor sub-pixels are used for imaging. As there is no overlapping in the light rays coming from neighboring MLs, there is no crosstalk in the final signals acquired by the sensor. However, when there is a mismatch in the *f*-numbers, it can result in two nonideal outcomes: either the angular resolution is reduced due to the smaller number of sub-pixels in use ($f/\#_{Main\ lens} > f/\#_{MLA}$), or the crosstalk is introduced by light rays coming from adjacent MLs ($f/\#_{Main\ lens} < f/\#_{MLA}$). It is worth noting that when the MLA exhibits a packing density of less than 100%, the parameter *D* used in the calculation for the *f*-number matching should take the value of the pitch of the MLA instead of the diameter of the individual MLs.

2.2   Microlens Arrays

An MLA is a regularly arranged array of miniaturized lenses, each with a micron-sized aperture and sag height, as depicted in **Figure 2.5**. MLAs can be divided into two types: the refractive MLAs and diffractive MLAs. The refractive MLs are capable of performing essential refractive functions like traditional lenses, such as focusing and imaging. The diffractive MLs are typically Fresnel zone plates that employ the diffraction principles of light to modulate the phase of the light waves [32-34]. MLAs draw inspiration from their counterpart, the compound eyes found in arthropods, which widely exist in nature [35-37]. In the compound eyes, each ommatidium is equipped with its own lens, and therefore, the configuration usually suffers from poor image resolution [37]. However, the MLAs, which are the counterpart of the ommatidia arranged on a flat plane, possess characteristics of a large field of view, lower aberrations, and a high level of integration [35, 38].
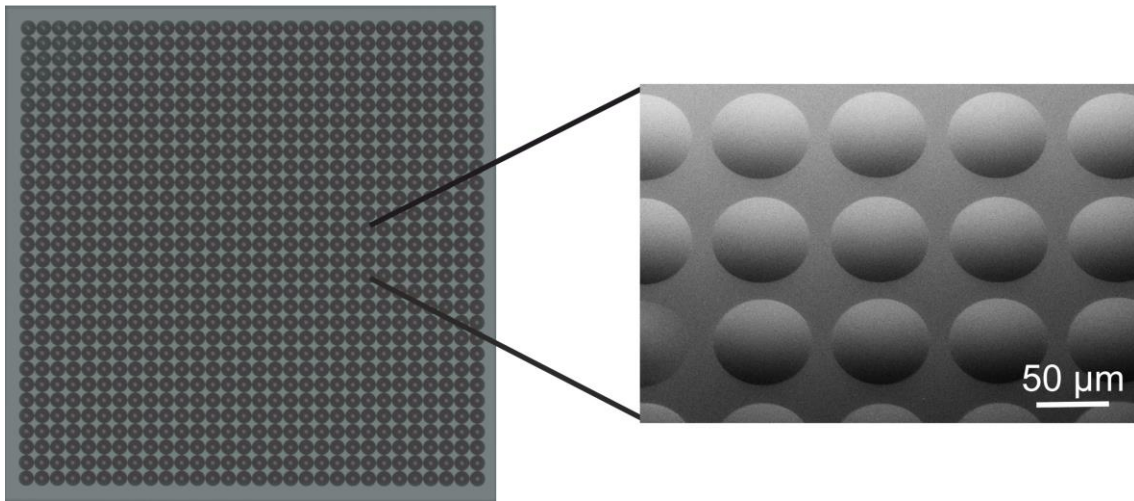
Figure 2.5: A microlens array in a square layout.

Therefore, MLAs find widespread usage in numerous applications that demand high compactness and light-shaping capability. For example, MLAs are used in CMOS and CCD image sensors, where one ML is positioned on top of each pixel, significantly increasing their light-collecting efficiency and sensitivity [39]. Furthermore, MLAs play an essential role in Shack-Hartmann wavefront sensors, where MLAs divide the incoming wavefront into segments and focus the light from each subaperture onto the sensor [40]. By employing this focusing effect, MLAs also contribute to fields such as anti-counterfeiting [41] and solar cells [42]. MLAs further serve as beam collimators for LED arrays for displays [43], optical fiber bundles [44], and vertical-cavity surface-emitting lasers (VCSELs) [45]. As homogenization components, MLAs are found in laser beam shaping [46, 47], LED lighting, and projectors [48, 49]. Besides their use as imaging components in light field cameras, MLAs are integrated into the imaging system for photolithography and microscopy [50-52].

2.2.1 Geometrical and Physical Characteristics

In order to meet the diverse demands of all different kinds of applications, it is essential to consider the important parameters associated with MLAs. First are the geometrical parameters of the array. To evaluate an MLA, one of the most important criteria is the fill factor (FF), defined as the proportion of the surface area of the apertures of the MLs to the entire area of the array. In many use cases, a high FF is preferred as it plays a pivotal role in achieving higher light throughput, consequently leading to enhanced efficiency in light collection and extraction [53, 54].
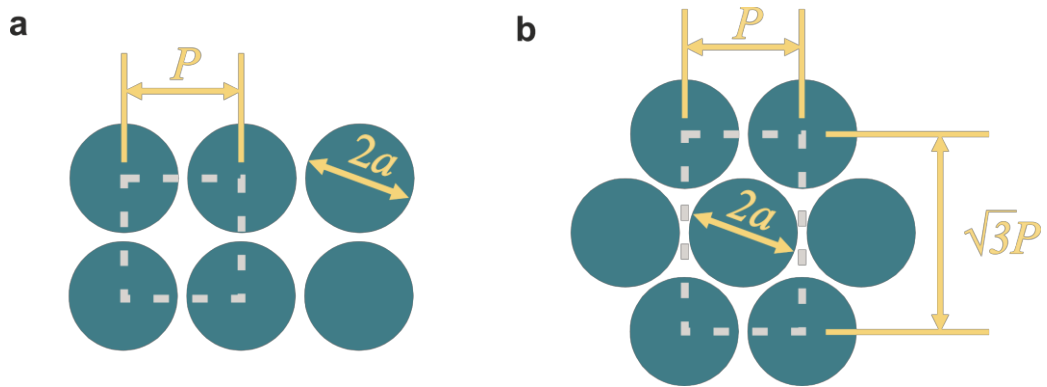
Figure 2.6: Two-dimensional geometrical model of a microlens array. (a) A square layout. (b) A hexagonal layout. This model can be used for the calculation of the fill factor. *P* stands for the pitch between two horizontally adjacent microlenses, and *a* represents the radius of each individual microlens.

Figure 2.6a and b illustrate the 2D geometry of an MLA in a square layout and a hexagonal layout, respectively. Using this model, the FFs in the two different layouts can be calculated following the equations respectively:

$$FF_{square} = \frac{\pi a^2}{P^2} \tag{2.5}$$

$$FF_{hexagonal} = \frac{2\pi a^2}{\sqrt{3}P^2} \tag{2.6}$$

Here, *a* denotes the radius of each individual ML, and *P* stands for the lateral pitch of the MLA, which is the distance between the centers of two horizontally neighboring MLs. From the figure and the equations, it can be seen that the maximum achievable FF is obtained when horizontally adjacent MLs are placed right next to each other without any gaps in between, i.e., *P = 2a*. For a square layout, this upper limit of FF is approximately 78.5%, whereas for a hexagonal layout, it reaches roughly 90.7%. These maximum values apply only to MLAs with circular MLs, and the FF can approach nearly 100% when MLs have a square or a polygon aperture.

For each individual ML, the geometrical parameters also involve those in the longitudinal direction along the optical axis. **Figure 2.7** depicts the cross-sectional geometry of a single plano-convex ML along the optical axis, where *d* is the diameter of the ML, *a* equivalent to *d*/2 denotes the radius, *h* is the sag height, *ROC* is the radius of curvature (ROC) of the convex surface, and *φ* is the half aperture angle.
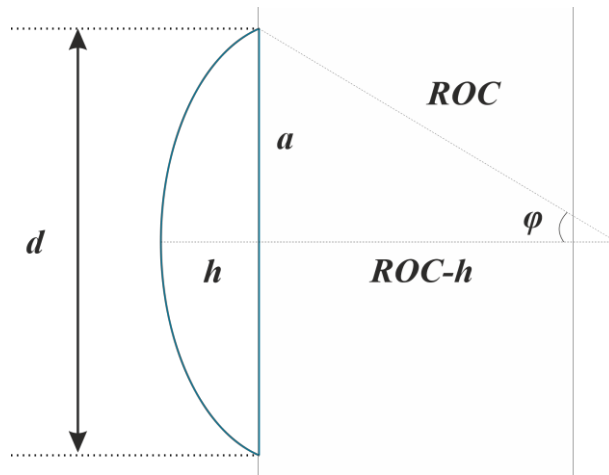
Figure 2.7: Geometry of an individual plano-convex microlens.

In an optical system, the *f*-number given by Equation 2.4 is commonly used to describe the brightness of the image when the object is distant. However, when the object is in the near field, a more suitable indicator of the capability of the optical system for light collection and resolution is the numerical aperture (NA) [31]:

$$NA = n_i \sin \varphi \approx n_i \sin\left[\tan^{-1}\left(\tfrac{a}{f}\right)\right] \tag{2.7}$$

where n_i is the refractive index (RI) of the surrounding medium. Since the resolving power of an optical system is proportional to the wavelength and inversely proportional to the NA, immersing the lenses in a medium such as oil or water, which has a higher RI than air, can lead to improved resolution.

For spherical MLs, the ROC of the convex surfaces can be calculated by the following equation:

$$ROC = \frac{a^2}{2h} + \frac{h}{2} \tag{2.8}$$

For plano-convex lenses, the ROC of the flat surface is infinite ($ROC_2 = \infty$), and the ROC of the convex surface ($ROC_1 = ROC$) plays a major role in bending the light rays. The focal length of the MLs can be calculated by:

$$f = \frac{1}{(n-1)(\varepsilon_1 - \varepsilon_2) + \frac{(n-1)^2}{n} h\varepsilon_1\varepsilon_2} = \frac{1}{(n-1)\varepsilon_1} = \frac{ROC}{n-1} \tag{2.9}$$

Here, ε is the inverse of the ROC. Since the ROC of the plane surface is infinite, ε_2 becomes zero. n denotes the RI of the material, and the lens is placed in air ($n_{air} = 1.0003 \approx 1$).
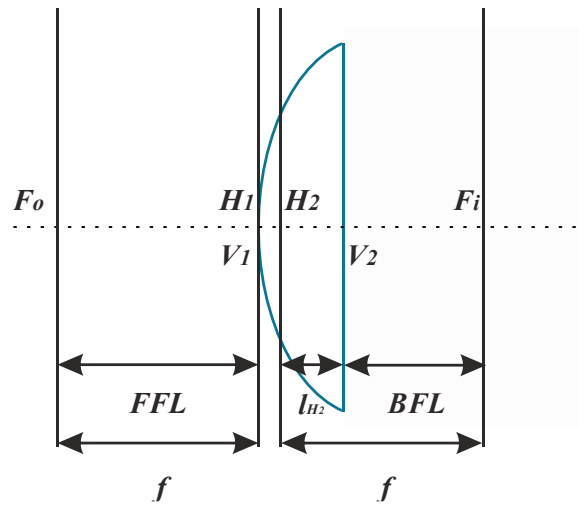
Figure 2.8: The basic optical model of a plano-convex lens. The positions of the primary and secondary principal points H_1 and H_2 (principal planes), and the object and image focal points F_o and F_i (focal planes) of a plano-convex lens are depicted, respectively. The focal length corresponds to the distance between a focal point and the corresponding principal point. The front focal length (FFL) is the distance between the object focal point F_o and the vertex of the first surface of the lens V_1. The back focal length (BFL) is the distance between the image focal point F_i and the vertex of the second surface of the lens V_2.

A basic optical model can be used for plano-convex lenses, as illustrated in **Figure 2.8**. In the model, there exists a pair of principal points and principal planes and a pair of focal points and focal planes. The principal planes are conceptual planes where the bending of light, or refraction, is assumed to occur. In the context of a plano-convex lens, one principal plane is tangential to the convex surface, while the other lies within the lens itself. In **Figure 2.8**, the position of the secondary principal plane with respect to the vertex of the second surface of the lens is given by:

$$l_{H_2} = -\frac{f(n-1)h}{nROC} \tag{2.10}$$

The value is negative, which indicates that the secondary principal plane lies to the left of the second surface of the lens. As a rule of thumb, the distance between these two principal planes approximately equals one-third of the lens thickness [31]. The principal points denote the intersection points of the principal planes with the optical axis. The focal length is the distance between a focal point and its corresponding principal point. The front focal length (FFL) is the distance between the object focal point F_o and the vertex of the first surface of the lens, whereas the back focal length (BFL) is the distance between the image focal point F_i and the vertex of the second surface of the lens. It is worth noting that when the convex surface faces the object, the BFL is shorter than the

focal length. In many practical scenarios, MLAs are fabricated on substrates with a considerable thickness, leading to the possibility of the focal point lying within the substrate when its thickness is significant. Conversely, when the flat surface is oriented towards the object, the BFL is equivalent to the focal length, and the focal point will not be situated inside the substrate. Therefore, in practical measurements of focal length, determining the BFL is often more feasible than measuring the focal length because the principal planes are just hypothetical planes rather than physical planes. Consequently, it is common to position the flat surface facing the incoming light in practical measurements. This simplifies the process of determining the focal length, as it only involves measuring the distance from the focal point to the vertex of the convex surface.

2.2.2 Imaging Capability

In an optical system, the contrast, also called modulation, is used to describe the visibility of a pattern and is given by the Michelson formula [55]:

$$M = \frac{I_{max} - I_{min}}{I_{max} + I_{min}} \tag{2.11}$$

where I_{max} and I_{min} are the maximum and minimum intensity of the object, respectively. When an optical system captures an image, the contrast within that image undergoes a transformation. Therefore, the modulation transfer function (MTF) is defined as the ratio between the image contrast and the original object contrast [31].

Given that the optical system is linear and spatial-invariant, the system analysis method of a linear time-invariant (LTI) system can be adopted and adapted. Here, the object can be treated as the input signal and the image as the output signal. The function of the optical system is solely to convert the input signal into the output signal. The only primary difference between an optical system and an LTI system lies in the fact that the LTI system processes information that varies over time, while the optical system deals with spatially varying information. Therefore, the Fourier analysis method is used extensively in describing and analyzing optical systems.

Conceptually, the optical system can be viewed as a linear, invariant spatial frequency filter. When the optical system captures an image of an object, which is decomposed into a spectrum of different frequencies, it effectively transforms the image. During the transformation, the frequencies of the object signal remain unaltered, but their contrast diminishes, accompanied by a phase shift. At a specific cut-off frequency, the contrast decreases to zero. This relationship between frequency, contrast reduction, and phase shift is referred to as the optical transfer function (OTF). The OTF is, therefore, usually employed to depict the transformation ability of the system for different frequency components. As an essential indicator of the imaging performance of the system, the OTF can be calculated by taking a Fourier transform of the point spread function [56].

The OTF is a complex function comprising the amplitude component known as the MTF and the phase component referred to as the phase transfer function (PhTF). Typically, the MTF characterizes the combined effects of diffraction and aberrations, while the PhTF represents asymmetrical aberrations and suboptimal centering of optical elements [31]. In an ideal, aberration-free system, the MTF is solely constrained by the diffraction limit. For a circular aperture, the diffraction-limited MTF is given by [57]:

$$MTF(\xi) = \frac{2}{\pi} \left\{ \cos^{-1} \left(\frac{\xi}{\xi_c} \right) - \frac{\xi}{\xi_c} \left[1 - \left(\frac{\xi}{\xi_c} \right)^2 \right]^{\frac{1}{2}} \right\} \tag{2.12}$$

where ξ is the spatial frequency, and $\xi_c = [\lambda \cdot (f/\#)]^{-1}$ is the cut-off frequency. In such an ideal system, the PhTF is zero for all spatial frequencies and in all directions. Nevertheless, real-world optical systems inevitably exhibit aberrations. Hence, the OTF, which encompasses the total impact of optical aberrations and diffraction effects, serves as a reliable quantitative means for evaluating optical systems, regardless of whether they possess minimal or substantial aberrations.

2.3 Bragg Mirrors

Optical filters are fundamental components present in virtually every modern optical instrument. As the name suggests, these devices are designed to selectively allow specific wavelengths of light, or colors, to pass through while effectively blocking others. For this purpose, two common types of optical filters are widely used. The first type is known as the CF, which is made from color dyes or pigments. The CF realizes the filtering function by exploiting the inherent properties of the materials they comprise, which enable selective absorption of particular spectral components. The second category, arguably the most important, is the optical interference filter. These filters rely on a highly precise thin film thickness control. Optical interference filters are essential optical components that employ the multilayer interference phenomenon to achieve precise spectral control and manipulation.

Since the CFs rely on the inherent absorption properties of their constituent materials, the intensity spectrum distribution remains unaltered regarding the wavelength. Only the transmittance is adjusted by altering the thickness of the CFs or modifying the concentration of the dye/pigment. Therefore, the spectral characteristics of the CFs do not exhibit angular dependency and have been widely applied in displays and cameras. However, since the dyes and the pigments are primarily organic components, they are susceptible to gradual fading and degradation over time. Additionally, due to their typically broad absorption spectra, they are unsuitable for applications demanding steep cut-on/cut-off edges in transmission, ultra-high transmission/reflection, or narrow bandwidths.

Furthermore, the spectral tunability of the CFs is constrained since their filtering capabilities are fundamentally tied to their constituent materials.

In contrast, optical interference filters provide a significantly greater degree of freedom in shaping the spectral characteristics. These filters consist of multiple thin films composed of two or more materials with different refractive indices or a single material with varying porosity. By meticulously tuning the arrangement of these layers, their thickness, and the material composition, it is possible to tailor the spectra across all dimensions precisely to meet a wide range of specific requirements. These filters can be made into different forms, such as antireflection coatings, high-reflectance mirrors, notch, edge, and band-pass filters. Since the constituent materials are interchangeable, both organic and inorganic materials can be employed to construct the interference filters, each offering distinct advantages. Incorporating inorganic materials ensures a long lifetime, resistance to degradation, and, with some materials, the ability to withstand harsh environmental situations such as abrasion, extreme temperatures, and high humidity. Mechanical flexibility can be achieved when employing organic materials, making them suitable for wearable devices. Additionally, by including specific stimuli-responsive polymers, the filters can be transformed into sensors capable of detecting physical, chemical, or biological stimuli [58]. As a result, interference filters have become indispensable components within optical devices serving a multitude of fields, including life sciences, consumer electronics, automotive, manufacturing, remote sensing, space, and defense.

Bragg mirrors, also referred to as dielectric mirrors, represent a common category of optical interference filters. These mirrors are characterized by a periodic distribution of RI along their thickness direction. Bragg mirrors fulfill various roles in diverse optical systems. Dielectric laser mirrors and dichroic beamsplitters serve as essential discrete components within diverse laser systems. Meanwhile, distributed Bragg reflectors in the form of Bragg mirrors are integral components in VCSELs [59]. In addition, Bragg mirrors can be employed as both functional and visually appealing coatings for solar cells [60, 61]. Beyond these applications, they also find applications in the field of radiative cooling [62].

2.3.1 The Propagation of Light

Based on the electromagnetic theory of light, the reflection and refraction phenomenon of light occurring at the interface between two different dielectric media will be discussed. Here, only non-absorbing dielectric media, which are homogeneous and isotropic, are considered. In absorbing media, the extinction coefficient k has to be considered. As illustrated in **Figure 2.9**, within the *x-z* plane, a plane wave incident on the interface with an incident angle θ_0. The two media have the refractive indices of n_0 and n_1, respectively. Typically, the electric field vector E is used to represent the light wave, and the incident wave can be decomposed into two orthogonal components. One of these components

oscillates in a direction perpendicular to the incident plane (E_s), while the other oscillates parallel to the incident plane (E_p). The incident wave undergoes decomposition into a reflected wave and a refracted (transmitted) wave.
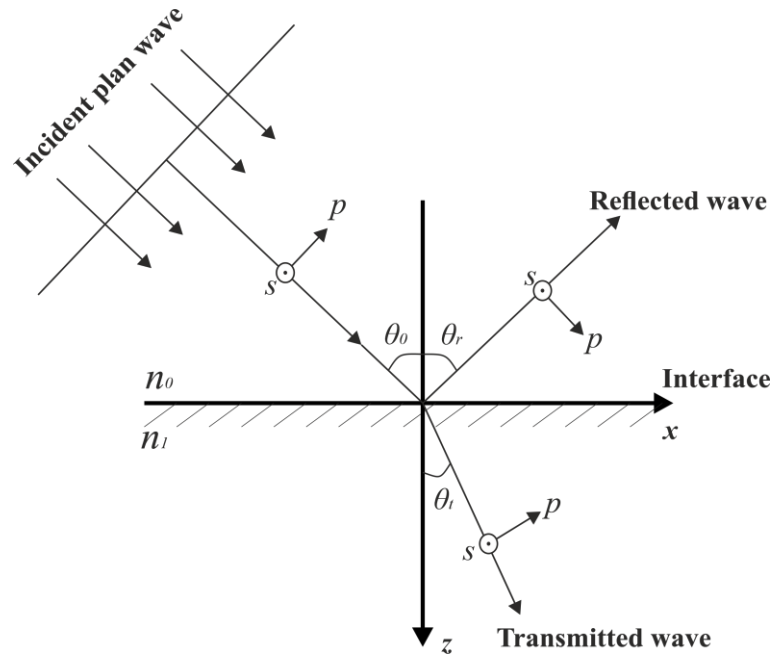
Figure 2.9: The reflection and refraction of a plane wave of incident on an interface of two media. In this illustration, the convention for defining the positive directions of the two electric field vector components E_s and E_p at oblique incidence is indicated. The two media have refractive indices of n_0 and n_1, respectively.

The wave functions of these three waves can be expressed as follows:

$$E_i = E_{i0}\exp\left\{i\left[\omega_i t - \frac{2\pi n_0}{\lambda_0}(x\sin\theta_0 + z\cos\theta_0)\right]\right\} \tag{2.13}$$

$$E_r = E_{r0}\exp\left\{i\left[\omega_r t - \frac{2\pi n_0}{\lambda_0}(x\sin\theta_r + \beta_r y - z\cos\theta_r)\right]\right\} \tag{2.14}$$

$$E_t = E_{t0}\exp\left\{i\left[\omega_t t - \frac{2\pi n_1}{\lambda_0}(x\sin\theta_t + \beta_t y + z\cos\theta_t)\right]\right\} \tag{2.15}$$

where E_{i0}, E_{r0}, E_{t0}, ω_i, ω_r, ω_t are the amplitude vectors and the angular frequencies of the three wave functions, respectively. t denotes time, λ_0 is the wavelength of light in free space, θ_0, θ_r, θ_t corresponds to the angles of incidence, reflection, and refraction in that order, and β_r and β_t are direction cosines in the y-direction of the light wave propagation. According to the boundary conditions, at the interface ($z = 0$) for all x, y, and t, the tangential components of the electric field vectors must remain continuous. Therefore, the coefficients of the variables in the phase factors must be identical in each term. Firstly,

$\omega_i = \omega_r = \omega_t$, which indicates that there is no change in the frequency of the light throughout these interactions. Next, $0 = \beta_r = \beta_t$, which demonstrates that both the reflected and transmitted light beams are confined to the incidence plane (x-z plane). Subsequently, $\theta_0 = \theta_r$, which is the reflection law, showing that the angle of incidence equals the angle of reflection. Furthermore, θ_t can be replaced by θ_1, the Snell's law is derived:

$$n_0 \sin \theta_0 = n_1 \sin \theta_1 \tag{2.16}$$
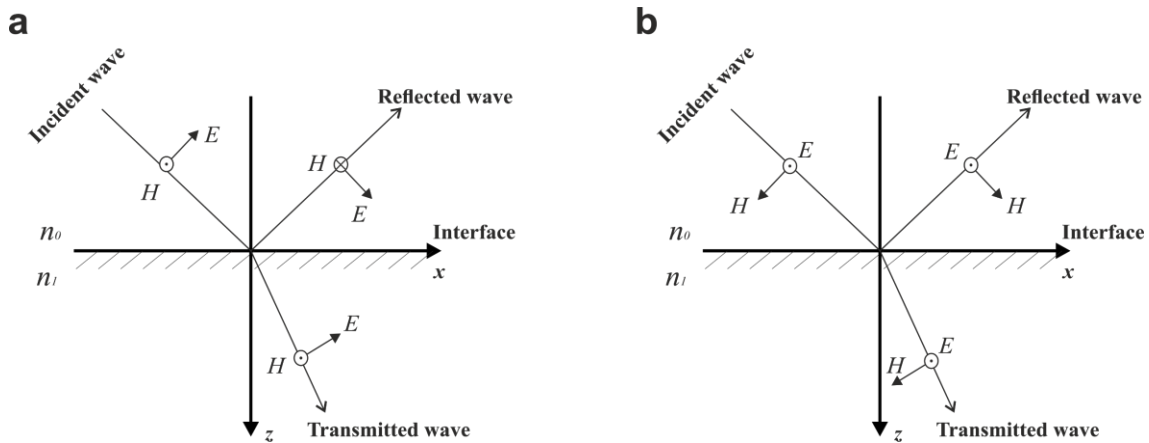
Figure 2.10: Conventions for the positive directions of the electric and magnetic field vectors $\boldsymbol{E}$ and $\boldsymbol{H}$. (a) For p-polarized TM waves. (b) For s-polarized TE waves.

In order to determine the changes in the amplitudes of the waves, the two components of the electric field vector are considered separately, and the two configurations are illustrated in **Figure 2.10**. The boundary conditions apply for both the electric and magnetic field vectors, so their components, which are parallel to the interface, have to be continuous at the interface. For the p-polarized TM waves:

$$E_i \cos \theta_0 + E_r \cos \theta_0 = E_t \cos \theta_1 \tag{2.17}$$

$$H_i + H_r = H_t \tag{2.18}$$

Furthermore, the relationship between the electric and magnetic field vectors is given by:

$$\boldsymbol{H} = y(\boldsymbol{s_0} \times \boldsymbol{E}) = n y_0 (\boldsymbol{s_0} \times \boldsymbol{E}) \tag{2.19}$$

Here, $\boldsymbol{s_0}$ is the unit wave vector, y is defined as the characteristic optical admittance of the medium, and y_0 is the optical admittance in free space, which is a constant. Then equation 2.18 can be written as:

$$y_0 E_i - y_0 E_r = y_1 E_t \tag{2.20}$$

The same rules apply to s-polarized TE waves. As a result, Fresnel's equations can be derived from the ratios $r = E_r/E_i$ and $\tau = E_t/E_i$:

$$r_p = \frac{n_0 \cos\theta_1 - n_1 \cos\theta_0}{n_0 \cos\theta_1 + n_1 \cos\theta_o} \tag{2.21}$$

$$r_s = \frac{n_0 \cos\theta_0 - n_1 \cos\theta_1}{n_0 \cos\theta_0 + n_1 \cos\theta_1} \tag{2.22}$$

$$\tau_p = \frac{2n_0 \cos\theta_0}{n_0 \cos\theta_1 + n_1 \cos\theta_o} \tag{2.23}$$

$$\tau_s = \frac{2n_0 \cos\theta_0}{n_0 \cos\theta_0 + n_1 \cos\theta_1} \tag{2.24}$$

where r and τ are the amplitude reflection and transmission coefficients, respectively. Based on the equations above, it can be seen that the transmitted light waves do not undergo any phase change. In contrast, for the reflected waves, when light travels from the less dense medium (with a lower RI) to the denser one, with an incidence angle smaller than the Brewster angle, the reflected wave experiences a phase shift of π, which is referred to as the half-wave loss. Since the tangential components of the electric and magnetic field vectors are mostly considered, the effective optical admittance η is introduced, defined as the ratio between the tangential component of the magnetic field vector and that of the electric field vector. At normal incidence, the effective admittance equals the optical admittance ($\eta = y$). At oblique incidence, the effective admittances are given by:

$$\eta_p = \frac{y}{\cos\theta} = \frac{n y_0}{\cos\theta} \tag{2.25}$$

$$\eta_s = y \cos\theta = n y_0 \cos\theta \tag{2.26}$$

The reflectance and transmittance can be calculated by:

$$R = |r|^2 = \left(\frac{\eta_0 - \eta_1}{\eta_0 + \eta_1}\right)^2 = \begin{cases} \left(\frac{n_0 \cos\theta_1 - n_1 \cos\theta_0}{n_0 \cos\theta_1 + n_1 \cos\theta_0}\right)^2 & (p - \text{polarized}) \\ \left(\frac{n_0 \cos\theta_0 - n_1 \cos\theta_1}{n_0 \cos\theta_0 + n_1 \cos\theta_1}\right)^2 & (s - \text{polarized}) \end{cases} \tag{2.27}$$

$$T = \frac{y_1}{y_0} |\tau|^2 = \begin{cases} \frac{4 n_0 n_1 \cos\theta_0 \cos\theta_1}{(n_0 \cos\theta_1 + n_1 \cos\theta_0)^2} & (p - \text{polarized}) \\ \frac{4 n_0 n_1 \cos\theta_0 \cos\theta_1}{(n_0 \cos\theta_0 + n_1 \cos\theta_1)^2} & (s - \text{polarized}) \end{cases} \tag{2.28}$$

As the behavior of light in the thin film is the superposition of the Fresnel coefficients of the light waves at the interfaces of the layered medium, the characteristics of multilayer films can be analyzed using these coefficients.

2.3.2 Multilayer Optical Interference

Optical interference is a significant manifestation of the wave nature of light. Light waves adhere to the principle of wave superposition, wherein within the overlapping region of the light waves, some points experience reinforcement of oscillations while others undergo attenuation. When the light waves involved in the superposition satisfy the condition of coherence, the intensity of the light waves at the superposition point depends on the phase difference between the light waves. Constructive interference occurs when the phase shift is an even integer multiple of π (0, $\pm 2\pi$, $\pm 4\pi$, …), resulting in maximum intensity. Conversely, the minimum intensity is obtained when the phase difference is an odd integer multiple of π (0, $\pm\pi$, $\pm 3\pi$, …), and the condition is referred to as destructive interference.
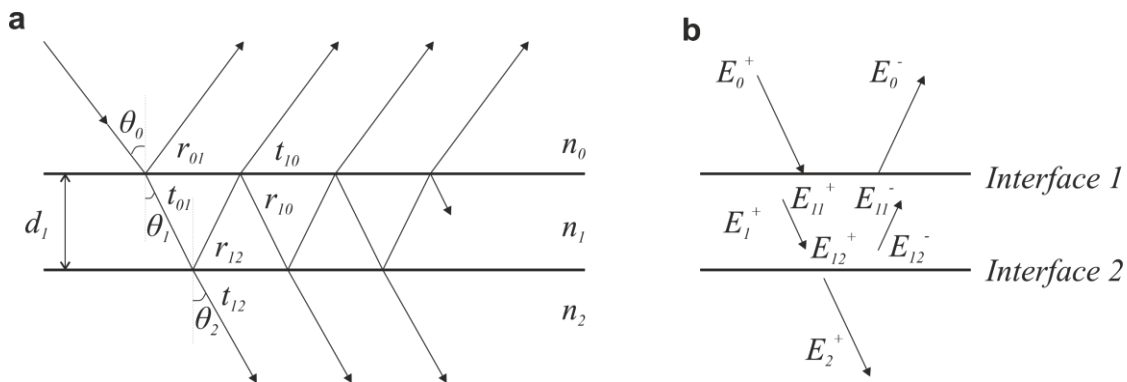
Figure 2.11: Light incident on a single-layer thin film. (a) The multiple beam interference in the single thin film. (b) The conventions defining the positive and negative directions of light propagation.

For a single-layer thin film, the multiple reflected and transmitted optical beams interfere with each other, respectively. The phase difference between two neighboring transmitted/reflected beams can be calculated:

$$2\delta_1 = \frac{4\pi}{\lambda} n_1 d_1 \cos\theta_1 \tag{2.29}$$

where d_1 is the thickness of the layer. The complex amplitude of the m-th transmitted beam can be written as $\tau_{01}\tau_{12}r_{12}{}^{m-1}r_{10}{}^{m-1}e^{-i2(m-1)\delta}E_0$. The first and m-th reflected beams can be written as $r_{01}E_0$ and $\tau_{01}\tau_{10}r_{12}{}^{m-1}r_{10}{}^{m}e^{-i2(m-1)\delta}E_0$, respectively. τ and r are the Fresnel coefficients at the interfaces with light coming from opposite directions, as depicted in **Figure 2.11**. The total composite transmitted and reflected waves are the sum of the respective beams to infinity:

$$E_t = \frac{\tau_{01}\tau_{12}}{1-r_{21}r_{10}e^{-i2\delta_1}}E_i \tag{2.30}$$

$$E_r = \left(r_{01} + \frac{r_{12}\tau_{01}\tau_{10}e^{-i2\delta_1}}{1-r_{12}r_{10}e^{-i2\delta_1}}\right)E_i \tag{2.31}$$

Accordingly, the transmittance and reflectance are given by:

$$T = \frac{(\tau_{01}\tau_{12})^2}{(1-r_{21}r_{10})^2+4r_{21}r_{10}\sin^2\delta_1} \tag{2.32}$$

$$R = \frac{(r_{10}-r_{12})^2+4r_{10}r_{12}\sin^2\delta_1}{(1-r_{10}r_{12})^2+4r_{10}r_{12}\sin^2\delta_1} \tag{2.33}$$

Alternatively, all waves in the same direction in each medium can be grouped, as illustrated in **Figure 2.11**b. Applying the boundary conditions for the tangential components of electric and magnetic field vectors at the interfaces, the following equations can be obtained:

$$E_0 = E_0^+ + E_0^- = E_{11}^+ + E_{11}^- = E_{12}^+e^{i\delta_1} + E_{12}^-e^{-i\delta_1} \tag{2.34}$$

$$H_0 = H_0^+ - H_0^- = \eta_1 E_{11}^+ - \eta_1 E_{11}^- = \eta_1 E_{12}^+e^{i\delta_1} - \eta_1 E_{12}^-e^{-i\delta_1} \tag{2.35}$$

$$E_2 = E_{12}^+ + E_{12}^- \tag{2.36}$$

$$H_2 = \eta_1 E_{12}^+ - \eta_1 E_{12}^- \tag{2.37}$$

The above equations can be transformed into the matrix form:

$$E_0\begin{bmatrix}1\\Y\end{bmatrix} = \begin{bmatrix}\cos\delta_1 & \frac{i}{\eta_1}\sin\delta_1 \\ i\eta_1\sin\delta_1 & \cos\delta_1\end{bmatrix}\begin{bmatrix}1\\\eta_2\end{bmatrix}E_2 \tag{2.38}$$

Where $Y = H_0/E_0$ is defined as the input optical admittance, the first matrix on the right side of the equation is called the characteristic matrix of a thin film, and the multiplication of all the matrices on the right side is called the characteristic matrix of the assembly. In this way, the two surfaces of the single-layer thin film can be represented by one equivalent interface, where the light incident from the first medium to the other medium with an admittance of Y. The reflectance of the thin film can then be written as:

$$R = \left|\frac{\eta_0-Y}{\eta_0+Y}\right|^2 \tag{2.39}$$

And Y is calculated as:

$$Y = \frac{\eta_2\cos\delta_1+i\eta_1\sin\delta_1}{\cos\delta_1+i(\eta_2/\eta_1)\sin\delta_1} \tag{2.40}$$

From the equations above, it can be seen that when the effective optical thickness of the thin film is the multiple integers of a quarter wave, i.e., δ being a multiple integer of π,

the extremes occur for the reference wavelengths. When the effective optical thickness equals an odd integer of a quarter wave, $Y = \eta_1^2/\eta_2$, and the reflectance at the reference wavelength reaches its maximum value when $n_1 > n_2$ and its minimum value when $n_1 < n_2$. Conversely, the situation is reversed when the effective optical thickness is an even integer of a quarter wave. However, in this case, $Y = \eta_2$, indicating that the thin film does not influence the spectral properties. Therefore, such a thin film is usually called the virtual layer for the reference wavelength. Nevertheless, for other wavelengths, this layer still has an impact; thus, the virtual layers are frequently employed to smoothen the spectral characteristics of the thin film.
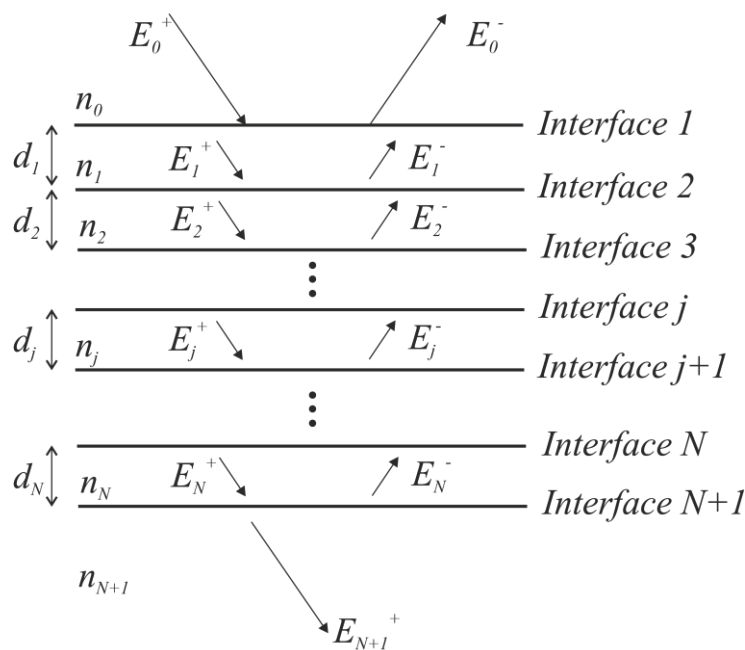
Figure 2.12: Light incident on a multilayer thin film.

The same approach can be extended to analyze multilayer thin film stacks. These stacks can also be equivalently represented by a solitary virtual interface with the second medium characterized by an optical admittance of Y. As illustrated in **Figure 2.12**, at each interface j and j+1:

$$\begin{bmatrix} E_{j-1} \\ H_{j-1} \end{bmatrix} = \begin{bmatrix} \cos \delta_j & \dfrac{i}{\eta_j} \sin \delta_j \\ i\eta_j \sin \delta_j & \cos \delta_j \end{bmatrix} \begin{bmatrix} E_{j+1} \\ H_{j+1} \end{bmatrix} \tag{2.41}$$

Due to the continuity of E and H at the interfaces, the characteristic matrix is simply the result of multiplying the individual characteristic matrices of each layer:

$$E_0 \begin{bmatrix} 1 \\ Y \end{bmatrix} = \left\{ \Pi_{j=1}^{N} \begin{bmatrix} \cos \delta_j & \frac{i}{\eta_j} \sin \delta_j \\ i\eta_j \sin \delta_j & \cos \delta_j \end{bmatrix} \right\} \begin{bmatrix} 1 \\ \eta_{N+1} \end{bmatrix} E_{N+1} \tag{2.42}$$

The reflectance of the stack can be calculated using equation 2.39. Since the quarter-wave layers are used frequently, certain conventions are used to describe the thin film structure. Typically, H is used to represent the quarter-wave layers with a high RI, while L is used for the quarter-wave layers with a low RI.

2.3.3 Characteristics of Bragg Mirrors

A standard Bragg mirror layer structure is the structure of a high-reflectance dielectric mirror, which is a typical quarter-wave stack. In this stack, layers with high and low refractive indices are alternately stacked and arranged. When the RI of the L layer is lower than that of the substrate, the stack structure can be written as S|(LH)^N|A, where S, L, H, and A correspond to the substrate, low-RI layer, high-RI layer, and air, respectively. The parameter N denotes the total number of bilayers. Within such stacks, the beams reflected from interfaces return to the preceding interface with equal phases, leading to constructive interference at the front surface. In theory, the reflectance of a quarter-wave stack can achieve nearly 100%.

Under normal incidence conditions, the central wavelength of a Bragg mirror is determined by the following relation:

$$\lambda_c = 4n_H d_H = 4n_L d_L \tag{2.43}$$

where n_H and n_L are the refractive indices of the H and L layers, while d_H and d_L are the thicknesses of the H and L layers, respectively. It can be seen that the central wavelength can be altered by adjusting the material composition and, even more simply, by changing the layer thickness. For example, as the thickness of these layers increases, the reflectance peaks of the mirrors undergo a red shift towards longer wavelengths. For the central wavelength λ_c, the optical admittance of the equivalent medium can be expressed according to equation 2.40:

$$Y = n_S \left(\frac{n_H}{n_L} \right)^{2N} \tag{2.44}$$

where n_S denotes the RI of the substrate. Thus, the reflectance at the central wavelength, which is the maximum reflectance, can be computed as follows:

$$R = \left[\frac{1-n_S\left(\frac{n_H}{n_L}\right)^{2N}}{1+n_S\left(\frac{n_H}{n_L}\right)^{2N}}\right]^2 \tag{2.45}$$

From this equation, it can be seen that the maximum reflectance increases with the number of layers and the RI contrast between H and L layers. When $Y \gg 1$, the reflectance is approximated as:

$$R = 1 - \frac{4n_S\left(\frac{n_H}{n_L}\right)^{2N}}{\left(1+n_S\left(\frac{n_H}{n_L}\right)^{2N}\right)^2} \approx 1 - \frac{4n_L^{2N}}{n_S n_H^{2N}} \tag{2.46}$$

It is important to note that in practice, when the number of layers in a stack is increased to a certain number, continuing to add more layers ceases to improve its reflectance any more. Due to the growing absorption and scattering losses, they can no longer be neglected, leading to a decrease in reflectance with increasing layers.

The refractive index contrast also determines the stopband width (W) for the Bragg mirrors and can be calculated using the following equation [63]:

$$W \approx \frac{4\lambda_0}{\pi}\sin^{-1}\left(\frac{n_H-n_L}{n_H+n_L}\right) \tag{2.47}$$

When the difference in the RI of the constituent materials is larger, a broader reflection band can be obtained.

2.4 Inkjet Printing

Inkjet printing is a technology where a large number of picoliter-volume droplets are ejected from nozzles onto the substrates. This technology is a versatile manufacturing tool that enables the digital creation and precise application of the graphics onto substrates. With this feature, inkjet printing has found wide applications in industries such as packaging, textiles, and advertising [64, 65]. Moreover, considering the digital fabrication manner, the droplet positioning precision, and the extremely low volume of each droplet, the potential of inkjet printing extends from its traditional role in printing.

Inkjet printing has found its vital role in functional printing, especially for fabricating nano- and micro-scale functional optical, electrical, and optoelectronic devices. Given its digital nature and remarkable precision reaching down to the micrometer scale, inkjet printing has emerged as a crucial tool for the production of intricate functional devices. Over the last decades, there has been a growing trend of integrating inkjet printing into various technologies involving functional materials. For instance, inkjet printing serves as a versatile method for directly producing and structuring optical components like

MLAs and scattering layers [66, 67]. Besides, its application extends to functional layers in perovskite as well as organic solar cells [68-70]. In the field of displays, inkjet printing is of particular interest and finds its use in fabricating organic light-emitting diodes [71-73], CFs for liquid crystal displays [74], plasma display panels [75], and quantum dot light-emitting diodes [76]. Furthermore, inkjet printing is applied in selective deposition processes when fabricating thin-film transistors [77, 78]. In the field of printed circuit boards, inkjet printing offers distinctive advantages for printing legends, solder masks, and metal components [78, 79]. With novel features such as flexibility and higher integration possibilities introduced by inkjet printing, different kinds of sensors have been successfully manufactured by inkjet printing [80-82].

During the inkjet printing process, ink droplets with suitable rheological properties are properly generated and expelled through the nozzles. Subsequently, these ink droplets reach the substrates, where they coalesce to create patterns ranging from dots and lines to complete films or various custom shapes. Finally, the printed material undergoes solidification, giving it the final structure.

Compared to other fabrication technologies used in nano- and micro-fabrication, inkjet printing presents numerous advantages. It is a high-throughput and non-contact method, making it compatible with a broad range of substrates, ranging from rigid to flexible substrates. When the printing process is optimized for one surface, transferring the process to other surfaces is usually feasible. In addition, the precise control over the deposited ink volume enhances the accuracy of fabrication. The droplet volume is usually in the pico-liter range, giving micro-structures in the lateral dimensions and nanoscale thickness in the vertical dimension. Moreover, it allows for fast production. Together with its limitless design possibilities, rapid prototyping can be achieved by using inkjet printing. Additionally, it significantly reduces material wastage, especially when valuable functional inks are used [83].

2.4.1 Continuous and Drop-on-Demand Inkjet Printing Technology

Based on the fundamental principles, inkjet printing technologies are divided into continuous inkjet (CIJ) and drop-on-demand (DOD) inkjet printers. **Figure 2.13** shows the working principles of a CIJ, a thermal DOD, and a piezoelectric DOD printer, which are the most used inkjet printing systems. The CIJ method is commonly used for marking and coding applications. In a CIJ system, a continuous stream of droplets is formed via the Plateau-Rayleigh instability and is generated from the nozzle by applying pressure to the ink channel. The droplets pass through a charging station, where the electric field from the charging electrode undergoes controlled changes. Only specific droplets are charged, distinguishing them from the uncharged background droplets, which are not used for printing. The background droplets continue along their initial trajectory and are collected

in a gutter. This collected ink is redirected into the recycling system, improving the material efficiency. However, these droplets are already exposed to the external environment, thus introducing contamination risks. Meanwhile, the charged droplets, deflected by the applied electric field, are directed to hit targeted spots on the substrate.
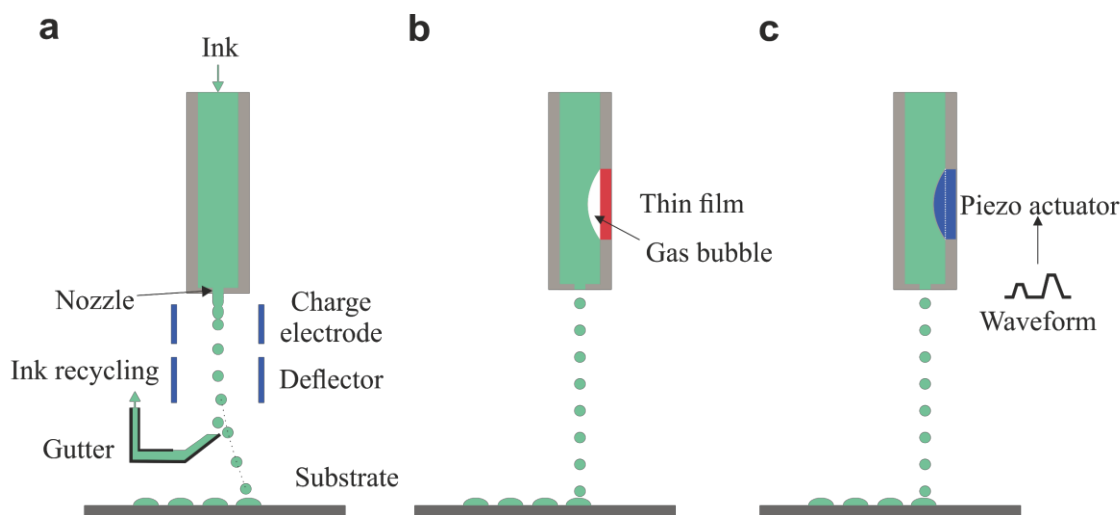
Figure 2.13: Schematic diagrams of the working principles of different inkjet printing systems. (a) Continuous inkjet printer. (b) Drop-on-demand (DOD) thermal inkjet printer, where a gas bubble is produced using a thin-film heater. (c) DOD piezoelectric inkjet printer, where the wall of the ink channel undergoes mechanical deformation by a piezo actuator.

In contrast, instead of generating a continuous stream of droplets, the DOD systems eject individual ink droplets only as demanded. In the ink-jetting process, a pressure pulse is introduced into the ink channels to expel droplets from nozzles. All ejected droplets are used for printing, minimizing the material waste to nearly zero. There are two widely used types of DOD systems: thermal DOD printers and piezoelectric DOD printers. In thermal DOD systems, as seen in Figure 2.13b, bubbles are created by rapidly vaporizing ink via heating a thin film heat element to high temperatures. Under this condition, a highly volatile component in the ink is required for bubble formation through vaporization. Due to the frequent thermal changes, these printheads usually have a limited lifespan. Additionally, the working principle poses challenges in achieving precise control over ejected droplet volumes.
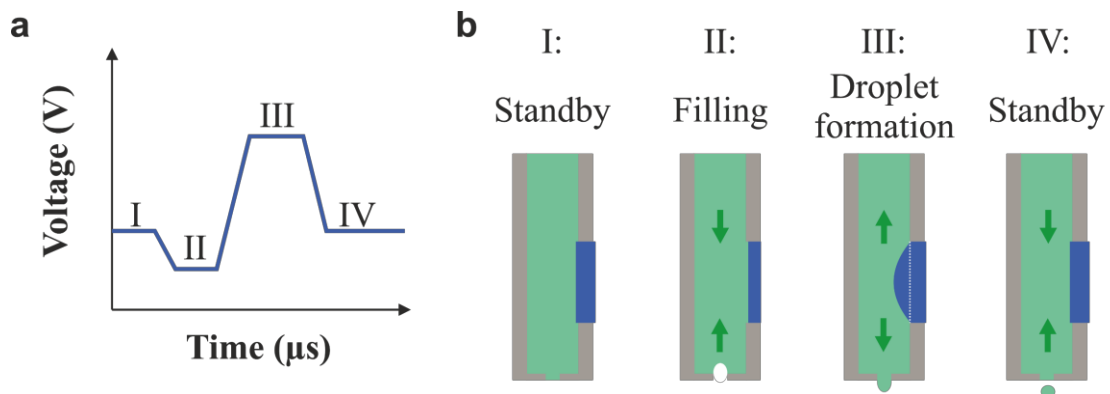
Figure 2.14: The droplet ejection process in a piezoelectric printhead. (a) Typical waveform applied to the printhead. (b) The schematic illustration of different stages for droplet formation in a drop-on-demand piezoelectric printhead.Stage I: standby phase. Stage II: filling. Stage III: droplet formation. Stage IV: droplet ejection and return to standby phase.

In the other type of DOD system, the piezoelectric printer depicted in **Figure 2.13**c, the heat elements are replaced by the piezoelectric elements, one for each nozzle. Applying voltage to the printhead with a specific waveform causes mechanical deformation of the piezoelectric components. When the deformation exceeds a certain threshold, the pressure within the ink channel propels a droplet from the nozzle. **Figure 2.14** illustrates an example of the voltage waveform and the different stages of droplet formation in a DOD piezoelectric printhead. Initially, the piezoelectric element has a slight deformation, and the ink channel is in a standby phase. Upon applying a lower voltage to the printhead, negative pressure builds up in the channel, contracting ink from the reservoir. Simultaneously, ink contracts from the direction of the nozzle, forming a meniscus. Subsequently, a positive pulse causes the piezoelectric element to expand, generating a pressure wave in the ink channel, leading to the formation of a droplet. In the final stage, reducing the voltage restrains the ink, resulting in the ejection of the droplet. The droplet forms a spherical shape due to surface tension, and the printhead returns to the standby phase. The described sequence represents a single pulse, and these processes typically unfold within the microsecond range. Multiple pulses can be generated to increase the volume of the final droplet. This process allows for precise control of droplet volumes and velocity. It has been successfully applied to micro-fabrication using various types of inks, including water-based [84-86], solvent-based [66, 87, 88], nanoparticle dispersion [89-91], and UV-curable inks [92-94].

2.4.2   Ink Printability

Understanding the fluid dynamics throughout the printing process is essential for inkjet printing. These processes include activities in the printhead, such as ink flow in channels, droplet generation, the impact of ink wetting on the nozzle plate, and fluid dynamics in

post-ejection processes after the droplets land on the substrate. The intricate nature of these fluid dynamics involves a complex interplay among all various factors. Therefore, both ink formulations and printing parameters must be meticulously adjusted to ensure smooth droplet ejection and achieve the desired final printed structure. The parameters within the ink formulation, such as density, surface tension, viscosity, boiling point, and vapor pressure, can significantly impact the printing process.

In inkjet fluid dynamics, a set of dimensionless numbers, defined by the ratio of various forces, are used to determine the printability of the ink. The first relevant number is Reynolds number (*Re*), which is defined as the ratio of inertial forces and viscous forces of the fluid, and the number is given by [95]:

$$Re = \frac{vl}{v} = \frac{\rho vl}{\mu} \tag{2.48}$$

where *v* is the velocity of the droplets (in m/s), *l* is the characteristic length (in m), which is the nozzle diameter or orifice size, $v = \mu/\rho$ is the kinematic viscosity (in m^2/s), which is the ratio of the dynamic viscosity of the ink μ (in Pa·s) over the density of the ink ρ (in kg/m^3). A small *Re* value indicates dominance of the laminar flow. The viscous forces have a higher impact on the fluid situations than the inertial forces; thus, the turbulences are minimized. On the contrary, a large *Re* value indicates the turbulent flow regime, where the inertial forces dominate.

The next significant number is Weber number (*We*), which is the ratio of the inertial forces over the surface tension forces [96]:

$$We = \frac{\rho v^2 l}{\gamma} \tag{2.49}$$

where γ is the surface tension of the ink (in N/m). As in inkjet printing, the surface tension of the ink is not negligible; the Weber number is then used to indicate droplet formation and ejection. At low *We* values, the influence of surface tension is more prominent, and the momentum is insufficient to form a separate droplet from the nozzle. At high *We* values, the droplets are formed and ejected from the nozzle; however, potential splashing of the droplets might occur due to inertial forces that are too high. The other ratio, which is the one between the viscous and surface tension forces, is called capillary number (*Ca*) and equals *We* over *Re*.

In order to relate all three forces together, the Ohnesorge number (*Oh*) is introduced. Ohnesorge number is expressed as the ratio of the viscous forces over the square root of the multiplication of inertial and surface tension forces. This number and its inverse number *Z*, which is more commonly used in inkjet printing, are expressed as:

$$Oh = \frac{\sqrt{We}}{Re} = \frac{\mu}{\sqrt{\gamma Vl}} \tag{2.50}$$

$$Z = \frac{1}{Oh} = \frac{\sqrt{\gamma v l}}{\mu} \tag{2.51}$$

From the expressions, it can be seen that usually, a small Z number indicates a more dominating role of viscous forces. In contrast, a large Z number corresponds to a greater influence of the inertial and surface tension forces over viscosity, leading to the formation of unwanted breakup of droplets into satellite droplets. As can be seen, these numbers are all interwoven and dependent on each other.
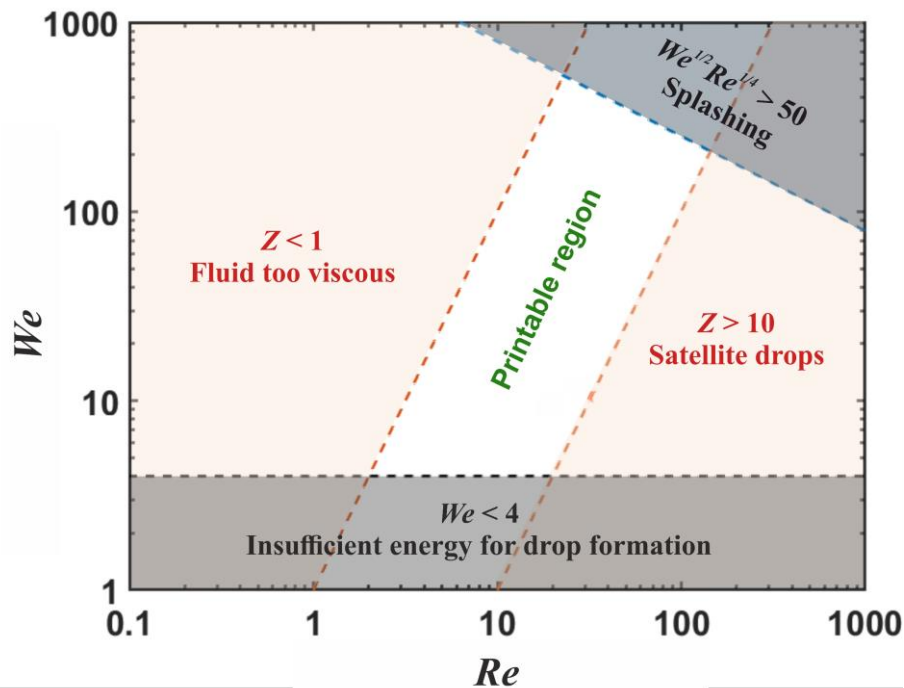
Figure 2.15: Printability map in the parameter space of Reynolds number Re versus Weber number We. The four limiting factors indicate the regions for unreliable inkjet printing. If $Z < 1$, the fluid is too viscous to be ejected, while $Z > 10$ indicates the emergence of satellite drops accompanying the primary droplet. When $We < 4$, the kinetic energy of the fluid is insufficient to form a droplet, while $We^{1/2}Re^{1/4} > 50$ leads to splashing on the substrate. The printable region is situated in the white region in the center, where Weber, Reynolds, and Z numbers have intermediate values.

With these dimensionless numbers, a parameter space of the Reynolds number versus the Weber number can be created to indicate the region for reliable DOD inkjet printing, as can be seen in **Figure 2.15**. The criterion for the viscosity of the ink to be printable is given by Reis et al. that Z should be in the range of $1 < Z < 10$ [97]. If Z is too low, the ink becomes excessively viscous, making it challenging for the nozzles to expel it. Conversely, a high Z value signifies an increased likelihood of Rayleigh Plateau instability,

leading to the breakup of liquid jets into satellite droplets accompanying the primary drop. Moreover, a droplet requires a sufficient amount of kinetic energy to surpass the surface tension between the liquid and air at the nozzle, and this constraint is given by the Weber number range $We > 4$ [98]. Furthermore, it is essential to consider the threshold at which droplet begins splashing on the substrate. An established empirical criterion suggests that $We^{1/2}Re^{1/4} < 50$ for splashing-free inkjet printing on a flat and smooth surface [99]. All these criteria listed above are plotted as straight lines in **Figure 2.15**, and the printable region for reliable inkjet printing lies in the middle, characterized by intermediate values of Weber, Reynolds, and Z numbers.

It is crucial to acknowledge that the fluid flow is generally chaotic, and even slight alterations can cause significant changes in the flow dynamics. Therefore, the fluid mechanics involved in inkjet printing constitute an intricate issue with many intertwined parameters. The abovementioned criteria provide a guideline for ink printability to a certain extent. Other parameters, such as the boiling point, vapor pressure, and particle size of the nanoparticulate inks, also need to be taken into account for the nozzle clogging issue. In addition, for non-Newtonian inks like polymer solutions, where viscosity has a strong nonlinearity, additional factors such as polymer molecular weight and ink concentration play a role in determining ink printability [98]. The printable region needs to be further optimized and adapted.

2.4.3   Ink and Substrate

Once the droplet is formed, it is ejected and received by the substrate. The liquid droplets subsequently wet the substrate, potentially merge with other droplets, and undergo solidification. These interactions between the ink and the substrate are pivotal for the formation of the final printed structures.
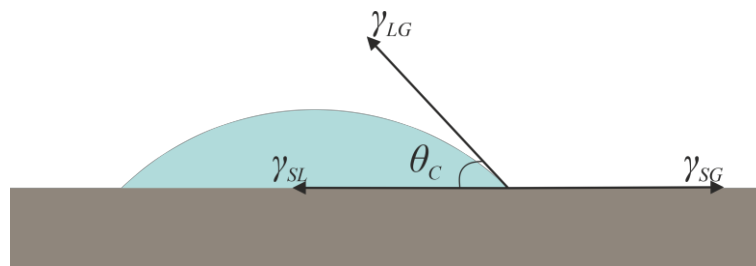
Figure 2.16: Schematic of a liquid ink droplet on a solid substrate with the contact angle θ_C. The surface tensions between different phases in the Young equation are shown as γ_{SG}, γ_{SL}, and γ_{LG}.

The contact angle θ_C of the droplet on a substrate is defined as the angle between the tangent of the liquid-gas interface and the tangent of the liquid-solid interface at the three-

phase contact line. This angle serves as a crucial parameter for the quantitative characterization of the wetting behavior of inks on substrates. In fluid mechanics, there is another dimensionless number known as the Bond number, which signifies the ratio between the gravitational force and capillary force [100]:

$$B_o = \frac{\Delta \rho g l^2}{\gamma} \tag{2.52}$$

where $\Delta \rho$ denotes the density difference between two phases and g is the gravitational acceleration. Typically, in DOD inkjet printing, the characteristic length falls within the micrometer range, giving a $B_o \ll 1$. Therefore, whether in the stages of droplet formation or the interaction between the droplet and substrate, gravitational forces can be neglected, and the surface tension dominates. Under equilibrium status, the contact angle can be calculated following the Young equation:

$$\gamma_{SG} = \gamma_{SL} + \gamma_{LG} \cos \theta_C \tag{2.53}$$

where θ_C is the contact angle, γ_{SG} is the surface tension between solid and ambient gas, namely the surface free energy (SFE), γ_{SL} denotes the interfacial tension between the liquid and solid, and γ_{LG} is the surface tension of the liquid.

Various wetting scenarios under different contact angles are illustrated in **Figure 2.17**. When the contact angle is less than 90°, the ink exhibits good wetting on the substrate, where $\theta_C = 0°$ indicates complete wetting and spreading. Conversely, when the contact angle exceeds 90°, the ink demonstrates poor wettability on the substrate and shows dewetting.
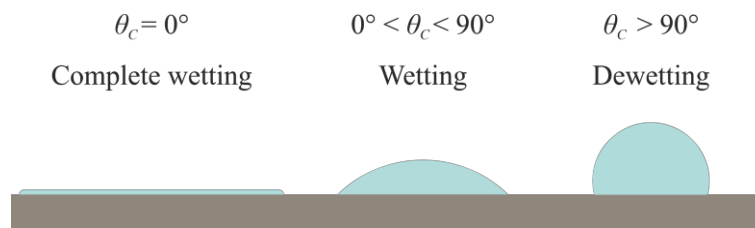
Figure 2.17: Illustration of various wetting scenarios. Progressing from left to right, the increase in contact angle indicates a transition from wetting to dewetting.

Since the SFE of the substrates and the interfacial tension cannot be measured directly, different models have been proposed to calculate the SFE of a solid from contact angle measurements. One of the most commonly used models is the Owens-Wendt-Rabel-Kaelble model, where the surface tensions are divided into dispersive component and polar component, and the following equation can be derived [101, 102]:

$$\frac{\gamma_{LG}(1+\cos\theta)}{2\sqrt{\gamma_{LG}^D}} = \sqrt{\gamma_{SG}^D} + \sqrt{\gamma_{SG}^P}\sqrt{\frac{\gamma_{LG}^P}{\gamma_{LG}^D}} \tag{2.54}$$

where γ_{SG}^D, γ_{SG}^P, γ_{LG}^D, and γ_{LG}^P denote the dispersive and polar components of SFE of the substrate and surface tension of the liquid, respectively. For an unknown solid, the SFE can be determined by measuring the contact angles of two or more known liquids on its surface. Once the SFE of the substrate is identified, the wettability of the ink has to align with the desired final structure. For example, ensuring good wetting is essential when printing thin films or closed structures. On the other hand, for printing individual and fine structures such as MLs, a high aspect ratio can be achieved through dewetting, and adjusting the wettability allows for tuning the aspect ratio of the MLs.
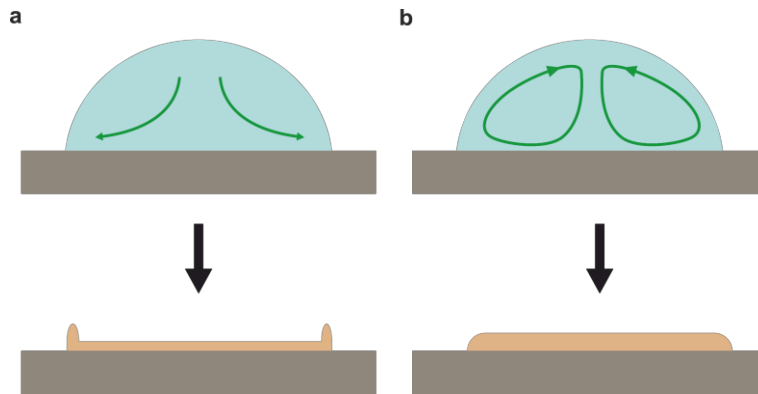
Figure 2.18: Schematic of droplet evaporation regimes. (a) Capillary-flow regime. The capillary flow brings the solute/suspends from the middle outwards to the edges, leading to the coffee-ring effect. (b) Marangoni flow participates in evaporation. The Marangoni flow circulates the solutes/particles from the edges back to the middle, counteracting the capillary flow.

The phase transition of a liquid ink droplet into a solid state mostly occurs through either solvent evaporation or chemical reactions such as crosslinking. In solvent evaporation, the liquid at the three-phase contact line–the edge of the droplet–evaporates rapidly, as shown in **Figure 2.18**a. This results in an increased ink concentration at the edge, creating a gradient that induces strong outward capillary flow [103]. This flow transports liquid from the middle of the droplet to the periphery. As a consequence, solutes or dispensed particles are continuously carried by the flow to the edge until the droplet is completely dried. This process leaves behind an accumulation of solutes or particles at the edge, exhibiting a phenomenon known as the coffee-ring effect.

The coffee-ring effect poses a significant challenge in achieving a uniform and homogeneous printed pattern. Therefore, various strategies have been used to suppress the coffee-

ring effect. One approach involves preventing the pinning of the contact line associated with the contact angle hysteresis [104]. This can be achieved by employing hydrophobic or microtextured superhydrophobic substrates [105, 106]. However, the poor wetting of the ink on hydrophobic substrates results in an inhomogeneous and potentially open printed pattern. Therefore, this approach is most suitable for printing small patterns such as individual micro-mesas. Additionally, it has been observed that changing the shape of the nanoparticles from spheres to ellipsoids can effectively suppress the coffee-ring effect [107].

Another widely adopted and practical method is introducing Marangoni flow into the evaporation process, as illustrated in **Figure 2.18**b. Marangoni flow occurs when there is a gradient in surface tension, and solutes or particles are transported with the flow toward regions with higher surface tension [108]. Typically, this surface tension gradient is induced either by creating a temperature gradient or by introducing a composition gradient in a multi-component liquid. The generation of a temperature gradient can be accomplished by heating the substrate [109]. On the other hand, to create the surface tension gradient, a complex solvent system with solvents having different vapor pressures is usually developed, leading to selective evaporation and, thus, the Marangoni flow.

3   State of the Art

In this chapter, a comprehensive overview of the current state-of-the-art fabrication technologies related to microlens arrays (MLAs) and Bragg mirrors is provided. Both direct and indirect deposition methods for MLAs are presented, with comparisons of their respective advantages and disadvantages. Subsequently, prior endeavors involving inkjet-printed MLAs on both unstructured and pre-structured surfaces are explored, and the challenges and limitations encountered in these works are discussed. Moving from MLAs to Bragg mirrors, a close look at the fabrication technologies used for Bragg mirrors is provided, including both traditional methods and solution-processing technologies. The achieved reflectance of Bragg mirrors fabricated through various solution-processing methods is outlined, and a comparative analysis is conducted on their scalability and patterning capability.

3.1   Fabrication of Microlens Arrays

A variety of fabrication techniques have been developed for manufacturing microlens arrays (MLAs). One common approach begins with the fabrication of mesa arrays using processes such as the 'Lithographie, Galvanoforming, Abformung' (LIGA) process [110], photolithography [111, 112], or laser catapulting [113]. Subsequently, a thermal reflow process is introduced to transform the micro mesas into the desired spherical microlens (ML) shape, as shown in **Figure 3.1**a and b. Compared to photolithography and the LIGA process, which involve multiple fabrication steps and rely on photomasks for patterning, laser catapulting is a method enabling faster and maskless manufacturing. Nevertheless, the subsequent thermal reflow process necessitates elevated temperatures, posing challenges in achieving high numerical apertures (NAs) for MLs [114].

Additionally, without the need for a thermal reflow process, convex MLAs have been produced using grayscale lithography [115] and a laser-based printing approach [116]. At the same time, electrowetting has been applied for the fabrication of concave MLAs [117, 118], as seen in **Figure 3.1**c. These approaches demonstrate the potential for achieving a high fill factor (FF) of nearly 100% for MLAs. Nonetheless, they are not suited for fast prototyping and mass production. Due to the high number of fabrication steps and the need for masks, precise illumination patterns, or templates, these methods are complicated, costly, time-consuming, and material-consuming. Alternatively, MLAs can be fabricated in a relatively straightforward manner through surface patterning followed by a self-organization process of deposited material [119], as depicted in **Figure 3.1**d. However, it is important to note that with this approach, the substrate requires pre-patterning, which involves an extra time-consuming and mask-aided process. In addition, achieving

precise control over the aspect ratio of the MLs can be challenging. Furthermore, attaining a high FF is difficult due to the self-organization in this solution processing method.
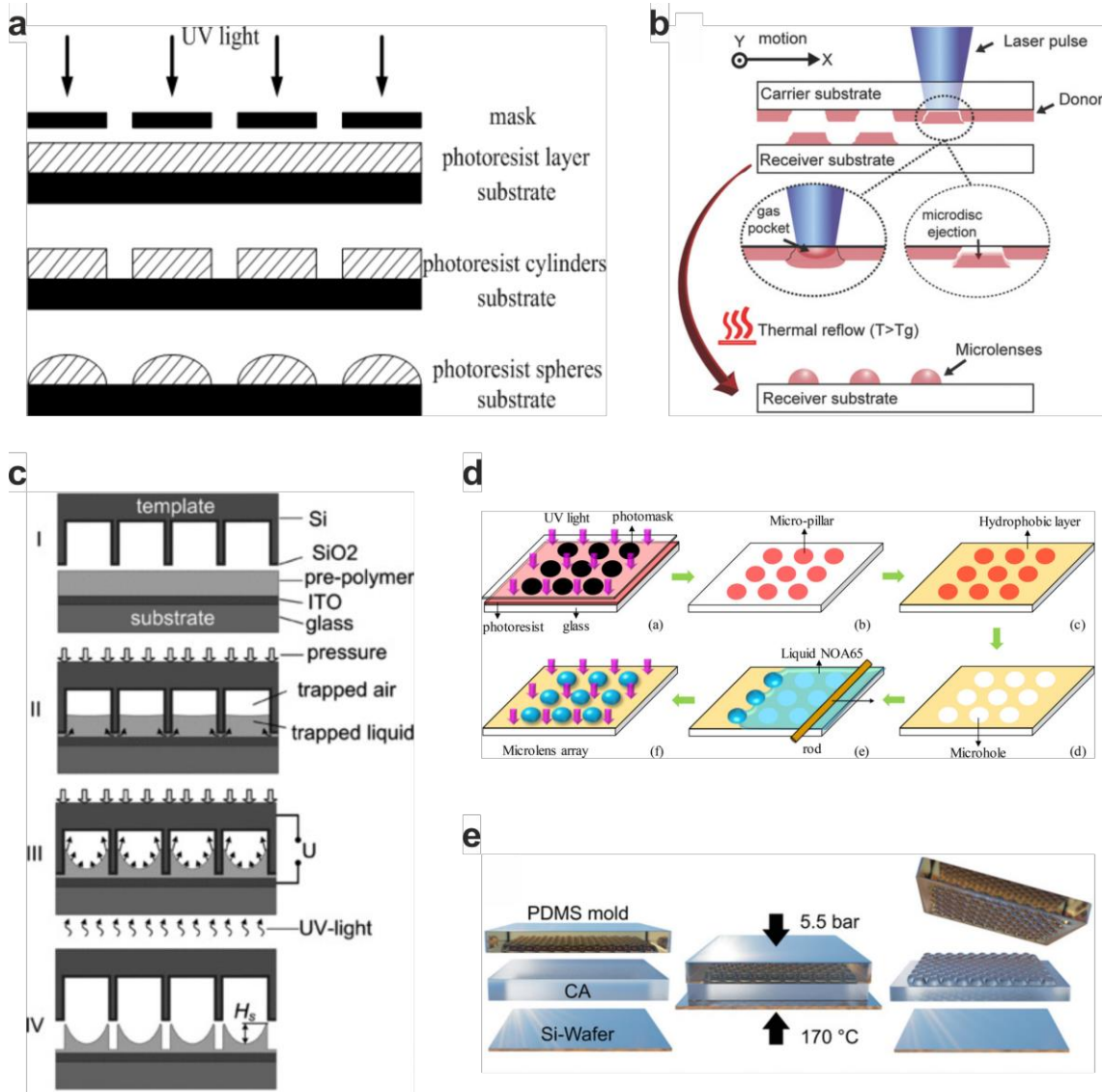
Figure 3.1: Different fabrication methods for microlens arrays (MLAs). (a) Thermal reflow method. A micro-mesa array is initially created on the substrate by photolithography. Subsequently, the micro mesas transform into microlenses through a thermal reflow process. The schematic is reprinted from [112] with permission from IEEE. (b) Thermal reflow method with micro-mesa array produced by laser catapulting, reprinted from [113] with permission from Wiley-VCH. (c) Electrowetting method. A concave MLA is fabricated using electrowetting, reprinted from [117] with permission from Wiley-VCH. (d) Self-assembly method. The wettability of the surface is pre-patterned by photolithography, reprinted from [119] with permission from American Chemical Society. (e) Hot

embossing method. A mold with a negative pattern is used to imprint the MLA structure onto the substrate, reprinted from [120] with permission from Wiley-VCH.

After successfully manufacturing an MLA, it can serve as a master in various instances, enabling the direct replication of new MLAs through imprinting [121-123], as illustrated in **Figure 3.1**e. However, challenges associated with imprinting remain, including issues of contamination and damage caused by the direct contact of materials with templates. Additionally, there is a limitation in flexibility when adjusting the geometrical parameters of MLAs due to the reliance on the templates. Therefore, an additive manufacturing process that not only matches or surpasses the fabrication speed of existing methods but also offers significantly greater flexibility is desired for MLA fabrication.

As additive manufacturing techniques, electrohydrodynamic jet (E-jet) printing and direct laser writing have been used to fabricate MLAs with high precision [124, 125]. However, E-jet printing requires microelectrodes on the substrate, and direct laser writing involves intricate systems with high complexity and ultrafast lasers, resulting in elevated costs. Furthermore, the sequential voxel-by-voxel method in direct laser writing imposes limitations on throughput.
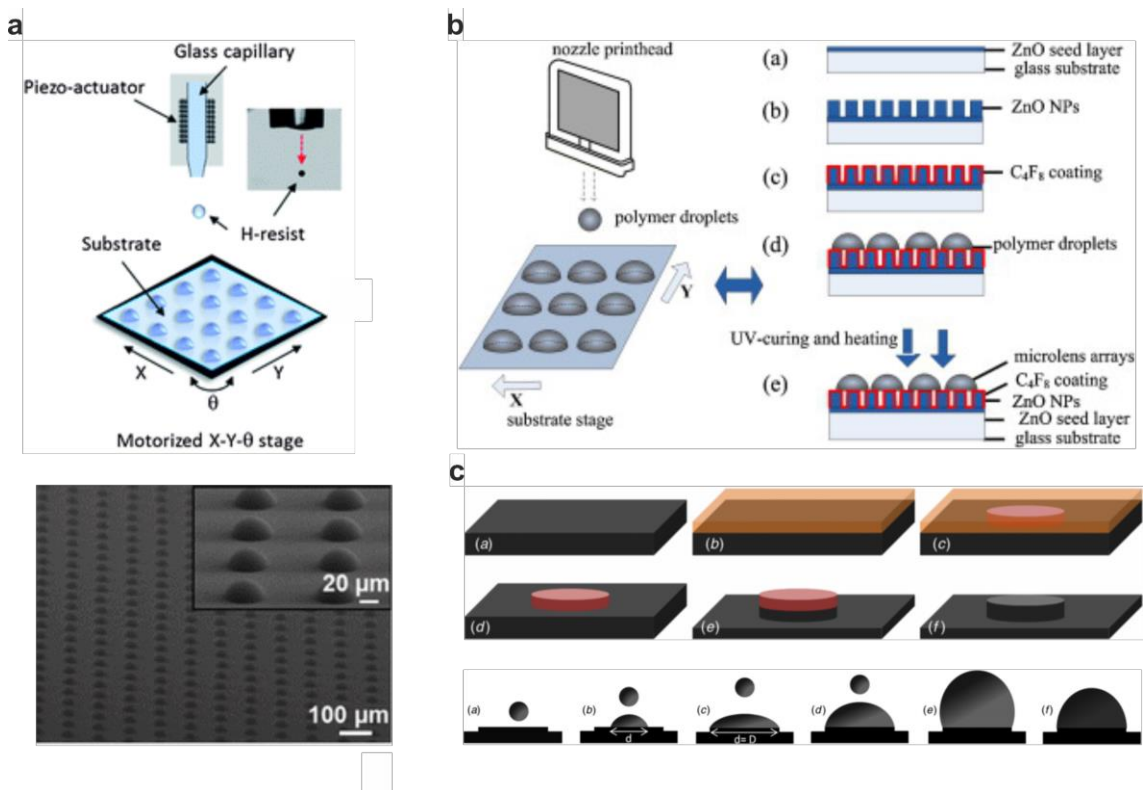
Figure 3.2: Inkjet printing is used for additive manufacturing of microlens arrays (MLAs). (a) Schematic of the MLAs deposited by drop-on-demand inkjet printing, the

scanning electron microscopy (SEM) image of the fabricated MLAs is shown below, reproduced from [126] with permission from Royal Society of Chemistry. (b) MLAs with high numerical apertures are manufactured by inkjet printing on nano-textured and hydrophobically-coated surfaces, reproduced from [127] with permission from Elsevier. (c) Substrates are pre-structured, forming pedals to constrain the jetted droplets spatially. The aspect ratio of microlenses is tuned by jetting varying numbers of droplets within the confined area, reproduced from [128] with permission from Institute of Physics Publishing.

In contrast, inkjet printing, serving as another technique for maskless additive manufacturing of MLAs, presents a multitude of advantages [129-131]. Firstly, inkjet printing is a straightforward and adaptable process, digitally controlling MLA fabrication in real-time and facilitating rapid prototyping. Secondly, the precise amount of material required for the MLs is used in the printing process, minimizing material wastage and enhancing cost-effectiveness. Besides being a non-contact technique, inkjet printing offers the flexibility to transfer the printing process to various substrates easily. Finally, the scalability of inkjet printing is achievable through the incorporation of more nozzles or multiple printheads, enabling excellent throughput and mass production of MLAs.

Since 1994, inkjet printing has been used to fabricate MLAs with sol-gel-based inks as well as UV-curable inks [132-134], as shown in **Figure 3.2**a. The NA of MLs can be adjusted by introducing a self-assembled monolayer (SAM) or nanotextures on the substrate [135], as depicted in **Figure 3.2**b. However, achieving MLAs with a high FF through inkjet printing poses significant challenges. Minor deviations in the placement of ink droplets often result in the merging of neighboring droplets, jeopardizing the quality of the MLAs. Additionally, the volume shrinkage of MLs resulting from the evaporation of the solvent or the curing process leads to a lower FF. Therefore, the results achieved in these previous works show low uniformity and a low FF, significantly below 78.5%, the upper limit of a square-aligned circular MLA. Furthermore, ensuring stable jetting and maintaining the reproducibility of the printed MLs remains a challenge. To address these challenges, substrates have been pre-structured, forming either pedals or wells to constrain the jetted droplets spatially [128, 136]. This approach enhances the placement accuracy of MLAs, and it allows for the tuning of MLA geometrical properties by jetting varying numbers of droplets within the confined area, as shown in **Figure 3.2**c [137]. However, the introduction of the pre-structuring process, which is completed by, e.g., photolithography, substantially adds to the complexity of the entire fabrication process. As a result, the disadvantages of this approach surpass the benefits associated with inkjet printing technology. So far, the development of suitable inks and reliable printing to facilitate high-FF MLAs through inkjet printing has not been realized.

3.2 Fabrication of Bragg Mirrors
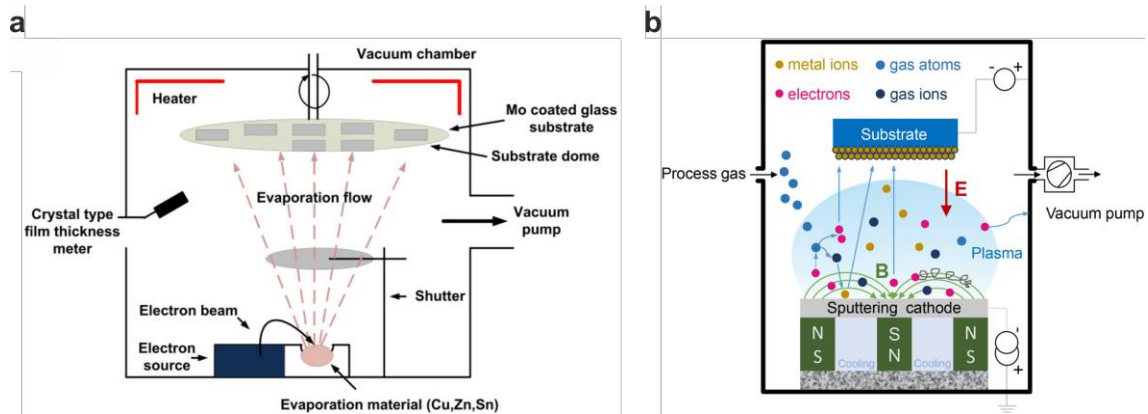
Figure 3.3: Examples of physical vapor deposition methods for the fabrication of Bragg mirrors. (a) Schematic of electron-beam evaporation, reproduced from [138] with permission from Springer Nature. (b) Principle of magnetron sputtering, reproduced from [139] with permission from Elsevier.

In contrast to MLA fabrication, where micro-structuring plays an essential role, achieving a uniform thin film deposition is the key for Bragg mirrors. Various deposition technologies have been employed in the manufacturing of Bragg mirrors. The prevalent technology used in industry is physical vapor deposition (PVD) [140], a conventional deposition method for thin optical films. Chemical vapor deposition (CVD) is also widely used in industry for some specific applications [140]. In PVD technologies, the material target is vaporized by thermal processes [141, 142] or energetic processes conducted under high-vacuum conditions. In thermal evaporation chambers, the material target is heated until the vapors are generated. The vapors travel in a straight line to the substrate and condense on it, which is kept at a temperature where the material solidifies. Thermal evaporation is the most straightforward and cost-effective PVD technique. However, its drawbacks encompass the low packing density of molecules, the need for high temperatures, and limitations in material selection. Over the recent two decades, there has been a shift away from thermal evaporation toward energetic processes [143], such as electron-beam evaporation shown in **Figure 3.3**a [144, 145], ion-assisted deposition [146, 147], ion plating [148, 149], and sputtering [150, 151]. The deposited thin films exhibit a higher packing density in comparison to films produced through thermal evaporation, owing to the high kinetic energy induced in the atoms hitting the substrates. Especially the sputtering method, as a highly energetic process compared to other evaporation techniques, employs magnetron plasma or ion beam for sputtering the material, namely magnetron sputtering, as depicted in **Figure 3.3**b [152, 153] and ion-beam sputtering [154, 155], respectively. Despite the production of hard and dense thin films via sputtering, the associated

machinery is costly, and usually, high mechanical stress is introduced into the resulting thin films. Additionally, ion-beam sputtering suffers from a very low deposition rate.

Similar to PVD, CVD processes typically require vacuum conditions. In CVD processes, the initial material is the precursor of the desired material, and chemical reactions are initiated to convert the precursor into the target material. The most commonly employed CVD methods for Bragg mirrors are plasma-enhanced CVD [156, 157] and atomic layer deposition [158, 159]. However, due to their low deposition rates and high costs, they are often used as complementary deposition methods to PVD in specific applications, particularly for films requiring exceptionally high uniformity or conformal films on 3D objects. Both PVD and CVD methods are highly specialized with limited flexibility. In many of the processes, substrate options are restricted due to the presence of high temperature or high energy. In addition, both methods require a combination with lithographic approaches to achieve lateral patterning. Furthermore, the size of the Bragg mirrors is constrained by the dimensions of vacuum chambers in PVD and CVD processes.
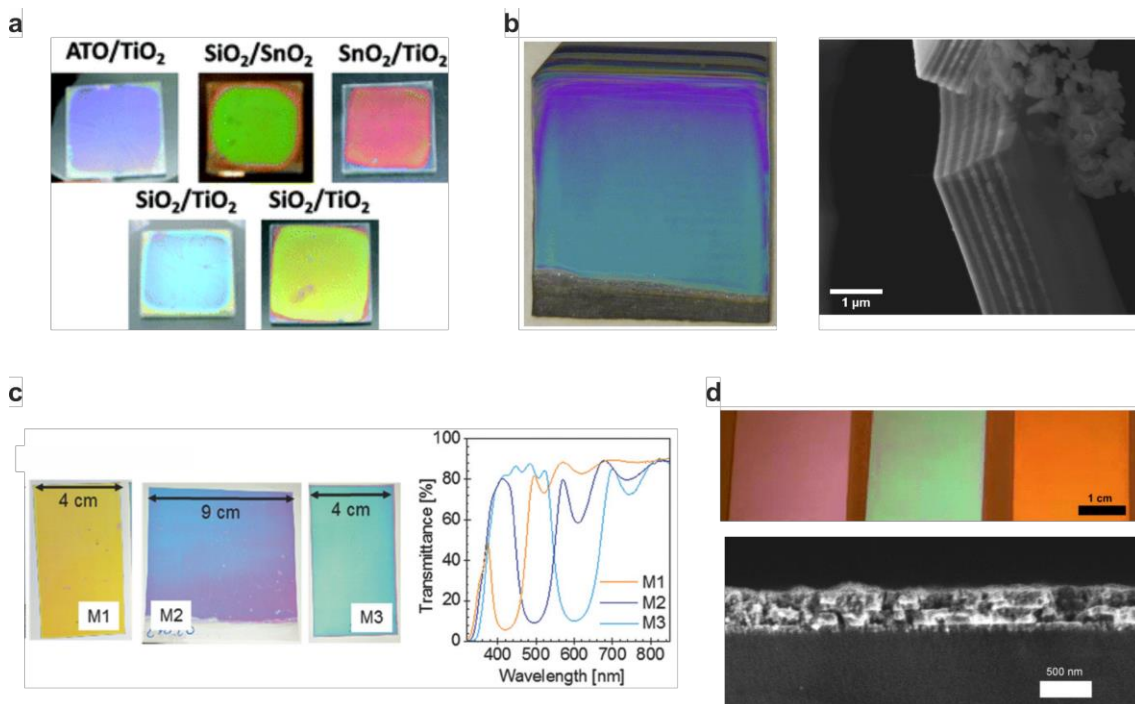
Figure 3.4: Bragg mirrors fabricated by various solution-processing methods. (a) Bragg mirrors by spin coating. The striations and comets can be clearly seen, reproduced from [160] with permission from Royal Society of Chemistry. (b) Bragg mirrors by dip coating. Left: image of the Bragg mirror. Right: scanning electron microscopy (SEM) image of the Bragg mirror. The image shows the gradient in the deposited thin layers, reproduced from [161] with permission from Elsevier. (c) Bragg mirrors by blade coating. Left: image of Bragg mirrors. Right: transmission spectra of the Bragg mirrors, reproduced from

[162] with permission from Wiley-VCH. (d) Image and SEM image of the mirrors fabricated by self-assembly, reproduced from [163] with permission from Wiley-VCH.

In recent times, alternative solution-based processes, including spin coating, as shown in **Figure 3.4**a [164, 165]; sol-gel methods through dip coating, as shown in **Figure 3.4**b [166, 167]; blade coating, as shown in **Figure 3.4**c [168]; self-assembly, as shown in **Figure 3.4**d [169]; and holographic photopolymerization [170], have gained interest due to their low costs and high flexibility. However, there are some major shortcomings in the methods mentioned above. Regarding spin coating, drawbacks include the considerable wastage of the material, restrictions on the size of the substrate, and the occurrence of inhomogeneities in thin films, such as striations and comets, which result in suboptimal mirror quality [160]. On the contrary, blade coating is suitable for large-scale production; nevertheless, achieving precise control over thin film quality is a considerable challenge [162]. Self-assembly is a time-consuming process, and achieving high reproductivity poses significant challenges [171, 172]. Furthermore, none of the mentioned approaches allow for lateral patterning of Bragg mirrors.

Table 3.1: Previously reported Bragg mirrors by solution processing methods

Fabrication Method	Max. Reflectance	No. of Bilayers	Materials	Scalability	Lateral Patterning
Spin Coating [165]	56%	3	SiO_2/TiO_2	No	No
Spin Coating [173]	80%	10	SiO_2/ZrO_2		
Spin Coating [174]	93.8%	11	CA/CHIPs		
Spin Coating [175]	> 95%	10	PMMA-co-PHEMA-co-PEGDMA/TiO_2		
Spin Coating [176]	> 90%	3	Clay		
Dip Coating [177]	99.7%	7	SiO_2/TiO_2	Limited	No
Dip Coating [178]	> 99%	10.5	PFP/TiO_2		
Self-Assembly [179]	> 93%	9	SiO_2/TiO_2	Limited	No
Blade Coating [162]	95%	7	SiO_2/TiO_2	Yes	No
Blade Coating [180]	93.3%	7	SiO_2/TiO_2		

To construct the mirrors, many different materials can be used in solution processing. This includes first inorganic materials, encompassing common metal oxides such as SiO_2, TiO_2, SnO_2, ZrO_2, ZnO, Fe_2O_3,[181-183], as well as fluorides such as MgF_2 and AlF_3 [184], and clays [176]. Integration of organic materials has also been explored, leveraging their mechanical flexibility or responsiveness to stimuli. Examples include polystyrene, poly(methyl methacrylate), polyisoprene, poly(ethylene terephthalate), and block copolymers [185-187]. In addition, hybrid combinations of both have been intensively investigated [174, 188-190]. A more detailed comparison of various solution processing methods and the used materials is shown in **Table 3.1**.

4 Methods and Characterization

In this chapter, the experimental methods and characterization tools used during the work are reported. Section 4.1 starts to describe the methods used in this work, including the substrate preparation, the fabrication methods, and the methods used for light field reconstruction. In Section 4.2, the optical, rheological, and electrical characterization methods used for the fabricated components and devices are discussed, which provide thorough analyses of the fabricated devices in this work.

4.1 Methods

4.1.1 Substrate Preparation

Glass substrates for microlens arrays

For the fabrication of microlens arrays (MLAs), the 22×22 mm^2 glass substrates (Carl Roth) were used. For the demonstration of large and patterned MLA fabrication, large 10 $\times$ 10 cm^2 soda-lime glass substrates with a thickness of around 1.1 mm (Carl Roth) were used. For the fabrication of MLAs and color filter arrays for the light field camera in Chapter 6, ultra-thin borosilicate coverslip glass substrates (Carl Roth) with a 1.5H thickness of 170 ± 5 μm were used to fulfill the manufacturing requirements. All types of glass substrates were first placed in acetone in an ultrasonic bath for 10 minutes and dried with nitrogen. Subsequently, they were put in isopropyl alcohol for 10 minutes in an ultrasonic bath and dried with nitrogen afterward. These cleaned substrates were applied as bare glass substrates. The larger borosilicate glass substrates were used for preparing the polydimethylsiloxane (PDMS) substrates.

Substrates with self-assembled-monolayer deposition for microlens arrays

In this work, four different siloxanes were applied on the substrate to increase or decrease its surface free energy (SFE), including triethoxyoctylsilane (TEOS; Sigma-Aldrich, 98%), trimethoxy-(3,3,3-trifluorpropyl)-silane (TTFPS; Sigma-Aldrich, $\geqslant 97.0\%$), 3-aminopropyltriethoxysilane (APTES; Acros Organics, 99%), and triethoxyphenylsilane (TEPS; Sigma-Aldrich, >98%). The solutions were prepared by adding individual siloxane in ethanol to achieve a volume concentration of 1 vol%. The prepared SAM solutions were deposited onto the glass substrates by spin coating. During spin coating, the substrates were spun at a speed of 1500 revolutions per minute (rpm) for 45 seconds with an initial acceleration of 500 rpm/s. For more details on spin coating, refer to Section 4.1.2.

Subsequently, the substrates were placed on a hotplate at 95 °C for 5 minutes. After annealing, the substrates were rinsed with isopropyl alcohol and dried with nitrogen.

Flexible substrates for microlens arrays

The flexible PDMS substrates were produced by initially blending a pre-polymer base of PDMS Sylgard 184 silicone elastomer (Dow Corning) and its curing agent in a mass ratio of 10:1. After thoroughly stirring the mixture, it was degassed in a vacuum desiccator for 30 minutes. The degassed mixture was then poured onto a clean glass plate and solidified after being put on a hotplate at 100 °C for 30 minutes. The resulting PDMS substrate was carefully peeled from the glass plate and was cut into a size of 10×4 cm^2. In addition, the flexible polyethylene terephthalate (PET; Melinex 506, Puetz Folien) foils with a thickness of 175 µm were cut into a size of 22×22 mm^2, cleaned in deionized water in an ultrasonic bath for 10 minutes and dried with nitrogen.

Glass substrates and flexible substrates for Bragg mirrors

For the fabrication of Bragg mirrors, the 25×25 mm^2 soda lime glass substrates (Carl Roth) with a thickness of around 1.1 mm were used as the rigid substrates, and the 120×120 mm^2 PET foils (Melinex 506, Puetz Folien) with a thickness of 175 µm were used as the flexible substrates. Both types of substrates were first placed in deionized water in an ultrasonic bath for 10 min and dried with nitrogen. Then, the procedure was repeated by replacing deionized water with acetone and then isopropyl alcohol. Each step involved 10 minutes in an ultrasonic bath and subsequent drying with nitrogen. Before printing, the substrates were treated with oxygen plasma within a plasma chamber PlasmaFlecto 30 from Plasma technology, applying a power of 100 W for a duration of 10 minutes.

4.1.2   Fabrication Methods

Spin coating
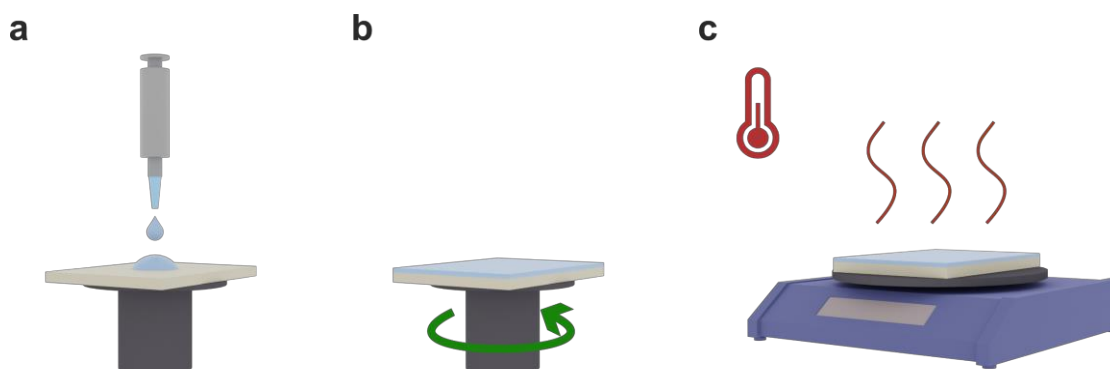
Figure 4.1: Schematic illustration of the spin coating process. (a) The material is deposited on the substrate, which is fixed by a chuck. (b) The material is spread over the

substrate during spinning. (c) The film is then baked on a hotplate for a certain time for solvent evaporation and annealing.

Spin coating is one of the most commonly used solution-processing methods for the deposition of uniform thin films on flat substrates. The thickness range of the films is usually from the micrometer scale to the nanometer scale [191]. In the spin coating process, first, the substrate is placed on a chuck, which fixes the substrate either by mechanical structures or vacuum. The prepared solution is then applied to the center of the substrate, as shown in **Figure 4.1**a. Subsequently, the substrate is spun at a high speed to deposit the material uniformly on the substrate, as seen in **Figure 4.1**b. Due to the centrifugal force, a homogeneous thin film is formed. For a solution with a certain viscosity, the thickness of the thin film is determined by the acceleration rate, the spinning rate, and the spinning duration. The deposited thin films were then placed on the hotplate for solvent evaporation and annealing, as depicted in **Figure 4.1**c.

Inkjet Printing

Prior to inkjet printing, the inks were prepared by placing them in an ultrasonic bath for degassing. Subsequently, the cartridge was filled with the ink using polytetrafluoroethylene (PTFE) filters with a pore size of 0.2 μm. The inkjet printer used in this work is the inkjet printer PixDro LP50 from Suss Microtec. The drop-on-demand (DOD) piezoelectric print heads DMC 11610 and DMC 11601 from Fujifilm Dimatix were used in the printer. The fabrication processes were all conducted in a cleanroom with a controlled ambient temperature of 21-22 °C and humidity at 40-50%. For more details about inkjet printing, refer to Section 2.4.

4.1.3 Reconstruction Approaches

The detailed modeling of a spectral light field camera can be found in Section 2.1. The proposed approaches were applied to reconstruct the spectral light field from the coded measurements, consisting of one based on compressed sensing and another utilizing deep learning [192]. As a comparative benchmark, EPINET was also applied [193], acknowledged as one of the leading approaches for disparity estimation in conventional RGB light fields, particularly within the Human-Computer Interaction benchmarks [194]. EPINET was applied to estimate disparity from non-spectrally-coded light fields for reference and evaluation purposes.

The reconstruction method based on compressed sensing involves a dictionary learning approach. The spectral light field dictionary was generated in accordance with the methodology presented in [195] with a comprehensive synthetic spectral light field dataset [196]. The reconstruction process relied on l_0−norm minimization, with the fast-iterative shrinkage/thresholding algorithm chosen for its rapid convergence [197]. To address the

challenge of large dimensionality, mini-batch stochastic gradient descent was employed as an additional optimization technique to minimize the reconstruction error, as outlined in [192].

The requisite information from full light fields typically consists of low-dimensional details, such as the central view or disparity. Consequently, a deep learning approach was employed to extract the desired information from the measurements directly. Specifically, the objective was to extract the central spectral view $I(s,t,\lambda)$ and the disparity $D(s,t)$ information from the encoded light field L^* [198]. The 4D light fields underwent a transformation where the two angular dimensions were consolidated into a shared axis. This involved reshaping from (u,v,s,t,λ) to (s,t,uv,λ). Through the application of three-dimensional (3D) convolution, local-angular features were adeptly extracted from the light fields. The overall loss function employed is as follows:

$$L = \sum_{i=1}^{N} w_i \left(L_{main}^{(i)} + \sum_{j=1}^{N_{aux}^{(i)}} \alpha_j^{(i)} \beta_j^{(i)} L_{aux,j}^{(i)} \right) \Big/ \left(1 + \sum_{j=1}^{N_{aux}^{(i)}} \alpha_j^{(i)} \right) \tag{4.1}$$

where $w_i > 0$ represents the weight assigned to task i, and N_{aux} is the number of auxiliary loss functions $L_{aux,j}$, which support the main loss function L_{main}. The dynamic weights α_j and β_j were trained with the additional loss functions L_α and L_β, which can be expressed as [199]:

$$L_\alpha = \sum_j \left| \alpha_j - max \left\{ 0, \frac{\langle G_{main}, G_{aux,j} \rangle}{\|G_{main}\| \cdot \|G_{aux,j}\|} \right\} \right| \tag{4.2}$$

$$L_\beta = \sum_j \left| \beta_j \cdot \|G_{aux,j}\| - \|G_{main}\| \right| \tag{4.3}$$

where G_{main} and $G_{aux,j}$ correspond to the gradients of the main and auxiliary loss functions, respectively.

4.2 Characterization

To ensure the overall performance of the fabricated optical components and systems in this work, a variety of different characterization methods are applied to assess the materials, inks, substrates, and final devices. In addition to the constituent materials, the rheology of the formulated inks, as well as their interaction with substrates, have to meet certain criteria to enable a reliable printing process. Moreover, morphological and optical characterization tools are needed to evaluate both the morphology of the fabricated layers and the optical properties of the completed components and devices.

4.2.1 Material Characterization

Spectroscopic ellipsometry
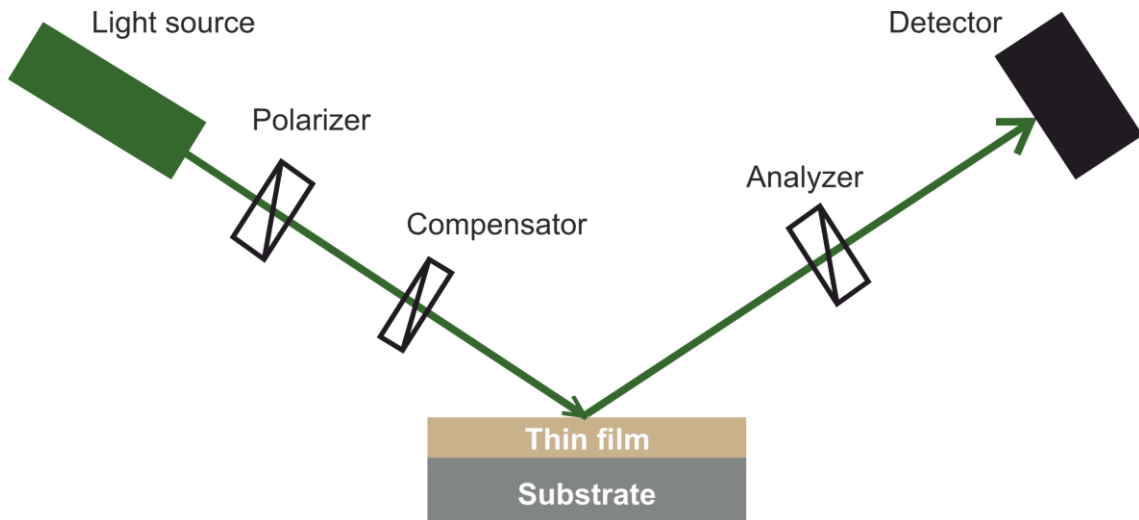
Figure 4.2: Schematic illustration of ellipsometry. The light coming from a light source goes through a polarizer and becomes linearly polarized light. This light then passes through a compensator, which introduces a phase shift, and hence, the light becomes circularly polarized light. This light beam hits the sample, which is a thin film deposited on a substrate. The light from the specular reflection passes through a rotating analyzer and is detected with a photodiode.

Ellipsometry is a non-contact and non-destructive technique for characterizing the dielectric properties of layers, such as complex refractive indices (RI) of a thin film. The schematic is illustrated in **Figure 4.2**. The RI and extinction coefficients of the different SU-8 ink materials, the poly(methyl methacrylate) (PMMA), and the TiO_2 nanocomposite studied in this work were measured by ellipsometry. The ellipsometry method used in this work is carried out in a reflection configuration with a spectroscopic ellipsometer VASE ellipsometer from J.A. Woollam. Being more complicated than single-wavelength ellipsometry, light comes from a xenon vapor lamp source and is guided into a monochromator in a spectroscopic ellipsometer. The monochrome light then goes through a polarizer and becomes linearly polarized light. Subsequently, this light goes through a compensator, which is a crystal retarder here. A phase shift is introduced, and the light becomes circularly polarized light. This light beam hits the sample, which is a thin film deposited on a substrate, and the light from the specular reflection passes through a rotating analyzer. The resulting light is detected with a photodiode.

In ellipsometry, the complex amplitude reflection coefficient ratio, ϱ, is measured. It is defined as the ratio between the complex amplitude reflection coefficients of the p- and

s-components. It incorporates the change in the polarization states between the incident and reflected light:

$$\varrho = \frac{r_p}{r_s} = \tan \Psi \, e^{i\Delta} \qquad (4.4)$$

where the ellipsometric parameters $\tan\Psi$, which represents the amplitude ratio, and Δ, which denotes the phase difference, are obtained from the real and imaginary parts of ϱ, respectively. It is worth noting that r_p and r_s in Section 2.3 are special cases for non-absorbing dielectric media. In absorbing media, the extinction coefficient has to be considered, and the complex RI has to be used for the calculations.
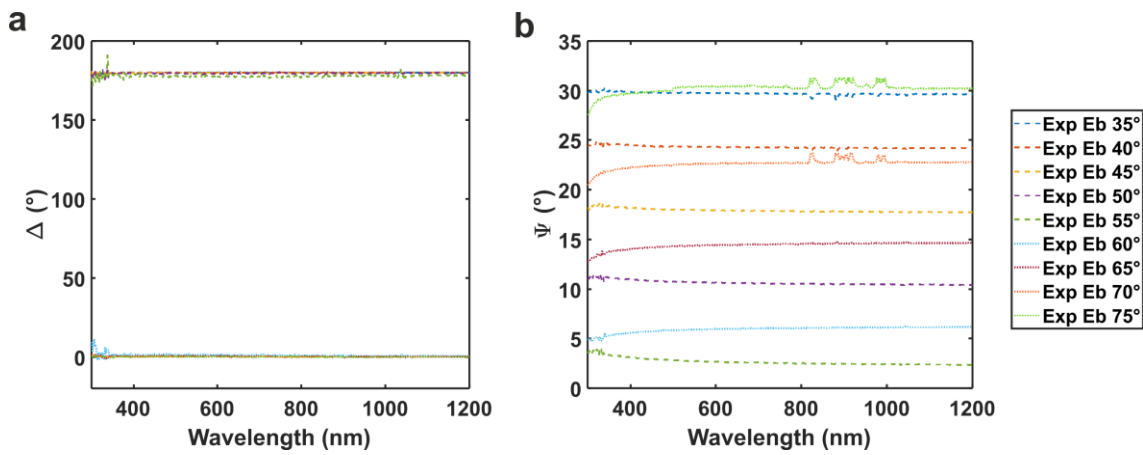
Figure 4.3: Measured spectra of the ellipsometric parameters for the TiO$_2$ nanocomposite layer at different angles of incidence. (a) Measured phase difference Δ. (b) Measured amplitude component Ψ.

Subsequently, the measured ellipsometric parameters need to be fit into a suitable model to extract the desired optical constants. For example, the measured spectra of the ellipsometric parameters Ψ and Δ of the TiO$_2$ nanocomposite are shown in **Figure 4.3**. In this work, a model consisting of a Tauc-Lorentz oscillator and a rough layer was applied to fit the measured ellipsometric parameters, giving a mean square error of 1.5 when three angles were fitted simultaneously. The measured data were processed in the ellipsometric analysis program WVASE from J.A. Woollam.

4.2.2 Ink and Substrate Characterization

Surface tension measurement

The surface tension of the inks, the SFE of the substrates, and the static contact angles of inks on different substrates were determined using an optical contact angle measuring and contour analysis system OCA 200 from DataPhysics Instruments. All the measurements

were carried out under standard atmospheric conditions. A drop with a microliter volume is hanging at the tip of a needle to measure the surface tension. A 10× zoom lens is used in the setup, and the image or video of the drop is captured for subsequent calculations.
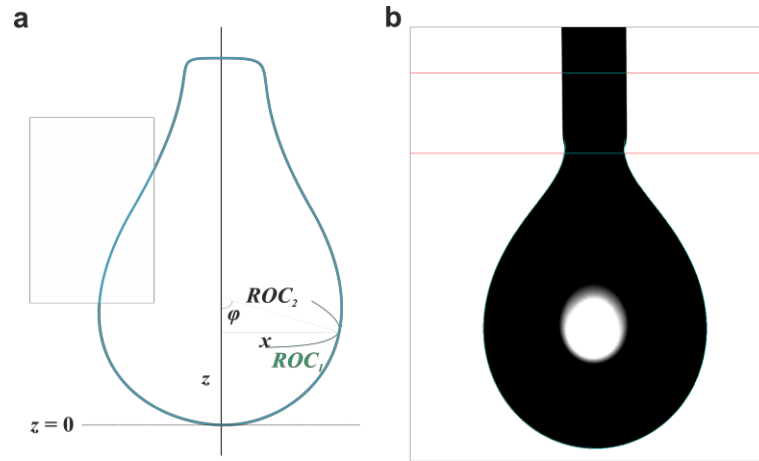
Figure 4.4: Surface tension measurement of the fluids. (a) Two-dimensional geometrical model of a pendant drop for the estimation of the surface tension. (b) Image of a water pendant drop used for surface tension reference measurement.

The surface tension is measured in the pendant drop mode, as depicted in **Figure 4.4**. For a pendant drop, the capillary pressure differences across the interface caused by surface tension can be described by the Young-Laplace equation:

$$\Delta P = -\gamma \left(\frac{1}{ROC_1} + \frac{1}{ROC_2} \right) \tag{4.5}$$

where ΔP is the Laplace pressure, and ROC_1 and ROC_2 are the principal radius of curvature (ROC) of the point, i.e., the circumferential and meridional ROC, respectively. Apart from the surface tension, for the microliter scale drop here, gravity also plays a role in its final shape. Since the drop gets stretched due to gravity, the drop has a pear-like shape, and a pressure difference is induced along the vertical direction [200]. According to Pascal's law, there is hydrostatic pressure between the two points, and the Young-Laplace equation is modified as:

$$\Delta P(z) = \Delta P_0 + \rho g z \tag{4.6}$$

where g is the acceleration of gravity and z is the vertical distance of the point to the reference plane. Following **Figure 4.4**a, the equation can be written as [201]:

$$\frac{2}{ROC_0} = \frac{1}{ROC_1} + \frac{1}{ROC_2} + \frac{\rho g z}{\gamma} = \frac{1}{ROC_1} + \frac{\sin \varphi}{x} + \frac{\rho g z}{\gamma} \tag{4.7}$$

49

where ROC_0 is the ROC of the vertex. When the drop hanging at the needle reaches its maximum volume, the image of the drop is captured, and its shape undergoes a numerical fit to the theoretical drop shape. In the end, the surface tension is determined. A reference measurement with water was carried out, as seen in **Figure 4.4**b. The obtained surface tension from the drop shape analysis was 72.12 mN/m, showing a good agreement with literature values [202].

Contact angle and surface free energy measurements
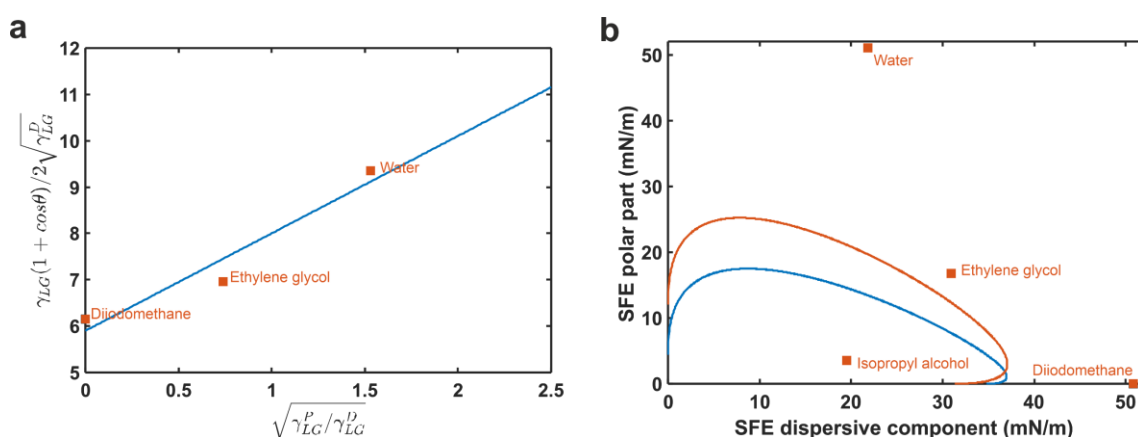
Figure 4.5: The surface free energy (SFE) measurement. (a) The linear regression line based on the Owens-Wendt-Rabel-Kaelble model to determine the SFE. (b) Wetting envelopes of substrates (solid lines) and coordinates of four different common solvents.

Using the same system (OCA 200, DataPhysics Instruments), the contact angles of the inks on specific substrates and the SFE of different substrates were determined using the sessile drop mode. A microliter scale drop is deposited onto the target substrate and reaches an equilibrium after a certain time. The system detects the outline of the drop and the baseline between the substrate and the drop. This process directly yields the contact angles, which are angles of the tangents at the intersections.

When the SFE of a substrate needs to be measured, several known liquids are used to measure their contact angles on the substrate. In this work, water, ethylene glycol, and diiodomethane were used to determine the SFE of the substrate. To calculate the SFE, the Owens-Wendt-Rabel-Kaelble model, as described in Section 2.4.3, is applied. The model divides the surface tension of the liquid and SFE of the solid into polar and dispersive components. Following Equation 2.54, a linear regression line is plotted from the measurement results, where the slope indicates the polar component of SFE, and the intercept represents the dispersive component of SFE, as illustrated in **Figure 4.5**a. Once the polar and dispersive components of the SFE of a solid are known, a wetting envelope of this solid can be plotted with a specific contact angle, typically 0°, as depicted in **Figure 4.5**b.

The wetting behavior of known liquids can then be intuitively assessed based on their locations relative to the wetting envelope. A good wetting is expected if the solvent is located within the envelope, whereas a poor wetting is anticipated when it is far from the envelope.

Rheometry
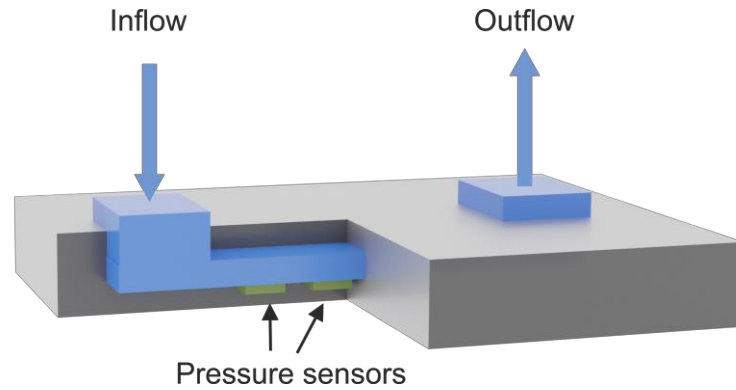
Figure 4.6: Schematic illustration of the rectangular-slit viscometer.

The viscosity of inks is a critical indicator for assessing the printability of the inks. As discussed in Section 2.4.2, if viscosity is too low, satellite droplets might occur during jetting, whereas excessively high viscosity impedes droplet ejection from the nozzles. The viscosity of the fluids was measured using a viscometer m-VROC from RheoSense. The viscometer is based on a rectangular slit microfluidic channel with a uniform cross-section, as shown in **Figure 4.6**. The test liquid flows in the channel from one side and is pumped to the end at a controlled constant fluid rate. Multiple micro-electro-mechanical-systems pressure sensors positioned along the slit measure the decrease in pressure as the test liquid flows through the channel. The decrease in pressure correlates with the shear stress at the boundary walls and, hence, the viscosity. The shear rate and shear stress can be calculated by [203]:

$$\dot{\gamma} = \frac{6Q}{wh^2} \tag{4.8}$$

$$\Gamma = \frac{wh\Delta P}{2(w+h)l} \tag{4.9}$$

where $\dot{\gamma}$ is the shear rate if the liquid is a Newtonian fluid, Q is the constant flow rate, Γ is the shear stress, ΔP is the measured pressure drop over a distance of l, and w and h are the width and height of the rectangular slit, respectively. Accordingly, the dynamic viscosity can be calculated by their ratio:

$$\mu = \frac{\Gamma}{\dot{\gamma}} \tag{4.10}$$

51

Concerning non-Newtonian fluids, the shear rate has to be corrected, and the true wall shear rate can be obtained using the Weissenberg-Rabinowitsch-Mooney correction [204]:

$$\dot{\gamma}_{true} = \frac{\dot{\gamma}}{3}\left[2 + \frac{d(\ln \dot{\gamma})}{d(\ln \Gamma)}\right] \tag{4.11}$$

4.2.3 Device Characterization

Focal length measurement and imaging test

The setup for the focal length measurement and imaging test of the fabricated MLAs in Chapter 5 and 6 involved a light source, which is a collimated LED at 530 nm M530L4-C4 from Thorlabs, a motorized precision linear stage from Owis, which moves the samples along the optical axis, an 60× objective lens with a numerical aperture (NA) of 0.85, and a CCD camera to capture the images. In the imaging test, a 40× objective lens was used to replace the 60× objective lens.

Optical microscopy

Given that many components fabricated in this work exhibit micrometer-scale structures, a specific level of magnification is required for optical layer and structure characterization. Hence, optical microscopy is extensively used in this work. The resolution of an optical microscope is limited by diffraction, which is described by the size of the Airy disk. Typically, the resolution of a microscope can be defined as the full-width-half-maximum of the point spread function:

$$FWHM = \frac{0.51\lambda}{NA} \tag{4.12}$$

Therefore, to reach a higher resolution, it is desirable to either employ objectives with higher NA or use a shorter wavelength for the light source. Typically, an objective with a higher magnification corresponds to a higher NA. In this work, microscope images were taken by an optical microscope, specifically Axioplan 2 imaging system from Carl Zeiss, which is equipped with a CCD camera AxioCam ICc3. Objectives with magnifications ranging from 2.5× to 50× were used. The microscope uses a reflected broadband light source for illumination.

Confocal microscopy
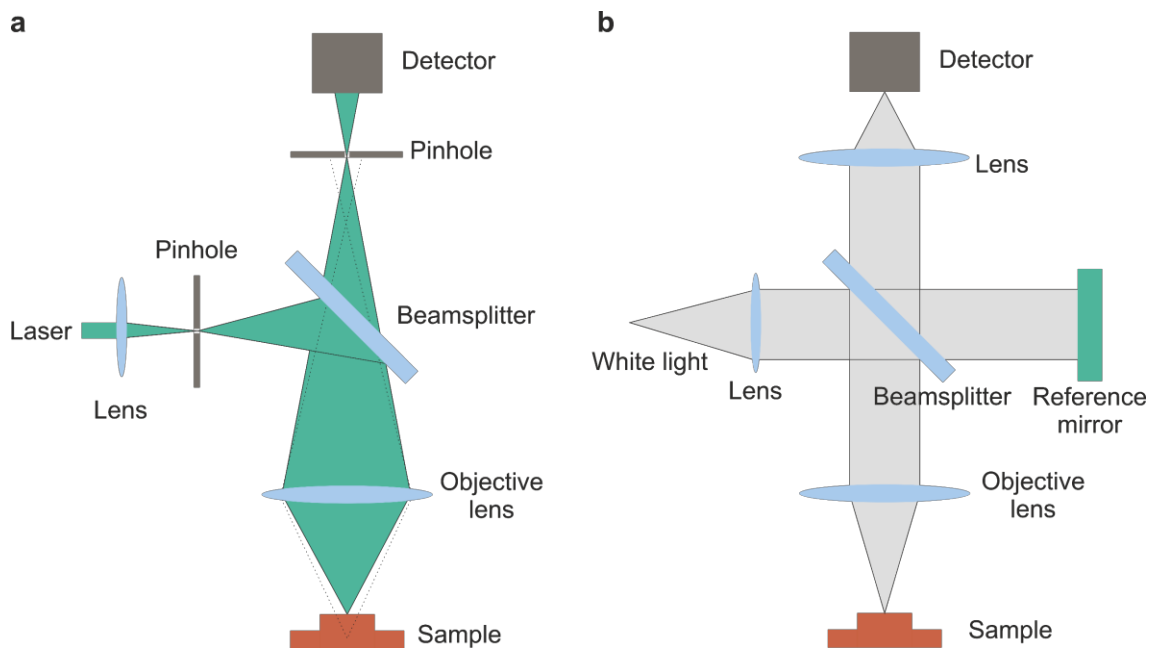
Figure 4.7: Schematic illustration of optical methods for measuring the three-dimensional surface profiles. (a) Confocal laser scanning microscopy. Two pinholes at conjugated planes are used to enhance the resolution. (b) White light interferometry. An interferometer is used to extract height information from the interference fringes captured from the superposition of the measurement light beam and reference light beam.

The confocal laser scanning microscope (CLSM) is a microscopy technique that employs pinholes at conjugated planes to eliminate out-of-focus light and, therefore, enhance the resolution. As depicted in **Figure 4.7**a, the light beam emitted from a light source goes through a pinhole, which can be deemed as a point source. Light coming from the pinhole is focused onto the object. When the object point is precisely in focus, the light is reflected and follows the same conjugated path, converging to another pinhole, which is placed at the conjugated plane. Consequently, only light from the targeted distance, where the object points are in focus, is collected. CLSM functions as a form of tomography. The laser scans the surface of the sample in each plane, and a two-dimensional (2D) image is reconstructed. Additionally, the height of the sample is adjusted to capture its 2D images at different heights, ultimately resulting in a reconstructed volume image of the sample. In this work, the 3D surface profiles of the MLAs arranged in a square layout were acquired using a 3D optical surface metrology system, Leica DCM8, with an objective of 50× magnification.

White light interferometry

An additional characterization tool for the 3D surface structure analysis is white light interferometry. Utilizing the optical interference effect, it provides exceptional resolution in the height direction, where the data are extracted from the pattern of the interference fringes. As illustrated in **Figure 4.7**b, the incident light beam is split into two beams by a beamsplitter. The measurement light beam is directed towards the sample, while the reference light beam is directed to a reference plane. After reflection, the two beams again combine into a single beam, and the detector captures interference fringes resulting from the superposition of waves. In this work, the 3D surface profiles of the MLAs arranged in a hexagonal layout, the surface profiles of the printed thin films, and the surface profiles of the printed droplets for estimating the shrinkage in volume were characterized using a 3D optical profilometer based on white light interferometry, ContourGT-X, from Bruker.

Stylus profilometry

In addition to the non-contact optical characterization methods mentioned above, contact methods are also used for surface morphology characterization and thickness measurement. Stylus profilometry involves using a probe to directly scan the sample surface in a contact manner, typically along one direction. As the stylus traverses the surface, it moves upward when encountering surface elevations and downward when it is at the valleys. From the collected data, a 1D surface profile is then directly reconstructed. Compared to CLSM and white light interferometry, stylus profilometry has a lower resolution and provides fewer details; however, it is a straightforward and fast-scanning tool, especially suitable for measurements across large dimensions. In this work, the thicknesses of the fabricated thin films were measured using a stylus profilometer DektakXT from Bruker.

Atomic force microscopy

In order to obtain more detailed information with a significantly higher resolution from the fabricated surface in both lateral and vertical directions, atomic force microscopy (AFM) is used. AFM is a typical type of scanning probe microscopy that uses a fine-tipped probe to scan the sample surface with a lateral resolution of approximately 1 nm and a vertical resolution of about 0.1 nm [205]. Unlike stylus profilometry, the tip used in AFM has to be extremely fine to ensure high resolution, and both contact and noncontact modes are possible with AFM. The schematic illustration of AFM is shown in **Figure 4.8**a.
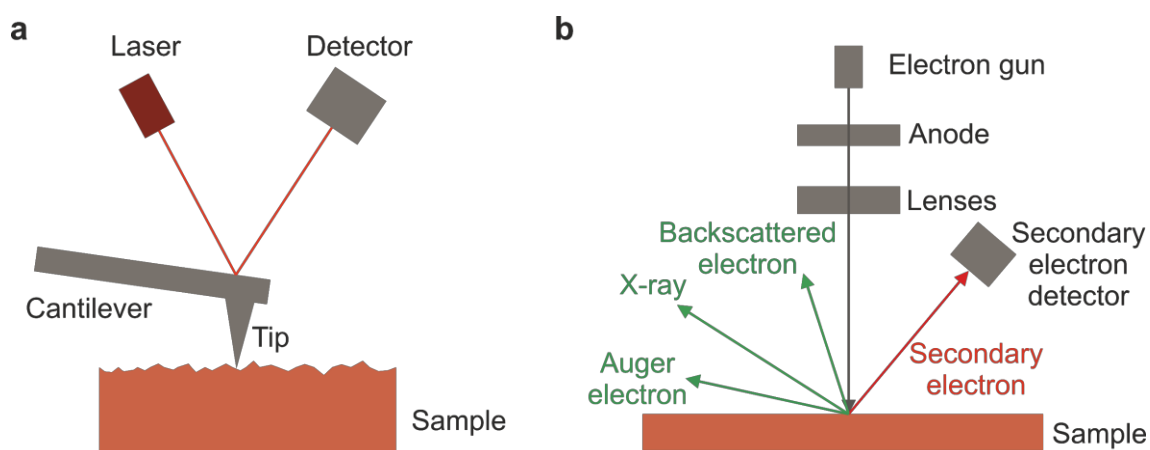
Figure 4.8: Schematic illustration of different microscopy methods. (a) Atomic force microscopy. A probe is used to scan the surface in two dimensions. High-resolution surface topography is obtained. (b) Scanning electron microscopy. Electron microscopy provides much higher resolution than optical microscopy due to the lower wavelength of electrons.

In AFM, the probe is used to scan the sample surface in two dimensions, and a laser beam is reflected from the cantilever and captured by a detector. In contact mode, as the probe scans the surface, forces are applied to the tip according to the morphology, which deflects the laser beam incident on the cantilever. The deflection of the laser beam, therefore, encompasses changes in the cantilever and the height information. In non-contact mode, the cantilever is oscillating at a frequency close to its resonant frequency. As the probe scans the surface, variations in the height profiles cause changes in the oscillation. In the AFM system, a feedback loop is used to adjust the distance between the tip and the surface to maintain the oscillation. This information then provides the 2D topography of the scanned area. AFM is a characterization method that provides highly detailed surface information, including height profiles and compositions. However, the scanning area is typically limited, and there is a tradeoff between the scanning speed and resolution. In this work, the detailed surface morphology was measured using the AFM system NanoWizard from Bruker Nano, and the surface information was subsequently analyzed using the software Gwyddion.

Scanning electron microscopy

Scanning electron microscopy (SEM) is a commonly used type of electron microscopy where an electron beam is used to scan the object and construct magnified images. In SEM, electrons generated from an electron gun are accelerated between the anode and cathode. After going through an electromagnetic lens system, the electron beam is focused on the specimen. A raster scanning is carried out to construct the 2D images.

Upon the electrons hitting the sample, they interact with the specimen at different depths within the sample, as can be seen in **Figure 4.8**b. A variety of interactions take place,

generating signals that can be used for specimen analysis. The two most prominent interactions are the elastic scattering and inelastic scattering of electrons. In elastic scattering, the direction of the electrons undergoes a drastic change, and the electrons are reflected, which are called backscattered electrons. In terms of inelastic scattering, the incident high-energy electrons lose their energy, and secondary electrons are emitted. The inelastic scattering usually happens at a small depth in the substrate, and therefore, secondary electron signals are used to measure the morphology of the sample. In this work, the secondary electron signals are used for layer morphology characterization.

The Everhart-Thornley detector collects the emitted secondary electrons by applying a low voltage to the collector screen. The collected electrons are accelerated through an applied high voltage and go into a scintillator, where the signals are converted into photons. The converted photons are then guided through a photomultiplier to obtain an amplified signal, which provides the intensity distribution into the image.

The resolution of the final image is determined by the spot size of the focused electron beam, which depends on the working distance and the final aperture size. A better resolution can be achieved by using a smaller working distance or decreasing the size of the final aperture. However, a small working distance leads to a decreased depth of focus. Therefore, optimization of the parameters is essential to achieve good image quality.

In this work, the SEM images were obtained using the system SUEPRA 55 from Carl Zeiss. Prior to the SEM measurements, the dielectric samples were prepared by sputtering an ultra-thin conductive layer, such as gold, on the surface. When the sample is non-conductive, electrons can be trapped on the surface of the sample and cause the so-called charging effect. This effect causes false signals in the area and, therefore, has to be eliminated. Since the sputtered conductive layer is very thin, the morphological feature of the sample surface is maintained. The SEM images of the top surfaces were captured at an acceleration voltage of 5 kV. The cross-sectional SEM images were taken at an acceleration voltage of 3 kV. The samples for cross-sectional images were first prepared using focused ion beam milling with the Zeiss Crossbeam 1540 EsB device. The cross-sectional SEM image shown in this work was partially colored layer by layer via outline tracing using the software CorelDraw.

Spectrophotometry

The spectral characteristics of the fabricated devices in this work were measured by spectrophotometry. It is a quantitative characterization tool for the reflectance, transmittance, and absorptance of a measured sample over the wavelength range from UV and visible to infrared radiation. As illustrated in **Figure 4.9**, in a spectrophotometer, light sources covering different wavelength ranges are used to generate light beams. The light beam first goes through a monochromator, where a grating is used to split the spectrum into different spatial locations. The scanning takes place by rotating the grating. Subsequently, a part

of the spectrum passes through an ultranarrow slit with a micrometer-scale width. Afterward, the monochrome light beam first goes to a beamsplitter, which splits it into a reference beam and a measurement beam. The measurement light beam goes through the sample, and the transmitted light is detected. By comparing it to the reference signal, the transmittance of the sample can be obtained. To measure the diffuse or total transmittance or reflectance of the sample, an integrating sphere needs to be applied at different positions relative to the sample to collect the light. The inner walls of the integrating sphere are coated with highly diffuse reflective materials, and thus, the incident light is evenly distributed in the integrating sphere through diffuse scattering.
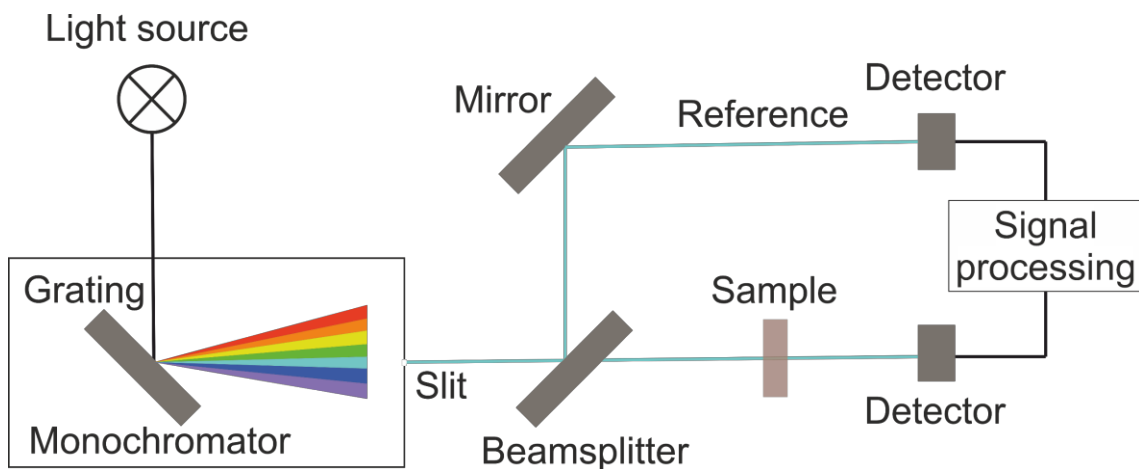
Figure 4.9: Schematic illustration of a UV-visible-NIR spectrophotometer. The detectors can be positioned within an integrating sphere for total transmittance and reflectance measurements.

In this work, all transmittance and reflectance spectra were measured using the spectrophotometer Lambda 1050+ UV/VIS/NIR from PerkinElmer with an embedded integrating sphere module applied. The reflectance spectra were measured under an angle of 8°. In the angle dependence study in Chapter 7, the reflectance spectra were obtained using the spectrophotometer without the integrating sphere module.

Optical simulation

After the transmittance and reflectance spectra of the fabricated Bragg mirrors in Chapter 7 were measured, they were compared to the results obtained from the optical simulation. In this work, the optical simulation of the Bragg mirrors was conducted using the simulation program Optical, which is based on the transfer matrix method [206]. The experimental input parameters are the optical constants, i.e., the RI and extinction coefficients, of the constituent materials, which were determined by spectroscopic ellipsometry, and the thicknesses of the individual layers, which were measured by stylus profilometry. The

optical simulation software returns the transmittance and reflectance data of a stack at a specific incident angle, and the values are compared with the measurement results. For the design and optimization of the Bragg mirrors, the software Essential Macleod from Thin Film Centers was used.

5 Fabrication of Microlens Arrays by Inkjet Printing

Microlens arrays (MLAs) have diverse applications in various fields, such as sensors, projection, and display. Multiple fabrication methods have been used for fabricating MLAs, with inkjet printing standing out for its advantages in terms of simplicity, versatility, and cost-effectiveness. However, previous approaches involve additional manufacturing steps, such as photolithography, to pre-structure the substrate for enhanced uniformity and a high fill factor (FF). In this chapter, the fabrication of MLAs on unstructured substrates using inkjet printing is introduced. The optimized UV-curable ink and surface treatment with self-assembled monolayers are discussed. The automated quantitative evaluations prove the excellent uniformity of the printed MLAs, and an unprecedented FF is achieved among all inkjet-printed MLAs on unstructured substrates. In the end, digitally controlled large-area fabrication on both rigid and flexible substrates is demonstrated. Parts of the results presented in this chapter have previously been published in the journal Advanced Optical Materials [207].

5.1 Introduction
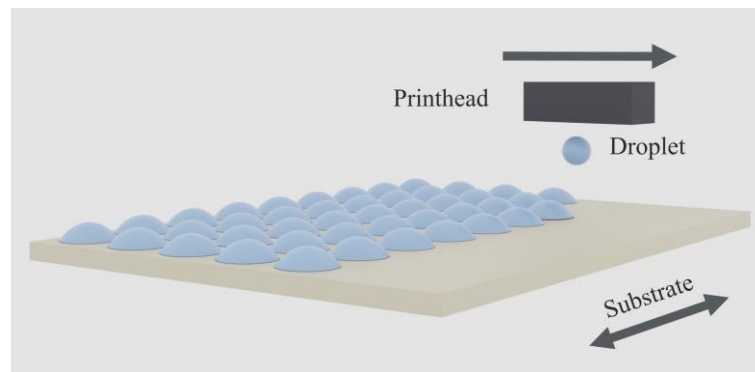
Figure 5.1: Schematic illustration of the inkjet printing of microlens arrays.

A microlens array (MLA) plays a crucial role as a miniaturized component in micro-optical systems, offering advantages such as flexibility of integration, high compactness, and designable optical characteristics [208-210]. Inkjet printing has demonstrated its effectiveness in the rapid and flexible fabrication of MLAs. The drop-on-demand (DOD) inkjet printer expels droplets at designated locations on the substrate, where the liquid droplets with a small Bond number form into a spherical lens shape due to surface tension.

The fabrication of an MLA is completed after subsequent solidification. **Figure 5.1** depicts the schematic of the inkjet printing process for MLAs.

However, obtaining high-fill-factor (high-FF) MLAs through inkjet printing poses a challenge. To address this challenge, in this chapter, MLAs with excellent quality and an unprecedented FF of 88% are demonstrated. This is achieved without surface structuring steps prior to inkjet printing, which has not been realized by previous work. Various numerical apertures (NAs) for MLAs are obtained through the application of diverse self-assembled monolayers (SAMs), demonstrating the potential for continuous tuning of the NA. In addition, the printed MLAs exhibit outstanding uniformity, with a standard deviation in the radii of microlenses (MLs) being below 2.5% and in sag height being below 3.9%. The formulated UV-curable ink and the optimized printing process show high stability, significantly enhancing the positioning accuracy of the MLs. Thanks to the improved positioning accuracy, densely arranged hexagonal MLAs are printed. The high FF of 88% is achieved through the minimal shrinkage of the UV-curable ink and the instantaneous in situ UV curing. The developed ink and printing process demonstrates the possibility of significantly decreasing fabrication costs and process complexity in MLA fabrication while maintaining a high level of FF in MLAs. Furthermore, it allows for printing MLAs on both rigid glass substrates and flexible foil substrates or directly on optoelectronic devices such as light-emitting devices and photodiodes, expanding the range of integration possibilities and applications for MLAs.

5.2   Ink Formulation and Fabrication

SU-8 shows a high transmittance in the wavelength range beyond 360 nm and exhibits high chemical resistance [211]; hence, it is selected to be included in the ink. Since SU-8 has a high viscosity, it is necessary to incorporate diluents in the ink to bring the ink viscosity into the appropriate range for inkjet printing. However, when cyclopentanone, a common solvent for SU-8 which does not react with it during UV-exposure, is added to the ink (Ink-Cyclopentanone), a strong coffee-ring effect was observed in the printed thin film, as depicted in **Figure 5.2**a and b. As described in Section 2.4.3, the coffee-ring effect is caused by the capillary flow during solvent evaporation [107]. Therefore, in order to mitigate the drying effects, such as the coffee-ring effect, the non-reactive diluent was implanted to substitute the reactive diluent. The three-dimensional (3D) image and the height profile of a printed film using the ink with the non-reactive diluent ink (Ink-25) are shown in **Figure 5.2**c and d, respectively.
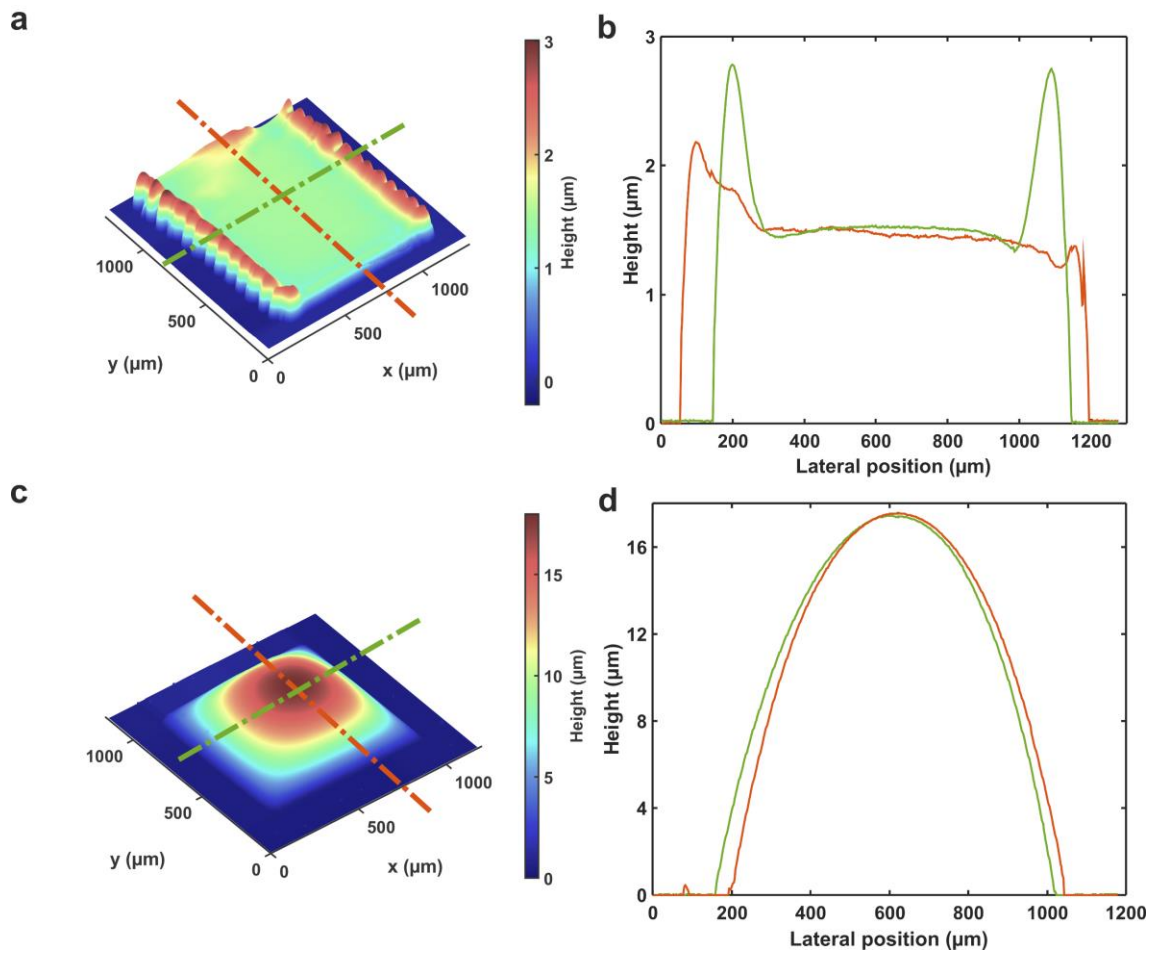
Figure 5.2: Final shapes of the printed thin films using inks with non-reactive and reactive diluents. (a) A three-dimensional (3D) image of a thin film printed using Ink-Cyclopentanone (SU-8 mixed with non-reactive diluent). (b) Surface profiles extracted from (a) along the dashed lines in the x-direction (green) and y-direction (red), respectively. (c) A 3D image of a thin film printed using Ink-25 (SU-8 mixed with reactive diluent). (d) Surface profiles extracted from (c) along the dashed lines in the x-direction (green) and y-direction (red), respectively.

Since the FF of an MLA is determined by the proportion of the ML-covered area to the total array area, in order to obtain a high FF through inkjet printing, it is important to achieve the minimal volume shrinkage of the MLs after both UV curing and hard bake processes. Hence, SU-8 2150, which has the highest solid concentration among all SU-8 products, is selected as the primary component in the ink. A reactive diluent Erisys GE-20, which undergoes cross-linking with SU-8 molecules upon UV exposure, is chosen as the diluent for SU-8 2150 to reduce the viscosity to an appropriate range for inkjet printing while keeping the volume shrinkage minimal. The height profiles of an Ink-25 droplet after three different stages are shown in **Figure 5.3**.
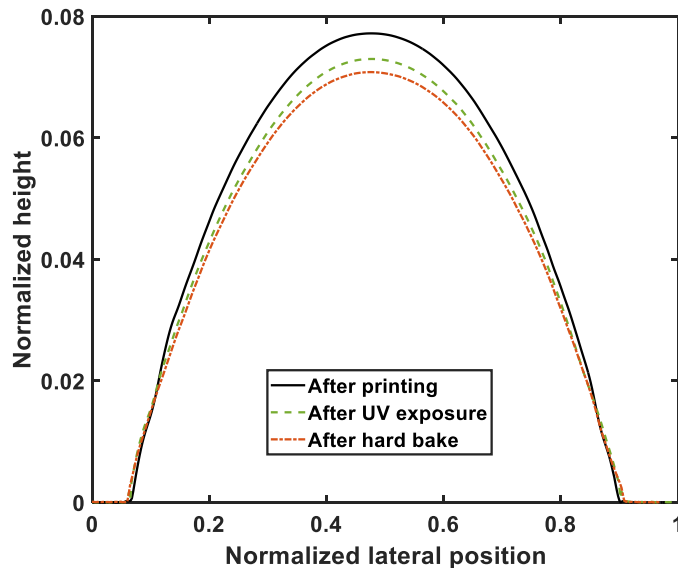
Figure 5.3: Height profiles of an Ink-25 droplet on the substrate at three different stages. These include inkjet printing, UV exposure, and hard bake. The vertical and lateral axes are normalized to the length of the captured square image of 200 µm.

After the droplet was exposed to UV at 40 °C for 3 minutes, the droplet height showed a decrease of 2.46%, while the diameter showed an increase of 2.10% compared to the dimensions right after the printing process. The final shape was obtained after UV curing and hard bake at 95 °C for 3 minutes, and it showed a further decrease in the sag height by 5.44% and an increase in the diameter by 1.05% compared to its shape directly after printing. Since one droplet has a Bond number much smaller than 1, the shape of the droplet on the substrate is determined by the surface tension and can be assumed to be a spherical cap. Therefore, the volume of a printed ML can be calculated from its sag height h and radius a:

$$V = \frac{\pi}{6}(3a^2 h + h^3) \tag{5.1}$$

Based on the calculations, the volume of the Ink-25 droplet was reduced by only 3.58%. It is noteworthy to highlight the minimal shrinkage (or expansion) of the Ink-25 ML in the lateral directions, which contributes to the high FF in MLA fabrication.

Figure 5.4 shows the comparison of the shrinkage between an Ink-25 droplet and an Ink-Cyclopentanone droplet prior to UV exposure, where the droplets were exposed under ambient conditions. As can be seen from the figure, the shape of the Ink-25 droplet remained nearly constant in the air for over 10 minutes, whereas the height of the Ink-Cyclopentanone droplet showed a significant reduction over time.
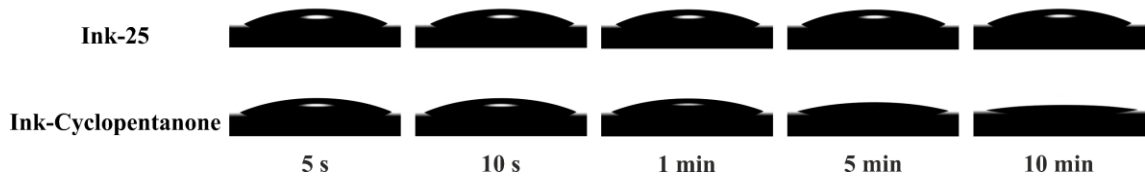
Figure 5.4: Captured side view images of an Ink-25 droplet (upper row) and an Ink-Cyclopentanone droplet (lower row) under ambient conditions over a time duration of 10 minutes.

Table 5.1: Rheological properties of SU-8 inks at different concentrations

Ink	wt% SU-8	Density (g/cm^3)	Surface tension (mN/m)	Viscosity @ 40 °C (mPa·s)	Ink suitability
Ink-10	10%	1.0850 ± 0.0017	35.99 ± 0.18	13.96 ± 0.16	Non-curable
Ink-15	15%	1.0893 ± 0.0058	35.48 ± 0.21	14.69 ± 0.07	Non-curable
Ink-20	20%	1.0907 ± 0.0012	35.06 ± 0.12	16.61 ± 0.05	Printable, curable
Ink-25	25%	1.0963 ± 0.0085	34.51 ± 0.16	23.35 ± 0.06	Printable, curable
Ink-30	30%	1.0997 ± 0.0039	34.65 ± 0.35	30.34 ± 0.08	Non-printable
Ink-35	35%	1.1101 ± 0.0073	35.50 ± 0.22	40.15 ± 0.09	Non-printable

In order to determine the ideal concentration of SU-8 in the reactive diluent, inks with different SU-8 concentrations were formulated. The rheological characteristics of these inks are presented in **Table 5.1**. As indicated in the table, increasing the SU-8 concentration from 10 wt% to 35 wt% leads to a significant increase in the ink viscosity, from 13.96 (± 0.16) mPa·s to 40.15 (± 0.09) mPa·s at 40 °C, which is the maximum temperature of the used printhead. Meanwhile, the surface tension and density of the inks exhibit only slight variations and no clear trend. However, the contact angle of the ink droplet on the glass substrate shows an increase with SU-8 concentration increasing, as seen in **Figure 5.5**.

Figure 5.5: Contact angle measurements of different SU-8 inks on bare glass substrates in ambient conditions. With the SU-8 concentration increasing, an increase in the contact angle is seen.

The Weber and Reynolds numbers of the inks with different SU-8 concentrations are calculated as described in Section 2.4.2, where the characteristic length takes the value of the nozzle orifice size of 21.5 µm. Subsequently, the SU-8 inks from in **Table 5.1** are plotted in the *Re – We* parameter space, with each solid line indicating the theoretical printability of a specific ink at varying droplet ejection velocities, as illustrated in **Figure 5.6**. The figure shows that Ink-30 and Ink-35 possess too high viscosity with a Z number smaller than 1, placing them outside the printable window. Meanwhile, all other inks fall within the printable window.
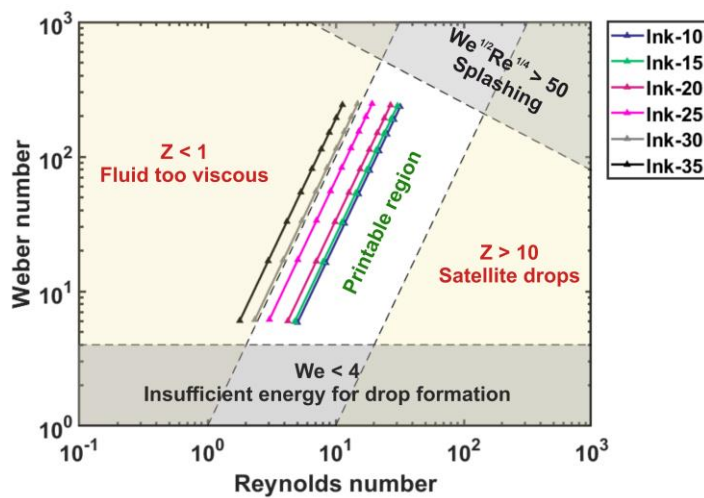
Figure 5.6: Printability map in the parameter space of *Re* versus *We*. Different colors in the solid lines represent inks with different SU-8 concentrations, while each line represents one ink with different droplet ejection velocities. The white region indicates the printable window.
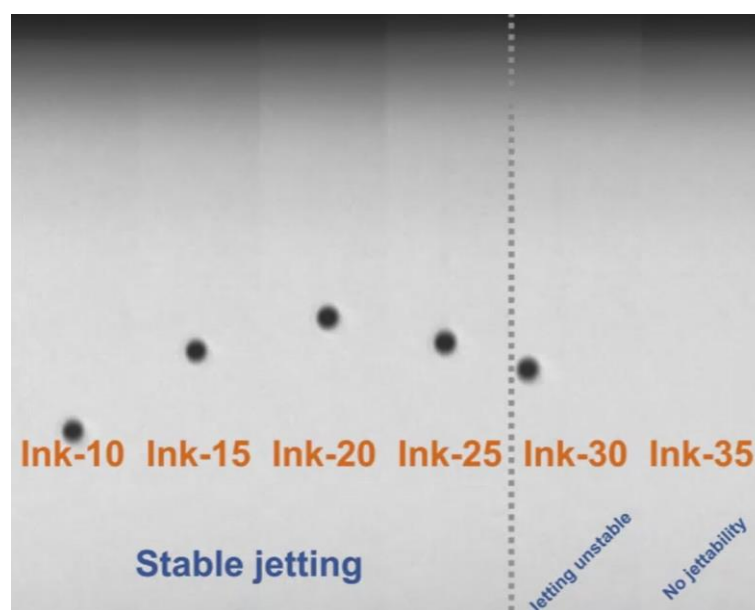
Figure 5.7: Side view of ejected droplets of different inks from the printhead. Ink droplets from Ink-10, Ink-15, Ink-20 and Ink-25 show stable ejection. The Ink-30 droplet shows unstable behavior and deviates from the planned straight trajectory. No droplet of Ink-35 is ejected.

The experimental validation further confirms the printability of the inks, which coincides with the theoretical prediction. To achieve uniform ML shapes and decrease the number of defects, it is necessary that the ejected droplets from the printer have the desired sphere shapes without the formation of satellite droplets. Stable droplet ejection without the formation of satellites was realized for Ink-10, Ink-15, Ink-20, and Ink-25, enabled by the suitable ink formulation along with a customized waveform, as shown in **Figure 5.7**. However, the droplet of Ink-30 appears to be unstable during jetting and deviates from the target trajectory. Moreover, with Ink-35, no droplet ejection was observed, as expected from its high viscosity. Hence, to ensure stable droplet ejection, an upper limit of below 30% is defined for the SU-8 concentration.

The suitability of the ink for MLA fabrication depends on not only the stable droplet ejection but also the subsequent UV-curing process, which sets the lower limit of the SU-8 concentration. Since the reactive diluent molecule can only crosslink with the SU-8 molecule, as the concentration of the reactive diluent rises, the required UV exposure dose becomes higher. If the SU-8 concentration is too low, the ink cannot be cured anymore because crosslinking becomes very challenging. A UV-LED (Hamamatsu) was used to cure the printed MLAs. Following inkjet printing, the MLAs were placed under UV exposure at 40 °C for various durations of time. Subsequently, the MLAs were hardbaked at 95 °C for 3 minutes. Afterward, the MLAs were immersed in the developer of SU-8 (MicroChem) for a duration of 1 minute. If the MLA structures remain intact after

the development process, the MLAs are deemed cured. On the contrary, if the structures were removed during development, even after one hour of UV exposure, MLAs are regarded as non-curable. Using this method, it was determined that Ink-10 and Ink-15 are considered non-curable with 385 nm radiation exposure due to the low concentration of SU-8. Therefore, Ink-20 and Ink-25 are the two inks capable of enabling both stable printing and effective curing.
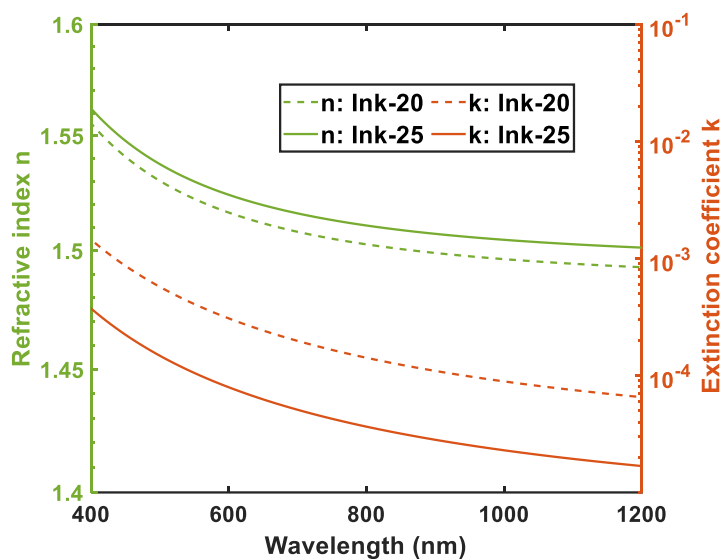
Figure 5.8: Refractive indices *n* (green lines) and extinction coefficients *k* (red lines) of the thin films produced with Ink-20 (dashed lines) and Ink-25 (solid lines), respectively. The measurement was conducted using spectroscopic ellipsometry.

Comparing Ink-20 and Ink-25, the latter required significantly less UV dose (3-minute exposure) than Ink-20 (10-minute exposure). Furthermore, the refractive indices and extinction coefficients of the ink material were measured as thin films through spectroscopic ellipsometry in the wavelength range from 400 nm to 1200 nm. The results, as illustrated in **Figure 5.8**, show a decrease in refractive indices with increasing wavelength, approaching the refractive index (RI) of glass. Additionally, in this wavelength range, both materials exhibit minimal extinction coefficients, demonstrating low optical losses. In a comparison between the film formed by Ink-20 and Ink-25, the latter exhibits a slightly higher RI and, at the same time, lower optical loss, which are desired properties of the MLA material. Hence, the subsequent work in this chapter focuses on Ink-25, and the word 'ink' in the following sections of this chapter specifically refers to Ink-25.
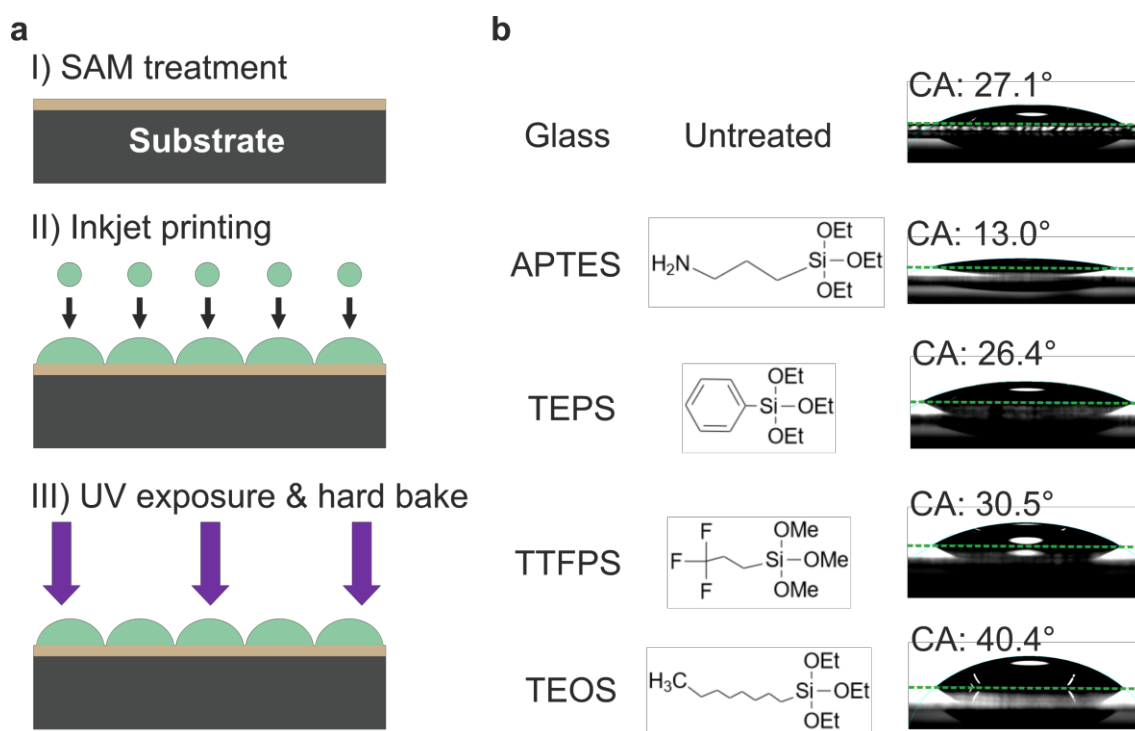
Figure 5.9: Process of manufacturing printed microlens arrays (MLAs) on substrates with and without surface treatment. (a) The three steps of the MLA fabrication: I) Substrate treatment with self-assembled monolayers; II) Inkjet printing of MLAs on the substrate; III) UV exposure and hard bake of the printed MLAs. (b) Contact angles of the ink on substrates with different siloxanes. The green dashed lines in the contact angle images indicate the interface between the droplet and the substrate.

The MLAs were then fabricated with the selected ink, and the process for fabricating MLAs with different aspect ratios is depicted in **Figure 5.9**a. Initially, a SAM film was applied to the glass substrate by spin coating. Following the SAM treatment, MLs were directly inkjet-printed on the surface, followed by UV exposure and hard bake. In this study, four different siloxanes were used for demonstration, including 3-aminopropyltri-ethoxysilane (APTES), triethoxyphenylsilane (TEPS), trimethoxy-(3,3,3-trifluorpropyl)-silane (TTFPS), and triethoxyoctylsilane (TEOS). These siloxanes were selected for their diverse surface free energy (SFE) properties. These siloxanes comprise one customizable side chain and three anchor groups, as shown in **Figure 5.9**b. The anchor groups establish a bond with the substrate, while the customizable side chain allows modification to tune the resulting SFE of the substrate [212]. By tuning the SFEs, the ink droplet can have different static contact angles on the substrate, ranging from a low contact angle of 13.0° on APTES to 27.1° on the bare glass substrate, and the angle increases further to 40.4° on TEOS. It has to be pointed out that this range of the contact angle can be extended since additional siloxanes can be used to increase the SFE to values higher than APTES

or decrease the SFE to values lower than TEOS, offering the potential to tune the aspect ratio or the NA of the MLs further.

Ink formulations mentioned above are prepared as follows: SU-8 2150 (Kayaku Advanced Materials) with a solid concentration of 76.75% and a viscosity of 80000 mPa·s was added in the inks. It was diluted in the reactive diluent Erisys GE-20 (Huntsman) in the concentration of 10 wt%, 15 wt%, 20 wt%, 25 wt%, 30 wt% and 35 wt% for Ink-10, Ink-15, Ink-20, Ink-25, Ink-30 and Ink-35, respectively. The ink for reference, Ink-Cyclopentanone, which is the ink with non-reactive diluent, comprises SU-8 2150, which was diluted in cyclopentanone (Sigma-Aldrich, ⩾99%) to reach a concentration of 25 wt%. Ink-25 was used as the primary ink for the fabrication of MLAs in Chapter 5 and 6.

Before printing, the formulated inks were placed in an ultrasonic bath for 10 minutes. The 10-pL DMC 11610 cartridges were used in the inkjet printing, and the jetting frequency of 1 kHz was chosen during printing. A custom waveform for jetting was created to ensure the ideal shape of generated droplets at this frequency without tails or satellite droplets. Throughout printing, a single nozzle was used for jetting, with the temperature of the printhead set to 32 °C to ensure a suitable viscosity and smooth jetting. The temperature of the substrate was set to 24 °C. Following every printing run, the full or partial MLA was cured at 40 °C with an LED (Hamamatsu) for 3 minutes, which exhibits a central wavelength of 385 nm. For the high-FF MLAs, the total UV exposure time for the whole array was then added up to 6 minutes due to the two printing runs involved. Subsequently, the cross-linking concluded with a hard bake process where the printed MLAs were placed on a hotplate at 95 °C for 10 minutes. The pitch of the MLAs can be varied by adjusting the printing resolution. The resolution of the printing recipe for the square layout of the MLA was set at 320 dots per inch (dpi) × 320 dpi, and for the high-FF hexagonal layout of the MLA, it was set to 356 dpi in the x-direction and 278 dpi in the y-direction.

5.3   Automated Quantitative Evaluation

Following the manufacturing process, MLAs were printed on the bare glass substrate and SAM-treated substrates. **Figure 5.10** displays the two-dimensional (2D) optical microscope images of the printed MLAs on differently-treated substrates and the reconstructed 3D surface profiles of four MLs from these MLAs. In order to see more MLs in the MLAs while still being able to see the details, the 20× objective lens was used in the optical microscope. From the 2D microscope images, it can be seen that the MLAs exhibit exceptional uniformity in terms of both ML shapes and their positions in the arrays. Besides, as the SFE decreases from the APTES-treated substrate to the TEOS-treated substrate, the diameter of the MLs shows a reduction. Meanwhile, the sag height increases, as seen in the 3D surface profiles reconstructed from confocal microscopy measurements with a 50× magnification objective lens. This increase in the aspect ratio results in steeper edges

of the MLs, causing laser light to scatter or reflect outside of the system's receiving angle. Consequently, in the peripheral regions of MLs on the TTFPS- and TEOS-treated substrates, some areas of data were not captured in the measurement. Despite the lack of complete 3D contours of the MLs, these measurements accurately capture the substrate surface and the vortices of the MLs, and thus, the sag heights of the MLs can be determined.
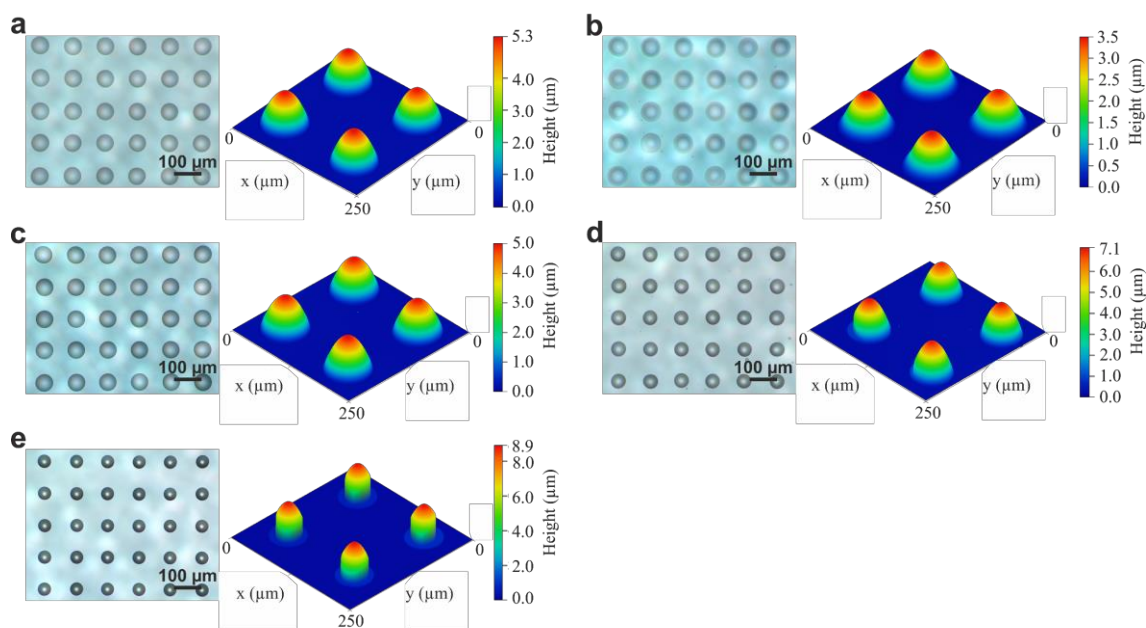
Figure 5.10: Two-dimensional (2D) microscope images and reconstructed three-dimensional (3D) surface profiles of microlens arrays (MLAs) in a square layout on differently-treated substrates. The 2D optical microscope images were captured with a 20× magnification objective lens. The 3D surface profiles were taken by confocal microscopy using a 50× magnification objective lens. (a) Untreated glass substrate. (b) 3-aminopropyltri-ethoxysilane (APTES)-treated substrate. (c) Triethoxyphenylsilane (TEPS)-treated substrate. (d) Trimethoxy-(3,3,3-trifluorpropyl)-silane (TTFPS)-treated substrate. In the 3D surface profile, some data at the periphery of the microlenses are missing due to the steep edges. (e) Triethoxyoctylsilane (TEOS)-treated substrate. Since the aspect ratio of microlenses is the highest here, the range of the missing data area is larger. The reconstructed surface profiles no longer accurately reveal the real shape of the MLA.
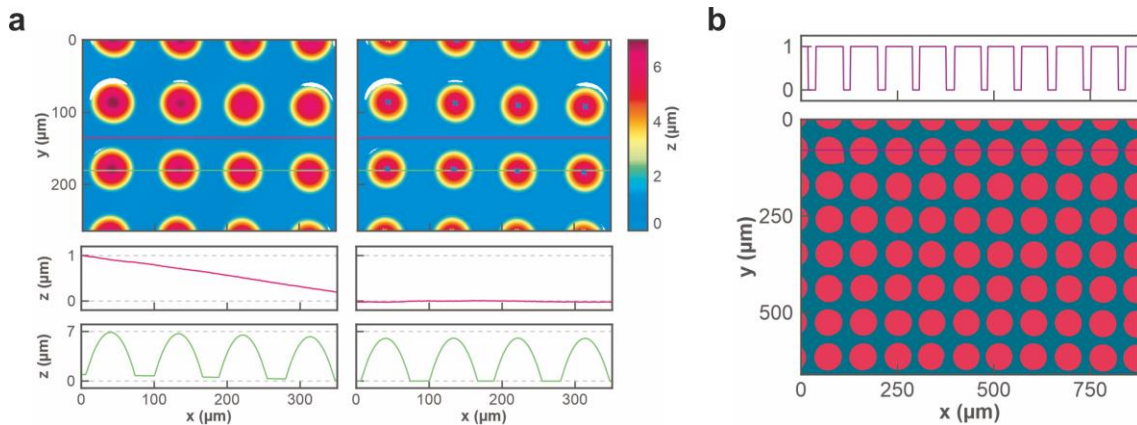
Figure 5.11: Automated quantitative evaluation of microlens arrays (MLAs). (a) Evaluation of sag heights of the microlenses (MLs). The sag heights were extracted from the three-dimensional surface profiles of the MLAs displayed in the first row. The two-dimensional cross-sectional surface profiles of the substrate surface (red line) and along the MLs (green line) are shown in the middle and bottom rows, respectively. The image on the right was de-tilted and leveled for accurate measurements based on the surface profile extracted from the left image. (b) Assessment of the radii of the MLs in a two-step process. The lower image is a filled binary image following the edge detection with the Canny algorithm. In the upper image, a binary profile corresponding to the purple line in the lower image is depicted.

To quantitively evaluate the MLAs with the desired statistics, a custom-designed automated evaluation process was developed and used for the printed MLAs [213]. Firstly, the sag height values of the MLs were derived from the 3D surface profiles of the MLAs, as illustrated in **Figure 5.11**a. Since the microscope stage has a tilt, the algorithm first assessed this tilt from the substrate surface. If the tilt is too large, the image needs to be de-tilted. Afterward, the image was leveled, and the sag height data were determined by measuring the maxima of the image. Secondly, the ML radii were extracted using the 2D microscope images measured in the same system, as shown in **Figure 5.11**b. The algorithm first modified the images according to the measured tilt in the previous step. The Canny algorithm was then applied to detect the edges of the MLs, and then these closed ML regions were filled using morphological fill. Subsequently, radius estimation was derived from the cross sections of the filled binary images, and this estimation was then used in the subsequent multi-scale Hough transform, where the precise center and radius of each ML were individually determined.
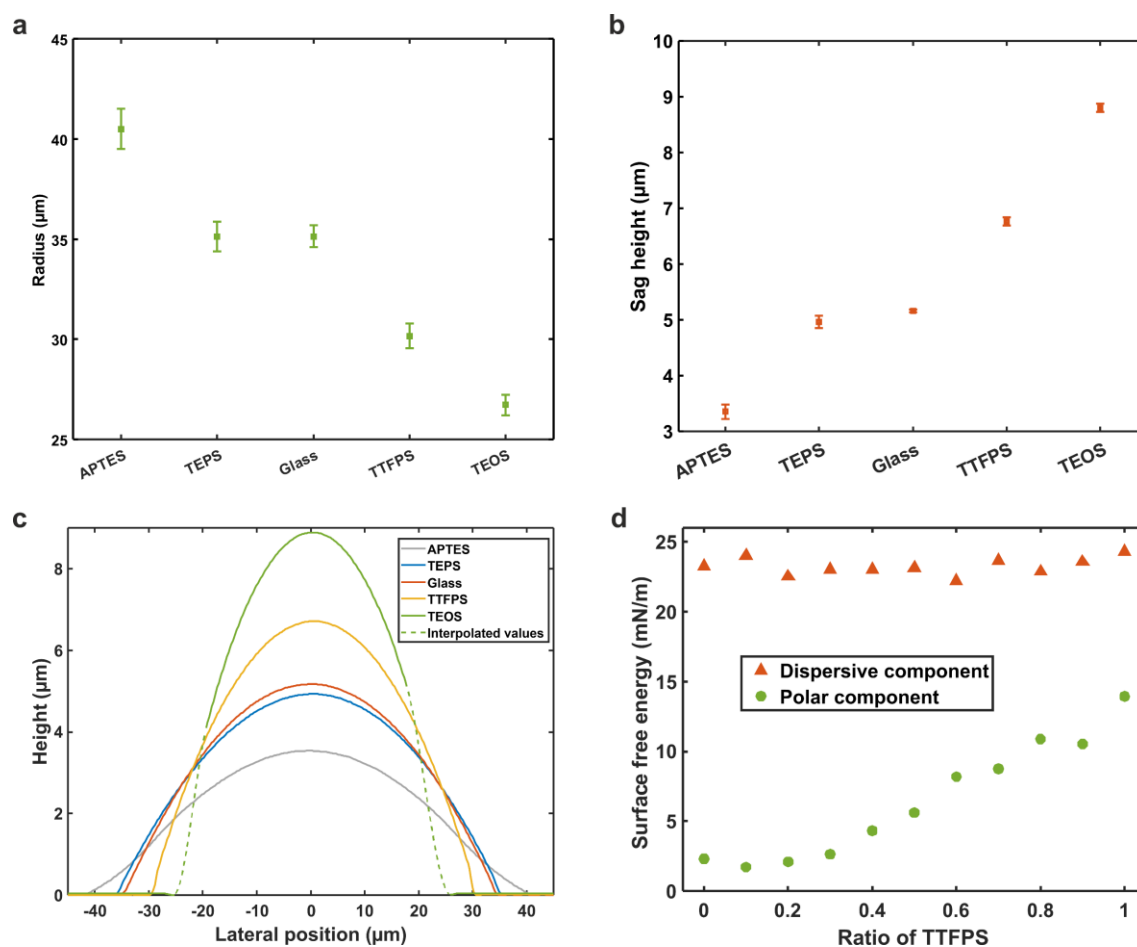
Figure 5.12: Geometrical parameters of microlenses (MLs) extracted using the automated evaluation method. (a) The radii of the MLs printed on the bare glass substrate and different self-assembled-monolayer-treated substrates, with the error bars representing the standard deviation for more than 100 MLs. (b) The sag heights of the MLs on the differently-treated substrates. Additional siloxanes or mixed siloxanes can be used to fine-tune the values. (c) The average surface profiles of the MLs from these different microlens arrays. (d) The dispersive and polar components of the surface free energy (SFE) of the substrates treated with a binary mixture of trimethoxy-(3,3,3-trifluorpropyl)-silane (TTFPS) and triethoxyoctylsilane (TEOS), showing the fine-tuning of the SFE.

The obtained radii and sag heights of the MLs on the bare glass substrate and different SAM-treated substrates are depicted in **Figure 5.12**a and b, respectively. By selecting different SAMs, the SFE of the substrate was adjusted, where APTES gives a maximum SFE and TEOS gives a minimum. As the SFE reduces, the ML radius experiences a decrease from 40.50 ± 1.02 µm on APTES to 26.72 ± 0.51 µm on TEOS. Meanwhile, since the ejected ink volume was constant, the sag height, accordingly, shows an increase from 3.36 ± 0.13 µm on APTES to 8.80 ± 0.08 µm on TEOS. The uniformity of the printed

MLAs on all different substrates is proven by the standard deviations for the radii, which are under 1.02 µm, and for the sag heights, which are below 0.13 µm.

An intuitive comparison in the shapes of the MLs is given by the 2D surface profiles of the MLs, as shown in **Figure 5.12**c. These profiles are obtained from the 3D contour images of the printed MLAs on differently treated substrates, and the missing data in the periphery area of MLs on TEOS were replaced by data obtained from spline interpolation. The lowest aspect ratio of 0.08 has been obtained on APTES, while MLs on TEOS achieve a relatively high aspect ratio of 0.33. Given the broad range of the siloxanes available for SFE tuning and the limited siloxanes studied here, a much wider aspect ratio range can be achieved with additional siloxanes giving lower SFE than TEOS or higher SFE than APTES. When MLs of a specific aspect ratio are desired, an appropriate siloxane providing the target SFE can be chosen. However, with one single siloxane, only discrete and fixed SFE values can be obtained on the glass substrate. By mixing two siloxanes for the SAM deposition, fine-tuning the SFE is possible [214]. An example of the SFE fine-tuning with the binary mixture of TTFPS and TEOS is shown in **Figure 5.12**d. As can be seen from the figure, the dispersive component of the SFE exhibits very slight changes with different mixture ratios. In contrast, the polar component increases with the fraction of TTFPS in the mixture.

Table 5.2: Geometrical parameters of printed microlens arrays on differently treated substrates obtained using the automated evaluation

Substrate	Radius (µm)	Sag height (µm)	Standard deviation in spacing	
			x-direction (µm)	y-direction (µm)
Glass	35.14 ± 0.55	5.16 ± 0.03	1.46	0.89
APTES	40.50 ± 1.02	3.36 ± 0.13	1.71	1.63
TEPS	35.12 ± 0.75	4.97 ± 0.11	2.62	1.32
TTFPS	30.15 ± 0.62	6.76 ± 0.08	1.35	2.74
TEOS	26.72 ± 0.51	8.80 ± 0.08	0.95	1.63

In addition to statistics on the geometrical parameters of the MLs, parameters of the array alignment, i.e., the spacing in each lateral direction, can be derived once the ML centers are determined. These parameters can be found in **Table 5.2**. The spacing between the MLs was set to 227 µm, and the obtained standard deviations for the ML spacings in the x- and y-direction are all below 2.74 µm. Therefore, the standard deviations are all below 1.21% of the target value, demonstrating a uniform alignment of the array.

5.4 High-Fill-Factor Microlens Arrays by Inkjet Printing
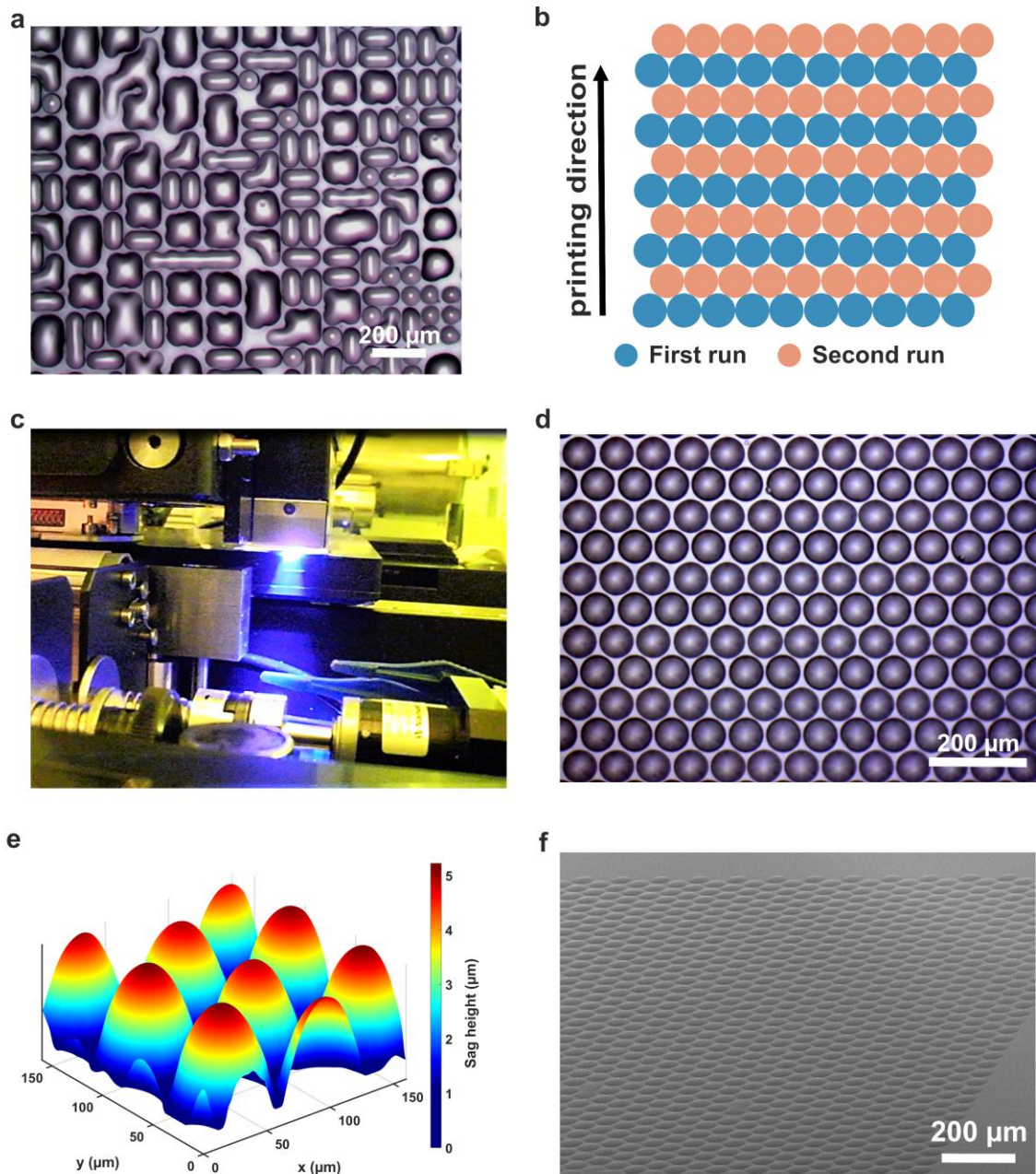
Figure 5.13: The high-fill-factor (high-FF) microlens arrays (MLAs) fabricated by inkjet printing. (a) Light microscope image of a densely-packed MLA design printed in one printing run. (b) Scheme of the two-run printing strategy for the high-FF MLAs. The first printing run is indicated by the blue microlenses, which are subsequently exposed to the UV light in situ. The microlenses shown in orange are printed in the second printing run following the same process. (c) Photo showing the in-situ UV curing of the printed MLAs.

(d) Light microscope image of a densely-packed high-FF MLA in a hexagonal layout. (e) Three-dimensional surface contour of the hexagonally-arranged high-FF MLA. (f) The scanning electron microscopy image of one part of the high-FF MLA.

In order to achieve a high FF in the MLA, the spacing between the adjacent MLs has to be minimized. However, since the droplets ejected on the substrate are in the liquid form, any slight deviations in their location during ejection or substrate movements result in the coalescence of the neighboring MLs, especially when the droplet ejection is not stable enough, as shown in **Figure 5.13**a.

In addition, the MLAs have to be printed in the hexagonal layout instead of the square layout to achieve an even higher FF. Therefore, a printing strategy was developed to achieve a minimal spacing between the MLs, where two printing runs are involved for printing one MLA. The scheme of this two-run printing strategy is illustrated in **Figure 5.13**b. Initially, the MLs in every alternate horizontal line were printed in the first run and are indicated in blue. These MLs are subsequently exposed to in-situ UV exposure, as shown in **Figure 5.13**c. In the second run, the remaining half of the MLs were printed and cured in the same process, and these MLs are indicated in orange in **Figure 5.13**b. By this means, the MLs printed in the first run were pinned by the UV-curing after the first run, resulting in lower possibilities of droplet coalescence during the second printing run.

The printed high-FF MLA has densely packed MLs and shows a high uniformity, as can be seen in **Figure 5.13**d. The 3D surface contour of several MLs in the high-FF MLA and its scanning electron microscopy (SEM) image are displayed in **Figure 5.13**e and f, respectively, highlighting the high uniformity in terms of the diameter, the height of the MLs and the spacing between the MLs. According to Equation 2.6, the FF of the MLA can be determined. The achieved smallest pitch value, P, was 71.35 µm with a lateral printing resolution of 356 dpi. Besides, the MLs have an average radius a of 35.14 µm. Therefore, a remarkable FF of 88% was accomplished for inkjet-printed MLAs, and this unprecedented value on a flat substrate surface was achieved owing to the stable droplet ejection, the in-situ UV curing, and the two-run printing strategy.

5.5 Optical and Surface Characterization
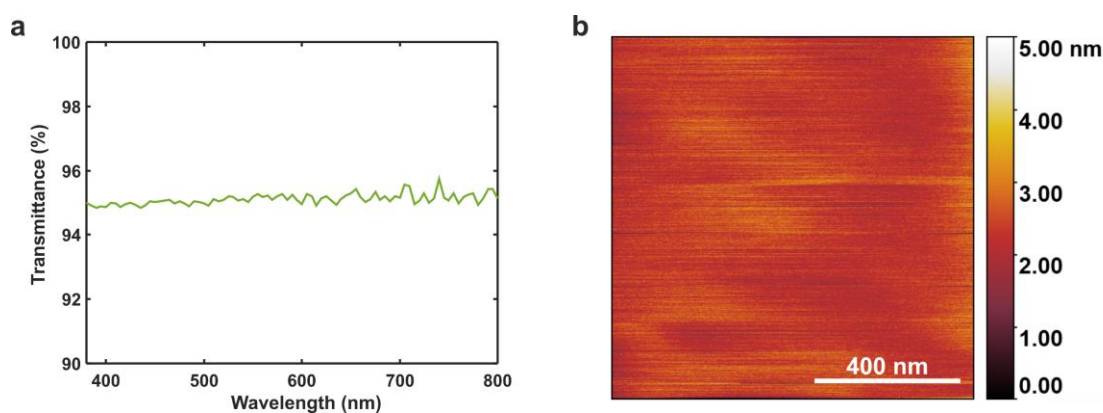
Figure 5.14: Transmission and surface characterization of the printed microlens arrays (MLAs). (a) Transmission spectrum of the MLA on the glass substrate. The wavelength range is from 380 nm to 800 nm. (b) Atomic force microscopy image of a small area on top of a microlens. The measured root-mean-square roughness is 300.7 pm.

For applications in the visible light range, the high transmittance of the MLAs in the range is desired. **Figure 5.14**a shows the transmission spectrum of the printed MLA on the glass substrate from 380 nm to 800 nm, exhibiting a high and constant transmittance over the whole visible light range. Additionally, for imaging applications, a smooth surface of the MLs is necessary to mitigate unwanted light scattering and is critical for the MLs. The typical root-mean-square (RMS) roughness values of the ML are in the range of 1 to 10 nm [215]. In this work, the surface of the printed MLA was measured using atomic force microscopy (AFM) over a small area in the central top area of the ML, as shown in **Figure 5.14**b. The RMS roughness of the surface is around 300.7 pm, indicating a highly smooth surface of the ML.

For imaging applications, the focal length of the MLs is of critical importance and needs to be characterized. The schematic for the focal length measurement setup for the MLAs is illustrated in **Figure 5.15**a. A collimated light source was used, and a printed MLA was positioned on a linear motorized precision stage with a positioning accuracy of 1 μm. As discussed in Section 2.2.1 and shown in **Figure 2.8**, only at the convex side can the focal length be directly measured as the distance between the focal point and the vertex point. Therefore, the printed MLAs were placed so that the convex side of them was facing the camera. At the end, a light microscope with an objective lens and a CCD camera was used to magnify and capture the images. In the measurement setup, all the optical components were aligned along the identical optical axis. The measurement process involved first positioning the linear stage for the camera to image the plane side of the MLA.

Subsequently, the MLA was moved towards the light source to let the camera capture the focal plane image.
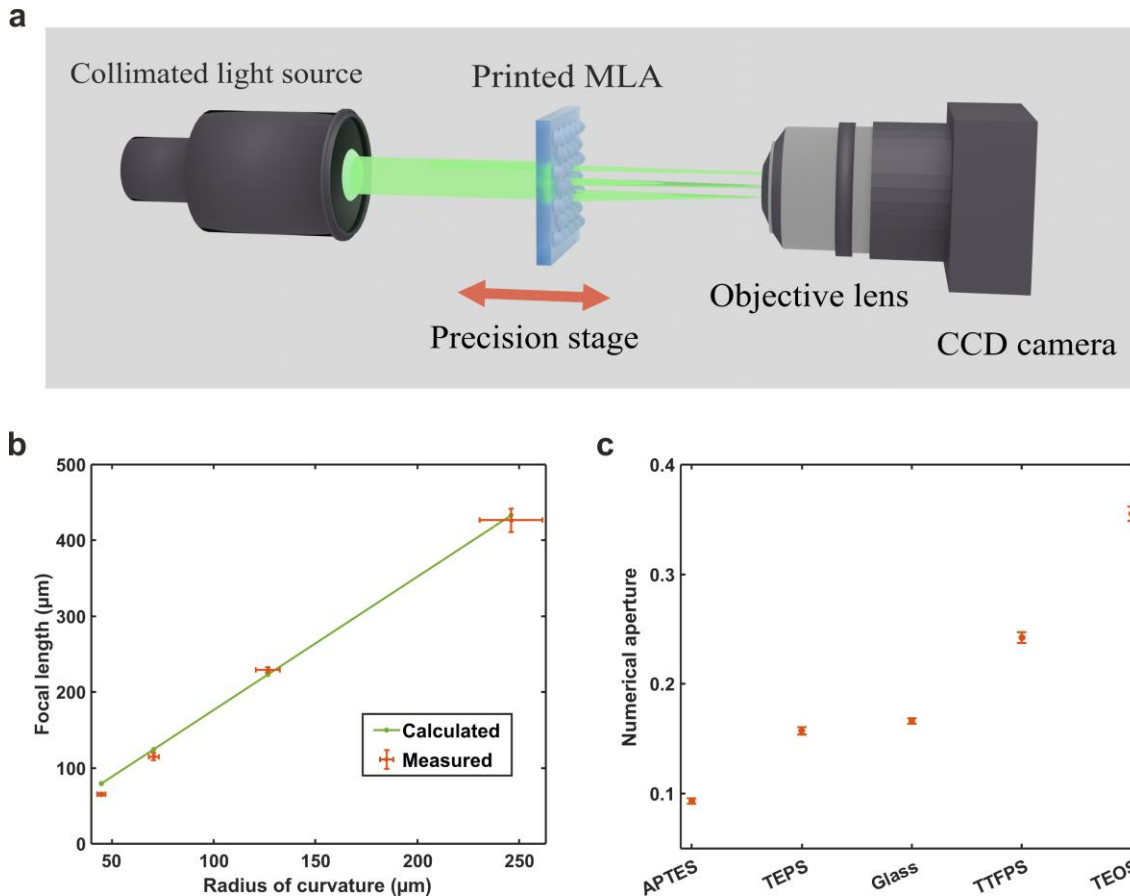
Figure 5.15: Focal length measurement of the microlens arrays (MLAs). (a) Setup for measuring the focal length of the printed MLAs. The MLA was placed on a linear motorized precision stage and placed at the locations where the focal plane and the vortex plane of the MLA were imaged by the CCD camera. (b) Calculated focal lengths in relation to the radius of curvature of the microlenses (MLs) (green line) and the measured values (red marks). (c) Calculated numerical apertures based on the measured focal lengths and radii of the MLs.

Based on the measured radius and the sag height values in **Table 5.2**, the focal lengths of the MLs can be calculated according to Equation 2.9. These are compared with the measured values, and a good match is shown between the values, as depicted in **Figure 5.15**b. The focal lengths of the MLAs, printed on four different siloxanes, ranged from 65.3 μm on TEOS to 426.7 μm on APTES. Using the measured radii and focal lengths of the MLs, the NA values of them can be calculated according to Equation 2.7, and the results are

plotted in **Figure 5.15**c. The MLAs printed on APTES yielded a small NA number of around 0.09, while on TEOS, this value increased to a relatively high number of 0.38.
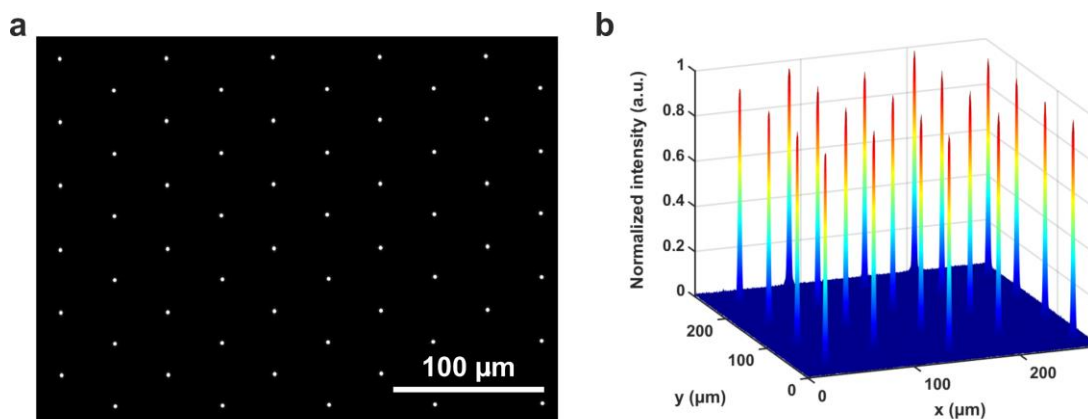
Figure 5.16: Focal plane of a printed microlens array. (a) Image of the focal plane captured by the CCD camera. (b) Normalized light intensity distribution on the focal plane.

The image of the focal plane and the light intensity distribution along this plane are displayed in **Figure 5.16**a and b, respectively. The foci, as well as the intensity peaks, are uniformly and evenly distributed in the hexagonal layout. Assessing the imaging capability of the printed MLAs is important. Therefore, on-axis optical transfer functions (OTFs) in both tangential (T) and sagittal (S) planes were calculated by conducting the Fourier transformation of the measured point spread function [216]. The MTFs of the MLAs, which are the amplitudes of the OTFs, were obtained and are plotted in **Figure 5.17**a to e. In each of the figures, the theoretical diffraction limits with the respective NA were calculated following Equation 2.12 and plotted for reference. The MTFs show the combined effects of diffraction and aberrations. As can be seen, the MTFs of all the different MLAs are consistently above 0.5 up to a spatial frequency of 50 cycles/mm, indicating a good imaging performance of the MLAs. The MLA with the best imaging quality is the one on the bare glass substrate, with the MTF being very close to the theoretical diffraction limit and staying above 0.7 until 100 cycles/mm. This might result from the high uniformity of the MLA, as shown in **Table 5.2**, and lower optical aberrations associated with the relatively low aspect ratio.

Furthermore, using this MLA as an example, its MTFs on the T- and S-planes exhibit proximity to each other. This indicates minimal aberrations caused by asymmetry of the optical component, such as astigmatism. In general, the MTF curves in the T- and S-plane of each MLA stay close to each other, demonstrating high imaging quality. It is worth noting that the MTFs that have been calculated here also include those from the objective lens. Since the NA of the 60× objective lens is 0.85, its MTF is much higher than the MTFs of the MLs and, therefore, is negligible.
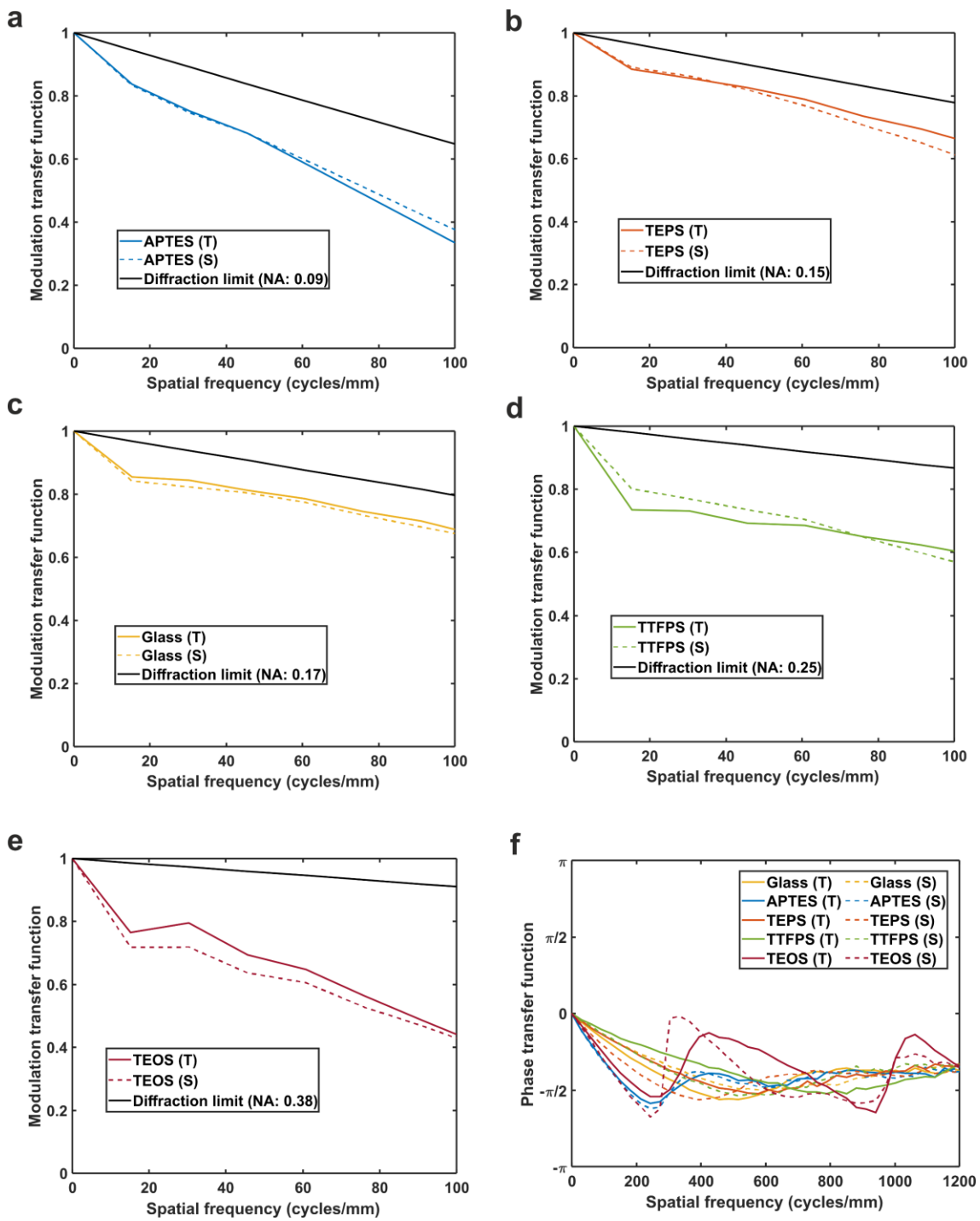
Figure 5.17: Modulation transfer functions (MTFs) and phase transfer functions (PhTFs) of the microlens arrays (MLAs) on differently treated substrates. The colored solid lines indicate the values in the tangential plane (T), and the colored dashed lines represent the values in the sagittal plane (S). The black solid lines in the MTF figures represent the diffraction limit with the respective numerical aperture (NA). (a) MTF of MLA printed on 3-aminopropyltriethoxysilane (APTES). (b) MTF of MLA on triethoxyphenylsilane (TEPS). (c) MTF of MLA on the bare glass substrate. (d) MTF of MLA on trimethoxy-

(3,3,3-trifluorpropyl)-silane (TTFPS). (e) MTF of MLA on triethoxyoctylsilane (TEOS). (f) PhTFs of the MLAs on different substrates.

Furthermore, the phase transfer functions (PhTFs) of the printed MLAs were derived from the phase of the OTFs, and the results are depicted in **Figure 5.17**f. As discussed in Section 2.2.2, the PhTF stays zero in all directions and for all spatial frequencies in an ideal and aberration-free optical element, and it usually represents the asymmetrical aberrations and poor centering of the lenses. The PhTFs of different MLAs remain between -π/4 and π/4 up to 50 cycles/mm. Meanwhile, the functions on the T- and S-plane show a small difference in low spatial frequency ranges, proving low asymmetrical aberrations and good centering.
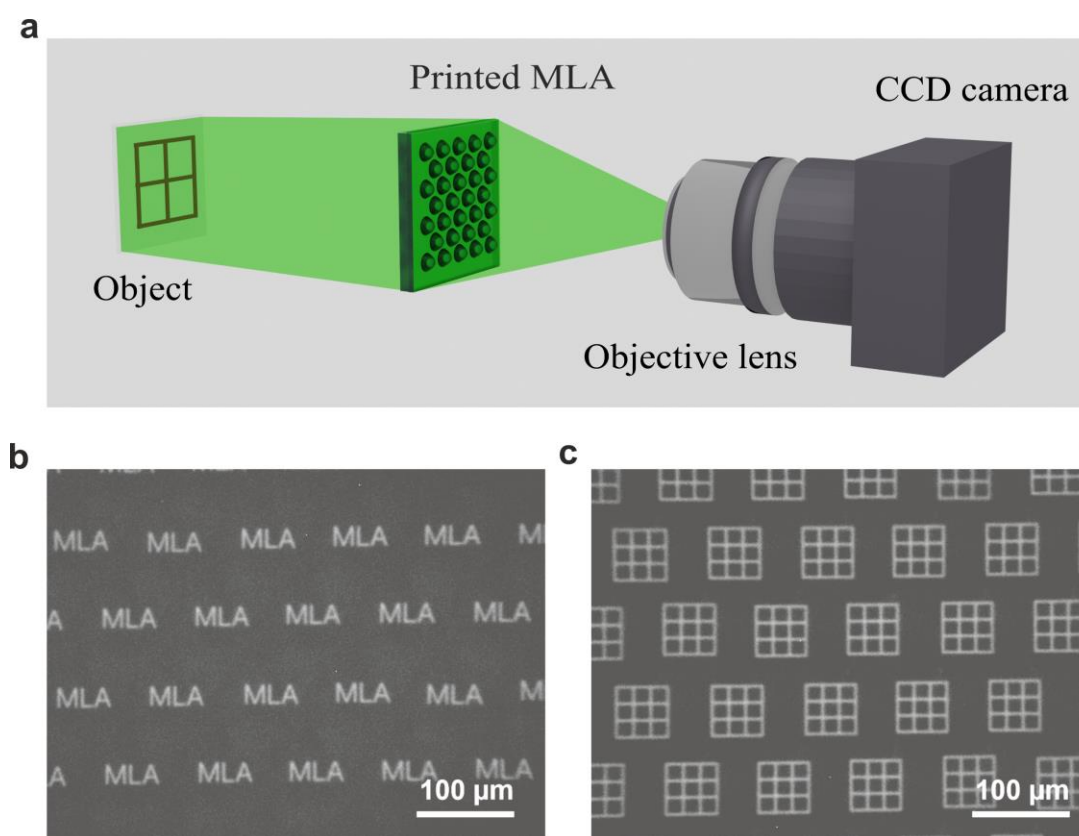
Figure 5.18: Imaging capability characterization of the printed microlens arrays with different objects. (a) Schematic of the imaging characterization setup for the printed microlens arrays. The height of the objects is around 5 cm. (b) Magnified captured image of the word 'MLA'. Each microlens imaged the object onto the image plane, giving hexagonally distributed images of the word. (c) Magnified captured image of a 3 × 3 square grid. The image of a grid is usually used to assess the distortion of an optical system.

To gain a more intuitive understanding of the imaging quality of the printed MLAs, they were used to image objects such as letters and a 3 × 3 square grid pattern. An imaging characterization setup similar to the one depicted in **Figure 5.15**a was built, with an illuminated object replacing the collimated light source, as demonstrated in **Figure 5.18**a. When the MLA was used to image a single object, each ML imaged the object onto the image plane, resulting in an array of miniaturized images distributed in a hexagonal layout on the image plane. For example, as shown in **Figure 5.18**b, when the MLA was used to image the letters 'MLA', the CCD camera captured the magnified image of the MLA image plane, which contains an array of the letters. Meanwhile, these miniaturized letters are uniformly distributed, clear, and easily readable from the image, demonstrating the excellent imaging quality of the printed MLAs.

Additionally, the MLA was used to image a 3 × 3 square grid, which is a pattern typically used for the evaluation of the distortion of the image. The captured image can be found in **Figure 5.18**c. As can be seen from the figure, the small grids on the image still have straight grid lines and show no distortion, further highlighting the high quality of the printed MLAs.

5.6 Fabrication of Different Microlens Arrays on Flexible and Large Substrates
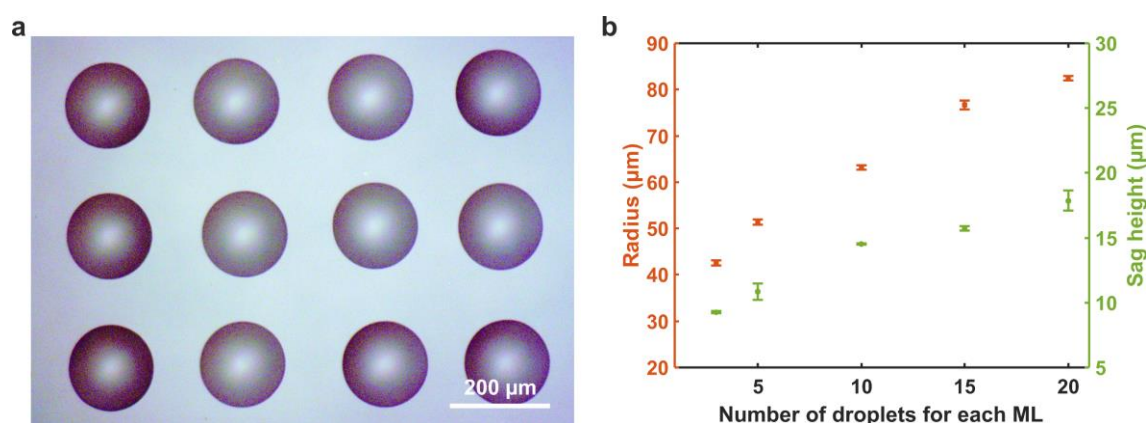
Figure 5.19: Large microlenses (MLs) obtained by printing multiple droplets at a single location. (a) Microscope image of a printed microlens array, where each ML comprises 20 droplets. (b) Change in the geometrical parameters of the MLs with different numbers of droplets. The radii (red marks) and sag heights (green marks) of the MLs increase significantly with the increased number of droplets. The error bars indicate the standard deviations.

Different strategies can be applied when MLs with a larger dimension are desired. The first option is to print more than one droplet at a single spot; thus, larger MLs can be obtained. The microscope image of an MLA where each ML comprises 20 droplets is presented in **Figure 5.19**a. Moreover, the changes in the radius and sag height of the MLs with the varying number of droplets can be seen in **Figure 5.19**b. With an increasing number of droplets, both parameters increase significantly, while the aspect ratio remains constant as long as $B_o \ll 1$. With 20 droplets, the radius of the ML can be increased to 82.48 µm and the sag height to 17.86 µm. Another way to achieve larger dimensions in the MLs is to employ printheads with a higher deposited droplet volume. When industrial printheads with grayscale jetting functions are used, the number of droplets printed per spot can be digitally controlled, and the dimension range of MLs in the same array can be broadened.
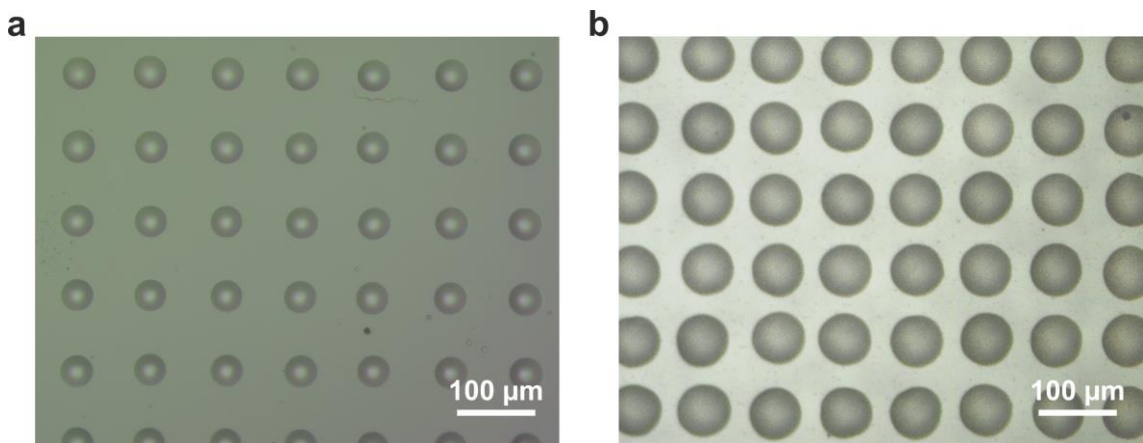
Figure 5.20: Microscope images of the inkjet-printed microlens arrays (MLAs) on different flexible substrates. (a) MLA on a pristine polydimethylsiloxane substrate. (b) MLA on a pristine polyethylene terephthalate foil.

As inkjet printing is a non-contact method, the printing process can be transferred to different substrates. This possibility was demonstrated by inkjet printing MLAs on polydimethylsiloxane (PDMS) substrate and polyethylene terephthalate (PET) foil. PDMS is a flexible and stretchable material, and the microscope image of an MLA fabricated on a PDMS substrate can be found in **Figure 5.20**a. The pristine PDMS exhibits low SFE, and therefore, the printed MLs have a small radius of 19.16 ± 0.63 µm and a high sag height of 8.23 ± 0.18 µm. A relatively high aspect ratio of 0.43 is obtained. Furthermore, the process was carried out on the commonly used flexible PET substrate, and the image of an MLA on PET foil is shown in **Figure 5.20**b. Since PET foil has an SFE slightly higher than glass, a medium aspect ratio of 0.13 is achieved with a radius of 35.58 ± 0.87 µm and a sag height of 4.57 ± 0.09 µm. The slight deformation in some MLs might result from the defects and dust on the PET foil.
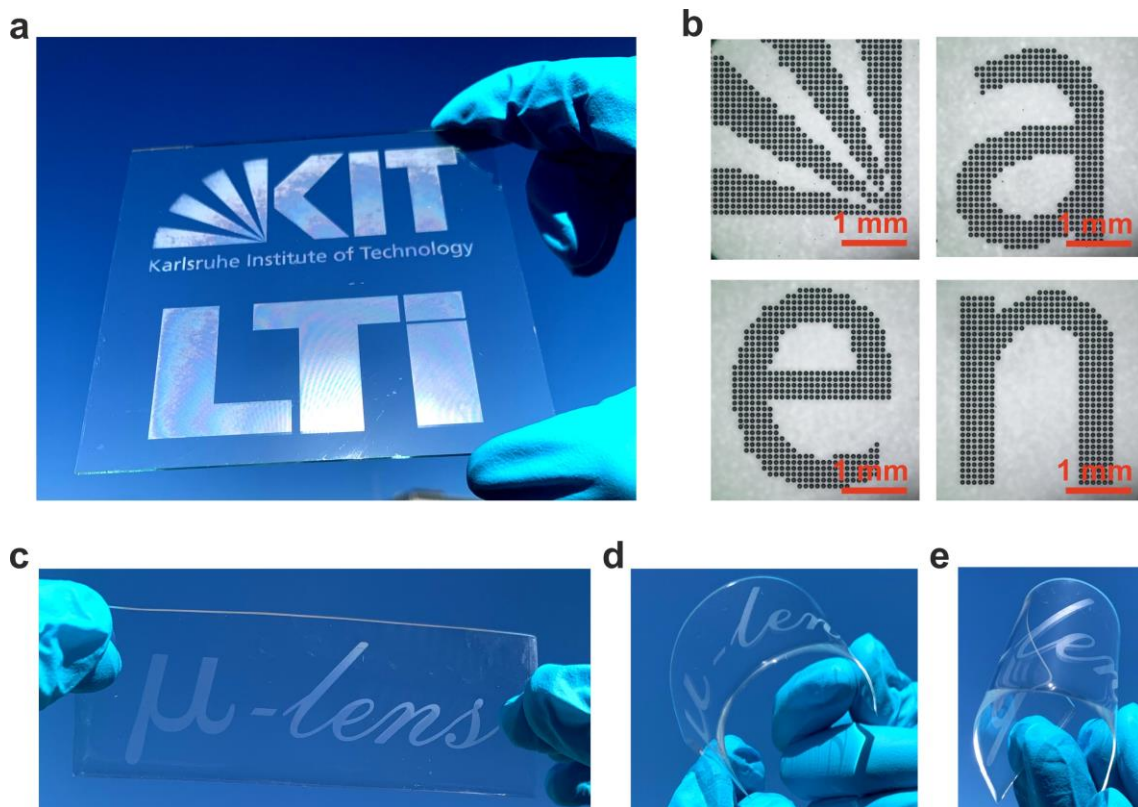
Figure 5.21: Images of the microlens arrays (MLAs) printed in patterns on large and flexible substrates. (a) Photo of the MLA printed on a 10×10 cm^2 large glass substrate. The MLA was printed in the pattern of the university logo and the institute logo. (b) Microscope images of the detailed pattern and letters in (a). (c) Photo of the MLA printed on a flexible 10×4 cm^2 polydimethylsiloxane (PDMS) substrate with the substrate unbent. (d) The PDMS substrate was bent. (e) The PDMS substrate was twisted and bent.

The upscaling capability of the inkjet printing method is demonstrated by printing MLAs on large substrates, as shown in **Figure 5.21**a. The MLA was printed on a 10×10 cm^2 large glass substrate. Moreover, inkjet printing allows for lateral patterning of the arrays, such as texts or arbitrary binary patterns. The figure shows the printed MLA in the form of two logos, and the defined pattern was well-reproduced and can be clearly seen. A closeup look into the printed MLA can be found in **Figure 5.21**b, where the microscope images of selected areas from **Figure 5.21**a show high uniformity and a designed pattern. Moreover, the lateral patterning feature was also shown with MLAs printed on a wide 10×4 cm^2 PDMS flexible band. The band is shown in its natural flat state in **Figure 5.21**c, in a slightly-bent state in **Figure 5.21**d, and a strongly bent and twisted state in **Figure 5.21**e.

5.7 Summary

In this chapter, the versatile fabrication method of MLAs through inkjet printing has been successfully demonstrated. Achieving a high quality and a high FF was made possible through a process using a modified solvent-free SU-8 ink formulation combined with customized printing parameters and in-situ UV curing. A remarkable FF of 88% was achieved with MLAs printed in a hexagonal layout on a substrate without any pre-structuring steps. The developed automated quantitative assessments provide meaningful statistics and confirm the exceptional uniformity of the printed MLAs. By applying various SAMs on the substrate, MLs with different NAs were obtained. The standard deviations of the MLA geometrical parameters are very low, being below 2.5% for the radii and below 3.9% for the sag heights. Furthermore, the feasibility of fine-tuning NA by mixing different siloxanes was demonstrated. The printed MLAs demonstrate high MTFs and the potential to be used for imaging applications. Their excellent imaging performance can be seen from the clear and sharp images they have captured.

Moreover, inkjet printing allows for customization in patterns, diverse sizes, and large-scale production. The MLAs were then printed in different patterns, including letters in different fonts and logos, and on diverse rigid and flexible substrates, such as glass and PDMS substrates. In addition, printing MLAs on a large substrate was demonstrated. Therefore, this work has proven the straightforward and cost-effective fabrication of MLAs by inkjet printing. The additive manufacturing nature of inkjet printing opens new possibilities for MLA fabrication; for instance, MLAs can be printed directly atop optoelectronic devices, such as photodiodes and LEDs, thereby expanding the scope of integration possibilities and potential applications.

6 Multispectral Light Field Cameras Based on Inkjet-Printed Microlens Arrays and Color Filters

The need to acquire comprehensive optical data from real-world scenes is increasing in the contemporary landscape of advancing optical sensing technologies, coupled with their diverse applications. This necessity arises from the growing importance of precise reconstruction and analysis in various domains. To capture three-dimensional spatial and spectral information from a given scene, it is common to apply multiple devices or engage in time-intensive scanning processes. This chapter presents a novel compact multispectral light field camera to enable the simultaneous acquisition of spatial and spectral data within a single snapshot. Next, the fabrication technology is introduced. The key components, i.e., microlens and color filter arrays, are fabricated by inkjet printing, enabling exceptional precision and seamless integration. The microlens and color filter arrays are fabricated on a common substrate, demonstrating a meticulous alignment between the two arrays. The compact nature of the developed multispectral light field camera introduces a variety of opportunities for diverse mobile applications, spanning domains such as autonomous driving and ubiquitous consumer electronics like smartphones, extending to advanced medical technologies such as endoscopes. Parts of the results presented in this chapter are adapted from [217].

6.1 Introduction

The simultaneous acquisition of three-dimensional (3D) and spectral data within the visible and near-infrared (NIR) spectral range provides substantial characteristics for a recorded scene in nearly all technically relevant scenarios [218]. The plenoptic function can represent the aggregate ensemble of light rays within a scene, also acknowledged as the five-dimensional light field. This comprehensive representation describes light flow at each point within the spatial domain and in every direction [219]. Massive amounts of information are included in the light field, and these can be applied in various fields, including mobile applications, industrial automation, computer vision, and medical technology. In autonomous driving, various image-based measurement techniques are employed, encompassing basic stereo cameras, light detection and ranging (LIDAR), and infrared (IR) cameras. Optical sensors are used in automobiles, particularly in the IR spectrum, to evaluate the surrounding environment and identify persons, objects, or

potential dangers. In this scenario, the 3D depth data and spectral data are crucial to respond effectively.

Furthermore, the spectrum of a scene can be applied to classify items and substances that are crucial in the fields of remote sensing, agriculture, food, medical and biological research, industrial production quality management, and recycling operations. In addition, 3D information is also quite valuable in these fields for the purpose of classification. For instance, knowing the precise position and shape of an object during production or a recycling process can be utilized to enhance classification accuracy or adjust the recorded spectra when exposed to varying illumination conditions [219].

However, conventional cameras only capture a reduced dimensional representation of the plenoptic function. Typically, cameras are divided into two categories: color/spectral cameras and 3D cameras. Upon acquiring an image, spectral cameras project the five-dimensional plenoptic function onto two spatial dimensions. These cameras are designed specifically to capture the spectrum component of the plenoptic function. The integration of two-dimensional (2D) spatial and angular data into the final image acquisition eliminates the three-dimensional information of the scene. Spectral cameras that are extensively employed in both scientific and industrial fields are spatially, spectrally, or spatio-spectrally scanning cameras [220, 221]. In such cameras, the information to be captured is subjected to a one-dimensional reduction to enhance either spatial or spectral resolution. The diminished dimension during acquisition is subsequently added back through a scanning process.

Nevertheless, the use of these cameras is restricted to static scenes due to the limitations imposed by the scanning process. In dynamic scenarios or when recording is desired, the necessity of snapshot cameras arises. Consequently, cameras have evolved with the incorporation of multispectral color filter arrays (CFAs) with demosaicing techniques [222-224]. Snapshot spectral cameras mostly rely on intricate optical systems to encode spectral information onto the sensor prior to acquisition, incorporating, e.g., coded apertures and CFAs [225-230]. Nevertheless, the optics and calibration procedures for such systems are very intricate and cumbersome, posing challenges for direct integration into mobile or automotive applications since they require accommodating moving scenes or exposure to vibrations commonly encountered in these applications.

Conversely, 3D cameras primarily capture the spatial dimensions of the plenoptic function and often exhibit limitations in resolving the spectral characteristics of the scene or typically only at a suboptimal level of resolution. Monocular 3D cameras present a highly attractive option for industrial and mobile applications in contrast to multi-camera systems, owing to their compact design and mechanical robustness. Moreover, calibration for these cameras typically occurs solely in controlled laboratory settings, with subsequent field use necessitating minimal additional calibration. For example, light field cameras are able to measure 3D spatial data in snapshots [231, 232]. They directly capture

86

the angular dependence of incident light rays on the sensor. Typically, this technology involves incorporating a microlens array (MLA) in front of the image sensor, wherein the rays originating from distinct directions are imaged onto discrete pixels positioned beneath each microlens (ML) [233-235].

In combination with both types of cameras, spectral 3D cameras offer a comprehensive measurement of the plenoptic function and, hence, an attractive method for dynamic and mobile applications. Given the inherent two-dimensional nature of imaging sensors, the measurement and processing of desired information necessitate both optical and digital signal processing techniques. Several approaches have been applied to develop spectral 3D cameras. The most extensively researched method involves spectrally encoding an MLA-based light field camera through the use of a CFA positioned in the primary lens plane. In this context, the CFA must be meticulously designed and aligned to ensure that each pixel is spectrally encoded individually beneath the corresponding ML [236-238]. Nevertheless, the design and calibration of this approach are complicated, demanding high precision in the placement of the CFA and the highly accurate alignment between the CFA, the MLA, and the sensor. Any deviations can result in crosstalk and spectral overlaps, thereby compromising the reconstruction quality. A camera array has been developed using a similar methodology of spectrally encoding the angular component of the light field. This array comprises N × N cameras arranged in a quadratic configuration, with each camera dedicated to recording a distinct narrowband selective wavelength range, aiming to achieve spectral 3D imaging capabilities [239-241]. Nevertheless, the calibration process for this setup is time-consuming, and the substantial size imposes severe limitations on its practical applicability beyond specialized laboratory environments. An alternative approach involves hybrid camera systems comprising an independent light field camera and a spectral snapshot camera. The images captured by these two components are subsequently fused to construct the spectral light field [242]. However, this method suffers from the same limitations as the multi-camera systems and is practically applicable only within controlled laboratory conditions.

In this work, a novel method for realizing a spectral light field camera through the utilization of inkjet printing fabrication technology and customized digital image processing is demonstrated. The distinctive aspect of this approach lies in the compact and flexible nature of the spectral light field camera because the MLA, the CFA, and the sensor were intricately integrated and encased within a conventional camera housing. The camera necessitated a single-time calibration procedure conducted in laboratory settings, after which it demonstrated mechanical robustness. The miniaturized components, i.e., the MLAs and CFAs, were independently fabricated on two opposite sides of the same substrate. With inkjet printing technology, rapid adaptation and prototyping were achieved. Furthermore, inkjet printing allows for precise and digital registration between the CFA and the MLA.

The innovative integration of spectral and 3D cameras has yielded a compact and mobile optical 3D sensor capable of delivering spatially resolved spectral information. Consequently, this approach presents various opportunities for diverse mobile applications, including but not limited to autonomous driving, production technology, consumer electronics like smartphones, and medical technology such as endoscopes.

6.2   Fabrication of the Optical Components

6.2.1   Overall Fabrication Flow
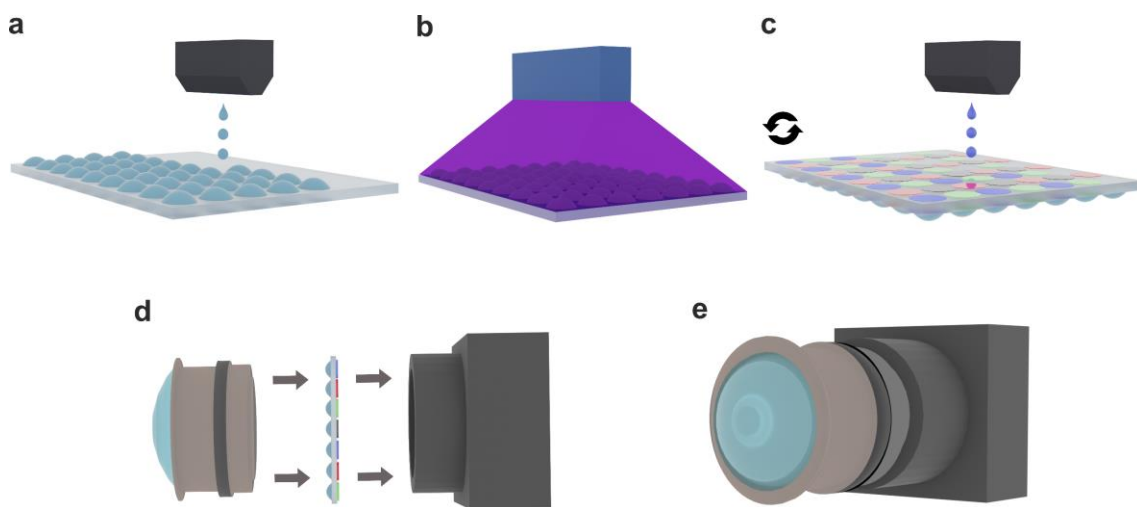
Figure 6.1: Schematic illustration of the fabrication steps for a multispectral light field camera. (a) Firstly, a microlens array (MLA) is inkjet printed on one side of the substrate. (b) The MLA is subsequently cured by UV radiation. (c) On the other side of the substrate, a color filter array is inkjet printed, and each color filter aligns with a respective microlens. (d) The optical component with both arrays is integrated into a camera housing. (e) A compact multispectral light field camera is accomplished.

The optical components—specifically, the MLA and CF —were fabricated on a single substrate to achieve a high compactness of the system. The precise alignment of the MLA, the CFA, and the sensor is pivotal for ensuring the quality and accuracy of the final reconstruction; hence, inkjet printing, known for its capability to achieve accurate registration of printed arrays in a digital manner, was employed for the fabrication of both MLAs and CFAs.

Moreover, inkjet printing brought several additional advantages to the development of the system. Firstly, it enables limitless design possibilities, allowing for the realization of different array layouts and facilitating fast iterations and rapid prototyping for exploring

various designs. Secondly, the versatility of inkjet printing allows for customized fabrication, even for single devices, thereby reducing costs and time compared to traditional methods. Additionally, the drop-on-demand (DOD) characteristic of inkjet printing significantly minimized material wastage, especially given applications where valuable functional inks are used. Lastly, the precise control over the deposited ink volume in the picoliter range enables fine-tuning of the geometries of individual MLs and the thicknesses and sizes of color filters (CFs), thereby adjusting their optical characteristics with high precision. The entire fabrication sequence is illustrated in **Figure 6.1**. Initially, an MLA is fabricated on one side of the substrate by inkjet printing. The printed MLA is then exposed to UV illumination and heated in a hard bake step for solidification. Subsequently, on the opposite side of the substrate, a CFA is inkjet printed, ensuring each color filter aligns with a corresponding microlens. After both arrays are fabricated, this optical component is seamlessly integrated into a camera housing, realizing a compact multispectral light field camera.

6.2.2 Fabrication of Microlens Arrays by Inkjet Printing
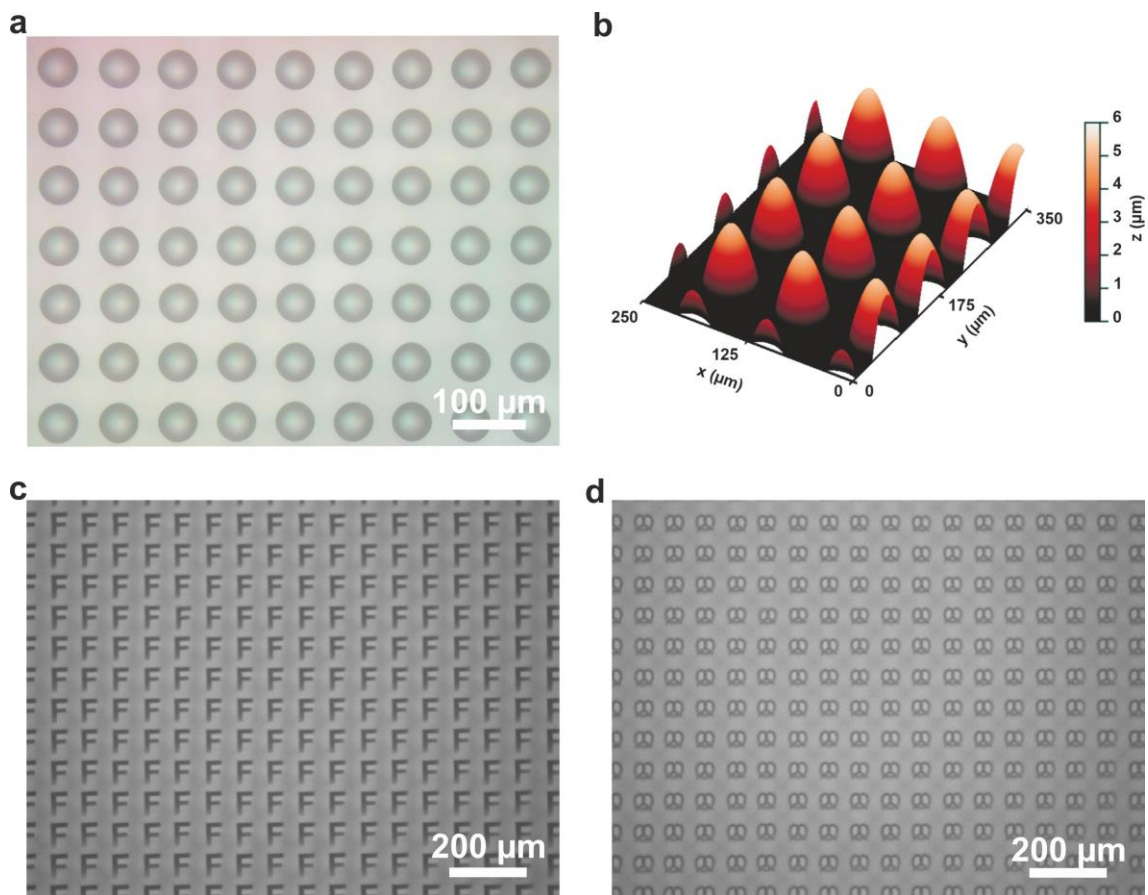
Figure 6.2: Inkjet-printed microlens array (MLA) arranged in a square layout. (a) Microscope image of the printed MLA. (b) The three-dimensional surface profile of the printed

MLA measured by confocal microscopy. The color bar on the right side indicates the range of sag heights. (c) Captured image of a letter 'F' imaged by a printed MLA. (d) Captured image of a pretzel pattern imaged by a printed MLA.

As depicted in **Figure 6.1**a, the MLA was first directly printed onto a substrate using a DOD inkjet printer. As elaborated in Chapter 2.2, the droplets on the micrometer scale are influenced mainly by surface tension and are assumed to have spherical shapes. Therefore, after subsequent solidifications, MLs are formed. Employing the ink developed in Chapter 5 and following the same process, the inkjet printing process was carried out. The printhead temperature was set to 37 °C, and the waveform was adjusted accordingly to ensure stable droplet ejection and to prevent satellite droplets. The printing resolution of the MLAs was set at 280 dpi × 280 dpi to reach the desired pitch value. The post-treatment process was the same as with all other MLAs.

The 2D image of the printed MLA in a square layout captured using a light microscope is presented in **Figure 6.2**a. Its 3D surface profile was constructed from the measurements using a confocal microscope, and the results are shown in **Figure 6.2**b. The printed MLs in the images exhibit good uniformity and excellent alignment. The quantitative analysis was carried out following the method in Section 5.3, and the obtained results are listed in **Table 6.1**.

Table 6.1: Geometrical parameters of the fabricated microlens arrays.

	Radius	Sag height	Lateral spacing	Vertical spacing
Mean value (μm)	31.37	5.16	91.78	91.79
Standard deviation (μm)	0.44	0.11	2.13	0.85
Relative standard deviation	1.42%	2.20%	2.32%	0.93%

The printed MLs show a mean radius of 31.37 μm and a relative standard deviation of 1.42%. Meanwhile, the average sag height was determined to be 5.16 μm, with a relative standard deviation of 2.20%. The statistical analysis underscores a high level of uniformity in the printed MLs. In terms of the array alignment, the relative standard deviations for spacing along lateral and vertical directions were found to be 2.32% and 0.93%, respectively, indicating exceptional regularity within the array. Using these values, the focal length of the MLs, in conjunction with the substrate, was calculated as around 185 μm, while the back focal length (towards the image sensor) was around 70.6 μm. The pitch of the printed MLA set at 90.71 μm during printing was considered the entrance pupil diameter, resulting in an *f*-number of 2.04.

Furthermore, the imaging performance of these MLAs was demonstrated using the letter 'F' and a more complex pattern, a pretzel sketch, as the object. The resulting images, magnified by a 10× objective and captured by a CCD camera, are displayed in **Figure 6.2**c and d, respectively. In addition to the evidently high regularity of the MLs, the imaging capability of the MLA on the new substrates is again proven. This high-quality imaging is further validated through subsequent tests after being integrated into a camera.

6.2.3 Fabrication of Color Filter Arrays by Inkjet Printing

Following the printing of the MLA, the fabrication process required the fabrication of a CFA on the opposite side of the substrate to encode each ML with an individual CF. Achieving precise registration between two arrays, each comprising more than ten thousand elements poses a considerable challenge for traditional fabrication methods. This challenge was effectively addressed by employing inkjet printing to fabricate the CFA.

The CFA exhibits a layout with repetitive 2 × 2 units, each comprising four spectral channels: red, green, blue, and NIR. Four organic dyes were employed, mixed with poly(methyl methacrylate) (PMMA) solutions, to fabricate the CFA. The concentrations of the organic dyes in the final inks are listed in **Table 6.2**.

Table 6.2: Concentrations and final thicknesses of different color filters.

Spectral channel	Dye concentration (mg/mL)	Thickness (μm)
Red	50	2.45
Green	50	2.17
Blue	50	1.63
NIR	25	1.69

PMMA solutions were prepared was follows: PMMA with a molecular weight of 15 kDa (Sigma-Aldrich) was dissolved in 1,3-dimethoxybenzene (Sigma-Aldrich, ≥98%) and 10 vol% of hexylbenzene (Sigma-Aldrich, 97%) to reach a final concentration of 100 mg/mL. Four inks for the CFs were prepared by incorporating and blending organic dyes from Kremer Pigmente into the prepared PMMA solutions. The blue filters employed solvent blue 67, while the red filters comprised solvent red 160. A green colorant was formulated as a mixture of solvent yellow 89 and solvent blue 67 in a 1:1 mass ratio. The components for the NIR filter were formulated as a mixture of solvent blue 67 and solvent red 10 in a 1:1 mass ratio. For the red, green, and blue filters, the final concentrations of the organic dyes in the ink formulations were all 50 mg/mL, while for the NIR filters, the concentration of the dyes was 25 mg/mL. The concentrations were adjusted to reach the

desired transmission behavior of the respective CFs. The prepared inks underwent agitation on a stirrer for 30 minutes prior to the printing process.

Prior to printing CFAs, a 1-minute treatment with oxygen plasma was carried out for the opposite side of the substrate with the fabricated MLA, i.e., the bare glass surface, in a plasma chamber (Plasma technology). After filtering with the polytetrafluoroethylene (PTFE) filters, the inks were loaded into cartridges. The 1-pL DMC 11601 cartridges were used in the inkjet printing, and the jetting frequency of 1 kHz was maintained during printing. Custom waveforms for all four inks were created to ensure the ideal shape of generated droplets at this frequency without tails or satellite droplets. Throughout printing, a single nozzle was used for jetting. The temperature of the printhead was set to 28 °C, and the temperature of the substrate was maintained at 24 °C. Following the printing of the entire array, the samples were left in ambient conditions for 30 minutes to ensure solvent evaporation. The printing resolution of the CFAs was set at half of the resolution used for MLAs, i.e., 140 dpi × 1400 dpi.

Utilizing the digital alignment feature of the printer, each CF was precisely deposited at the backside of an individual ML. The microscope image of the printed CFA is shown in **Figure 6.3**a. Over an area of several mm^2, thousands of CFs can be seen, and the printed CFA exhibits excellent regularity. A closeup microscope image showing the 2 × 2 CFA unit is presented in **Figure 6.3**b. The transmittance of the CFs was regulated by controlling both the concentration of the dyes in the inks and adjusting the thickness of the CFs, with the latter determined by the number of printing cycles. Monitoring the thickness of the CFs was accomplished using a stylus profilometer, and the final thickness of each CF is shown in **Table 6.2**.

Using a spectrophotometer, the transmission spectra of the printed CFs were measured with an embedded integrating sphere. These spectra were then weighted by the quantum efficiency of the monochrome camera sensor CMV4000, which was later used as the sensor of the light field camera. The spectra are illustrated in **Figure 6.3**c. In order to ensure uniformity, the thickness of each CF was controlled so that the integral of the light intensity reaching the camera sensor pixel was of the same magnitude for each spectral channel. **Figure 6.3**d shows the microscope image of the complete optical component with both MLA and CFA, viewed from the MLA side, showing the proper spectral encoding of the MLA.
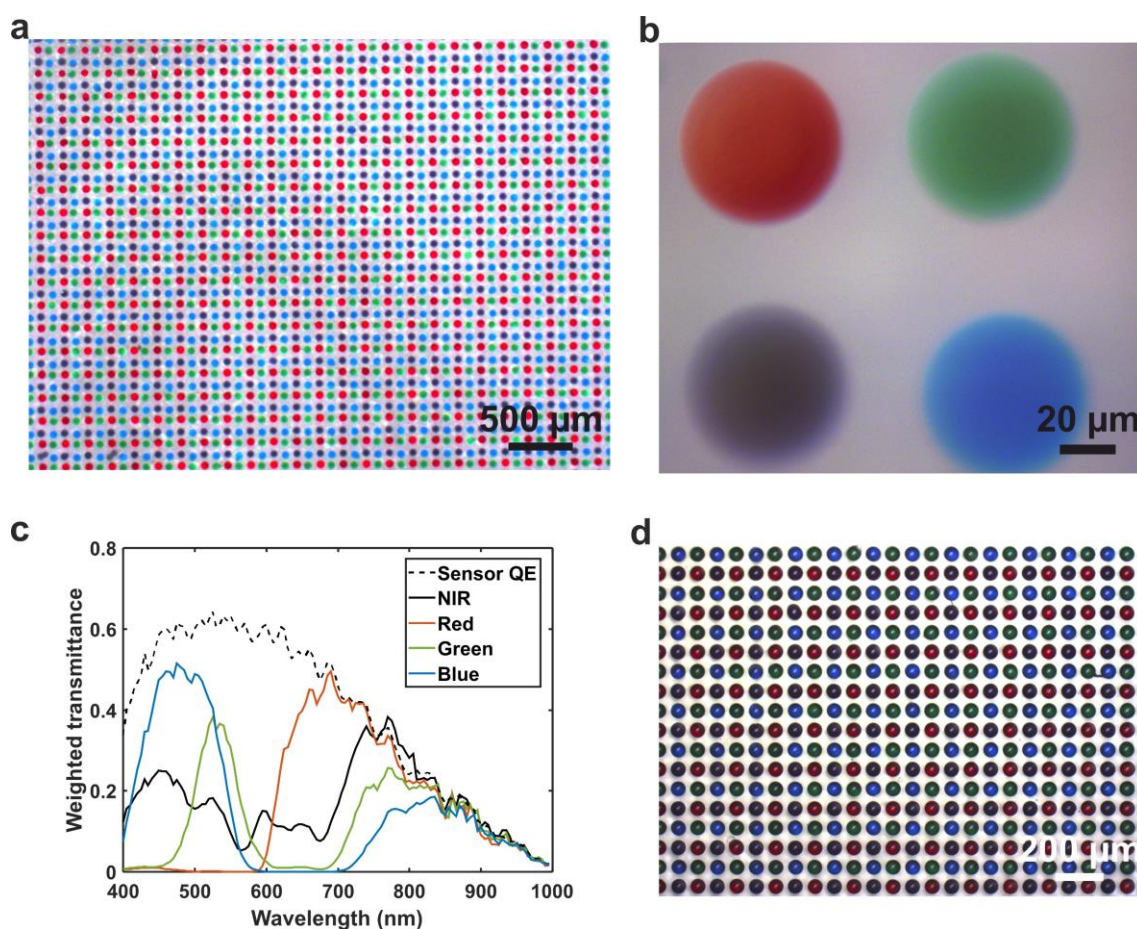
Figure 6.3: Inkjet-printed color filter arrays (CFAs). (a) Microscope image over a large area in the printed CFA. (b) Closeup microscope image of a 2 × 2 printed CFA unit. (c) Quantum efficiency of the camera sensor alongside the correspondingly weighted transmittance spectra for four spectral channels: NIR, red, green, and blue. (d) Microscope image of the encoded microlens array (MLA), captured from the MLA side. The scale bar is 200 μm.

6.3 Integration into a Light Field Camera and Calibration
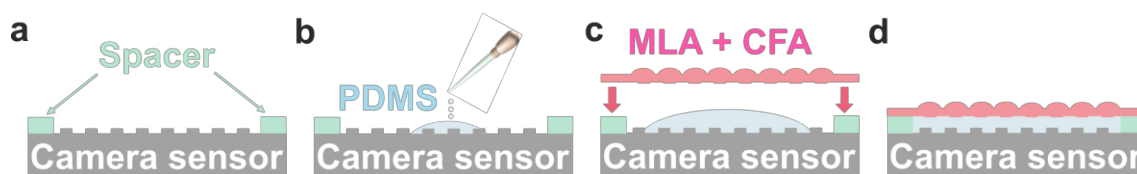
Figure 6.4: Schematic illustration of the integration process of the fabricated optical arrays into the camera. (a) Spacers with the desired thickness were positioned on the

periphery of the camera sensor. (b) A polydimethylsiloxane (PDMS) mixture was uniformly applied to the sensor. (c) The fabricated optical component with a microlens array and a color filter array was meticulously placed on the spacers. Gentle pressure was applied to the component. (d) After placement, the sensor was left in the ambient conditions for a period of 24 hours, allowing the PDMS to cure fully.

Following the manufacturing of the optical component with MLA and CFA, the component was seamlessly integrated into an industrial camera (Lt425, Teledyne Lumenera) equipped with the sensor with an optical format of 1 inch and a pixel size of 5.5×5.5 μm^2. Consequently, an angular resolution of 9×9 was targeted, given the diameter value of the printed MLs. The optical component was subsequently fixed on the camera sensor using polydimethylsiloxane (PDMS)—an optically transparent material. The PDMS adhesive was prepared by blending its pre-polymer base with the cross-linking curing agent in a mass ratio 5:1. Air bubbles were eliminated after this mixture was degassed in a desiccator for 30 minutes.

The distance between the optical component and the sensor was set to match the BFL of the MLA, ensuring that the camera sensor was at the focal plane of the MLAs. When PDMS served as the image space medium, the BFL of the MLA increased to around 99 μm. To match this distance, two precision glass spacers, each with a thickness of 100 μm (Corning), were positioned at the edges of the camera sensor, as illustrated in **Figure 6.4**a. Following this, 10 μL of the PDMS mixture was uniformly applied to the sensor, as shown in **Figure 6.4**b. Subsequently, the optical component with MLA and CFA was meticulously positioned on the spacers, and gentle pressure was applied, as seen in **Figure 6.4**c. The camera sensor was left in the ambient conditions for a duration of 24 hours, allowing the PDMS adhesive to cure fully, as shown in **Figure 6.4**d. Finally, the camera sensor was reassembled into the camera housing.

Figure 6.5a shows the image of the camera sensor after the PDMS adhesive was fully cured. The optical component was tightly fixed onto the sensor. In total, two different types of prototypes were constructed using the same processes. The first type is equipped with an uncoded MLA, i.e., without CFA, and the second type is built with a spectrally coded MLA, i.e., with a CFA. They were referred to as Mono and Spectral, respectively. Prototype Mono was used for reference, enabling an assessment of the quality of the fabricated MLA and the integration of the system, particularly in terms of light field reconstruction. **Figure 6.5**b and c present images of these two prototypes of different types, respectively. In the images, the front main lens is unattached; therefore, the fabricated optical component can be clearly seen. After the front main lens with a focal length of 75 mm and a *f*/number of 2.4 was attached, a remarkably compact yet robust camera can be seen in **Figure 6.5**d, exhibiting a total length of approximately 5 cm excluding the main

lens. With a total length smaller than a hand palm, the cameras show great potential in being applied in mobile applications where high compactness is desired.
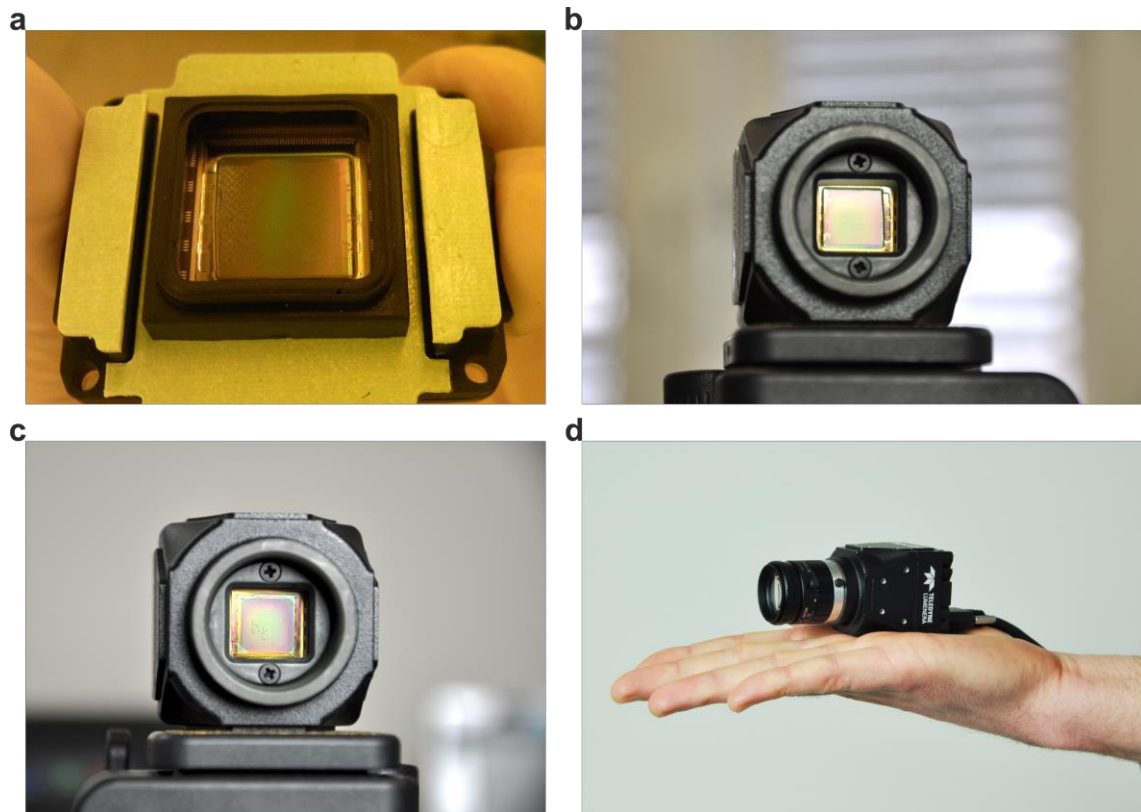
Figure 6.5: The integrated light field cameras. (a) The camera sensor after the optical component was attached using polydimethylsiloxane adhesive. (b) Prototype Mono with inkjet-printed microlens array (MLA) without a front main lens. (c) Prototype Spectral with inkjet-printed MLA and color filter array without a front main lens. (d) The complete prototype with a main lens held in hand. The size of the compact prototype is smaller than a hand palm.

After the prototypes were successfully constructed, the calibration of them was conducted using the procedure outlined in a previous work [243]. This calibration method relies on white images, which are images of a diffuse white scene. The images were created with a white light source and a diffuser. Through the analyses of the white images, the centers of the MLs were estimated as a crucial step in decoding the light field from the sensor data [244]. Ultimately, the light fields were cropped, and a light field resolution of {9,9,96,96} was achieved, with a spatial resolution of 96×96 and an angular resolution of 9×9.

6.4   Reconstruction results

Using the prototype Mono, where the MLA was uncoded, the reconstruction for three different scenes is illustrated in **Figure 6.6**. The reconstructed central views are presented in the first row, which was formed using the central pixels beneath the MLs. Despite using a limited number of pixels for reconstruction, the images exhibit high contrast and sharpness in the central views. Notably, if the MLA was misaligned or inaccurately tilted concerning the camera sensor, the images would show significant blurring. The displayed sharpness in the images affirms the high quality of the fabricated MLA and the precise integration of the MLA component into the camera. Moreover, the estimated disparity maps are shown in the second row, which clearly show the classification of different objects with different distances, where the objects closer to the camera appear in red, and the ones with the largest distances appear in blue. The disparity interval d (in pixels) is indicated below each image.
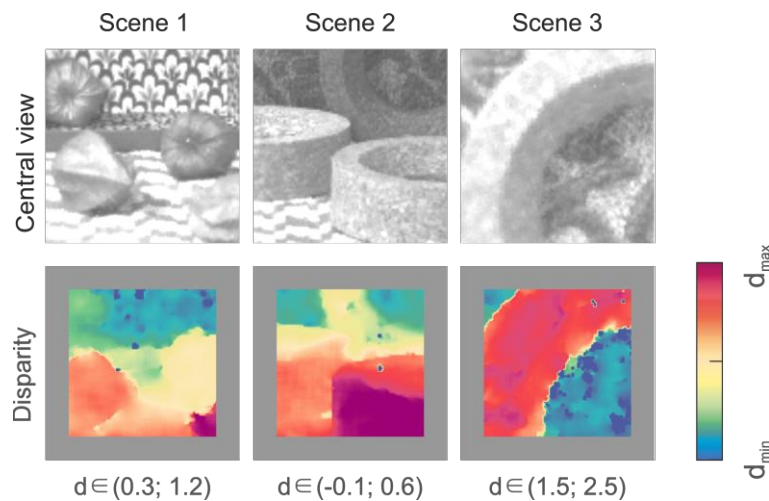
Figure 6.6: Reconstruction of three scenes using the prototype Mono. The monochrome central view and the estimated disparity data were reconstructed by applying EPINET. Owing to the network architecture of the approach, a margin of 11 pixels is displayed in gray in the periphery of the disparity maps, indicating areas where no estimations were conducted. The color represents the disparity information; the disparity ranges are shown at the bottom.

The central views from the four different spectral channels and the disparity information were reconstructed using the prototype Spectral. Two different approaches were applied for reconstruction: a compressed-sensing approach and a deep-learning approach. The reconstruction results are shown in **Figure 6.7**a and b, respectively. As can be seen from the central view images, due to the reduced number of pixels used for reconstruction, the resolution of the images is slightly lower compared to the central view images in **Figure**

6.6. However, the images exhibit high sharpness and good contrast, which again affirms the good integration of the entire light field camera. The intensity differences in the individual spectral channels are clearly visible in each case. Between the images obtained from the compressed-sensing method and deep-learning method, the central views exhibit no significant differences, aligning with the results obtained previously with a reference measurement system [245].
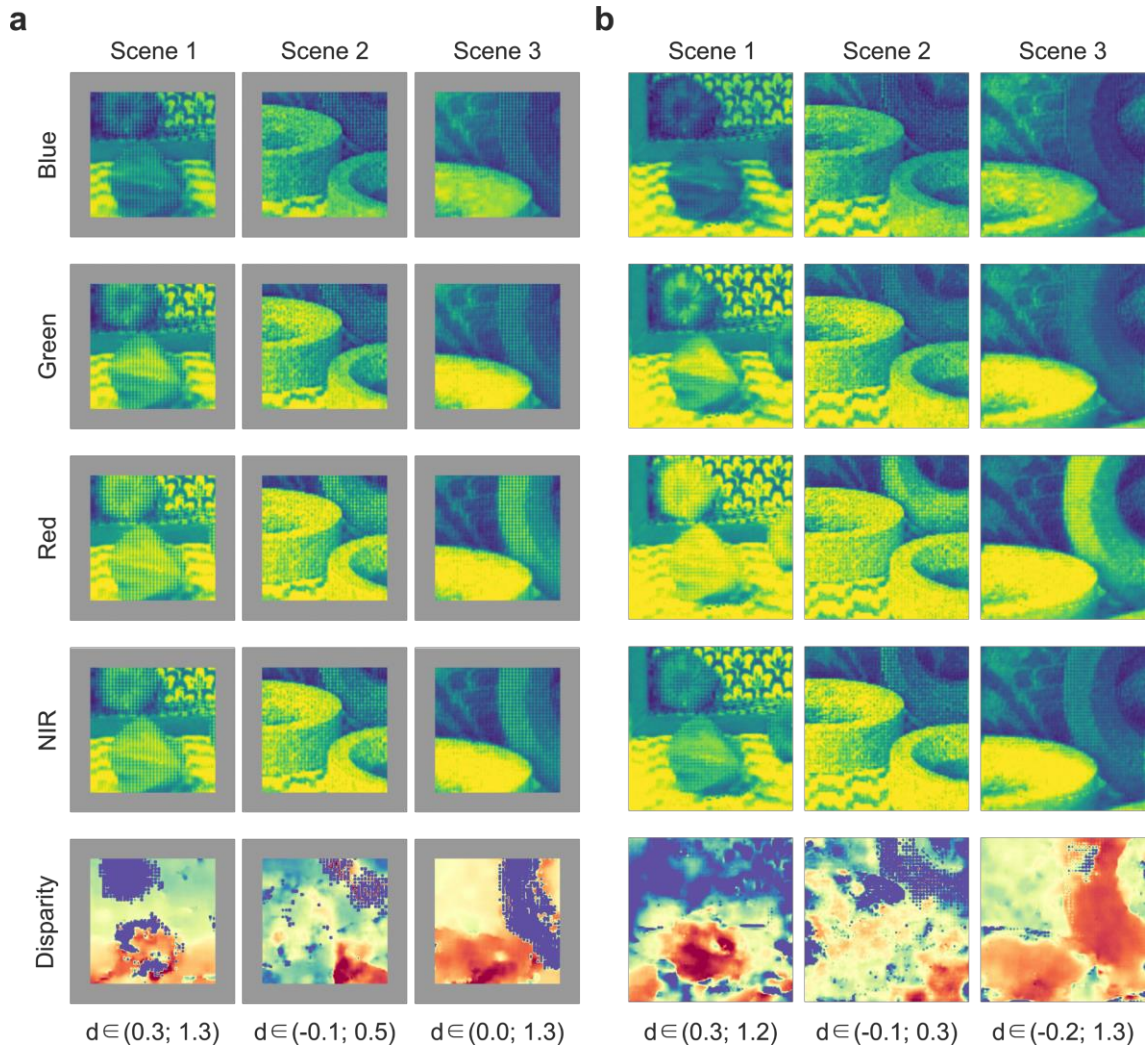
Figure 6.7: Reconstructed central views from different spectral channels in false-color representation and the disparity map using the prototype Spectral. (a) Reconstruction results using the compressed-sensing method. (b) Reconstruction results using the deep-learning method. The color bar in the disparity map is the same as in **Figure 6.6**.

Furthermore, significant differences in the intensity in the central view images from different spectral channels can be seen. To take Scene 1 as an example, using both reconstruction approaches, it is evident that the front object in the central view appears the

darkest in the blue channel. In contrast, in the red channel, the intensity is the highest. Besides, in the green channel, a significant contrast in the intensity of the two objects in the scene is clearly observable. This demonstrates the capability of the constructed spectral light field camera to capture and reconstruct the information from the additional dimension, i.e., the spectral dimension.

Moreover, the disparity information was also obtained from the reconstructed light fields. In principle, the disparity maps show satisfactory results and are able to provide high-quality data. Nevertheless, several artifacts can be seen from the disparity maps, especially when the deep-learning method was used for reconstruction. In the disparity maps, it can be seen that some regions appear in a clearly discernible pattern, which indicates that the reconstruction failed in these regions. These regions appeared in the results obtained with either reconstruction method. When the compressed-sensing method was used for reconstruction, the methodology might have resulted in these artifacts because the method relies on a random mask layout. Hence, an associated low coherence of the random mask and the used base dictionary might exist.

Despite the artifacts, the obtained results from the reconstruction demonstrate the simultaneous 3D spatial and spectral acquisition of the manufactured prototypes. Under various scenes, images of objects in different shapes and colors can be captured in one snapshot. The objects can be classified based on their position information given by the disparity data and their distinct composition provided by the spectral data.

6.5   Summary

In this chapter, a multispectral light field camera was conceptually designed, prototyped, and validated in measurements. The recorded light fields by the prototypes were successfully reconstructed using a compressed-sensing and a deep-learning method, yielding high-quality central view reconstructions, disparity estimation, and spectral contrasts. MLAs were fabricated as the main optical component, where in one prototype, it was applied without spectral encoding, i.e., without CFA, and in the other one, with spectral encoding. The optical components were efficiently manufactured using inkjet printing, demonstrating high uniformity and high optical quality with this additive manufacturing method. To spectrally encode the MLA in the prototype Spectral, a CFA with 2×2 spectral channel units was fabricated on the opposite side of the MLA on the substrate, where each CF was deposited precisely under a corresponding ML. Therefore, an accurate registration between the two arrays was ensured.

Furthermore, the optical component with the fabricated arrays was carefully fixed to the camera sensor and properly integrated into a camera housing. In the end, real scenes were imaged by the prototypes, and the reconstruction was carried out from these snapshots. The reconstruction results in terms of the central views, the disparity maps, and the

spectral central views exhibited high quality, providing information in both 3D spatial and spectral dimensions. Moreover, it is worth noting that this approach is not inherently limited to the number of spectral channels of four. Both the reconstruction and the manufacturing method are scalable to higher spectral resolutions. The reconstruction quality achieved from a single snapshot enables various possibilities for diverse applications, ranging from autonomous driving and consumer electronics to industrial automation and medical imaging.

7 Fabrication of Bragg Mirrors by Multilayer Inkjet Printing

Bragg mirrors, which are one of the most highly reflective types of optical interference filters, find extensive applications in optical and photonic systems owing to their ability to manage light and spectrum. Traditionally, Bragg mirrors are fabricated by physical and chemical vapor deposition. However, these methods are often expensive and lack the flexibility for lateral patterning. In this chapter, the fabrication of Bragg mirrors by fully inkjet printing is demonstrated for the first time. Firstly, the developed hybrid ink combination is introduced, which fulfills the requirements for inkjet printing and satisfies the orthogonal solubility conditions. The manufacturing of the Bragg mirrors consisting of up to ten bilayers is presented, where an ultra-high reflectance of 99% is achieved. Furthermore, the tunability of the central wavelength of these Bragg mirrors is demonstrated, ranging from visible into the near-infrared range. This tailoring of the photonic bandgap is realized by adjusting the layer thickness through variations in printing parameters and the number of layers in the mirrors. In the end, the fabrication of Bragg mirrors in different sizes, with defined lateral patterns, and on diverse substrates such as glass and foils are demonstrated. Parts of the results presented in this chapter have previously been published in the journal Advanced Materials [246].

7.1 Introduction

Bragg mirrors, also known as dielectric mirrors, are widely applied due to their ability to manipulate light and produce structural color. A Bragg mirror is a multilayer-stack device known as a one-dimensional photonic crystal (1DPC). A Bragg mirror comprises a structure with a periodically distributed refractive index (RI) along a single dimension in space [247]. In order to introduce the periodic distribution in RI, Bragg mirrors are usually built by alternating materials with at least two different RI, which can be different materials or the same material with different porosity [248]. Since the thickness of each layer is smaller than or comparable to the wavelength of light, multilayer interference takes place in Bragg mirrors. Therefore, Bragg mirrors exhibit a photonic bandgap (PBG), which is similar to the electronic bandgap in semiconductors [185]. Because of this, electromagnetic waves at specific wavelengths or frequencies are unable to propagate through the stack. The photonic stopband can be adjusted by tuning the material composition, i.e., the RI, the layer thickness, and the stacking sequence. Through the modification of these variables, Bragg mirrors can be tailored to fulfill specific requirements, such as long-pass filters, short-pass filters, and mirrors with ultra-high reflectivity. With the ability to reflect

specific spectral components and dichroic filtering, dielectric mirrors and dichroic beamsplitters play crucial roles as discrete elements in various optical and photonic devices. Additionally, distributed Bragg reflectors find applications in different integrated photonics, such as vertical-cavity surface-emitting lasers [249]. Moreover, Bragg mirrors play a vital role in fluorescence microscopy, optical sensors with high sensitivity [250], and are used as both functional and colorful coatings for solar cells [60, 61].

Yet, the prevailing methods for manufacturing Bragg mirrors in the industry are physical vapor deposition (PVD) and chemical vapor deposition (CVD), which involve expensive equipment and lack the capability for small-batch customization and lateral patterning. While certain solution-processing methods have been applied on a laboratory scale for Bragg mirror fabrication, such as spin coating, dip coating, doctor blading, and self-assembly, they come with inherent limitations, as outlined in **Table 3.1**. In spin coating, the drawbacks include substantial material wastage, constraints on substrate size, and the occurrence of defects on thin films, resulting in suboptimal mirror quality. While blade coating and self-assembly have the potential for large-scale production, achieving consistent layer thickness and ensuring high-quality thin films over a big area pose significant challenges. Furthermore, these solution-processing approaches are unable to realize precise lateral definitions of Bragg mirrors.

Inkjet printing can be a highly competitive and promising method for fabricating Bragg mirrors. As a solution-processing method, it holds the advantages of being low-cost and straightforward. Meanwhile, since inkjet printing is a digital printing technique, it has high versatility and is able to realize high-throughput fabrication [130]. Several other advantages are brought by inkjet printing for manufacturing Bragg mirrors. First, inkjet printing provides a cost-effective fabrication method. Based on the working principle of drop-on-demand (DOD) inkjet printing, it decreases material wastage to a large extent and, therefore, reduces material costs. Besides, the inkjet printing process is carried out in ambient conditions, hence saving energy costs compared to vacuum-assisted deposition techniques. Next, the ambient working conditions also enable the rapid prototyping of Bragg mirrors, allowing for the customization of small and big batches. In addition, inkjet printing is an additive manufacturing method. It enables precise lateral patterning of Bragg mirrors in a feature size of less than 50 μm, allowing for the maskless manufacturing of the same Bragg mirror in a defined pattern or different Bragg mirrors arranged on the same substrate. Additionally, inkjet printing has a high scalability in terms of both the dimension of the mirrors and the quantity of the mirrors, offering the potential for roll-to-roll manufacturing. Finally, the inkjet printing process is adaptable to various substrates, ranging from rigid substrates such as glass to flexible foils such as polyethylene terephthalate (PET) foils and the top surface of optoelectronic devices. Inkjet printing Bragg mirrors directly on sensors or emitters offers high integration and compactness for the devices. However, fabricating Bragg mirrors by inkjet printing is very challenging in

terms of both ink formulation and a stable multilayer printing process; hence, it has not been realized so far.

In this chapter, the digital fabrication of Bragg mirrors by a commercial desktop inkjet printer is demonstrated for the first time. This was accomplished by alternately printing a high-RI material, which is titanium dioxide (TiO_2) nanocomposite, and a low-RI material, which is poly(methyl methacrylate) (PMMA). Both materials were dispersed or dissolved in inks, which allowed for stable and repeatable inkjet printing. The reflectance peaks reached as high as 99% in the mirrors consisting of ten bilayers, and the peak values of over 80% were realized by mirrors with five bilayers. Furthermore, the central wavelength of the mirrors was tuned across the whole visible light range into the near-infrared (NIR) wavelength range by modifying the layer thicknesses, which was enabled by simply adjusting printing parameters. With inkjet printing, Bragg mirrors were fabricated on different substrates, including rigid glass substrates and flexible foils, in different sizes, where the Bragg mirrors exhibited excellent homogeneity in color over a large area and showed the possibility of lateral patterning. Therefore, the inkjet printing approach enables additive manufacturing of Bragg mirrors for various applications, ranging from microscale photonic elements, such as pixelated Bragg mirrors for a spectrometer with high spatial and spectral resolutions, to enhanced functionality and aesthetics in large-area displays, building integration and solar technologies.

7.2   Ink Development

The development of suitable inks and the establishment of a reproducible and reliable multilayer printing process are very challenging. First of all, in order to reach a high reflectance with a low number of layers, the solid components in the inks should be selected to provide a high contrast in RI. Second, the solvent system used for dissolving or dispersing the solid components has to be designed to allow the inks to meet the printability requirements for inkjet printing, as discussed in Section 2.4.2. Besides, the solvent system must exhibit low to medium volatility to prevent the clogging of the nozzles. Since multiple nozzles are used for jetting the droplets, if clogging happens to one nozzle, the deposited droplet volume changes, and the layer thickness of the solid thin film is strongly impacted. Due to the ultra-fine thickness of the layers, variations in the thicknesses result in a noticeable shift in the spectrum.
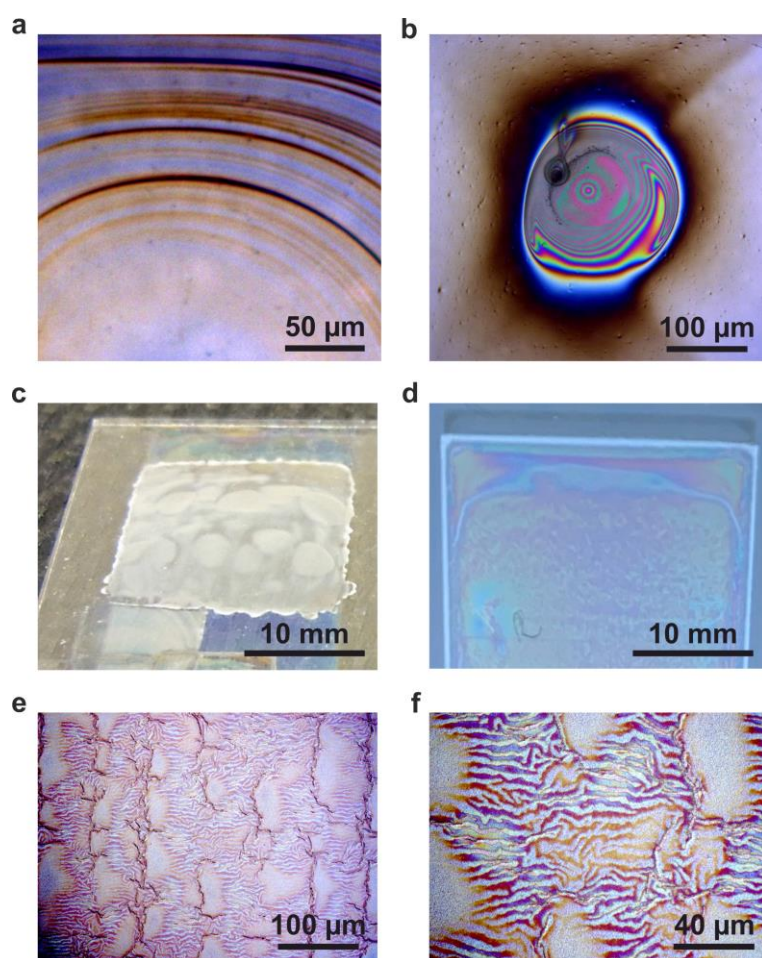
Figure 7.1: Non-ideal printed thin films exhibit various types of nonuniformities. (a) Microscope image of concentric coffee rings in a dried thin film. (b) Microscope image of materials accumulating in the center of a thin film after drying. (c) Image of a printed multilayer stack where the last printed layer dissolved the underneath thin film. (d) Image of a printed thin film. The film shows high non-uniformity. (e) Microscope image of an area of the thin film in (d). Wrinkles and cracks can be seen from the image, which results from the suboptimal curing process. (f) Close-up microscope image of (e).

Additionally, the ink formulations need to ensure a drying process that gives a uniform layer after solidification. Drying effects such as the coffee-ring effect and agglomeration, whose examples are shown in **Figure 7.1**a and b, need to be circumvented. Furthermore, since different inks are printed alternately upon dried thin films, all inks must meet the orthogonal solubility conditions. This means that each ink used for a stack does not dissolve the layers printed with the other inks. **Figure 7.1**c shows the situation when the solvent of one ink can dissolve the solid components of another ink. Local nonuniformity, such as defects from agglomeration, or global nonuniformity, such as gradient in layer thickness, are accumulated in the multiple printing processes and can lead to much more

severe nonuniformity in the final stack. With suitable inks, the fabrication process, including the printing parameters and the post-printing treatments, also needs to be optimized to achieve precise control and reproducibility of the layer thickness. When the process is not optimized, the thin films might exhibit wrinkles or cracks due to the induced mechanical stress, as shown in **Figure 7.1**d-f. Optimized inks, printing parameters, and post-treatment parameters are crucial to ensure optimal spectral performance, such as ultra-high reflectance. All these factors have to be satisfied, and they are closely interwoven with each other.
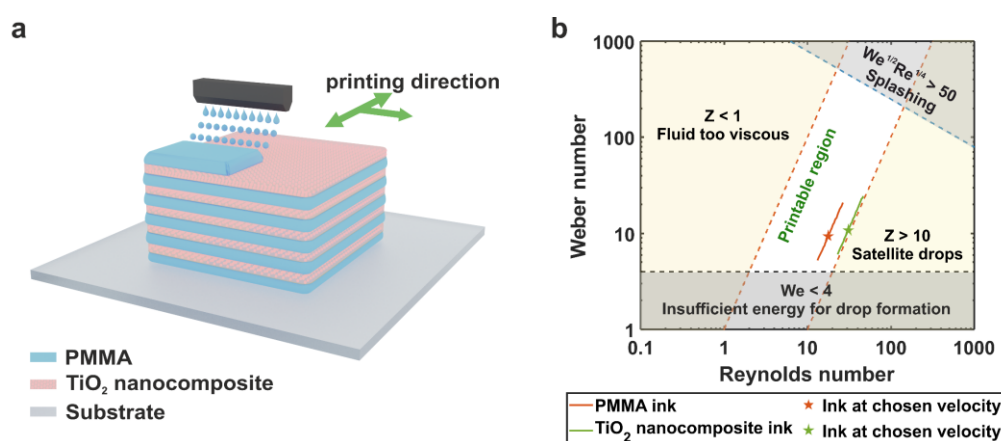
Figure 7.2: The inkjet printing process and inks adopted for the inkjet printing of the Bragg mirrors. (a) Schematic demonstration of the inkjet printing process used to fabricate Bragg mirrors. The constituent materials include PMMA and TiO_2 nanocomposite, where TiO_2 nanoparticles are embedded in a UV-curable polymer matrix. The two materials are alternately printed on each other to create a multilayer stack. (b) Printability map in the parameter space of *Re* versus *We*. The two solid lines represent the PMMA ink (red line) and the TiO_2 nanocomposite ink (green line) with different droplet ejection velocities. The two pentagrams indicate the two inks at the chosen ejection velocities for inkjet printing. The white region is the printable window.

Among all optical materials, TiO_2 was selected as the high-RI constituent material because it has one of the highest RI while being transparent in the visible light and near-infrared range. For the low-RI constituent material, PMMA was chosen because of its extensive use in optical applications, its flexibility, and its low RI to enable a high RI contrast to TiO_2. The inks with the chosen composites were developed to be suitable for the inkjet printing process. A TiO_2 nanocomposite ink, which is the TiO_2 nanoparticle dispersion combined with a UV-curable polymer matrix (PM) as the host, was used as the high-RI ink, while a PMMA solution was applied as the low-RI ink. With these two inks, the Bragg mirrors were fabricated by alternating the printing of the PMMA and TiO_2 nanocomposite inks on top of each other, as depicted in Figure 7.2a.

The rheological properties, including density, surface tension, and viscosity, of the PMMA and TiO$_2$ nanocomposite inks are presented in Table 7.1. **Figure 7.3**a depicts the shear viscosity of both inks, with PMMA ink measured at 28 °C and TiO$_2$ nanocomposite ink measured at 27 °C. These measurement temperatures were set to the printhead temperatures during printing. **Figure 7.3**b and c show the images of the droplets of the inks used for measuring the surface tension of the PMMA and TiO$_2$ nanocomposite inks, respectively.

Table 7.1: Rheological properties of the poly(methyl methacrylate) (PMMA) ink and TiO$_2$ nanocomposite ink

Ink	Density (g/cm^3)	Surface tension (mN/m)	Viscosity (mPa·s)
PMMA ink	1.04	38.45	5.05 @ 28 °C
TiO$_2$ nanocomposite ink	0.94	29.89	2.62 @ 27 °C
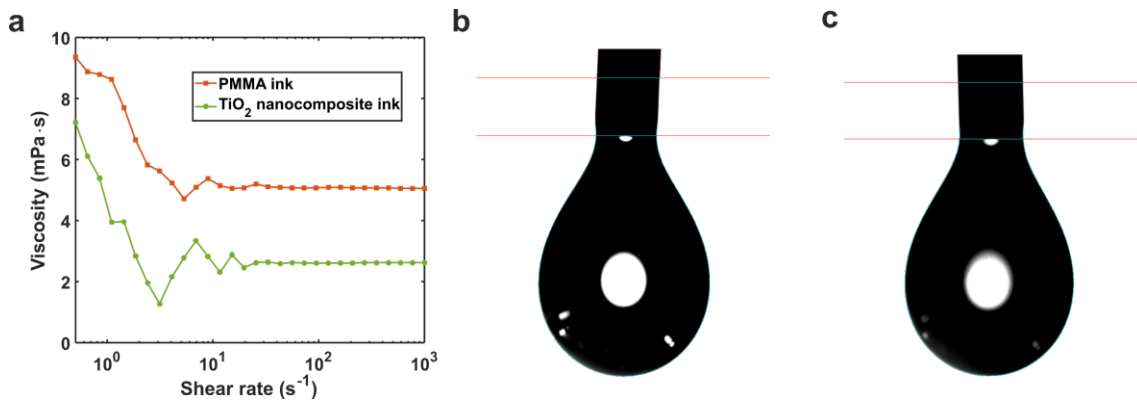
Figure 7.3: Rheological properties of the poly(methyl methacrylate) (PMMA) and TiO$_2$ nanocomposite inks. (a) The shear viscosity of the PMMA ink (red line) measured at 28 °C, and the TiO$_2$ nanocomposite ink (green line) measured at 27 °C. (b) The droplet of PMMA ink for surface tension measurement. The shape of the droplet is outlined, and the two red lines detect the reference needle for size calculation. (c) The droplet of TiO$_2$ nanocomposite ink for surface tension measurement.

The Weber and Reynolds numbers of both inks were calculated based on their rheological parameters as described in Section 2.4.2, and the characteristic length is the nozzle orifice size of 21.5 μm. Both PMMA and TiO$_2$ nanocomposite inks are plotted in the *Re – We* parameter space and the solid lines represent the theoretical printability of the inks at varying ejection velocities from 3.0 m/s to 6.0 m/s, as depicted in **Figure 7.2**b. The

pentagrams indicate the properties of the inks at the respective chosen ejection velocity during printing, which was 4.0 m/s for PMMA ink and 3.8 m/s for TiO_2 nanocomposite ink. As can be seen from the figure, both inks fall within the white area, i.e., the printable region, proving the theoretical printability of both inks.
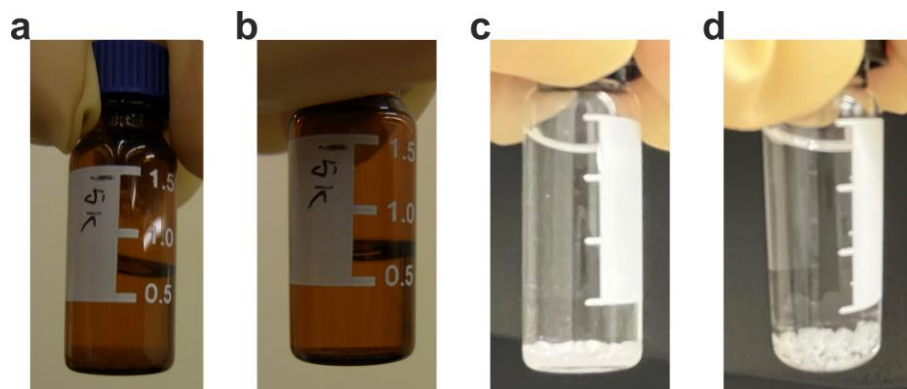
Figure 7.4: Evaluation of solubility of poly(methyl methacrylate) (PMMA) with different molecular weights in ethylene glycol monopropyl ether. (a) Image of the PMMA 15 kDa solution after preparation. (b) Image of the PMMA 15 kDa solution after 30 hours on a laboratory shaker at room temperature. (c) Image of the PMMA 65 kDa solution after preparation. (d) Image of the PMMA 65 kDa solution after 30 hours on a laboratory shaker at room temperature.

The solubility of PMMA with different molecular weights in the solvent of TiO_2 nanocomposite ink was evaluated according to the shake-flask solubility method [251]. Typically, low molecular weight results in lower ink viscosity at the same concentration but also higher solubility in solvents. PMMA with molecular weights of 15 kDa and 65 kDa were placed in separate vials. The solvent of the TiO_2 nanocomposite ink, ethylene glycol monopropyl ether (EGmpe), was added to both vials to achieve a concentration of 10 mg/mL, as shown in **Figure 7.4**a and c, respectively. The vials were positioned on a laboratory shaker for 30 hours at room temperature. As can be seen from **Figure 7.4**b, the solid material of PMMA 15 kDa was mostly dissolved in the solution after 30 hours, indicating high solubility of the PMMA 15 kDa in EGMPE. Consequently, PMMA 15 kDa is deemed unsuitable for the inkjet printing process.

In contrast, the residual solid material of PMMA 65 kDa can be clearly seen in the solution after 30 hours, as depicted in **Figure 7.4**d. Subsequently, 1 mL of supernatant liquid from the PMMA 65 kDa solution was taken and filtered using a 200 nm pore-size filter. Then, the liquid underwent solvent evaporation at 80 °C in a fume hood. Following solvent evaporation, the residual material was weighed, and the value was found to be below 0.01 mg, demonstrating the very low solubility of PMMA 65 kDa in the solvent of TiO_2 nanocomposite ink at room temperature. This low solubility ensures minimal dissolution

of the previously printed PMMA layer during the subsequent TiO$_2$ nanocomposite ink printing step, and the low solubility of the TiO$_2$ nanocomposite layer in the solvent of PMMA ink was also validated.
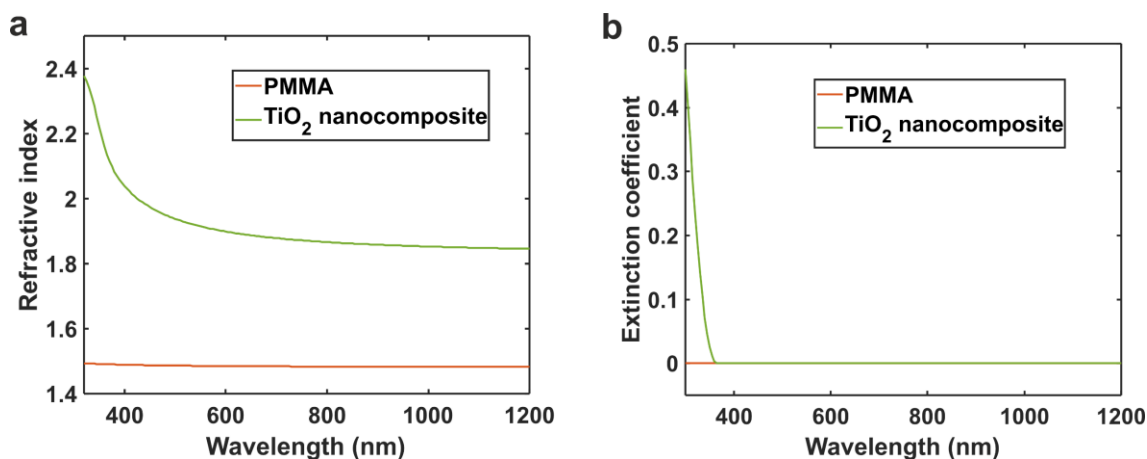
Figure 7.5: Refractive indices and extinction coefficients of poly(methyl methacrylate) and TiO$_2$ nanocomposite. (a) Refractive indices measured by ellipsometry. (b) Extinction coefficients measured by ellipsometry. Both materials exhibit zero extinction coefficients in the wavelength range from 370 nm to 1200 nm.

The RI and extinction coefficients of PMMA and TiO$_2$ nanocomposite were determined using spectroscopic ellipsometry, and the results are depicted in **Figure 7.5**. Specifically, the printed TiO$_2$ nanocomposite layer exhibits an RI of 2.08 at 380 nm, and it gradually decreases to 1.87 at 780 nm, as shown in **Figure 7.5**a. Meanwhile, the RI of the printed PMMA layer remains almost unchanged for the whole wavelength range, exhibiting an RI of 1.49 at 380 nm and 1.48 at 780 nm. This results in a high RI contrast of 0.39 to 0.59 in the visible light range, making these materials well-suited for use as the constituent material pair in the Bragg mirrors. In addition, the extinction coefficients of both materials were measured to be zero in the wavelength range 370 – 1200 nm, as illustrated in **Figure 7.5**b. This indicates negligible absorption and minimal scattering within this wavelength range [252, 253]. For further details of the spectroscopic ellipsometry measurement, refer to Section 4.2.1.

The inks used in this work were prepared as follows: The low-RI PMMA ink and its reference were prepared by dissolving PMMA with a molecular weight of 15 kDa (Sigma-Aldrich) and 65 kDa (PSS-polymer) each in 1,3-dimethoxybenzene (Sigma-Aldrich, $\geqslant$ 98%) and 10 vol% of hexylbenzene (Sigma-Aldrich, 97%) to reach a concentration of 40 mg/mL for printing and 10 mg/mL for solubility characterization. The high-RI TiO$_2$ nanocomposite ink was prepared by adding EGMPE (Sigma-Aldrich, 99.4%) to a TiO$_2$ nanocomposite dispersion (Avantamar). A final concentration of 3.8 wt% was reached. These

ink concentrations were predetermined to achieve the specific range of desired film thickness after curing, employing suitable printing parameters.

Prior to the printing process, both PMMA and TiO_2 nanocomposite inks were degassed in an ultrasonic bath treatment for 5 minutes. Following the filtering of the particles and agglomerates by the polytetrafluoroethylene (PTFE) filters, the inks were separately loaded into the 10-pL DMC 11610 cartridges. Throughout the printing process, a minimum of ten nozzles were applied. The printhead temperatures for the TiO_2 nanocomposite and PMMA ink were kept at 27 °C and 28 °C, respectively. The temperature of the substrates was maintained at 24 °C. Custom-designed waveforms, accommodating ejection frequencies of up to 2.5 kHz, were employed. As the rheological properties of the inks have been optimized for the printhead, the waveforms for both inks featured a single-peak structure with a maximum voltage of 22 V.

7.3 Fabrication of Bragg Mirrors by Inkjet Printing

According to Section 2.3.3, the central wavelength of a Bragg mirror is determined by Equation 2.43, the maximum reflectance at the central wavelength is given by Equation 2.45, and the stopband width is determined following Equation 2.47. From these equations, it can be seen that the central wavelength is dependent solely on the optical thickness of the H and L layers, which can be adjusted by altering the material composition or, more straightforwardly, by changing the layer thickness. With the same constituent materials, the primary factor that affects the maximum reflectance is the number of bilayers. Hence, a higher reflectance can be achieved by adding more layers to the stack. While the layer thickness can be controlled during inkjet printing by adjusting the printing parameters, key challenges include ensuring uniformity of printed layers, maintaining stable and reproducible droplet ejection, and achieving nanometer-level control of thickness.

To achieve tunability in central wavelength covering the entire visible light range, the H and L layer thickness was adjusted by varying the resolution of the printing pattern, specifically the deposited ink volume per unit area. In the printing process, more than one nozzle was applied. An illustrative schematic of the printing path configuration of nozzles with different numbers of nozzles is shown in **Figure 7.6**. With the printheads, the repeatability of the droplet size is below 3.5%, and when the printing parameters are optimized, this can be further decreased to around 0.5%. Applying more nozzles for the printing process brings several advantages. The increased number of nozzles significantly increases the printing speed. For instance, the time required to print the same area when using ten nozzles is ten times less than using only a single nozzle. Additionally, employing more than one nozzle allows for controlling the number of pixels skipped in both directions before reusing a nozzle. Along the in-scan direction, a quality factor of two was set, where two different nozzles were used to print one line. In the cross-scan

direction, at least nine pixels were skipped before reusing the same nozzle. In cases where there are variations from nozzle to nozzle, when fewer nozzles are used, the inhomogeneities caused by them appear in almost each printing line, and the droplets deposited may exhibit the same directional offset, resulting in inhomogeneity or discontinuity in printed layers. Therefore, using more nozzles is advantageous in masking the impact of failing or unstable nozzles, as the positions of the nozzles become more distributed with a higher nozzle count.
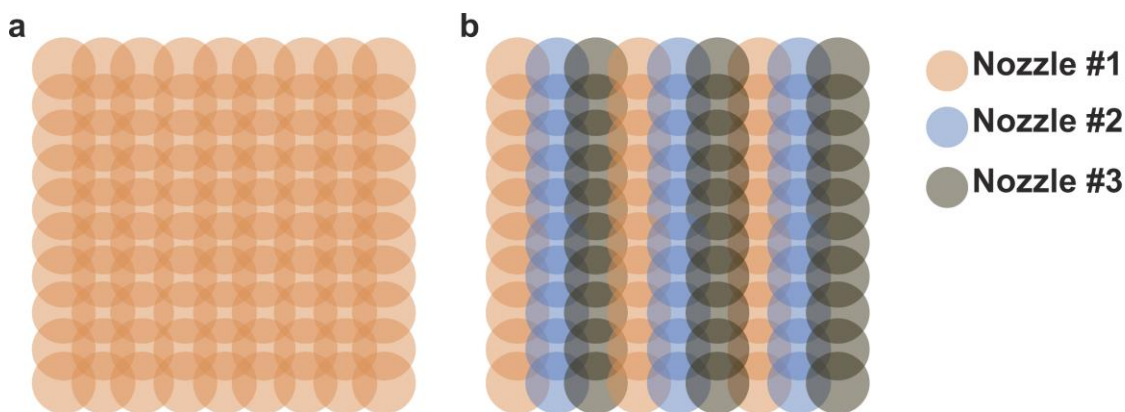
Figure 7.6: Schematic of the printing path arrangement of nozzles. (a) One single nozzle is used for printing the whole area. (b) Three different nozzles are used for printing the same area.

Initially, a first PMMA layer was directly printed onto the substrate, followed by drying under 10 mbar for 2 minutes and subsequently baking on a hotplate at 50 °C for 5 minutes. Afterward, a TiO_2 nanocomposite layer was printed atop the dried PMMA layer. The TiO_2 nanocomposite layer first went through drying under ambient temperature for 2 minutes, followed by a 5-minute prebake step on a hotplate at 100 °C. UV exposure was conducted for 10 minutes utilizing a UV-LED light source (Hamamatsu), followed by an additional 10-minute hard bake at 100 °C. The succeeding PMMA and TiO_2 nanocomposite layers were alternately printed and treated following the same processes. The layer thickness was determined by the resolution of the printing pattern, which dictates the ejected droplet volume per unit area. To achieve the desired thickness range, for the TiO_2 nanocomposite ink, the pattern resolution ranged from 550 to 900 dpi, and for the PMMA ink, it ranged from 500 to 700 dpi.

With the optimized printing parameters, the variation in individual droplets from the same nozzle or across used nozzles was minimized so that the layer thickness could be precisely controlled. In inkjet printing, the layer thickness is determined primarily by two factors, which are the ink concentration and the number of droplets deposited per unit area, which is decided by the resolution of the printing pattern. For a given ink, the main factor

affecting the thickness of the printed layer is then solely the deposited droplet volume. Assuming a uniform 1-inch^2 layer, its thickness is calculated by the equation:

$$d = \frac{V}{A} = N_{dpi,x} \cdot N_{dpi,y} \cdot V_{drop} \cdot c \qquad (7.1)$$

where d denotes the layer thickness, V represents the volume of the printed layer, A denotes the area of the layer, which is 1 inch^2, $N_{dpi,x/y}$ is the dpi number for the x- and y-directions, respectively, V_{drop} represents the single droplet volume and is 10 pL in this work, and c is the ink concentration. Assuming a decrement of $N_{dpi,x}$ by 1 and an increment of $N_{dpi,y}$ by 1, the number of droplets deposited can be changed in a step of one. Even if the ink concentration is 100%, which is pure solid material, the thickness resolution Δd is calculated to be around 0.016 nm. By decreasing the ink concentration, this thickness resolution can be further improved, indicating that inkjet printing theoretically provides an extremely fine thickness resolution.
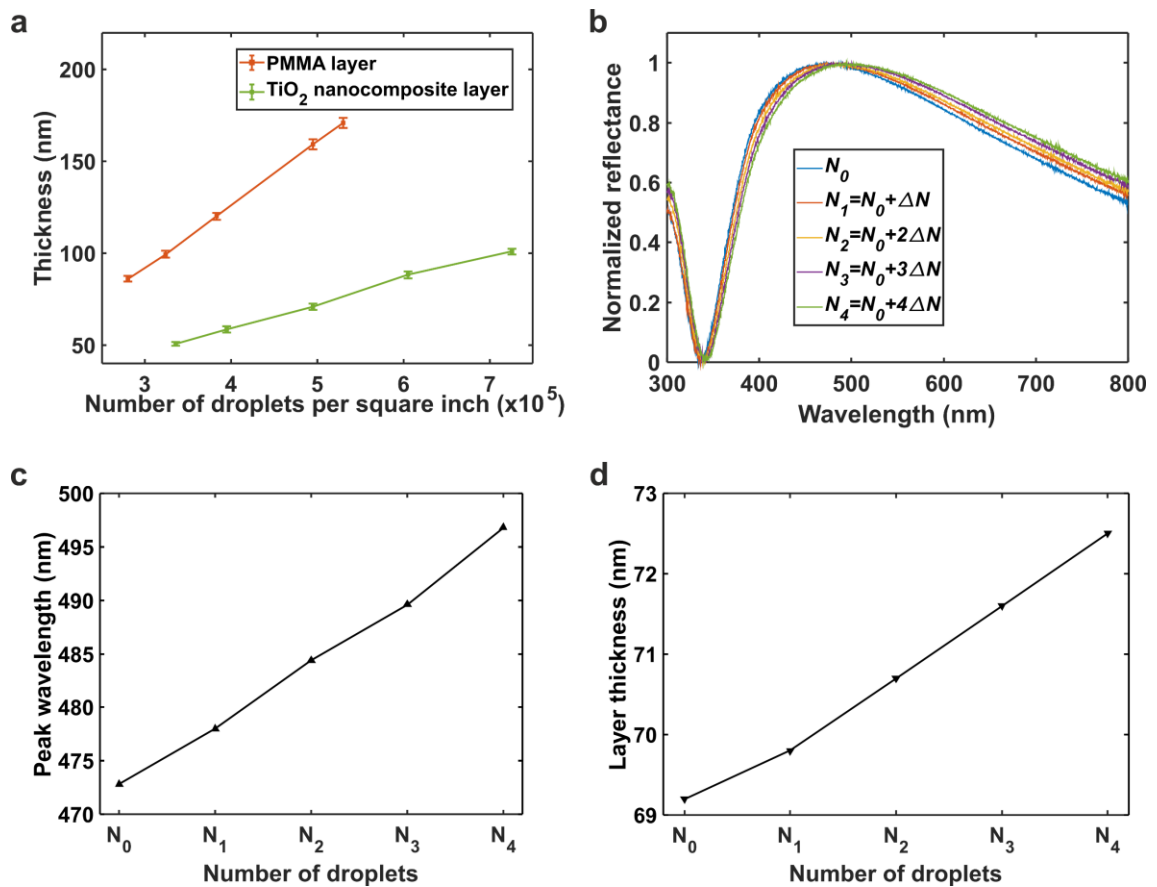
Figure 7.7: Layer thickness control with deposited number of droplets. (a) Thickness variation of the poly(methyl methacrylate) (PMMA) layer and the TiO$_2$ nanocomposite layer with respect to the number of droplets deposited per square inch. Each material was printed on top of the other to achieve the same wetting conditions as when printing Bragg

mirrors. The obtained thickness of both materials falls within the suitable range for quarter-wave stacks in the visible light range. (b) Reflectance spectra of TiO_2 nanocomposite single layers with various thicknesses, normalized for comparison. With an increasing number of deposited droplets from N_0 to N_4, the reflectance spectrum shifts toward longer wavelengths. The droplet number was increased in a constant step of 3342 (i.e., $\Delta N = 3342$). (c) The peak wavelength of the reflectance spectra in relation to the number of droplets deposited in the printed area. (d) The extracted layer thickness with respect to the number of droplets. The thickness resolution reached less than 1 nm.

The tunability of the layer thickness of the constituent materials by varying the number of droplets in a unit area is illustrated in **Figure 7.7**a. The thickness range obtained for both materials can achieve a good wavelength coverage of the visible light range. To demonstrate the achievable minimum thickness resolution, single TiO_2 nanocomposite layers with varying thicknesses were printed, and their normalized reflectance spectra are shown in **Figure 7.7**b. With the number of printed droplets increasing, the thickness of the thin film increases, and the reflectance spectrum shifts towards the long-wavelength range. These layers were printed in a 2×2 cm^2 area, with the number of droplets increasing from 309135 (N_0) to 322503 (N_4) in a constant step of 3342 ($\Delta N = 3342$). Subsequently, these spectra were fitted to the simulated spectra to extract thickness values for each layer. For more details, refer to the Appendix.

The peak wavelength of each spectrum can be seen in **Figure 7.7**c. As the number of printed droplets increases from N_0 to N_4, the central wavelength also increases, ranging from 472.8 to 496.8 nm. This corresponds to a rise in the layer thickness from 69.2 to 72.5 nm, as plotted in **Figure 7.7**d. A thickness resolution of 0.825 ± 0.150 nm has been achieved, which can be decreased further by reducing ΔN down to 1 or diluting the inks.

Following printing, the post-treatment steps play an as important role in achieving uniform and reproducible layers. The PMMA layer was dried under reduced pressure and baked to complete solvent evaporation. The TiO_2 nanocomposite layer, on the other hand, was solidified through UV curing and hard bake. In the UV curing step, intermixing of the layers can happen when the UV radiation dose is not sufficient. The UV-curable PM played a crucial role in improving the adhesion of the TiO_2 nanocomposite layer without requiring high temperatures.

7.4   Morphological and Optical Characterization
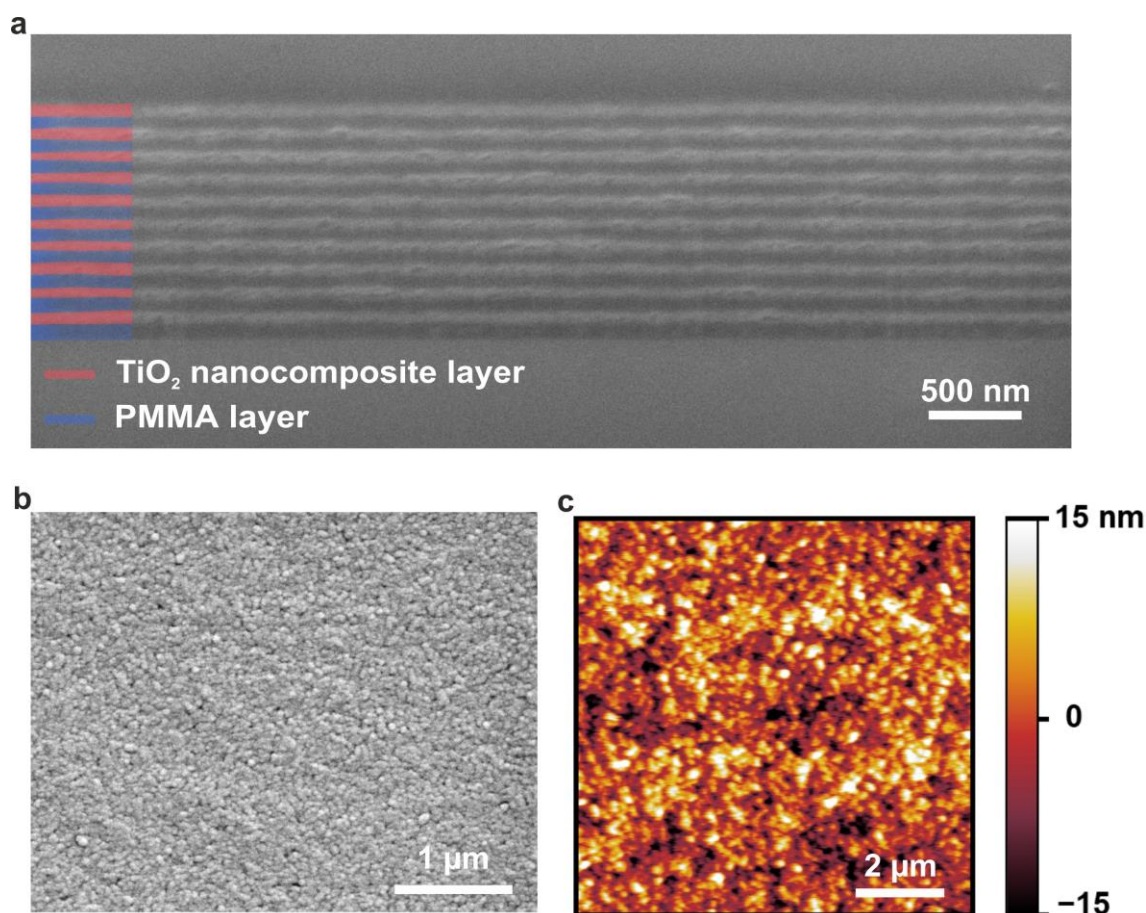
Figure 7.8: Scanning electron microscopy (SEM) and atomic force microscopy (AFM) images of the printed Bragg mirrors. (a) Cross-sectional SEM image of a Bragg mirror with ten bilayers by inkjet printing. The high-refractive-index (high-RI) and low-RI layers were partially colored for clarity. (b) SEM image, and (c) AFM image of the top TiO_2 nanocomposite surface of a Bragg mirror with ten bilayers. The surface root-mean-square roughness was measured to be 6.316 nm.

According to Equation 2.45, to achieve a highly reflective mirror with a reflectance exceeding 98%, it is necessary to stack a large number of at least ten bilayers in the Bragg mirrors. Therefore, Bragg mirrors with up to ten bilayers were fabricated with the developed inks and optimized printing parameters. **Figure 7.8**a displays the scanning electron microscopy (SEM) image of the cross-section of the printed Bragg mirror with ten bilayers. To ensure a closed layer on the substrate, the first (bottom) PMMA layer was printed with a higher thickness. Nevertheless, the spectral behavior of the final printed Bragg mirrors was barely impacted by this design choice because of the RI similarity of PMMA to the substrate. The multilayer structure in the image demonstrates uniform layer

thickness across a large area and the repeatable thickness in every other layer. In **Figure 7.8**b, the SEM image presents the top surface of the same Bragg mirror, showing the top TiO$_2$ nanocomposite layer featuring closely packed nanoparticles in a PM. The more quantitative surface morphology characterization of the top surface was carried out using atomic force microscopy (AFM), and the image is shown in **Figure 7.8**c. The surface root-mean-square (RMS) roughness, denoted as S_q, was determined to be 6.316 nm, satisfying the smooth surface criterion of $S_q/\lambda \leqslant 0.02$ in the visible light range [254]. In this regime, scattering primarily involves the first diffraction orders of the surface spectral components, where scattering is proportional to the square of the surface roughness [255]. Therefore, a moderate roughness mainly leads to the suppression of side interference fringes in transmission, while the bandwidth and the central wavelength of the main peak are minimally affected [162].
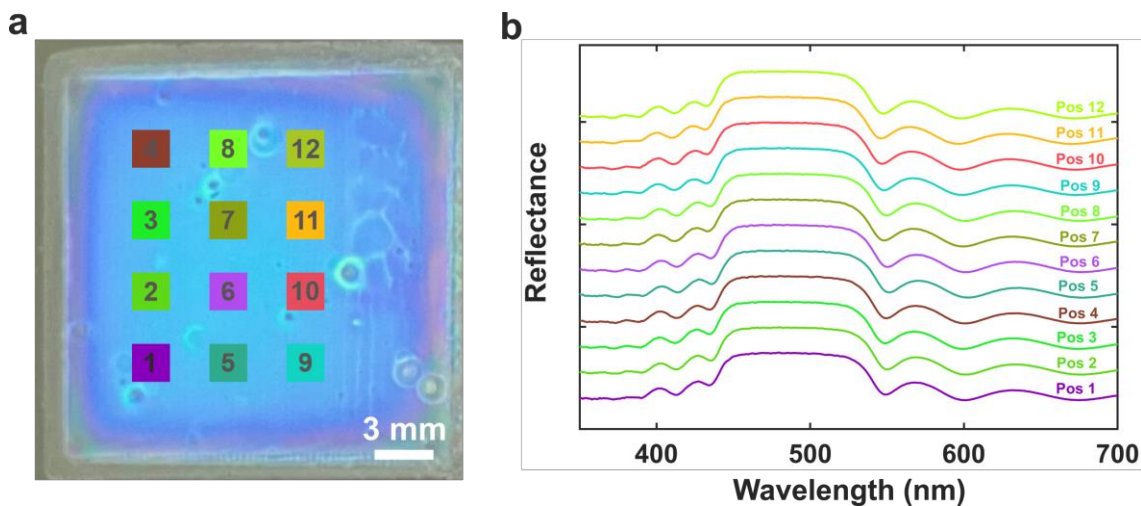
Figure 7.9: Uniformity analysis of the printed Bragg mirror. (a) Image of a printed Bragg mirror with ten bilayers, with the small squares denoting various spots of the mirror where the reflectance spectra were measured. (b) Reflectance spectra from the 12 different locations of the mirror in (a). Each reflectance spectrum is offset by 0.5 in the vertical direction for clarity.

Furthermore, the uniformity of the printed Bragg mirrors was analyzed. The global layer thickness variations in an area of around 10×12 mm^2 were characterized by measuring the reflectance spectra at several distinct and distributed locations on the Bragg mirror with ten bilayers. As depicted in **Figure 7.9**a, the reflectance spectra of the indicated 12 spots were measured. The results are illustrated in **Figure 7.9**b, where the spectra are overlaid in the same plot, sharing the same x-axis, while the reflectance values on the y-axis are shifted with a consistent step of 50% for clarity. The central wavelength exhibits an absolute variation within ± 2.5 nm and a standard deviation of ± 1.53 nm, indicating excellent uniformity in the printed Bragg mirrors.
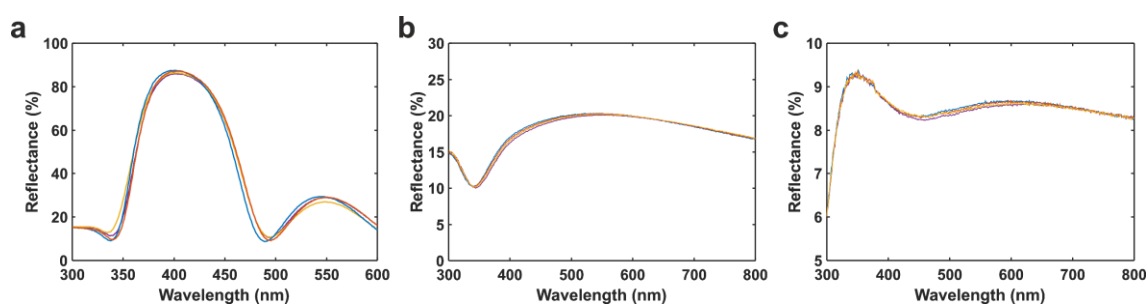
Figure 7.10: Reflectance spectra from four Bragg mirrors in the same batch. (a) Each mirror comprises five bilayers. The central wavelength exhibited a variation within ± 2 nm. (b) Each mirror comprises one bilayer. (c) Each mirror comprises only the first poly(methyl methacrylate) layer.

From the SEM image, the consistency and repeatability of the printing process are qualitatively demonstrated by the uniform layer thickness of each material. For a more quantitative characterization, a repeatability analysis of the printed Bragg mirrors was conducted by measuring the reflectance spectra of four mirrors in the same batch, which were fabricated using identical printing parameters and the same post-treatment procedures. The reflectance spectra of the mirrors with five bilayers are plotted in **Figure 7.10**a. The spectra exhibit a maximum variation in central wavelength of only ± 2 nm, indicating excellent repeatability of the printing process. The reflectance spectra of the Bragg mirrors comprising one bilayer and only the first PMMA layer are illustrated in **Figure 7.10**b and **Figure 7.10**c, respectively, demonstrating a high resemblance and, hence, a high repeatability.

The inkjet-printed Bragg mirrors are shown in **Figure 7.11**a. They were printed in a 2 × 2 cm^2 square format on glass substrates arranged in a 5 × 5 array. From the bottom row to the top row, the number of bilayers increases from one to five, where the brightness of the color also shows a visible increase. From left to right, the layer thickness increases, resulting in a shift of the central wavelength from the purple to red region. This visual representation demonstrates that the printed Bragg mirrors show great potential in visual and aesthetic aspects by the presented homogeneous color impressions. Apart from serving as high-reflectivity mirrors, the inkjet-printed Bragg mirrors also exhibit dichroic beamsplitter functionality as well. This dichroic filtering characteristic is demonstrated in **Figure 7.11**b, where a white light beam illuminated the sample from the far-right side while the mirror was positioned upright. The Bragg mirror predominantly reflects the blue light to the incident side while the remaining spectral components pass through, creating an orange shadow on the left side of the mirror.
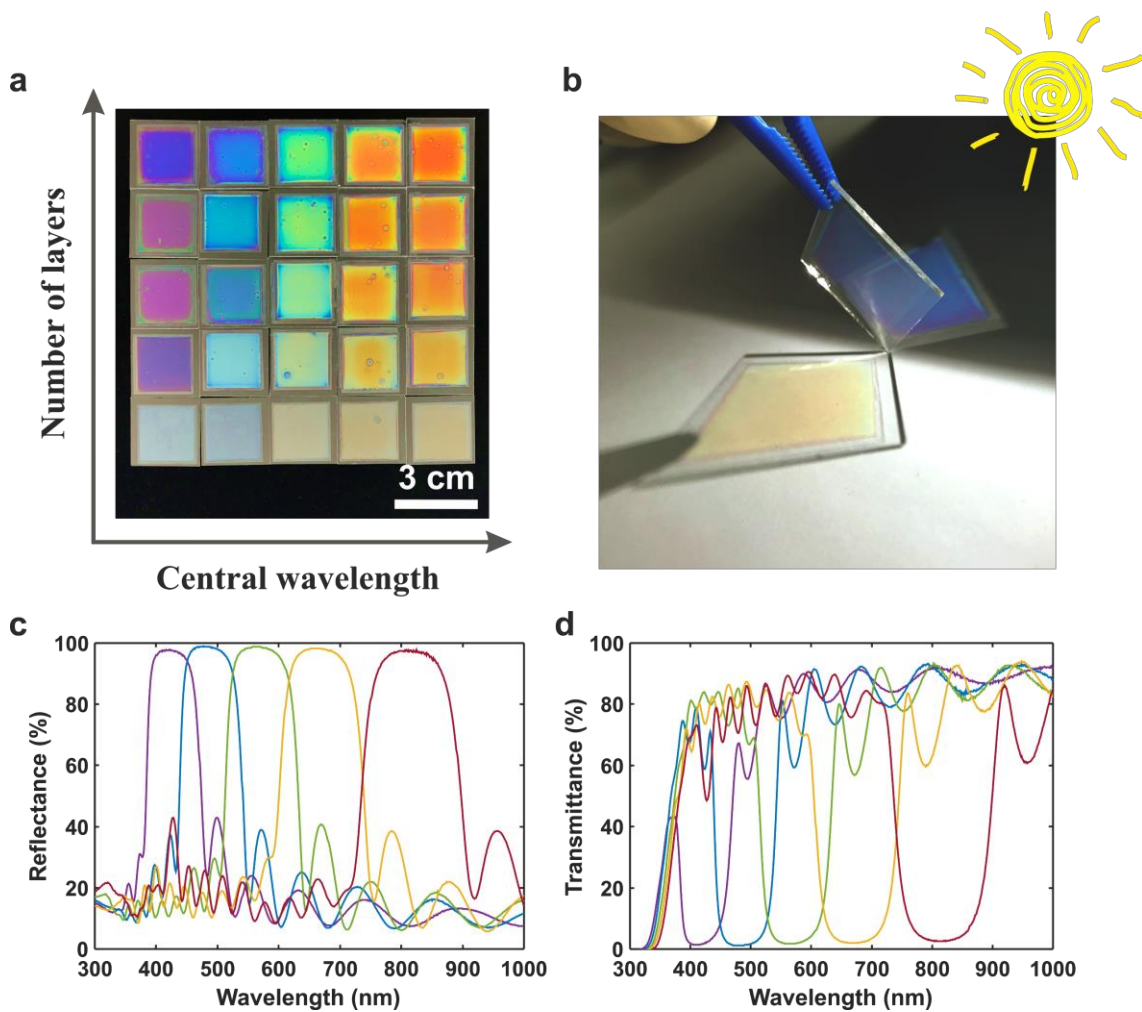
Figure 7.11: Images and reflectance spectra of Bragg mirrors with up to ten bilayers fabricated by inkjet printing. (a) Image of the printed Bragg mirrors with the number of layers increasing from bottom row to top row and the central wavelength increasing from left to right. (b) Demonstration of the dichroic filtering characteristic of the printed Bragg mirror, with a white light source illuminating the mirror from the far-right side. (c) Reflectance spectra of five printed Bragg mirrors with ten bilayers. The central wavelength, which is at 416, 477, 561, 662, and 808 nm, respectively, was tuned by changing the layer thickness, (d) Transmittance spectra of Bragg mirrors in (c).

In addition, the spectral characteristics of printed Bragg mirrors with ten bilayers were measured. **Figure 7.11**c and d depict the reflectance and transmittance spectra of these mirrors, respectively. These spectra exhibit exceptional reflective and dichroic properties at various central wavelengths 416, 477, 561, 662, and 808 nm. Notably, the Bragg mirrors with the central wavelengths at 477 and 561 nm achieve a remarkable maximum reflectance of approximately 99%, while the other Bragg mirrors reach a maximum reflectance of about 98%. The transmittance spectra exhibit good complementary to the

reflectance spectra, with consistent peak values, affirming the absence of absorption in the materials within the visible light range. The PBG shows broadening with increasing central wavelength, which agrees with Equation 2.47. It is worth noting that the printed Bragg mirrors exhibit a pronounced decrease in transmittance near and in the UV light range, attributed to light absorption in constituent materials PMMA and TiO_2 nanocomposite as well as the glass substrate. Particularly in the mirror with the minimum central wavelength of 416 nm, a noticeable drop in the left edge of the PBG is evident.
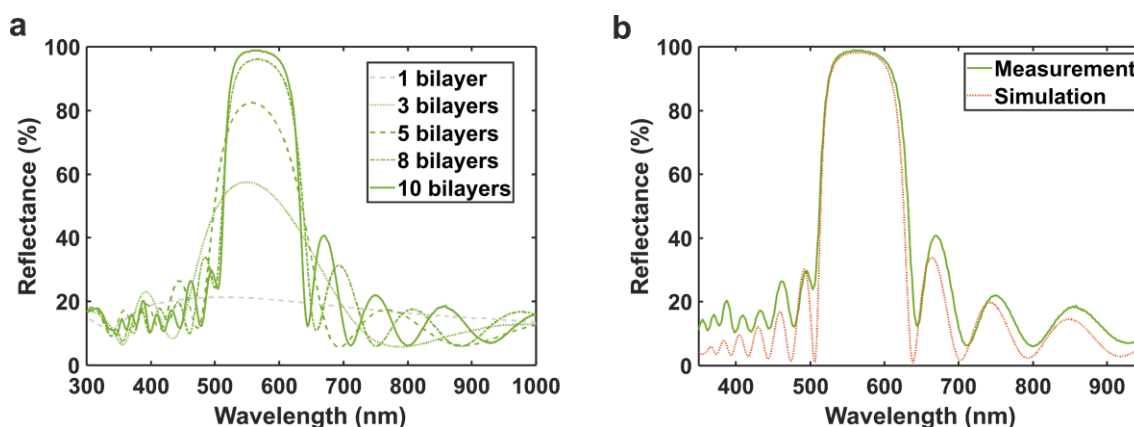
Figure 7.12: Reflectance spectra of printed Bragg mirrors. (a) Reflectance spectra of Bragg mirrors composed of an increasing number of bilayers. (b) Measured (green line) and simulated (red line) reflectance spectra of the Bragg mirror with 10 bilayers. The central wavelength of the mirrors for both figures is 561 nm.

As the number of constituent bilayers increases, the reflectance shows a significant rise. The example of the Bragg mirror with a central wavelength of 561 nm is shown in **Figure 7.12**a. Notably, with a single bilayer, the reflectance peak is very broad, with a maximum value of approximately 20%. As the number of layers adds up, the peak value increases to nearly 60% with three bilayers, surpassing 80% with five bilayers. This value is further extended to 96% with eight bilayers and reaches around 99% with ten bilayers. Meanwhile, these Bragg mirrors exhibit central wavelengths with minor differences within a few nanometers, demonstrating the effective control of layer thickness through optimized inks and fabrication processes.

Additionally, simulations were conducted to predict the reflectance spectra with the measured thickness values and the RI data. In these simulations, the PMMA and TiO_2 nanocomposite layers were assumed to have constant layer thickness each, except for the first PMMA bottom layer. **Figure 7.12**b presents a comparison between the simulated spectrum and the measured data. It can be seen that a good agreement has been achieved between the two spectra in terms of central wavelength, bandwidth, and reflectance peaks. The slightly larger bandwidth and higher reflectance values in the measured spectrum

might indicate that the RI contrast in the constituent materials is higher than measured. The difference in the side peaks may be attributed to scattering and the Bragg mirror detuning [256].
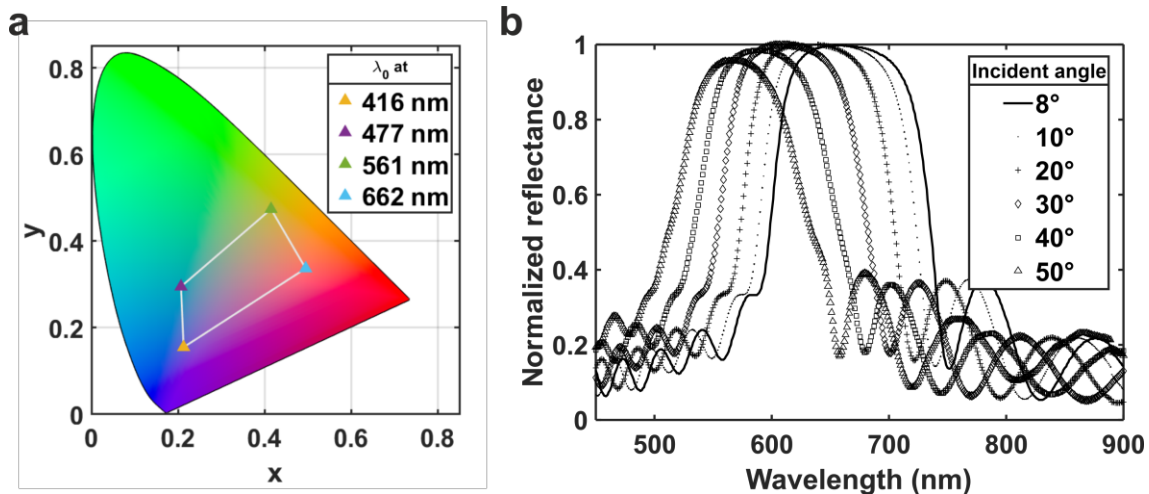
Figure 7.13: Color presentation and angle dependence of the Bragg mirrors. (a) The CIE chromaticity diagram with the color coordinates of the reflection from printed Bragg mirrors with ten bilayers. The mirrors were illuminated using a halogen lamp. (b) Reflectance spectra of the printed Bragg mirror upon different incident angles. The spectra are normalized to the maximum reflectance at the angle of incidence of 8°. The angle dependence is shown as the reflectance spectrum shifts to lower wavelengths and shows a slight decrease in the reflectance peak with the angle of incidence increasing from 8° to 50°.

Furthermore, the color presentation of the printed Bragg mirrors was characterized. The color coordinates of the printed Bragg mirrors with ten bilayers are plotted in the CIE chromaticity diagram, as seen in **Figure 7.13**a. The color coordinates were obtained from the reflection of the mirrors while being illuminated with a halogen lamp. Additionally, as discussed in Section 2.3, the reflection of the Bragg mirrors is subjected to angle dependence. An example is shown in **Figure 7.13**b, where the reflectance spectra of the printed Bragg mirror with a central wavelength of 561 nm were measured at different angles of incidence. As the angle of incidence increases, the reflectance spectrum of the Bragg mirror exhibits the characteristic blue shift, accompanied by a decrease in the reflectance peak value.

7.5 Lateral Patterning of Bragg Mirrors on Large Flexible Substrates
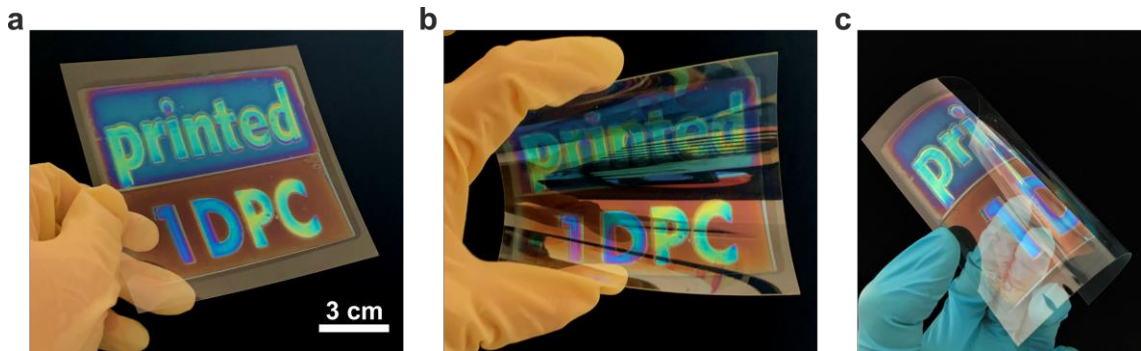
Figure 7.14: Images of Bragg mirrors fabricated with lateral patterning on a flexible substrate. (a) The Bragg mirror was printed on a 12×12 cm^2 polyethylene terephthalate foil. The mirror shows the lateral patterning with letters 'printed 1DPC' and two background blocks in different colors. The image shows its relaxed state. (b) The foil is slightly bent. (c) The foil is strongly bent in the other direction.

Once the inks have been developed and validated, the inkjet printing process becomes adaptable to a wide range of substrates. Adjustments to the printing parameters are necessary only for the initial PMMA layer based on the wettability characteristics of the substrate. In this work, Bragg mirrors are demonstrated not only on small and rigid glass substrates but also on large and flexible substrates. Bragg mirrors were printed on large and flexible 12×12 cm^2 PET foils, featuring a lateral pattern with letters 'printed 1DPC' and two background blocks with different central wavelengths. The results are shown in **Figure 7.14**. The printed Bragg mirror endures slight to strong bending, and this high degree of deformability enables the applications of the printed Bragg mirrors where mechanical flexibility is desired, for example, on curved surfaces in wearable devices. The remarkable color homogeneity over a large area demonstrates the upscaling capability of inkjet-printed Bragg mirrors, opening up opportunities in large-area applications such as building façade and coatings for architecture, which are still challenging for the traditional vacuum-based fabrication methods. Moreover, inkjet printing is compatible with other micro- and nanofabrication techniques, such as nanoimprinting, making it a suitable method for the deposition of dielectrics in diverse applications.

7.6 Summary

In this chapter, the fabrication of digitally manufactured Bragg mirrors through multilayer inkjet printing was demonstrated. The central wavelength of these mirrors was finely

adjusted from the purple to NIR wavelength range, specifically from 416 to 808 nm. This tuning was achieved by adjusting the layer thickness through changes in the number of droplets deposited per unit area. With this capability, a sub-nanometer thickness resolution was realized. In addition, the reflectance peak values were tuned by varying the number of printed bilayers. Remarkably, the maximum reflectance reached approximately 99% with only ten printed bilayers. Meanwhile, the printed Bragg mirrors exhibited excellent layer uniformity and overall high optical quality.

The flexibility of the inkjet printing process and the elimination of high sintering temperatures allowed for the printing of Bragg mirrors on both rigid glass substrates and flexible PET foils. Without the need for extra masks, mirrors in predefined lateral patterns were directly printed. The scalability of the inkjet printing process was proven by printing Bragg mirrors on large substrates. All these factors have demonstrated that inkjet printing is a highly competitive method for the production of Bragg mirrors on a large scale. This fabrication route offers a rapid, straightforward, material-efficient, and cost-effective approach. Inkjet-printed Bragg mirrors in various sizes and different patterns hold significant potential for diverse applications, ranging from integrated optical and photonic devices, particularly in sensing applications, to large-area uses such as coatings for architecture and building integrated photovoltaics.

8 Conclusion and Outlook

8.1 Conclusion

Within the context of this thesis, the device design, ink formulation, and fabrication of the key optical and photonic components, including microlens arrays (MLAs) and Bragg mirrors, are presented. Combining the three key enabling technologies, including micro/nano-photonics, advanced manufacturing, and advanced materials, the proposed approaches in this work offer a roadmap for the novel fabrication of micro-optical and nano-photonic components. Inkjet printing, the digital additive manufacturing method, provides high manufacturing precision, enhanced scalability, improved throughput, excellent freedom in rapid prototyping, and exceptional versatility for fast adaptation to a large diversity of applications.

One key micro-optical component found in numerous optical systems, such as image sensors, displays, and projection systems [39, 43, 48], is MLA. Even though various manufacturing methods have been applied for MLAs, inkjet printing has emerged in recent decades as an attractive and competitive fabrication tool due to its straightforwardness, direct micro-structuring capability, versatility, time- and cost-effectiveness [129-131]. Nonetheless, to reach an enhanced uniformity and a high fill factor (FF) of the MLAs, the previous work required extra production steps, such as photolithography, to pre-structure the substrate. Hence, the advantages of the inkjet printing technology were outweighed by the added complexity and increased effort. Therefore, in **Chapter 5**, the inkjet printing of MLAs with an unprecedented FF and exceptional uniformity on unstructured substrates is presented. Solvent-free UV-curable inks are developed by diluting SU-8 with a reactive diluent.

The ink formulations are meticulously adjusted to eliminate satellite droplets, enable a reliable printing process with optimized printing parameters, and simultaneously yield thin films with high transmission in the visible light range. The tunability of the geometrical parameters of the MLAs is demonstrated by applying selected self-assembled monolayers (SAMs) on the substrate, whereby different optical properties, i.e., the numerical apertures (NAs), in a range from 0.08 to 0.33, are achieved. In order to obtain an automated and quantitative evaluation, two-dimensional and three-dimensional (3D) information of the printed MLAs are collected and assessed with a developed algorithm. The statistical results demonstrate the outstanding uniformity of the printed MLAs, proven by the very low standard deviations of the geometrical parameters, which were less than 2.5% for the radii and below 3.9% for the sag heights. A high FF of 88% is achieved by printing MLAs in a closely packed hexagonal layout on substrates without any pre-structuring steps. This is firstly enabled by the low shrinkage of the droplet upon curing, thanks

to the very low solvent amount in the ink. Secondly, the reliable ejection process leads to highly accurate positioning of the microlenses (MLs).

Moreover, the in-situ UV curing process realizes rapid pinning of the printed droplets, and the two-run printing strategy ensures low merging possibilities of the neighboring droplets. Utilizing inkjet printing, MLAs can be printed in customized patterns, in small as well as large dimensions, on diverse rigid and flexible substrates and large-scale production. The printed MLAs demonstrate high-performance modulation transfer functions and excellent imaging capabilities. Hence, the inkjet-printed MLAs hold the potential to be used for advanced imaging applications.

Therefore, **Chapter 6** explores the application of inkjet-printed MLAs in a multispectral light field camera. MLAs with desired parameters are fabricated by inkjet printing. One monochrome prototype is built with an MLA solely to record the disparity information of the object. In the other prototype, additional spectral information from the object light field is desired, and hence, the MLA is spectrally coded. In this spectral prototype, a color filter array (CFA) with 2×2 spectral channel units is fabricated on the opposite side of the MLA, where a corresponding color filter (CF) codes each ML. A digital and precise registration between the MLA and the CFA is accomplished by inkjet printing. With polydimethylsiloxane (PDMS) adhesives, the inkjet-printed components are attached to the camera sensor at a specific distance, and proper integration into an industrial camera housing is realized. The prototypes are subsequently validated in measurements. Applying the prototypes, images are taken from several real scenes, followed by reconstruction steps from these snapshots. EPINET, compressed sensing, and deep learning are used for reconstruction, whereas EPINET mainly provides a reference monochrome light field reconstruction. The central views, disparity maps, and spectral central views obtained from reconstruction all exhibit high contrast and clarity, demonstrating the high uniformity and optical quality of inkjet-printed MLAs and CFAs. Furthermore, the high-quality central view images and disparity maps provide information in both 3D spatial dimensions, whereas the contrasts in spectral central views provide information in spectral dimension. Therefore, the accomplished prototypes demonstrate the capability for simultaneous acquisition of 3D spatial and spectral information in one snapshot, enabling their usage in various consumer, industrial, and medical scenarios.

Moving from the fabrication of micro-optics to nanophotonics, **Chapter 7** focuses on realizing the inkjet printing of Bragg mirrors, where multilayer inkjet printing and nanometer thickness precision are required. The rational ink selection and formulation prevent the printed layers from intermixing, enable precise control of the layer thickness, and ensure repeatable layer deposition. Bragg mirrors are fabricated with photonic bandgaps covering the entire visible light range and extending to the near-infrared range, with the central wavelengths adjusted from 416 to 808 nm. The spectral tuning is accomplished by changing the layer thickness, which is determined by the number of droplets deposited

per unit area at a specific ink concentration and a defined drying process. With the stable and repeatable printing process, a remarkable resolution in the layer thickness of the sub-nanometer is achieved. By adding up the number of bilayers constituting the Bragg mirrors the maximum reflectance at the central wavelength increases. Remarkably, with only ten printed bilayers, Bragg mirrors are able to reach a reflectance of around 99%. In addition, the quantitative spectral and morphological characterizations prove excellent layer uniformity and outstanding optical quality. Thus, inkjet printing is demonstrated to be highly competitive as a novel method for the fabrication of Bragg mirrors. Bringing the advantages of cost-effectiveness, straightforwardness, maskless lateral patterning, rapid prototyping, a wide substrate selection, scalability from micrometer to meter sizes, and sustainability in terms of materials and energy, extensive applications for inkjet-printed Bragg mirrors can be anticipated, and the elimination of constraints on novel photonic system designs that were previously imposed by conventional fabrication methods can be foreseen.

8.2   Outlook

This thesis contributes to the realization of utilizing inkjet printing for fabricating micro-optical components, including MLAs and CFAs, as well as nanophotonic Bragg mirrors. While the proposed methods have been applied on the laboratory scale, they demonstrate substantial potential for scalability at the industrial level. As a result, numerous possibilities are foreseen, providing directions for future research in areas such as further optimization of the devices, integration of novel materials, realization of active tuning mechanisms, and exploration of diverse applications for these devices:

Mass production and functional microlens arrays

As discussed in Chapter 5, there is potential for continuous tuning of NA with mixed siloxanes. Given the extensive range of commercial siloxanes, a significantly higher degree of tunability in NA and geometrical parameters can be achieved, especially when combined with multiple-droplet MLs. In addition, the spin-coating step for SAM deposition can be replaced by inkjet printing. This allows for the full inkjet printing of multi-NA MLAs using multiple printheads. Besides, stretchable materials can be applied for manufacturing MLAs on stretchable substrates, allowing for active mechanical tuning of their optical properties. Furthermore, functional materials, such as quantum dots, can be embedded in MLAs to provide added functionality. In terms of applications, inkjet printing can be employed for maskless fabrication of MLAs directly atop optoelectronic devices, such as image sensors and LED arrays, thereby enhancing manufacturing efficiency. It can be particularly appealing for industrial purposes.

Hyperspectral light field cameras

For light field cameras, it is worth noting that the developed approach is inherently scalable, both in terms of the reconstruction algorithm and the manufacturing method. In order to realize the transition from multispectral to hyperspectral imaging, narrowband optical filters consisting of multilayer thin films are potential candidates to replace the CFs. Hundreds of optical bands can be encoded in the light field using optical filters with an ultra-narrow bandwidth. These inkjet-printed optical filters are also of great interest in the field of micro-optics for optical displays and imaging technologies. With the successful demonstration of inkjet-printed Bragg mirrors, it is foreseeable that optical bandpass filters can be fabricated by inkjet printing, and an array of different bandpass filters can be directly fabricated in a maskless manner. However, achieving fully digital printing of optical filters on a micrometer scale poses challenges, particularly in addressing the enlarged edge effects for smaller scales.

Optical interference filters

In this work, the printed layers undergo drying, optional UV curing, and baking steps. Future work could explore the integration of instant photo-cross-linkable materials as potential substitutes. In addition, for applications where durability and high mechanical robustness are prioritized, the use of fully inorganic materials could replace organic materials. Moreover, the integration of responsive or functional materials into the constituent materials could enable high-sensitivity sensing or realize active tuning of the photonic bandgaps.

As a typical type of optical interference filter, inkjet printing of Bragg mirrors is demonstrated. This technology can be extended to the fabrication of all different kinds of optical interference filters, including short-pass, long-pass, notch filters, and antireflection coatings. Enhanced functionality can be achieved through the experimental realization of more complex stack designs.

Given the capability of inkjet printing for maskless patterning, it is conceivable to fabricate different filters on the same substrate with minimized gaps. In addition, filters with specific layouts can be directly fabricated on top of optoelectronic devices. Without the need for a vacuum, inkjet printing can overcome the size constraints for optical interference filters imposed by vacuum-assisted technologies, thereby revolutionizing the large-area optical filters and coatings for applications such as architectural glass and solar technologies.

Appendix

A. Appendix for Chapter 5

Table A.1: Automated evaluation of parameters of printed microlens arrays on differently treated substrates

Substrate	Rotation (°)	Tilt in x-direction (°)	Tilt in y-direction (°)	Total tilt (°)	Qacc	Qcv
Glass	0.049 ± 0.407	-0.012	-0.07	0.072	0.575 ± 0.095	1.0322 ± 0.166
APTES	-0.038 ± 0.403	0.009	-0.042	0.043	0.941 ± 0.473	1.045 ± 0.242
TEPS	0.005 ± 0.363	-0.014	-0.069	0.071	0.589 ± 0.150	1.155 ± 0.150
TTFPS	-0.081 ± 0.220	-0.011	-0.039	0.04	0.544 ± 0.123	1.075 ± 0.191
TEOS	-0.002 ± 0.002	-0.017	-0.063	0.065	0.598 ± 0.103	1.033 ± 0.156

B. Appendix for Chapter 7
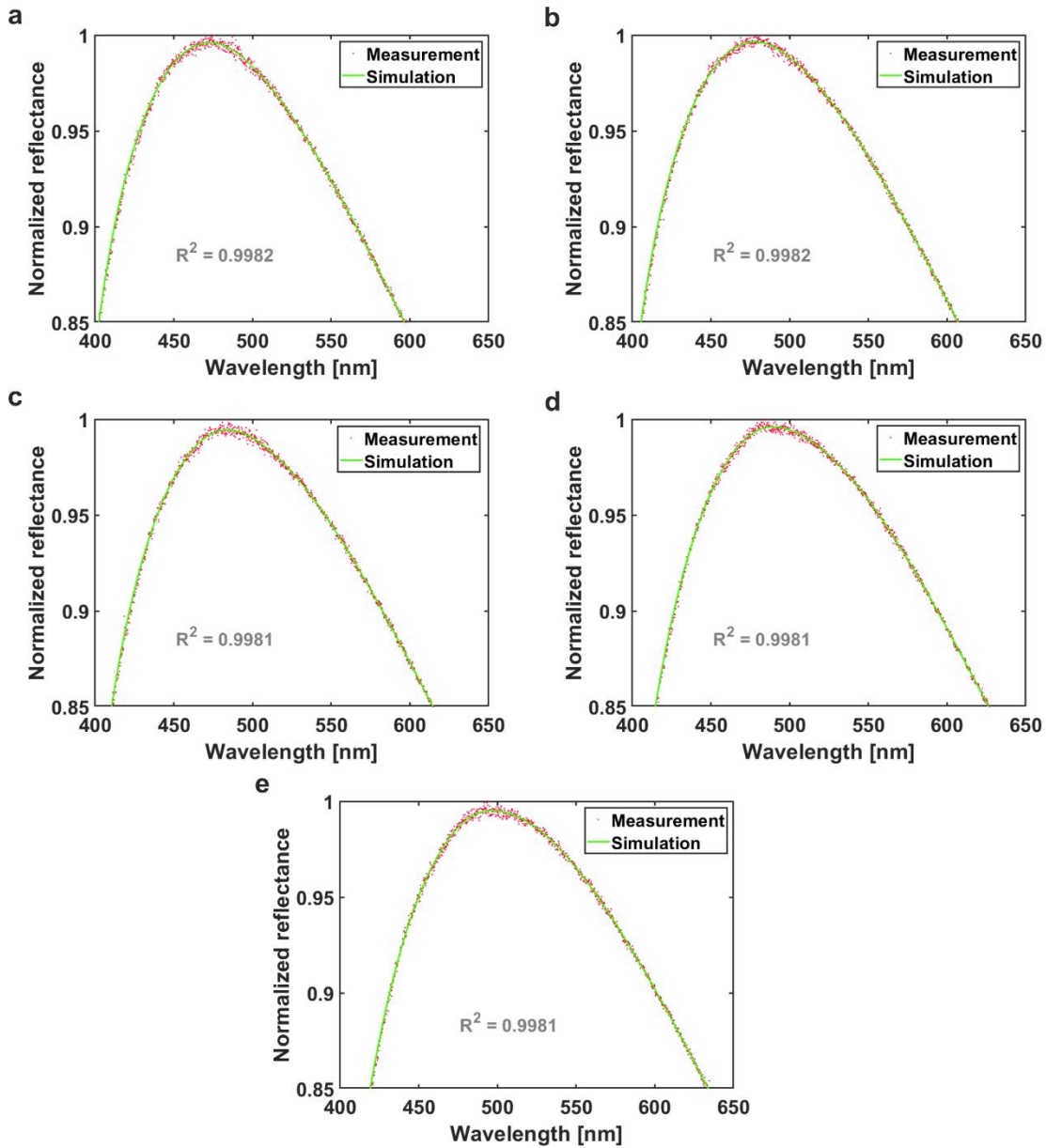
Figure B.1: Normalized reflectance spectra (red dots) and the fitted spectra (green lines) of the printed Bragg mirrors. The number of droplets deposited in the printed area was (a) 309135, (b) 312477, (c) 315819, (d) 319161, and (e) 322503. The coefficients of determination R^2 close to 1 indicate good fitting.

References

[1] J. Needham, L. Gwei-Djen, and L. Wang, *Science and Civilisation in China: Volume 4, Physics and Physical Technology, Part 3, Civil Engineering and Nautics*. Cambridge University Press, 1971.

[2] H. Römer, "A Short Survey of the History of Optics," in *Theoretical Optics*, 2004, pp. 1-13.

[3] https://spie.org/industry-resources/information/industry-report#_=_ (accessed.

[4] E. Commission, D.-G. f. Research, and Innovation, *Re-finding industry – Defining innovation*. Publications Office, 2018.

[5] N. Scoutaris, M. R. Alexander, P. R. Gellert, and C. J. Roberts, "Inkjet printing as a novel medicine formulation technique," *Journal of controlled release,* vol. 156, no. 2, pp. 179-185, 2011.

[6] U. Desa, "Transforming our world: The 2030 agenda for sustainable development," 2016.

[7] J. Das *et al.*, "Devices, systems, and methods for automated monitoring enabling precision agriculture," in *2015 IEEE international conference on automation science and engineering (CASE)*, 2015: IEEE, pp. 462-469.

[8] E. Honkavaara *et al.*, "Processing and assessment of spectrometric, stereoscopic imagery collected using a lightweight UAV spectral camera for precision agriculture," *Remote Sensing,* vol. 5, no. 10, pp. 5006-5039, 2013.

[9] M. Rosenberger and R. Celestre, "Smart multispectral imager for industrial applications," in *2016 IEEE International Conference on Imaging Systems and Techniques (IST)*, 2016: IEEE, pp. 7-12.

[10] J. Qin, K. Chao, M. S. Kim, R. Lu, and T. F. Burks, "Hyperspectral and multispectral imaging for evaluating food safety and quality," *Journal of Food Engineering,* vol. 118, no. 2, pp. 157-171, 2013.

[11] J. A. Palero, H. S. d. Bruijn, A. v. d. P.-v. d. Heuvel, H. J. C. M. Sterenborg, and H. C. Gerritsen, "In vivo nonlinear spectral imaging in mouse skin," *Opt. Express,* vol. 14, no. 10, pp. 4395-4402, 2006/05/15 2006, doi: 10.1364/OE.14.004395.

[12] W. R. Johnson, D. W. Wilson, W. Fink, M. Humayun, and G. Bearman, "Snapshot hyperspectral imaging in ophthalmology," *Journal of biomedical optics,* vol. 12, no. 1, pp. 014036-014036-7, 2007.

[13] Y. Zhang, S. J. Kiselewich, W. A. Bauson, and R. Hammoud, "Robust moving object detection at distance in the visible spectrum and beyond using a moving camera," in *2006 conference on computer vision and pattern recognition workshop (CVPRW'06)*, 2006: IEEE, pp. 131-131.

[14] C. Grimm, T. Fei, E. Warsitz, R. Farhoud, T. Breddermann, and R. Haeb-Umbach, "Warping of radar data into camera image for cross-modal supervision in automotive applications," *IEEE Transactions on Vehicular Technology,* vol. 71, no. 9, pp. 9435-9449, 2022.

[15]   M. Dummer, K. Johnson, S. Rothwell, K. Tatah, and M. Hibbs-Brenner, "The role of VCSELs in 3D sensing and LiDAR," in *Optical Interconnects XXI*, 2021, vol. 11692: SPIE, pp. 42-55.

[16]   Y. Choi *et al.*, "KAIST multi-spectral day/night data set for autonomous and assisted driving," *IEEE Transactions on Intelligent Transportation Systems,* vol. 19, no. 3, pp. 934-948, 2018.

[17]   G. A. Shaw and H. K. Burke, "Spectral imaging for remote sensing," *Lincoln laboratory journal,* vol. 14, no. 1, pp. 3-28, 2003.

[18]   N. M. Abd El-Ghany, S. E. Abd El-Aziz, and S. S. Marei, "A review: application of remote sensing as a promising strategy for insect pests and diseases management," *Environmental Science and Pollution Research,* vol. 27, pp. 33503-33515, 2020.

[19]   S. George *et al.*, "A study of spectral imaging acquisition and processing for cultural heritage," *Digital Techniques for Documenting and Preserving Cultural Heritage,* 2017.

[20]   E. K. Webb, "Optimising Spectral and 3D Imaging for Cultural Heritage Documentation Using Consumer Imaging Systems," University of Brighton, 2020.

[21]   A. Toulouse, J. Drozella, S. Thiele, H. Giessen, and A. Herkommer, "3D-printed miniature spectrometer for the visible range with a 100× 100 μm 2 footprint," *Light: Advanced Manufacturing,* vol. 2, no. 1, pp. 20-30, 2021.

[22]   Z. Pan, G. Healey, M. Prasad, and B. Tromberg, "Face recognition in hyperspectral images," *IEEE Transactions on Pattern Analysis and Machine Intelligence,* vol. 25, no. 12, pp. 1552-1560, 2003.

[23]   E. H. Adelson and J. Y. A. Wang, "Single lens stereo with a plenoptic camera," *IEEE Transactions on Pattern Analysis and Machine Intelligence,* vol. 14, no. 2, pp. 99-106, 1992, doi: 10.1109/34.121783.

[24]   R. Ng, "Fourier slice photography," in *ACM Siggraph 2005 Papers*, 2005, pp. 735-744.

[25]   R. Ng, M. Levoy, M. Brédif, G. Duval, M. Horowitz, and P. Hanrahan, "Light Field Photography with a Hand-held Plenoptic Camera," Stanford university, 2005-04 2005. [Online]. Available: https://hal.archives-ouvertes.fr/hal-02551481

[26]   R. Horstmeyer, G. Euliss, R. Athale, and M. Levoy, "Flexible multimodal camera using a light field architecture," in *2009 IEEE International Conference on Computational Photography (ICCP)*, 16-17 April 2009 2009, pp. 1-8, doi: 10.1109/ICCPHOT.2009.5559016.

[27]   B. C. David, M. L. James, U. Nora, D. Mark, and W. Paul, "VNIR hypersensor camera system," in *Proc.SPIE*, 2009, vol. 7457, p. 74570O, doi: 10.1117/12.833539. [Online]. Available: https://doi.org/10.1117/12.833539

[28]   K. Berkner and S. Shroff, "Optimization of Spectrally Coded Mask for Multi-modal Plenoptic Camera," in *Imaging and Applied Optics*, Toronto, 2011/07/10 2011: Optica Publishing Group, in OSA Technical Digest (CD), p. CMD4, doi: 10.1364/COSI.2011.CMD4. [Online]. Available: https://opg.optica.org/abstract.cfm?URI=COSI-2011-CMD4

[29]   M. Lingfei, S. Ting, K. Rich, and B. Kathrin, "Evaluation of multispectral plenoptic camera," in *Proc.SPIE*, 2013, vol. 8660, p. 86600D, doi: 10.1117/12.2006293. [Online]. Available: https://doi.org/10.1117/12.2006293

[30]   M. Schambach, J. Shi, and M. Heizmann, "Spectral Reconstruction and Disparity from Spatio-Spectrally Coded Light Fields via Multi-Task Deep Learning," in *2021 International Conference on 3D Vision (3DV)*, 1-3 Dec. 2021 2021, pp. 186-196, doi: 10.1109/3DV53792.2021.00029.

[31]   E. Hecht, "Optics 2nd edition," *Optics 2nd edition by Eugene Hecht Reading,* 1987.

[32]   L. Zhang *et al.*, "Microfabrication of a Diffractive Microlens Array on n‐GaAs by an Efficient Electrochemical Method," *Advanced Materials,* vol. 19, no. 22, pp. 3912-3918, 2007.

[33]   T. Hessler *et al.*, "Microlens arrays with spatial variation of the optical functions," *Pure and Applied Optics: Journal of the European Optical Society Part A,* vol. 6, no. 6, p. 673, 1997.

[34]   G. Intermite *et al.*, "Fill-factor improvement of Si CMOS single-photon avalanche diode detector arrays by integration of diffractive microlens arrays," *Opt. Express,* vol. 23, no. 26, pp. 33777-33791, 2015.

[35]   W. Yuan, L.-H. Li, W.-B. Lee, and C.-Y. Chan, "Fabrication of microlens array and its application: a review," *Chinese Journal of Mechanical Engineering,* vol. 31, no. 1, pp. 1-9, 2018.

[36]   J. Duparré and F. Wippermann, "Micro-optical artificial compound eyes," *Bioinspiration & biomimetics,* vol. 1, no. 1, p. R1, 2006.

[37]   K.-H. Jeong, J. Kim, and L. P. Lee, "Biologically inspired artificial compound eyes," *science,* vol. 312, no. 5773, pp. 557-561, 2006.

[38]   T. Kim *et al.*, "Replication of high refractive index glass microlens array by imprinting in conjunction with laser assisted rapid surface heating for high resolution confocal microscopy imaging," *Opt. Express,* vol. 27, no. 13, pp. 18869-18882, 2019.

[39]   S. Battiato, A. R. Bruna, G. Messina, and G. Puglisi, *Image processing for embedded devices*. Bentham Science Publishers, 2010.

[40]   M. M. Vekshin, A. S. Levchenko, A. V. Nikitin, V. A. Nikitin, and N. Yacovenko, "Glass microlens arrays for Shack–Hartmann wavefront sensors," *Measurement Science and Technology,* vol. 21, no. 5, p. 054010, 2010.

[41]   V. Kumar, S. Dottermusch, A. Chauhan, B. S. Richards, and I. A. Howard, "Expanding the Angle of Incidence Tolerance of Unclonable Anticounterfeiting Labels Based on Microlens Arrays and Luminescent Microparticles," *Advanced Photonics Research,* vol. 3, no. 6, p. 2100202, 2022.

[42]   A. Peer, R. Biswas, J.-M. Park, R. Shinar, and J. Shinar, "Light management in perovskite solar cells and organic LEDs with microlens arrays," *Opt. Express,* vol. 25, no. 9, pp. 10704-10709, 2017.

[43]   X. Bi, B. Fan, and W. Li, "Micro-lens-coupled LED neural stimulator for optogenetics," in *2015 IEEE Biomedical Circuits and Systems Conference (BioCAS)*, 2015: IEEE, pp. 1-4.

[44]   M. Hutley, R. Stevens, and D. Daly, "Microlens arrays," *Physics World,* vol. 4, no. 7, p. 27, 1991.

[45]   A. Tuantranont, V. Bright, J. Zhang, W. Zhang, J. Neff, and Y. Lee, "Optical beam steering using MEMS-controllable microlens array," *Sensors and Actuators A: Physical,* vol. 91, no. 3, pp. 363-372, 2001.

[46]   Y. Jin, A. Hassan, and Y. Jiang, "Freeform microlens array homogenizer for excimer laser beam shaping," *Opt. Express,* vol. 24, no. 22, pp. 24846-24858, 2016.

[47]   Y. Liang *et al.*, "Fabrication of a diamond concave microlens array for laser beam homogenization," *Optics & Laser Technology,* vol. 136, p. 106738, 2021.

[48]   P. Schreiber, S. Kudaev, P. Dannberg, and U. D. Zeitner, "Homogeneous LED-illumination using microlens arrays," in *Nonimaging Optics and Efficient Illumination Systems II*, 2005, vol. 5942: SPIE, pp. 188-196.

[49]   J.-W. Pan, C.-M. Wang, H.-C. Lan, W.-S. Sun, and J.-Y. Chang, "Homogenized LED-illumination using microlens arrays for a pocket-sized projector," *Opt. Express,* vol. 15, no. 17, pp. 10483-10491, 2007.

[50]   R. Voelkel, H. P. Herzig, P. Nussbaum, R. Daendliker, and W. B. Hugle, "Microlens array imaging system for photolithography," *Optical Engineering,* vol. 35, no. 11, pp. 3323-3330, 1996.

[51]   H. J. Tiziani and H.-M. Uhde, "Three-dimensional analysis by a microlens-array confocal arrangement," *Applied optics,* vol. 33, no. 4, pp. 567-572, 1994.

[52]   M. Levoy, Z. Zhang, and I. McDowall, "Recording and controlling the 4D light field in a microscope using microlens arrays," *Journal of microscopy,* vol. 235, no. 2, pp. 144-162, 2009.

[53]   H. M. Kim, M. S. Kim, G. J. Lee, Y. J. Yoo, and Y. M. Song, "Large area fabrication of engineered microlens array with low sag height for light-field imaging," *Opt. Express,* vol. 27, no. 4, pp. 4435-4444, 2019.

[54]   E. Wrzesniewski *et al.*, "Enhancing Light Extraction in Top‐Emitting Organic Light‐Emitting Devices Using Molded Transparent Polymer Microlens Arrays," *Small,* vol. 8, no. 17, pp. 2647-2651, 2012.

[55]   A. A. Michelson, *Studies in Optics*. Chicago University Press, 1962.

[56]   C. S. Williams and O. A. Becklund, *Introduction to the optical transfer function*. SPIE Press, 2002.

[57]   C. Johnson, "Circular aperture diffraction limited MTF: approximate expressions," *Applied Optics,* vol. 11, no. 8, pp. 1875_1-1876, 1972.

[58]   C. Fenzl, T. Hirsch, and O. S. Wolfbeis, "Photonic crystals for chemical sensing and biosensing," *Angewandte Chemie International Edition,* vol. 53, no. 13, pp. 3318-3335, 2014.

[59]   K. Waldrip, J. Han, J. J. Figiel, H. Zhou, E. Makarona, and A. Nurmikko, "Stress engineering during metalorganic chemical vapor deposition of AlGaN/GaN distributed Bragg reflectors," *Applied Physics Letters,* vol. 78, no. 21, pp. 3205-3207, 2001.

[60]   Y. Li *et al.*, "Enhanced light utilization in semitransparent organic photovoltaics using an optical outcoupling architecture," *Advanced Materials,* vol. 31, no. 40, p. 1903173, 2019.

[61]   G. Y. Yoo *et al.*, "Stable and colorful perovskite solar cells using a nonperiodic SiO2/TiO2 multi-nanolayer filter," *ACS nano,* vol. 13, no. 9, pp. 10129-10139, 2019.

[62]   M. Kim, D. Lee, Y. Yang, and J. Rho, "Switchable diurnal radiative cooling by doped VO 2," *Opto-Electronic Advances,* vol. 4, no. 5, pp. 200006-1-200006-7, 2021.

[63]   O. Stenzel, "Optical Coatings: material aspects in theory and practice," 2014.

[64]   G. Cummins and M. P. Desmulliez, "Inkjet printing of conductive materials: a review," *Circuit world,* vol. 38, no. 4, pp. 193-213, 2012.

[65]   H. P. Le, "Progress and trends in ink-jet printing technology," *Journal of imaging science and technology,* vol. 42, no. 1, pp. 49-62, 1998.

[66]   Y. J. Donie *et al.*, "Phase-separated nanophotonic structures by inkjet printing," *ACS nano,* vol. 15, no. 4, pp. 7305-7317, 2021.

[67]   Q. Jin *et al.*, "High Dynamic Range Smart Window Display by Surface Hydrophilization and Inkjet Printing," *Advanced Materials Technologies,* vol. 7, no. 5, p. 2101026, 2022.

[68]   S. Schlisske *et al.*, "Design and color flexibility for inkjet-printed perovskite photovoltaics," *ACS Applied Energy Materials,* vol. 2, no. 1, pp. 764-769, 2018.

[69]   S. K. Karunakaran *et al.*, "Recent progress in inkjet-printed solar cells," *Journal of Materials Chemistry A,* vol. 7, no. 23, pp. 13873-13902, 2019.

[70]   F. Schackmar *et al.*, "Perovskite solar cells with all‐inkjet‐printed absorber and charge transport layers," *Advanced Materials Technologies,* vol. 6, no. 2, p. 2000271, 2021.

[71]   D. Lee *et al.*, "P‐66: Ink Jet Printed Full Color Polymer LED Displays," in *SID Symposium Digest of Technical Papers*, 2005, vol. 36, no. 1: Wiley Online Library, pp. 527-529.

[72]   C. F. Madigan, C. R. Hauf, L. D. Barkley, N. Harjee, E. Vronsky, and S. A. Van Slyke, "30.2: Invited paper: Advancements in inkjet printing for OLED mass production," in *SID Symposium Digest of Technical Papers*, 2014, vol. 45, no. 1: Wiley Online Library, pp. 399-402.

[73]   P.-Y. Chen *et al.*, "71‐4: Uniformity Study on High Resolution OLED Display Fabricated by Ink Jet Printing Process," in *SID Symposium Digest of Technical Papers*, 2017, vol. 48, no. 1: Wiley Online Library, pp. 1045-1047.

[74]   E. Lee *et al.*, "67‐2: invited paper: ambient processing of quantum dot photoresist for emissive displays," in *SID Symposium Digest of Technical Papers*, 2017, vol. 48, no. 1: Wiley Online Library, pp. 984-987.

[75]   M. Furusawa *et al.*, "19.5 L: Late‐News Paper: Inkjet‐Printed Bus and Address Electrodes for Plasma Display," in *SID Symposium Digest of Technical Papers*, 2002, vol. 33, no. 1: Wiley Online Library, pp. 753-755.

[76]   P. Yang, L. Zhang, D. J. Kang, R. Strahl, and T. Kraus, "High‐resolution inkjet printing of quantum dot light‐emitting microdiode arrays," *Advanced Optical Materials,* vol. 8, no. 1, p. 1901429, 2020.

[77]   E. Shioya *et al.*, "48.1: LTPS TFTs with Metal Electrodes Formed by Inkjet Printing Technology," in *SID Symposium Digest of Technical Papers*, 2006, vol. 37, no. 1: Wiley Online Library, pp. 1575-1578.

[78]   P. J. Smith and D. H. Shin, *Inkjet-based micromanufacturing.* John Wiley & Sons, 2012.

[79]   J. G. Scott, "Digital printing for printed circuit boards," *Circuit World,* vol. 31, no. 4, pp. 34-41, 2005.

[80]   A. Moya, G. Gabriel, R. Villa, and F. J. del Campo, "Inkjet-printed electrochemical sensors," *Current Opinion in Electrochemistry,* vol. 3, no. 1, pp. 29-39, 2017.

[81]   X. Wang, M. Zhang, L. Zhang, J. Xu, X. Xiao, and X. Zhang, "Inkjet-printed flexible sensors: From function materials, manufacture process, and applications perspective," *Materials Today Communications,* vol. 31, p. 103263, 2022.

[82]   M. Seiberlich *et al.*, "Inkjet‐Printed Microlenses Integrated onto Organic Photodiodes for Highly Accurate Proximity Sensing," *Advanced Sensor Research,* p. 2300004, 2023.

[83]   W. Zapka, *Handbook of industrial inkjet printing: a full system approach*. John Wiley & Sons, 2017.

[84]   D. McManus *et al.*, "Water-based and biocompatible 2D crystal inks for all-inkjet-printed heterostructures," *Nature nanotechnology,* vol. 12, no. 4, pp. 343-350, 2017.

[85]   L. Li, Y. Guo, X. Zhang, and Y. Song, "Inkjet-printed highly conductive transparent patterns with water based Ag-doped graphene," *Journal of Materials Chemistry A,* vol. 2, no. 44, pp. 19095-19101, 2014.

[86]   M. Arin *et al.*, "Inkjet printing of photocatalytically active TiO_2 thin films from water based precursor solutions," *Journal of the European Ceramic Society,* vol. 31, no. 6, pp. 1067-1074, 2011.

[87]   C. Jiang *et al.*, "Coffee-ring-free quantum dot thin film using inkjet printing from a mixed-solvent system on modified ZnO transport layer for light-emitting devices," *ACS applied materials & interfaces,* vol. 8, no. 39, pp. 26162-26168, 2016.

[88]   Y. Sun *et al.*, "Solvent inkjet printing process for the fabrication of polymer solar cells," *Rsc Advances,* vol. 3, no. 30, pp. 11925-11934, 2013.

[89]   L. Nayak, S. Mohanty, S. K. Nayak, and A. Ramadoss, "A review on inkjet printing of nanoparticle inks for flexible electronics," *Journal of Materials Chemistry C,* vol. 7, no. 29, pp. 8771-8795, 2019.

[90]   M. Vaseem, K. M. Lee, A.-R. Hong, and Y.-B. Hahn, "Inkjet printed fractal-connected electrodes with silver nanoparticle ink," *ACS applied materials & interfaces,* vol. 4, no. 6, pp. 3300-3307, 2012.

[91]   N. Raut and K. Al-Shamery, "Inkjet printing metals on flexible materials for plastic and paper electronics," *Journal of Materials Chemistry C,* vol. 6, no. 7, pp. 1618-1641, 2018.

[92]   E. Saleh *et al.*, "3D inkjet-printed UV-curable inks for multi-functional electromagnetic applications," *Additive Manufacturing,* vol. 13, pp. 143-148, 2017.

[93] S. Seipel, J. Yu, A. P. Periyasamy, M. Viková, M. Vik, and V. A. Nierstrasz, "Inkjet printing and UV-LED curing of photochromic dyes for functional and smart textile applications," *RSC advances,* vol. 8, no. 50, pp. 28395-28404, 2018.

[94] A. Hudd, *Inkjet printing technologies*. World Scientific Publishing, Hackensack, NJ, USA, 2010.

[95] D. Lohse, "Fundamental fluid dynamics challenges in inkjet printing," *Annual review of fluid mechanics,* vol. 54, pp. 349-382, 2022.

[96] H. Roh *et al.*, "Enhanced Performance of Pixelated Quantum Dot Light-Emitting Diodes by Inkjet Printing of Quantum Dot–Polymer Composites," *Advanced Optical Materials,* https://doi.org/10.1002/adom.202002129 vol. 9, no. 11, p. 2002129, 2021/06/01 2021, doi: https://doi.org/10.1002/adom.202002129.

[97] N. Reis and B. Derby, "Ink jet deposition of ceramic suspensions: Modeling and experiments of droplet formation," *MRS Online Proceedings Library (OPL),* vol. 625, p. 117, 2000.

[98] B. Derby, "Inkjet printing of functional and structural materials: fluid property requirements, feature stability, and resolution," *Annual Review of Materials Research,* vol. 40, pp. 395-414, 2010.

[99] C. D. Stow, M. G. Hadfield, and J. M. Ziman, "An experimental investigation of fluid flow resulting from the impact of a water drop with an unyielding dry surface," *Proceedings of the Royal Society of London. A. Mathematical and Physical Sciences,* vol. 373, no. 1755, pp. 419-441, 1981/01/07 1981, doi: 10.1098/rspa.1981.0002.

[100] J. Kunes, *Dimensionless physical quantities in science and engineering*. Elsevier, 2012.

[101] D. Kaelble, "Dispersion-polar surface tension properties of organic solids," *The Journal of Adhesion,* vol. 2, no. 2, pp. 66-81, 1970.

[102] D. K. Owens and R. Wendt, "Estimation of the surface free energy of polymers," *Journal of applied polymer science,* vol. 13, no. 8, pp. 1741-1747, 1969.

[103] R. D. Deegan, O. Bakajin, T. F. Dupont, G. Huber, S. R. Nagel, and T. A. Witten, "Capillary flow as the cause of ring stains from dried liquid drops," *Nature,* vol. 389, no. 6653, pp. 827-829, 1997.

[104] H. B. Eral, D. 't Mannetje, and J. M. Oh, "Contact angle hysteresis: a review of fundamentals and applications," *Colloid and polymer science,* vol. 291, pp. 247-260, 2013.

[105] L. Chen and J. R. Evans, "Drying of colloidal droplets on superhydrophobic surfaces," *Journal of colloid and interface science,* vol. 351, no. 1, pp. 283-287, 2010.

[106] M. Dicuangco, S. Dash, J. A. Weibel, and S. V. Garimella, "Effect of superhydrophobic surface morphology on evaporative deposition patterns," *Applied Physics Letters,* vol. 104, no. 20, 2014.

[107] P. J. Yunker, T. Still, M. A. Lohr, and A. Yodh, "Suppression of the coffee-ring effect by shape-dependent capillary interactions," *nature,* vol. 476, no. 7360, pp. 308-311, 2011.

[108] B.-J. de Gans and U. S. Schubert, "Inkjet printing of well-defined polymer dots and arrays," *Langmuir,* vol. 20, no. 18, pp. 7789-7793, 2004.

[109] F. Girard, M. Antoni, and K. Sefiane, "On the effect of Marangoni flow on evaporation rates of heated water drops," *Langmuir,* vol. 24, no. 17, pp. 9207-9210, 2008.

[110] S.-K. Lee, K.-C. Lee, and S. S. Lee, "A simple method for microlens fabrication by the modified LIGA process," *Journal of Micromechanics and Microengineering,* vol. 12, no. 3, p. 334, 2002.

[111] H. Jung and K.-H. Jeong, "Monolithic polymer microlens arrays with high numerical aperture and high packing density," *ACS applied materials & interfaces,* vol. 7, no. 4, pp. 2160-2165, 2015.

[112] S. Di, H. Lin, and R. Du, "An artificial compound eyes imaging system based on mems technology," in *2009 IEEE International Conference on Robotics and Biomimetics (ROBIO)*, 2009: IEEE, pp. 13-18.

[113] S. Surdo, R. Carzino, A. Diaspro, and M. Duocastella, "Single‐shot laser additive manufacturing of high fill‐factor microlens arrays," *Advanced Optical Materials,* vol. 6, no. 5, p. 1701190, 2018.

[114] R. Magazine, B. van Bochove, S. Borandeh, and J. Seppälä, "3D inkjet-printing of photo-crosslinkable resins for microlens fabrication," *Additive Manufacturing,* vol. 50, p. 102534, 2022.

[115] Y. Kumaresan, A. Rammohan, P. K. Dwivedi, and A. Sharma, "Large area IR microlens arrays of chalcogenide glass photoresists by grayscale maskless lithography," *ACS Applied Materials & Interfaces,* vol. 5, no. 15, pp. 7094-7100, 2013.

[116] C. Florian, S. Piazza, A. Diaspro, P. Serra, and M. Duocastella, "Direct laser printing of tailored polymeric microlenses," *ACS applied materials & interfaces,* vol. 8, no. 27, pp. 17028-17032, 2016.

[117] X. Li, Y. Ding, J. Shao, H. Tian, and H. Liu, "Fabrication of microlens arrays with well‐controlled curvature by liquid trapping and electrohydrodynamic deformation in microholes," *Advanced Materials,* vol. 24, no. 23, pp. OP165-OP169, 2012.

[118] S. Yang, T. N. Krupenkin, P. Mach, and E. A. Chandross, "Tunable and latchable liquid microlens with photopolymerizable components," *Advanced Materials,* vol. 15, no. 11, pp. 940-943, 2003.

[119] M. Xu, Z. Zhou, Z. Wang, and H. Lu, "Self-assembled microlens array with controllable focal length formed on a selective wetting surface," *ACS applied materials & interfaces,* vol. 12, no. 6, pp. 7826-7832, 2020.

[120] N. Jürgensen *et al.*, "A single‐step hot embossing process for integration of microlens arrays in biodegradable substrates for improved light extraction of light‐emitting devices," *Advanced Materials Technologies,* vol. 6, no. 2, p. 1900933, 2021.

[121] Y. Ding *et al.*, "High‐throughput and controllable fabrication of soft screen protectors with microlens arrays for light enhancement of OLED displays," *Advanced Materials Technologies,* vol. 5, no. 10, p. 2000382, 2020.

[122] C. Fang *et al.*, "Antireflective paraboloidal microlens film for boosting power conversion efficiency of solar cells," *ACS applied materials & interfaces,* vol. 10, no. 26, pp. 21950-21956, 2018.

[123] N. Jürgensen *et al.*, "A single‐step hot embossing process for integration of microlens arrays in biodegradable substrates for improved light extraction of light‐emitting devices," *Advanced Materials Technologies,* vol. 6, no. 2, p. 1900933, 2021.

[124] Y. Zhong *et al.*, "In situ electrohydrodynamic jet printing-based fabrication of tunable microlens arrays," *ACS Applied Materials & Interfaces,* vol. 13, no. 33, pp. 39550-39560, 2021.

[125] T. Gissibl, S. Thiele, A. Herkommer, and H. Giessen, "Two-photon direct laser writing of ultracompact multi-lens objectives," *Nature photonics,* vol. 10, no. 8, pp. 554-560, 2016.

[126] J. Y. Kim, K. Pfeiffer, A. Voigt, G. Gruetzner, and J. Brugger, "Directly fabricated multi-scale microlens arrays on a hydrophobic flat surface by a simple ink-jet printing technique," *Journal of Materials Chemistry,* vol. 22, no. 7, pp. 3053-3058, 2012.

[127] Y. Luo *et al.*, "Direct fabrication of microlens arrays with high numerical aperture by ink-jetting on nanotextured surface," *Applied Surface Science,* vol. 279, pp. 36-40, 2013.

[128] L. Jacot-Descombes, M. Gullo, V. Cadarso, and J. Brugger, "Fabrication of epoxy spherical microstructures by controlled drop-on-demand inkjet printing," *Journal of Micromechanics and Microengineering,* vol. 22, no. 7, p. 074012, 2012.

[129] B. J. De Gans, P. C. Duineveld, and U. S. Schubert, "Inkjet printing of polymers: state of the art and future developments," *Advanced materials,* vol. 16, no. 3, pp. 203-213, 2004.

[130] J. del Barrio and C. Sánchez‐Somolinos, "Light to shape the future: from photolithography to 4D printing," *Advanced Optical Materials,* vol. 7, no. 16, p. 1900598, 2019.

[131] A. Teichler, J. Perelaer, and U. S. Schubert, "Inkjet printing of organic electronics–comparison of deposition techniques and state-of-the-art developments," *Journal of Materials Chemistry C,* vol. 1, no. 10, pp. 1910-1925, 2013.

[132] D. Xie, H. Zhang, X. Shu, and J. Xiao, "Fabrication of polymer micro-lens array with pneumatically diaphragm-driven drop-on-demand inkjet technology," *Opt. Express,* vol. 20, no. 14, pp. 15186-15195, 2012.

[133] D. MacFarlane, V. Narayan, J. Tatum, W. Cox, T. Chen, and D. Hayes, "Microjet fabrication of microlens arrays," *IEEE Photonics Technology Letters,* vol. 6, no. 9, pp. 1112-1114, 1994.

[134] V. Fakhfouri, G. Mermoud, J. Y. Kim, A. Martinoli, and J. Brugger, "Drop-on-demand inkjet printing of SU-8 polymer," *Micro and Nanosystems,* vol. 1, no. 1, pp. 63-67, 2009.

[135] Y. Luo *et al.*, "Direct fabrication of microlens arrays with high numerical aperture by ink-jetting on nanotextured surface," *Applied Surface Science,* vol. 279, pp. 36-40, 2013.

[136] M. Blattmann, M. Ocker, H. Zappe, and A. Seifert, "Jet printing of convex and concave polymer micro-lenses," *Opt. Express,* vol. 23, no. 19, pp. 24525-24536, 2015.

[137] L. Jacot-Descombes *et al.*, "Organic-inorganic-hybrid-polymer microlens arrays with tailored optical characteristics and multi-focal properties," *Opt. Express,* vol. 23, no. 19, pp. 25365-25376, 2015.

[138] E. Mkawi, Y. Al-Hadeethi, E. Shalaan, and E. Bekyarova, "Substrate temperature effect during the deposition of (Cu/Sn/Cu/Zn) stacked precursor CZTS thin film deposited by electron-beam evaporation," *Journal of Materials Science: Materials in Electronics,* vol. 29, pp. 20476-20484, 2018.

[139] Y. Deng, W. Chen, B. Li, C. Wang, T. Kuang, and Y. Li, "Physical vapor deposition technology for coated cutting tools: A review," *Ceramics International,* vol. 46, no. 11, pp. 18373-18390, 2020.

[140] H. Jiang *et al.*, "Plasma polymerized multi-layered photonic films," *Chemistry of materials,* vol. 15, no. 1, pp. 340-347, 2003.

[141] T. Kohoutek, J. Orava, T. Wagner, M. Hrdlicka, M. Vlcek, and M. Frumar, "Preparation of dielectric mirrors from high-refractive index contrast amorphous chalcogenide films," *Journal of Physics and Chemistry of Solids,* vol. 69, no. 8, pp. 2070-2074, 2008.

[142] M. Deopura, C. Ullal, B. Temelkuran, and Y. Fink, "Dielectric omnidirectional visible reflector," *Optics Letters,* vol. 26, no. 15, pp. 1197-1199, 2001.

[143] H. A. Macleod, "Recent developments in deposition techniques for optical thin films and coatings," *Optical Thin Films and Coatings,* pp. 3-23, 2018.

[144] N. Tajima, H. Murotani, and T. Matsudaira, "Optical multicoating using low-refractive-index SiO2 optical thin films deposited by sputtering and electron beam evaporation," *Thin Solid Films,* vol. 776, p. 139824, 2023.

[145] D. Ristau *et al.*, "Ultraviolet optical and microstructural properties of MgF 2 and LaF 3 coatings deposited by ion-beam sputtering and boat and electron-beam evaporation," *Applied optics,* vol. 41, no. 16, pp. 3196-3204, 2002.

[146] J. R. McNeil, A. C. Barron, S. Wilson, and W. Herrmann, "Ion-assisted deposition of optical thin films: low energy vs high energy bombardment," *Applied Optics,* vol. 23, no. 4, pp. 552-559, 1984.

[147] H. Takashashi, "Temperature stability of thin-film narrow-bandpass filters produced by ion-assisted deposition," *Applied Optics,* vol. 34, no. 4, pp. 667-675, 1995.

[148] A. J. Waldorf, J. Dobrowolski, B. T. Sullivan, and L. Plante, "Optical coatings deposited by reactive ion plating," *Applied optics,* vol. 32, no. 28, pp. 5583-5593, 1993.

[149] K. H. Guenther, "Recent advances in reactive low-voltage ion-plating deposition," *Optical Thin Films III: New Developments,* vol. 1323, pp. 29-38, 1990.

[150] G. Kienel, "Optical layers produced by sputtering," *Thin Solid Films,* vol. 77, no. 1-3, pp. 213-224, 1981.

[151] H. Yoda, K. Shiraishi, Y. Hiratani, and O. Hanaizumi, "a-Si: H/SiO 2 multilayer films fabricated by radio-frequency magnetron sputtering for optical filters," *Applied optics,* vol. 43, no. 17, pp. 3548-3554, 2004.

[152]   D. Gibson, I. Brinkley, E. Waddell, and J. Walls, "Closed field magnetron sputtering: new generation sputtering process for optical coatings," in *Advances in Optical Thin Films III*, 2008, vol. 7101: SPIE, pp. 107-118.

[153] J. Dobrowolski, J. R. Pekelsky, R. Pelletier, M. Ranger, B. T. Sullivan, and A. Waldorf, "Practical magnetron sputtering system for the deposition of optical multilayer coatings," *Applied optics,* vol. 31, no. 19, pp. 3784-3789, 1992.

[154] M. Lappschies, B. Görtz, and D. Ristau, "Application of optical broadband monitoring to quasi-rugate filters by ion-beam sputtering," *Applied optics,* vol. 45, no. 7, pp. 1502-1506, 2006.

[155]   D. Ristau and T. Gross, "Ion beam sputter coatings for laser technology," in *Advances in Optical Thin Films II*, 2005, vol. 5963: SPIE, pp. 315-326.

[156] L. Martinu and D. Poitras, "Plasma deposition of optical films and coatings: A review," *Journal of Vacuum Science & Technology A: Vacuum, Surfaces, and Films,* vol. 18, no. 6, pp. 2619-2645, 2000.

[157] J. Kowalski, H. Szymanowski, A. Sobczyk-Guzenda, and M. Gazicki-Lipman, "A stack multilayer high reflectance optical filter produced on polyester substrate with the PECVD technique," *Bulletin of the Polish Academy of Sciences Technical Sciences,* pp. 171-176-171-176, 2009.

[158] A. Szeghalmi, M. Helgert, R. Brunner, F. Heyroth, U. Gösele, and M. Knez, "Atomic layer deposition of Al 2 O 3 and TiO 2 multilayers for applications as bandpass filters and antireflection coatings," *Applied optics,* vol. 48, no. 9, pp. 1727-1732, 2009.

[159] Y. Li, W. Shen, X. Hao, T. Lang, S. Jin, and X. Liu, "Rugate notch filter fabricated by atomic layer deposition," *Applied Optics,* vol. 53, no. 4, pp. A270-A275, 2014.

[160] D. P. Puzzo, L. D. Bonifacio, J. Oreopoulos, C. M. Yip, I. Manners, and G. A. Ozin, "Color from colorless nanomaterials: Bragg reflectors made of nanoparticles," *Journal of Materials Chemistry,* vol. 19, no. 21, pp. 3500-3506, 2009.

[161] M. R. Dahlby, M. Barhoum, and M. H. Bartl, "Sol–gel-derived thin-film stacks with high radiation stability," *Thin solid films,* vol. 562, pp. 435-439, 2014.

[162] C. Bronnbauer *et al.*, "Printing of Large‐Scale, Flexible, Long‐Term Stable Dielectric Mirrors with Suppressed Side Interferences," *Advanced Optical Materials,* vol. 6, no. 1, p. 1700518, 2018.

[163] Z. Wu, D. Lee, M. F. Rubner, and R. E. Cohen, "Structural color in porous, superhydrophilic, and self‐cleaning SiO2/TiO2 Bragg stacks," *Small,* vol. 3, no. 8, pp. 1445-1451, 2007.

[164] S. Guldin and S. Guldin, "Tunable Mesoporous Bragg Reflectors Based on Block Copolymer Self-Assembly," *Inorganic Nanoarchitectures by Organic Self-Assembly,* pp. 117-127, 2013.

[165] S. Y. Choi, M. Mamak, G. Von Freymann, N. Chopra, and G. A. Ozin, "Mesoporous Bragg stack color tunable sensors," *Nano Letters,* vol. 6, no. 11, pp. 2456-2461, 2006.

[166] K. M. Chen, A. W. Sparks, H.-C. Luan, D. R. Lim, K. Wada, and L. C. Kimerling, "SiO 2/TiO 2 omnidirectional reflector and microcavity resonator via the sol-gel method," *Applied Physics Letters,* vol. 75, no. 24, pp. 3805-3807, 1999.

[167] H. A. McInnes, N. J. Bazin, J. E. Andrew, and A. Morris, "Aging studies of sol-gel-derived thin film single-layer and multilayer dielectric mirrors," in *Laser-Induced Damage in Optical Materials: 2000*, 2001, vol. 4347: SPIE, pp. 118-126.

[168] C. s. O. Ramírez Quiroz, C. Bronnbauer, I. Levchuk, Y. Hou, C. J. Brabec, and K. Forberich, "Coloring semitransparent perovskite solar cells via dielectric mirrors," *ACS nano,* vol. 10, no. 5, pp. 5104-5112, 2016.

[169] Z. Wu, D. Lee, M. F. Rubner, and R. E. Cohen, "Structural color in porous, superhydrophilic, and self‐cleaning SiO2/TiO2 Bragg stacks," *Small,* vol. 3, no. 8, pp. 1445-1451, 2007.

[170] A. Urbas *et al.*, "Optically switchable Bragg reflectors," *Advanced Materials,* vol. 16, no. 16, pp. 1453-1456, 2004.

[171] J. Ge and Y. Yin, "Responsive photonic crystals," *Angewandte Chemie International Edition,* vol. 50, no. 7, pp. 1492-1522, 2011.

[172] Y. Qiao, Y. Zhao, X. Yuan, Y. Zhao, and L. Ren, "One-dimensional photonic crystals prepared by self-assembly of brush block copolymers with broad PDI," *Journal of Materials Science,* vol. 53, pp. 16160-16168, 2018.

[173] J. C. Smirnov, M. E. Calvo, and H. Míguez, "Selective UV reflecting mirrors based on nanoparticle multilayers," *Advanced Functional Materials,* vol. 23, no. 22, pp. 2805-2811, 2013.

[174] T. S. Kleine *et al.*, "One dimensional photonic crystals using ultrahigh refractive index chalcogenide hybrid inorganic/organic polymers," *ACS Macro Letters,* vol. 7, no. 7, pp. 875-880, 2018.

[175] Z. Wang *et al.*, "Colorful detection of organic solvents based on responsive organic/inorganic hybrid one-dimensional photonic crystals," *Journal of Materials Chemistry,* vol. 21, no. 4, pp. 1264-1270, 2011.

[176] B. V. Lotsch and G. A. Ozin, "Clay Bragg stack optical sensors," *Advanced Materials,* vol. 20, no. 21, pp. 4079-4084, 2008.

[177] S. Rabaste *et al.*, "Sol–gel fabrication of thick multilayers applied to Bragg reflectors and microcavities," *Thin Solid Films,* vol. 416, no. 1-2, pp. 242-247, 2002.

[178] S. Bachevillier *et al.*, "Fully Solution‐Processed Photonic Structures from Inorganic/Organic Molecular Hybrid Materials and Commodity Polymers," *Advanced Functional Materials,* vol. 29, no. 21, p. 1808152, 2019.

[179] Z. Wu, D. Lee, M. F. Rubner, and R. E. Cohen, "Structural color in porous, superhydrophilic, and self‐cleaning SiO2/TiO2 Bragg stacks," *Small,* vol. 3, no. 8, pp. 1445-1451, 2007.

[180] C. Bronnbauer *et al.*, "Printable Dielectric Mirrors with Easily Adjustable and Well‐Defined Reflection Maxima for Semitransparent Organic Solar Cells," *Advanced Optical Materials,* vol. 3, no. 10, pp. 1424-1430, 2015.

[181] M. Calvo Roggiani, O. Sánchez Sobrado, G. S. Lozano Barbero, and H. R. Míguez García, "Molding with nanoparticle-based one-dimensional photonic crystals: A route to flexible and transferable Bragg mirrors of high dielectric contrast," *Journal of Materials Chemistry, 19, 3144-3148.,* 2009.

[182] L. D. Bonifacio, B. V. Lotsch, D. P. Puzzo, F. Scotognella, and G. A. Ozin, "Stacking the nanochemistry deck: structural and compositional diversity in one‐dimensional photonic crystals," *Advanced Materials,* vol. 21, no. 16, pp. 1641-1646, 2009.

[183] E. Redel, P. Mirtchev, C. Huai, S. Petrov, and G. A. Ozin, "Nanoparticle films and photonic crystal multilayers from colloidally stable, size-controllable zinc and iron oxide nanoparticles," *ACS nano,* vol. 5, no. 4, pp. 2861-2869, 2011.

[184] T. Murata, H. Ishizawa, I. Motoyama, and A. Tanaka, "Preparation of high-performance optical coatings with fluoride nanoparticle films made from autoclaved sols," *Applied optics,* vol. 45, no. 7, pp. 1465-1468, 2006.

[185] T. Kazmierczak, H. Song, A. Hiltner, and E. Baer, "Polymeric one‐dimensional photonic crystals by continuous coextrusion," *Macromolecular rapid communications,* vol. 28, no. 23, pp. 2210-2216, 2007.

[186] W. Cheng, T. Gorishnyy, V. Krikorian, G. Fytas, and E. Thomas, "In-plane elastic excitations in 1D polymeric photonic structures," *Macromolecules,* vol. 39, no. 26, pp. 9614-9620, 2006.

[187] M. Bockstaller, R. Kolb, and E. L. Thomas, "Metallodielectric photonic crystals based on diblock copolymers," *Advanced Materials,* vol. 13, no. 23, pp. 1783-1786, 2001.

[188] S. Guldin and S. Guldin, "Tunable Mesoporous Bragg Reflectors Based on Block Copolymer Self-Assembly," *Inorganic Nanoarchitectures by Organic Self-Assembly,* pp. 117-127, 2013.

[189] Z. Wang *et al.*, "Bioinspired water‐vapor‐responsive organic/inorganic hybrid one‐dimensional photonic crystals with tunable full‐color stop band," *Advanced Functional Materials,* vol. 20, no. 21, pp. 3784-3790, 2010.

[190] P. Lova *et al.*, "Polymer distributed bragg reflectors for vapor sensing," *ACS photonics,* vol. 2, no. 4, pp. 537-543, 2015.

[191] N. Sahu, B. Parija, and S. Panigrahi, "Fundamental understanding and modeling of spin coating process: A review," *Indian Journal of Physics,* vol. 83, no. 4, pp. 493-502, 2009.

[192] M. Schambach, J. Shi, and M. Heizmann, "Spectral reconstruction and disparity from spatio-spectrally coded light fields via multi-task deep learning," in *2021 International Conference on 3D Vision (3DV)*, 2021: IEEE, pp. 186-196.

[193] C. Shin, H.-G. Jeon, Y. Yoon, I. S. Kweon, and S. J. Kim, "Epinet: A fully-convolutional neural network using epipolar geometry for depth from light field images," in *Proceedings of the IEEE conference on computer vision and pattern recognition*, 2018, pp. 4748-4757.

[194]   K. Honauer, O. Johannsen, D. Kondermann, and B. Goldluecke, "A dataset and evaluation methodology for depth estimation on 4D light fields," in *Computer Vision–ACCV 2016: 13th Asian Conference on Computer Vision, Taipei, Taiwan, November 20-24, 2016, Revised Selected Papers, Part III 13*, 2017: Springer, pp. 19-34.

[195]   M. Schambach, J. Shi, and M. Heizmann, "Spectral reconstruction and disparity from spatio-spectrally coded light fields via multi-task deep learning," in *2021 International Conference on 3D Vision (3DV)*, 2021: IEEE, pp. 186-196.

[196]   M. Schambach and M. Heizmann, "A multispectral light field dataset and framework for light field deep learning," *IEEE access,* vol. 8, pp. 193492-193502, 2020.

[197]   A. Beck and M. Teboulle, "A fast iterative shrinkage-thresholding algorithm for linear inverse problems," *SIAM journal on imaging sciences,* vol. 2, no. 1, pp. 183-202, 2009.

[198]   M. Schambach, *Reconstruction from Spatio-Spectrally Coded Multispectral Light Fields*. KIT Scientific Publishing, 2022.

[199]   M. Schambach, *Reconstruction from Spatio-Spectrally Coded Multispectral Light Fields*. KIT Scientific Publishing, 2022.

[200]   https://www.dataphysics-instruments.com/knowledge/understanding-interfaces/pendant-drop-method/#! (accessed.

[201]   F. S. Kratz and J. Kierfeld, "Pendant drop tensiometry: A machine learning approach," *The Journal of Chemical Physics,* vol. 153, no. 9, 2020.

[202]   N. Vargaftik, B. Volkov, and L. Voljak, "International tables of the surface tension of water," *Journal of Physical and Chemical Reference Data,* vol. 12, no. 3, pp. 817-820, 1983.

[203]   https://www.rheosense.com/hs-fs/hub/296746/file-2438655427-pdf/Application_Notes/VROC_-_Principle.pdf (accessed.

[204]   C. J. Pipe, T. S. Majmudar, and G. H. McKinley, "High shear rate viscometry," *Rheologica Acta,* vol. 47, pp. 621-642, 2008.

[205]   https://www.bruker.com/en/products-and-solutions/microscopes/materials-afm/faq.html#ID_intro-to-afm (accessed.

[206]   E. Centurioni, "Generalized matrix method for calculation of internal light energy flux in mixed coherent and incoherent multilayers," *Applied Optics,* vol. 44, no. 35, pp. 7532-7539, 2005.

[207]   Q. Zhang *et al.*, "Fabrication of microlens arrays with high quality and high fill factor by inkjet printing," *Advanced Optical Materials,* vol. 10, no. 14, p. 2200677, 2022.

[208]   P. Gorzelak, M. A. Salamon, R. Lach, M. Loba, and B. Ferré, "Microlens arrays in the complex visual system of Cretaceous echinoderms," *Nature Communications,* vol. 5, no. 1, p. 3576, 2014.

[209]   S. Petsch, S. Schuhladen, L. Dreesen, and H. Zappe, "The engineered eyeball, a tunable imaging system using soft-matter micro-optics," *Light: Science & Applications,* vol. 5, no. 7, pp. e16068-e16068, 2016.

[210] J. Yong, H. Bian, Q. Yang, X. Hou, and F. Chen, "Mini-Review on Bioinspired Superwetting Microlens Array and Compound Eye," *Frontiers in Chemistry,* vol. 8, p. 575786, 2020.

[211] B. Bhushan, *Encyclopedia of nanotechnology* (no. 544.1). Springer Dordrecht, The Netherlands: , 2012.

[212] S. Schlisske *et al.*, "Substrate-independent surface energy tuning via siloxane treatment for printed electronics," *Langmuir,* vol. 34, no. 21, pp. 5964-5970, 2018.

[213] M. Schambach, Q. Zhang, U. Lemmer, and M. Heizmann, "Automated quality assessment of inkjet-printed microlens arrays," *tm-Technisches Messen,* vol. 88, no. 6, pp. 342-351, 2021.

[214] X. Bulliard *et al.*, "Enhanced performance in polymer solar cells by surface energy control," *Advanced Functional Materials,* vol. 20, no. 24, pp. 4381-4387, 2010.

[215] J. Béguelin, R. Voelkel, and T. Scharf, "Commented review on refractive microlenses and microlens arrays metrology," *Journal of Optical Microsystems,* vol. 1, no. 3, pp. 030901-030901, 2021.

[216] F. Liu, Q. Yang, F. Chen, F. Zhang, H. Bian, and X. Hou, "Low-cost high integration IR polymer microlens array," *Optics Letters,* vol. 44, no. 7, pp. 1600-1602, 2019.

[217] Q. Zhang, M. Schambach, Q. Jin, and U. Lemmer, "A Compact Multispectral Light Field Camera Based on an Inkjet-printed Microlens Array and Color Filter Array," 2024.

[218] N. Bolse *et al.*, "A digitally printed optoelectronic nose for the selective trace detection of nitroaromatic explosive vapours using fluorescence quenching," *Flexible and Printed Electronics,* vol. 2, no. 2, p. 024001, 2017.

[219] A. Laddi, S. Sharma, A. Kumar, and P. Kapur, "Classification of tea grains based upon image texture feature analysis under different illumination conditions," *Journal of Food Engineering,* vol. 115, no. 2, pp. 226-231, 2013.

[220] N. Tack, A. Lambrechts, P. Soussan, and L. Haspeslagh, "A compact, high-speed, and low-cost hyperspectral imager," in *Silicon Photonics VII*, 2012, vol. 8266: SPIE, pp. 126-138.

[221] S. Grusche, "Basic slit spectroscope reveals three-dimensional scenes through diagonal slices of hyperspectral cubes," *Applied optics,* vol. 53, no. 20, pp. 4594-4603, 2014.

[222] B. Geelen, N. Tack, and A. Lambrechts, "A compact snapshot multispectral imager with a monolithically integrated per-pixel filter mosaic," in *Advanced fabrication technologies for micro/nano optics and photonics VII*, 2014, vol. 8974: SPIE, pp. 80-87.

[223] Y. Monno, S. Kikuchi, M. Tanaka, and M. Okutomi, "A practical one-shot multispectral imaging system using a single image sensor," *IEEE Transactions on Image Processing,* vol. 24, no. 10, pp. 3048-3059, 2015.

[224] Y. Monno, M. Tanaka, and M. Okutomi, "Multispectral demosaicking using guided filter," in *Digital Photography VIII*, 2012, vol. 8299: SPIE, pp. 204-210.

[225] M. E. Gehm, R. John, D. J. Brady, R. M. Willett, and T. J. Schulz, "Single-shot compressive spectral imaging with a dual-disperser architecture," *Opt. Express,* vol. 15, no. 21, pp. 14013-14027, 2007.

[226] A. Wagadarikar, R. John, R. Willett, and D. Brady, "Single disperser design for coded aperture snapshot spectral imaging," *Applied optics,* vol. 47, no. 10, pp. B44-B51, 2008.

[227] X. Cao, H. Du, X. Tong, Q. Dai, and S. Lin, "A prism-mask system for multispectral video acquisition," *IEEE transactions on pattern analysis and machine intelligence,* vol. 33, no. 12, pp. 2423-2435, 2011.

[228] Y. August, C. Vachman, Y. Rivenson, and A. Stern, "Compressive hyperspectral imaging by random separable projections in both the spatial and the spectral domains," *Applied optics,* vol. 52, no. 10, pp. D46-D54, 2013.

[229] X. Lin, G. Wetzstein, Y. Liu, and Q. Dai, "Dual-coded compressive hyperspectral imaging," *Optics letters,* vol. 39, no. 7, pp. 2044-2047, 2014.

[230] C. V. Correa, C. A. Hinojosa, G. R. Arce, and H. Arguello, "Multiple snapshot colored compressive spectral imager," *Optical Engineering,* vol. 56, no. 4, pp. 041309-041309, 2017.

[231] Y. Bando, B.-Y. Chen, and T. Nishita, "Extracting depth and matte using a color-filtered aperture," in *ACM SIGGRAPH Asia 2008 papers*, 2008, pp. 1-9.

[232] C. Zhou, S. Lin, and S. K. Nayar, "Coded aperture pairs for depth from defocus and defocus deblurring," *International journal of computer vision,* vol. 93, pp. 53-72, 2011.

[233] E. H. Adelson and J. Y. Wang, "Single lens stereo with a plenoptic camera," *IEEE transactions on pattern analysis and machine intelligence,* vol. 14, no. 2, pp. 99-106, 1992.

[234] R. Ng, M. Levoy, M. Brédif, G. Duval, M. Horowitz, and P. Hanrahan, "Light field photography with a hand-held plenoptic camera," Stanford university, 2005.

[235] C. Perwass and L. Wietzke, "Single lens 3D-camera with extended depth-of-field," in *Human vision and electronic imaging XVII*, 2012, vol. 8291: SPIE, pp. 45-59.

[236] K. Berkner and S. Shroff, "Optimization of spectrally coded mask for multi-modal plenoptic camera," in *Computational Optical Sensing and Imaging*, 2011: Optica Publishing Group, p. CMD4.

[237] D. B. Cavanaugh, J. M. Lorenz, N. Unwin, M. Dombrowski, and P. Willson, "VNIR hypersensor camera system," in *Imaging Spectrometry XIV*, 2009, vol. 7457: SPIE, pp. 174-190.

[238] L. Meng, T. Sun, R. Kosoglow, and K. Berkner, "Evaluation of multispectral plenoptic camera," in *Digital Photography IX*, 2013, vol. 8660: SPIE, pp. 96-102.

[239] K. Zhu, Y. Xue, Q. Fu, S. B. Kang, X. Chen, and J. Yu, "Hyperspectral light field stereo matching," *IEEE transactions on pattern analysis and machine intelligence,* vol. 41, no. 5, pp. 1131-1143, 2018.

[240] I. Gheta, M. Mathias, M. Heizmann, and J. Beyerer, "Fusion of combined stereo and spectral series for obtaining 3D information," in *Multisensor,*

Multisource Information Fusion: Architectures, Algorithms, and Applications 2008, 2008, vol. 6974: SPIE, pp. 57-66.

[241]   L. Meng, T. Sun, R. Kosoglow, and K. Berkner, "Evaluation of multispectral plenoptic camera," in *Digital Photography IX*, 2013, vol. 8660: SPIE, pp. 96-102.

[242]   Z. Xiong, L. Wang, H. Li, D. Liu, and F. Wu, "Snapshot hyperspectral light field imaging," in *Proceedings of the IEEE Conference on Computer Vision and Pattern Recognition*, 2017, pp. 3270-3278.

[243]   M. Schambach and F. P. León, "Microlens array grid estimation, light field decoding, and calibration," *IEEE transactions on computational imaging,* vol. 6, pp. 591-603, 2020.

[244]   M. Schambach and F. P. León, "Microlens array grid estimation, light field decoding, and calibration," *IEEE transactions on computational imaging,* vol. 6, pp. 591-603, 2020.

[245]   M. Schambach, J. Shi, and M. Heizmann, "Spectral reconstruction and disparity from spatio-spectrally coded light fields via multi-task deep learning," in *2021 International Conference on 3D Vision (3DV)*, 2021: IEEE, pp. 186-196.

[246]   Q. Zhang *et al.*, "Fabrication of Bragg Mirrors by Multilayer Inkjet Printing," *Advanced Materials,* vol. 34, no. 33, p. 2201348, 2022, doi: https://doi.org/10.1002/adma.202201348.

[247]   M. Kolle, *Photonic structures inspired by nature*. Springer Science & Business Media, 2011.

[248]   M. E. Calvo, S. Colodrero, T. C. Rojas, J. A. Anta, M. Ocana, and H. Míguez, "Photoconducting Bragg mirrors based on TiO2 nanoparticle multilayers," *Advanced Functional Materials,* vol. 18, no. 18, pp. 2708-2715, 2008.

[249]   S. K. Rajendran, M. Wei, H. Ohadi, A. Ruseckas, G. A. Turnbull, and I. D. Samuel, "Low threshold polariton lasing from a solution‐processed organic semiconductor in a planar microcavity," *Advanced Optical Materials,* vol. 7, no. 12, p. 1801791, 2019.

[250]   H. Megahd, P. Lova, and D. Comoretto, "Universal design rules for flory–Huggins polymer photonic vapor sensors," *Advanced Functional Materials,* vol. 31, no. 9, p. 2009626, 2021.

[251]   E. Baka, J. E. Comer, and K. Takács-Novák, "Study of equilibrium solubility measurement by saturation shake-flask method using hydrochlorothiazide as model compound," *Journal of pharmaceutical and biomedical analysis,* vol. 46, no. 2, pp. 335-341, 2008.

[252]   P. Schwerdtfeger, "Absorption, scattering and extinction of light in ice and snow," *Nature,* vol. 222, no. 5191, pp. 378-379, 1969.

[253]   X. Fan, W. Zheng, and D. J. Singh, "Light scattering and surface plasmons on small spherical particles," *Light: Science & Applications,* vol. 3, no. 6, pp. e179-e179, 2014.

[254]   S. Schröder, A. Duparré, L. Coriand, A. Tünnermann, D. H. Penalver, and J. E. Harvey, "Modeling of light scattering in different regimes of surface roughness," *Opt. Express,* vol. 19, no. 10, pp. 9820-9835, 2011.

[255] T. Klaassen, M. P. Van Exter, and J. Woerdman, "Characterization of scattering in an optical Fabry-Perot resonator," *Appl. Opt.,* vol. 46, no. 22, pp. 5210-5215, 2007.

[256] C. Trapalis, M. Karakassides, G. Kordas, and X. Aslanoglou, "Study of a multilayer wavelength-selective reflector prepared by the sol-gel process," *Materials Letters,* vol. 25, no. 5-6, pp. 265-269, 1995.

List of Figures

List of Tables

List of Abbreviations

1DPC   One-dimensional photonic crystal

2D   Two-dimensional

3D   Three-dimensional

AFM   Atomic force microscopy

APTES   3-aminopropyltriethoxysilane

BFL   Back focal length

CF   Color filter

CFA   Color filter array

CIJ   Continuous inkjet

CLSM   Confocal laser scanning microscope

CVD   Chemical vapor deposition

DOD   Drop on demand

dpi   Dots per inch

EGMPE   Ethylene glycol monopropyl ether

E-jet   Electrohydrodynamic jet

FF   Fill factor

FFL   Front focal length

IR   Infrared

KET   Key enabling technology

LIDAR   Light detection and ranging

LIGA   Lithographie, Galvanoforming, Abformung

ML   Microlens

MLA   Microlens array

MTF   Modulation transfer function

NA   Numerical aperture

NIR   Near infrared

OTF   Optical transfer function

PBG   Photonic bandgap

PDMS   Polydimethylsiloxane

PET   Polyethylene terephthalate

PhTF   Phase transfer function

PM   Polymer matrix

PMMA   Poly(methyl methacrylate)

PTFE   Polytetrafluoroethylene

PVD   Physical vapor deposition

RI   Refractive index

RMS   Root mean square

ROC   Radius of curvature

rpm   Revolutions per minute

SAM   Self-assembled monolayer

SDG   Sustainability development goal

SEM   Scanning electron microscopy

SFE   Surface free energy

TEOS   Triethoxyoctylsilane

TEPS   Triethoxyphenylsilane

TTFPS   Trimethoxy-(3,3,3-trifluorpropyl)-silane

UV   Ultraviolet

VCSEL   Vertical-cavity surface-emitting laser

List of Symbols

$\Delta\rho$	Density difference between the two phases
Δd	Thickness resolution
ΔP	Pressure difference
Γ	Shear stress
Δ	Ellipsometric phase
Ψ	Ellipsometric amplitude component
α_j/β_j	Dynamic weight trained with the additional loss function L_α/L_β
β_r	Direction cosine in the y-direction of the reflected wave
β_t	Direction cosine in the y-direction of the refracted (transmitted) wave
γ	Surface tension
$\gamma^D{}_{LG}$	Dispersive component of the surface tension of the liquid
$\gamma^D{}_{SG}$	Dispersive component of the surface free energy
$\gamma^P{}_{LG}$	Polar component of the surface tension of the liquid
$\gamma^P{}_{SG}$	Polar component of the surface free energy
γ_{SG}	Surface tension between solid and ambient gas
γ_{SL}	Interfacial tension between the liquid and solid
γ_{LG}	Surface tension of the liquid
$\dot{\gamma}$	Shear rate of a Newtonian fluid
δ	Phase difference
ε	Inverse of the radius of curvature
η	Effective optical admittance
θ_0	Angle of incidence
θ_C	Contact angle

θ_r	Angle of reflection
θ_t/θ_1	Angle of refraction (transmission)
λ	Wavelength
λ_0	Wavelength of light in free space
λ_c	Central wavelength of a Bragg mirror
μ	Dynamic viscosity
ξ	Spatial frequency
ξ_c	Cut-off frequency
ρ	Density
τ	Amplitude transmission coefficient
υ	Kinematic viscosity
φ	Half aperture angle
ω_i	Angular frequency of the electric field of the incident wave
ω_r	Angular frequency of the electric field of the reflected wave
ω_t	Angular frequency of the electric field of the transmitted wave
ϱ	Complex amplitude reflectance coefficient ratio
A	Area
B_o	Bond number
Ca	Capillary number
D	Entrance pupil diameter
$\boldsymbol{E}$	Electric field
$\boldsymbol{E_i}$	Electric field of the incident wave
$\boldsymbol{E_{i0}}$	Amplitude vector of the electric field of the incident wave
$\boldsymbol{E_r}$	Electric field of the reflected wave
$\boldsymbol{E_{r0}}$	Amplitude vector of the electric field of the reflected wave

154

E_p — Electric field vector component oscillating parallel to the incident plane

E_s — Electric field vector component oscillating perpendicular to the incident plane

$\boldsymbol{E_t}$ — Electric field of the transmitted wave

$\boldsymbol{E_{t0}}$ — Amplitude vector of the electric field of the transmitted wave

F — Focal point

FF — Fill factor

$FWHM$ — Full width at half maximum

G_{main} — Gradient of the main loss function

$G_{aux,j}$ — Gradient of the auxiliary loss function

$\boldsymbol{H}$ — Magnetic field

I — Intensity

$\boldsymbol{L}$ — Light field

$\boldsymbol{L^*}$ — Spectrally-encoded light field

$L_{\alpha/\beta}$ — Additional loss functions

$L_{aux,j}$ — Auxiliary loss functions

L_{main} — Main loss function

$\boldsymbol{M}$ — Binary spectral encoding mask

M — Contrast/modulation

MTF — Modulation transfer function

N — Number of bilayers

$N_{0/1/2/3/4}$ — Number of droplets

N_{aux} — Number of auxiliary loss functions

$N_{dpi,x/y}$ — Dpi number for the x- and y-direction

Oh — Ohnesorge number

NA — Numerical aperture

P	Lateral pitch of a microlens array
Q	Flow rate
R	Reflectance
Re	Reynolds number
ROC	Radius of curvature
S_q	Surface root-mean-square roughness
T	Transmittance
V	Volume
V_{drop}	Single droplet volume
W	Stopband width of the Bragg mirror
We	Weber number
Y	Input optical admittance
Z	Inverse of the Ohnesorge number
a	Radius of the lens
d	Diameter of the lens
d_l	Thickness of a layer
d_H	Thickness of the high-refractive-index layer
d_L	Thickness of the low-refractive-index layer
f	Focal length
$f/\#$	f-number
g	Gravitational acceleration
h	Height
l	Length
l_{H2}	Position of the secondary principal plane with respect to the vertex of the second surface of the lens
n	Refractive index

156

n_i Refractive index of the surrounding medium

n_H Refractive index of the high-refractive-index layer

n_L Refractive index of the low-refractive-index layer

n_S Refractive index of the substrate

r Amplitude reflection coefficient

s_0 Unit wave vector

t Time

v Velocity of the droplet

w Width

w_i Weight assigned to task i

y Characteristic optical admittance of the medium

y_0 Optical admittance in free space

List of Publications

Peer-reviewed publications

Q. Zhang, Q. Jin, A. Mertens, C. Rainer, R. Huber, J. Fessler, G. Hernandez-Sosa, and U. Lemmer, Fabrication of Bragg Mirrors by Multilayer Inkjet Printing, Advanced Materials 34(33) (2022) 2201348.

Q. Zhang, M. Schambach, S. Schlisske, Q. Jin, A. Mertens, C. Rainer, G. Hernandez-Sosa, M. Heizmann, and U. Lemmer, Fabrication of microlens arrays with high quality and high fill factor by inkjet printing, Advanced Optical Materials 10(14) (2022) 2200677.

Q. Zhang, M. Schambach, Q. Jin, M. Heizmann, and U. Lemmer, A Compact Multispectral Light Field Camera Based on an Inkjet-printed Microlens Array and Color Filter Array, 2024, **submitted**.

Q. Jin, **Q. Zhang**, C. Rainer, H. Hu, J. Chen, T. Gehring, J. Dycke, R. Singh, U. W. Paetzold, G. Hernández-Sosa, R. Kling, and U. Lemmer, Inkjet-Printed Optical Interference Filters, Nature Communications, 2024, **in press**.

M. Seiberlich, **Q. Zhang**, A.V. Tunc, K. Xia, L.A. Ruiz - Preciado, S. Schlisske, K. Falis, N. Strobel, U. Lemmer, and G. Hernandez-Sosa, Inkjet-Printed Microlenses Integrated onto Organic Photodiodes for Highly Accurate Proximity Sensing, Advanced Sensor Research (2023) 2300004.

Q. Jin, **Q. Zhang**, J. Chen, T. Gehring, S. Eizaguirre, R. Huber, G. Gomard, U. Lemmer, and R. Kling, High Dynamic Range Smart Window Display by Surface Hydrophilization and Inkjet Printing, Advanced Materials Technologies 7(5) (2022) 2101026.

M. Schambach, **Q. Zhang**, U. Lemmer, and M. Heizmann, Automated quality assessment of inkjet-printed microlens arrays, tm-Technisches Messen 88(6) (2021) 342-351.

P. Maier, A. Kotz, J. Hebeler, **Q. Zhang**, C. Benz, A. Quint, M. Kretschmann, T. Harter, S. Randel, U. Lemmer, W. Freude, T. Zwick, and C. Koos, Freeform terahertz structures fabricated by multi-photon lithography and metal coating, 2024, **submitted**.

R. Huber, S. Eizaguirre, H. Mescher, C. Willig, **Q. Zhang**, and U. Lemmer, Fully Printed Temperature Sensor Array Comprising 625 60× 60 µm2 pixels, Advanced Sensor Research 2(2) (2023) 2200031.

H. Mescher, F. Schackmar, R. Huber, H. Eggers, M. Zuber, E. Hamann, G. Gramlich, J. Dangelmaier, **Q. Zhang**, A.G. Rösch, T. Zwick, G. Hernandez-Sosa, U. W. Paetzold, and U. Lemmer, Origami-inspired perovskite X-ray detector by printing and folding, npj Flexible Electronics 7(1) (2023) 9.

Conference contributions

Q. Zhang, Q. Jin, A. Mertens, R. Huber, J. Fessler, G. Hernandez-Sosa, U. Lemmer, Fabrication of patterned, flexible and large-scale Bragg mirrors by inkjet printing (Conference Presentation), Nanoengineering: Fabrication, Properties, Optics, Thin Films, and Devices XIX, SPIE, 2022, p. PC1220203.

U. Lemmer, **Q. Zhang**, Q. Jin, A. Roesch, Large area dichroic mirrors by multilayer inkjet printing, Novel Optical Systems, Methods, and Applications XXVI, SPIE, 2023, p. 126650H.

Q. Jin, **Q. Zhang**, J. Chen, T. Gehring, S. Eizaguirre Cabrera, R. Huber, G. Gomard, U. Lemmer, R. Kling, Pixelated Smart Window for High Dynamic Range Signage Displaying Applications, 6th Smart Materials and Surfaces (SMS 2021), Mailand, Italien, 20.10. 2021–22.10. 2021, 2021.

M. Schambach, **Q. Zhang**, U. Lemmer, M. Heizmann, Automated Quantitative Quality Assessment of Printed Microlens Arrays, M. Heizmann| T. Längle (2020) 51.

R. Huber, H. Mescher, G. Gramlich, **Q. Zhang**, G. Hernandez-Sosa, U. Lemmer, Fully printed high-density temperature sensor array, Organic and Hybrid Sensors and Bioelectronics XV, SPIE, 2022, p. PC122100F.

Acknowledgments

In this final section of the thesis, I would like to take this opportunity to express my gratitude to everyone who has inspired, supported, and accompanied me on this journey. Whether in research, organization, or life, you have all helped to bring this thesis to completion.

First and foremost, I wish to thank my supervisor, Prof. Dr. Uli Lemmer. I would like to thank him for offering me this Ph.D. position in the first place, as well as for his deepest support throughout my Ph.D. career, be it in terms of vision, research guidance, in-depth scientific discussions, great freedom to explore, trust in difficult times in academic aspects, and most importantly, guidance in my personal development and pushing me forward. His encouragement, humor, enthusiasm, dedication, and expertise have always inspired me, not only as a mentor in research but also in life. In addition, I would like to thank Prof. Harald Giessen for agreeing to be my second referee.

In addition, I am very fortunate and grateful to have been able to collaborate with many research groups during this process. I would like to thank Prof. Gerardo Hernandez-Sosa for guiding my Ph.D. process, especially regarding the printing activities, and for ensuring my experiments at innovationLab go smoothly. In addition, I would like to thank Dr. Guillaume Gomard for providing me with research ideas and broadening my research directions during the early stages of my PhD. This thesis was made possible thanks to the Light Field Camera project, so I would like to thank Prof. Michael Heizmann for supervising this collaborative project, as well as for his careful revision of the generated publications. I would also like to thank Dr. Maximilian Schambach for his great cooperation in this project and his support with the experimental equipment and algorithms.

I would also like to take this opportunity to thank my colleague Dr. Stefan Schlißke for his excellent guidance and mentoring during the early stages of my Ph.D., for teaching me about inkjet printing during the initial stages, and for providing me with wonderful ink formulas. I would like to thank my other colleagues at InnovationLab, Mervin, Christian, and Kai, for their help and fun academic and personal interactions during my experiments there.

I would also like to thank many of my colleagues at LTI: Adrian for the ellipsometer measurements, Christian for the viscosity measurements, Santiago for helping me with the UV LED boards, Ihteaz for the TiO_2 inks, Fabian and Helge for the advice on inkjet printing, and Roja for helping with the PL measurements. I would like to give many thanks to Raphael, Jan, Andres, Junchi, and Hankun for their careful reading of my thesis and suggestions for revisions.

I am particularly grateful to my office mates Robert, Adrian, Jan, and Hankun, who have made every day here so much fun. With them, there have been countless enjoyable moments, and we have all become good friends. I would like to thank other members of our lunch group, Junchi, Andres, and Leo. In addition, I would like to thank my other LTI colleagues Raphael, Isabel, Henning, Andreas, Andre, and the rest of the MNOS and LTI colleagues for the fun times at research and other events, as well as my students Yue, Fengxiang, Wenzhe, Weimu, and Marie. I would like to thank Christian Kayser for his support in all aspects of the experimental process and Jurana, Nicole, Astrid, and Claudia for their support in administrative matters.

I would like to thank 3DMM2O for the funding and the great platform; I have benefited a lot from the events, from other young scientists in various fields, and from the scientific and management modules.

Thank you to the team of Prio Optics: Qihao, Andres, and Gerda, with whom I have worked side by side this last year, for pushing the technology transfer based on the topic of my PhD thesis and exploring all its possibilities. It has been quite an adventure, and I would like to thank you for all the support.

Finally, I wish to express my gratitude to my most beloved family; it is their constant selfless support and love that has enabled me to accomplish milestones. This love is the cornerstone of this thesis. A special thanks to my boyfriend, who has been the best colleague and partner and whose constant and all-encompassing support has allowed me to move forward without hesitation.